Carnegie Mellon University
MELLON COLLEGE OF SCIENCE

THESIS

SUBMITTED IN PARTIAL FULFILLMENT OF THE REQUIREMENTS
FOR THE DEGREE OF

DOCTOR OF PHILOSOPHY IN THE FIELD OF PHYSICS

TITLE: "Galaxy Clusters in the Presence of Substructure."

PRESENTED BY: Evan Tucker

ACCEPTED BY THE DEPARTMENT OF PHYSICS

Matthew Walker	5/20/19
MATTHEW WALKER, CHAIR PROFESSOR	DATE

Scott Dodelson	5/23/19
SCOTT DODELSON, DEPT HEAD	DATE

APPROVED BY THE COLLEGE COUNCIL

Rebecca Doerge	5/23/19
REBECCA DOERGE, DEAN	DATE

Galaxy Clusters in the Presence of Substructure

by

Evan Tucker

Submitted in partial fulfillment of the
requirements for the degree of
Doctor of Philosophy
at
Carnegie Mellon University
Department of Physics
Pittsburgh, Pennsylvania

Advised by Professor Matthew G. Walker

May 17, 2019

Abstract

My thesis focused on developing an end-to-end program for dynamical analyses of galaxy clusters. The main interest of the thesis is to develop a dynamical mass estimator used for galaxy clusters that has the capability to account for substructure which is currently a limitation on most dynamical mass estimators. Through already established collaborations, I had access to a cutting-edge multi-object spectrograph, the Michigan/Magellan Fiber System (M2FS), on the 6.5m Clay-Magellan Telescope in Chile; therefore, a signifiant portion of my thesis involved the collection, data reduction, and spectral analysis of new galaxy spectra. As part of this collaboration, I became a core member of the M2FS observation team, which sent me to Chile about a half dozen times to aid in the observations with M2FS.

The early portions of my thesis project focused on the handling of newly obtained galaxy spectra with M2FS. The first M2FS observations of galaxies within clusters were collected in November 2013 as a pilot program for testing this instruments capabilities at observing unresolved stellar populations. My goal with this portion of the project was to familiarize myself with the M2FS instrument and it's observations as well as to learn how to reduce the collected data. As part of this familiarization, I learned first-hand how to observe with M2FS and aid in the collection of other observations over a variety of scientific interests. While reducing my own observations, I developed a front-end GUI to simplify the data reduction process and help expedite the reduction of future observations. Although, the data reduction pipeline I developed works well at reducing a subset of M2FS observations, I was unable generalize the pipeline fully to handle all M2FS configurations. This is due to variations between configurations such as resolution settings, multi-order spectra, and wavelength coverages.

I also helped in the collection of spectra with M2FS over a range of scientific purposes. For projects more related to my own work, I collected spectra for galaxies within the clusters Abell 1689, MACS0429, and CL 1301. MACS0429 was part of my own research project and so I detail in this thesis the targeting, observation, data reduction, and spectral fits.

In a first published paper, we report the results of a pilot program to use the Magellan/M2FS spectrograph to survey the galactic populations and internal kinematics of galaxy clusters. For this initial study, we present spectroscopic measurements for 223 quiescent galaxies observed along the line of sight to the galaxy cluster Abell 267 ($z \sim 0.23$). We develop a Bayesian method for modeling the integrated light from each galaxy as a simple stellar population, with free parameters that specify redshift ($v_{\rm los}/c$) and characteristic age, metallicity ([Fe/H]), alpha-abundance ([α/Fe]), and internal velocity dispersion ($\sigma_{\rm int}$) for individual galaxies. Parameter estimates derived from our 1.5-hour observation of A267 have median random errors

of $\sigma_{v_{\rm los}} = 20$ km s^{-1}, $\sigma_{\rm Age} = 1.2$ Gyr, $\sigma_{\rm [Fe/H]} = 0.11$ dex, $\sigma_{[\alpha/{\rm Fe}]} = 0.07$ dex, and $\sigma_{\sigma_{\rm int}} = 20$ km s^{-1}.

In a second paper currently under review, we develop and implement a model to analyze the internal kinematics of galaxy clusters that may contain subpopulations of galaxies that do not independently trace the cluster potential. The model allows for substructures within the cluster environment, disentangles cluster members from contaminating foreground and background galaxies, and includes an overall cluster rotation term as part of the cluster kinematics. We estimate the cluster velocity dispersion and/or mass while marginalizing over uncertainties in all of the above complexities. We use these results to explore the sensitivity of inferred cluster properties to the treatment of substructure. Compared to a model that assumes no substructure, our substructure model reduces the dynamical mass of A267 by $\sim 22\%$ and shifts the cluster mean velocity by ~ 100 km s^{-1}, approximately doubling the offset with respect to the velocity of A267's brightest cluster galaxy. Embedding the spherical Jeans equation within this framework, we infer for A267 a halo of mass $M_{200} = 7.0 \pm 1.3 \times 10^{14} M_{\odot}/h$ and concentration $\log_{10} c_{200} = 0.71 \pm 0.38$, consistent with the mass-concentration relation found in cosmological simulations.

A third paper (in preparation) presents the results of new M2FS spectroscopy for the cluster MACS0429. This cluster is part of the Cluster Lensing and Supernova Survey with Hubble (CLASH) and was the only CLASH cluster observable in the southern sky not covered by the spectroscopic follow-up program CLASH-VLT. We obtained over 700 spectra of ~ 300 unique galaxies along with a couple dozen strongly lensed background galaxies. We fit these spectra using the population synthesis previously model applied to Abell 267 thus obtaining parameter estimates describing the mean redshift, age, metallicity, chemical enrichment and velocity dispersion of each galaxy's stellar population.

Acknowledgments

I'd like to thank all the graduate students, post-docs and professors that helped me reach this pinnacle. Mario, for helping with observations and data reduction; you've taught me so much about the technical side of observational astronomy and instrumentation. Ed, for sharing in your expertise, life experiences, and helping to pass the time while observing in Chile. My committee, Rachel, Sergey, Hy, and Peter, for listening to my progression, showing patience as I learned, reading this thesis, and guiding my throughout this whole process.

And of course, I'd like to thank my wonderful advisor Matt. You provided a nurturing environment that truly helped me grow as a researcher. I cannot thank you enough for your support and guidance.

Lastly and most importantly, I'd like to dedicate this entire thesis to my life partner and best friend Alexandra. Without your unwavering dedication and support these past six years, I would have never been able to accomplish as much as I did. Everything that we achieve going forward is directly tied to the support you provided during the hardest years of my life. You are my rock, my protection, my everything. I love you.

Contents

List of Tables

List of Figures

Chapter 1

Introduction

In the 18th century, while hunting for comets within the Solar System, French astronomer Charles Messier continually observed objects that resembled comets but were not. Frustrated by this, he began compiling a list of these objects in 1771, so that he would not waste his time in the future with them. Over the next decade, he perpetually added to the growing list of about 100 objects. Unfortunately for Messier (or fortunately depending on how you look at it), his legacy within astronomical history has been directly tied to this list, now known as the Messier Catalogue. Unbeknownst to Messier, these objects were not local to the Solar System; in fact, some of these objects were not even local to the Milky Way galaxy!

Over a similar period of time, British astronomer F. William Herschel was also independently compiling a catalogue of similar celestial objects. Both Messier and Herschel noted the whispy, cloud-like features of these objects and fittingly called them nebulae. Nowadays, thanks to centuries of scientific advancement, the objects in these two catalogues are sub classified as open clusters, globular clusters, star forming regions, supernova remnants, planetary nebulae, and galaxies. Although Messier and Herschel did not study these objects in great detail, they did note that some of the nebulae (now known to be distant galaxies) appeared to form groups on the sky. This in essence was the first theorization of clusters of galaxies.

The true distance to these extragalactic nebulae was unknown until the early 20th century when American astronomers Vesto Slipher and Edwin Hubble began observing these galaxies spectroscopically in order to determine their radial velocities. The bulk of this scientific progress was pioneered by Slipher who was the first astronomer to measure a radial velocity for a spiral nebula. Because spiral galaxies are more extended (and now we know far more distant) than Milky Way stars, these measurements were tricky and could initially only be made for nearby bright galaxies such as Andromeda (M31 in Messier's catalogue, and NGC 224 in Herschel's). With about a dozen measured galaxy radial velocities, many astronomers began theorizing that these galaxies were far more distant than stars, and used these velocities to measure the motion of the Sun through the cosmos. Although astronomers disagreed on the

calculation of the solar motion because of the noisiness of the radial velocity data, there was consensus on one peculiar fact about the data: the majority of the spiral galaxies were receding.

Concurrent to these radial velocity measurement, Albert Einstein and Willem de Sitter were enthralled in a scientific debate surrounding two solutions to Einstein's field equations from his recently postulated General Theory of Relativity. According to de Sitter's solution, more distant objects recede at larger velocities, which was contradicted by Einstein's solution. As the debate continued into the 1920s, more astronomers began to accept General Relativity and gave increased credence to de Sitter's solution. In light of de Sitter's prediction on radial velocities and the observed trend that most galaxies are moving away from the Milky Way, astronomers were interested in establishing a relationship between observed galaxy properties and radial velocity. In 1922 Carl Wirtz established a a well-defined observational relationship between a galaxy's radial velocity and its apparent magnitude [1]. Although this relationship was compelling, it took two more years before a direct relation was established between distance and radial velocities.

In 1924 Edwin Hubble discovered Cepheid variable stars in galaxies with measured radial velocities, and used these stars to measure more accurate distances [2]. With these tools in hand Hubble measured the distances to over a dozen galaxies with measured radial velocities, plotted velocity as a function of distance and, in 1929, generated the first velocity-distance relationship which we now refer to as the Hubble Diagram [3]. The Hubble Diagram empowered astronomers to estimate distances to galaxies just from each galaxy's radial velocity. With distances in hand, the original musings of Messier and Hershel could be revisited and further investigated; both astronomers noticed galaxies appeared to "cluster" on the sky, and, with the added dimension of distances, nearby clusters such as Coma and Virgo were confirmed as systems.

Of the three most well studied clusters, the Coma Cluster holds a unique position in the history of galaxy cluster science (Virgo and Perseus are the other two). In 1785, while compiling his catalogues of nebulae, Herschel was one of the first Western astronomers to notice the cluster of galaxies in the Coma constellation [4]. Over the next 150 years, more than 300 galaxies were observed within the Coma cluster [5], and the first radial velocity measurements of some of the galaxies were made in 1931 [6]. Two years later, Swiss astronomer Fritz Zwicky published the first of a series of papers that fundamentally transformed astronomers' perception of the universe and, in essence, cemented galaxy clusters as one of the most important laboratories in cosmology and astrophysics.

Zwicky analyzed the few radial velocity measurements published for galaxies within the Coma cluster and deduced via the Virial Theorem the mass of the cluster [7]. Zwicky was one of the first astronomers to conduct such an analysis, but the truly ground breaking aspect of this study derived from the fact that Zwicky measured a mass of $> 4.5 \times 10^{13} M_{\odot}$ which far exceed the mass calculated by simply adding up

the mass of each individual galaxy [8]. Zwicky theorized that there must be some sort of invisible matter, which Zwicky named *dunkle materie* (dark matter), within the cluster system that dominates the total mass of the cluster and provides a strong enough gravitational potential to describe the motion of the galaxies within the Coma cluster. The theory of dark matter took nearly four decades to be widely accepted within the astronomical community, but nowadays it is one of the most puzzling problems tackled by physicists, astronomers, and cosmologists alike. And to this day galaxy clusters are still a unique probe of dark matter.

The dark matter problem is one of the main driving forces behind this thesis project. For this reason, the remainder of this chapter will focus on how galaxy clusters are used to study dark matter, which will lead into the main motivation for the thesis project as well as the main question that is trying to be solved. The remainder of the chapter will be laid out as follows: §1.1 will describe how clusters are used in the field of cosmology and how this leads to constraints on theories of dark matter, §1.2 will give a brief overview of the various methods for measuring galaxy cluster masses as well as the limitations of each method, and lastly §1.3 will list and explain some of the main methods currently used to study galaxy cluster substructure.

1.1 Galaxy Clusters as Cosmological Probes

1.1.1 Current Cosmological Models

In 1933, Fritz Zwicky discovered dark matter in the Coma galaxy cluster [7]; six years later Horace Babcock discovered that the Andromeda galaxy is rotating at a much higher rate than predicted indicating that the majority of its mass is at large radii [9]. Twenty years thereafter, Franz Kahn and Lodewijk Woltjer discovered that there must be significantly more matter within in the Milky Way - Andromeda system than their stellar mass in order to explain their gravitational attraction [10]. These early studies laid the ground work for the dark matter revolution that began in earnest in the 1970s [11]. Numerous observational and theoretical papers were published at this time that strongly showed that the Universe that we observe today (namely galaxies in the local universe) would be drastically different without the existence of dark matter [12, 13, 14]. These early studies challenged astronomers' fundamental perception of the matter within the universe. Prior to these results, astronomers believed that the majority of the matter in the universe was made up of baryons; however, based on the observations and theoretical frameworks mentioned above, astronomers realized that baryons made up only a small portion of the matter in the universe and the vast majority was in fact dark matter. These realizations laid the groundwork for one of the most important aspects of the most widely accepted cosmological model: ΛCDM.

In ΛCDM cosmology, the *DM* refers to dark matter and the fact that dark matter dominates gravitationally. Because the presence of dark matter can only be inferred

from its gravitational effect (in other words it does not emit light like baryons), there are many theories pertaining to the particle nature of dark matter. The majority of the theories of dark matter have been ruled out experimentally over the past few decades; however, in order to give historical context to our current understanding of the Universe, I will still give details of the theories that are no longer accepted or considered.

Early efforts by particle physicists to describe candidate dark matter particles were broken down into three families: hot, warm, and cold dark matter. A neutrino with mass $\sim$ 30eV is the prototype particle for hot dark matter because of its early time for non-interaction and relativistic nature until later times (see [15] for a good review). Neutrinos are of particular interest for dark matter theorists because of all candidate particles it is the only one to have been detected with earth-bound experiments [16]. Elementary particles with a larger mass than neutrinos $\sim$ 1keV have been theorized as warm dark matter candidates. Recent particle theory has suggested a sterile neutrino as one of the more attractive warm dark matter particle candidates [17]. The last and most widely accepted family of dark matter theories (for the reasons described below) uses much more massive particles $\sim$ 100GeV and is therefore referred to as cold dark matter.

There are many candidate particles that are considered cold dark matter and each candidate has its own mass scale. Some of the more popular particles put forward by particle theorists and astrophysicists are: a supersymmetric particle (photino with mass $\sim$ 0.5GeV, a Higgs fermion with mass $\gtrsim$ 5GeV or a gravitino are a few options suggested by [18]), an *invisible* axion [19], or a weakly interacting massive particle (WIMPs [20]). Others have put forward non-particle theories for dark matter such as massive compact halo objects (MaCHOs [21, 22]) which is a wide class of baryonic objects that emit little to no electromagnetic radiation and range from primordial black holes to white dwarfs. In order to search and put constraints on dark matter candidates, researchers use direct detection experiments, searches for electromagnetic radiation produced via decay or annihilation, as well as gravitational detection such as dynamics of dark matter halos or microlensing events for MaCHOs.

Out of the three families of dark matter theory, cold dark matter is by far the most widely accepted today. The first major triumph for cold dark matter came in the 1980s with the advancement of computational power and the first galaxy redshift survey [23]. The first cosmological simulations carried out used a hot dark matter model because neutrinos (the most favored of the hot dark matter particles) were already known to exist. However, this simulated universe when compared to the observed universe from the first redshift survey looked vastly different [24]. Because of the free-streaming cut-off in the power spectrum for hot dark matter, galaxies only form in superclusters which results in a much more clustered galaxy population than presented in redshift surveys. A few years later the first cosmological simulations were carried out with cold dark matter with much better success [25]. These simulations

looked remarkably similar to the redshift surveys.[1]

In the past few decades there has been mounting evidence in support of cold dark matter from halo formation histories (more on this in §1.2 below) to dark matter halo abundances and structure. The multi-wavelength analysis of the colliding galaxy cluster (now known as the Bullet Cluster) in 2004 is by far the most compelling evidence for dark matter and is frequently referred to as the smoking gun for the existence of dark matter [26, 27].

Despite the many triumphs of cold dark matter on large scales, there have been a few problems presented in the past few decades that result from discrepancies between observations and dark matter only simulations on small scales. The missing satellite problem arises from a decreased number of observed satellites of the Milky Way compared to dark matter only simulations of Milky Way sized halos [28, 29]. However, this tension has mostly been solved in part by new full sky surveys such as SDSS and DES which have discovered tens of new dwarf galaxies [30] as well as advancement in simulating baryonic physics in these simulations which decreases the number of subhalos that form satellite galaxies [31].

A second issue with the cold dark matter paradigm on small scales is known as the core - versus - cusp problem. According to dark matter only simulations, the density profiles of dark matter halos should rise steeply at small radii (known as cusps) [32]. However, this prediction differs from some observations of dwarf galaxies, which show density profiles with roughly constant density cores [33]. Similar to the missing satellites problem, this tension has mostly been resolved when dark matter only simulations begin to incorporate the effects of baryonic feedback. Furthermore, the effects of baryons on the creation of cores is related to the amount of mass in the stars formed within the central regions of the galaxy [34, 35].

Comparison of the Milky Way classical dwarfs' dark matter halos with subhalos formed in dark matter only simulations showed that the classical dwarfs actually reside in halos with smaller central densities than the most massive subhalos [36, 37]. This discrepancy suggested that the most massive subhalos have failed to form galaxies which is counterintuitive because if smaller subhalos form stars then the more massive subhalos should be "too big to fail". Feedback from baryonic physics is unable to fully remedy this issue; however, interactions between satellite galaxies and the Milky Way (tidal stripping, disk shocking, and ram pressure stripping) could potentially act as feedback which would reduce the central masses of satellite galaxies thus explaining the too-big-to-fail problem (see [38], for example).[2] The cold dark matter paradigm, despite these problems and potential solutions, is still the most widely accepted model

[1] In fact, these simulations were carried out for a few different cosmological parameters, and the authors claim (back in 1985) that the parameters $\Omega_m = 0.2$ and $\Omega_\Lambda = 0.8$ produce the most comparable results, which is close to the currently accepted values for these parameters far earlier than any physical evidence for a cosmological constant!

[2] For a more complete discussion on the small-scale challenges to the cold dark matter paradigm, I highly suggest the excellent recent review [39].

for dark matter, and is one of the key components of ΛCDM cosmology.

The accelerated expansion of the universe is the final component of ΛCDM cosmology. In 1998 two separate studies of distant supernovae independently determined that the expansion of the universe has been accelerating over the past 5 billion years [40, 41]; however, this discovery was the culmination of a theoretical and observational endeavor that began 80 years prior with Einstein. Shortly after completing his General Theory of Relativity (GR), Einstein developed one of the first GR cosmological models which correctly assumed that the universe is homogenous and matter-filled, but incorrectly assumed that the universe was static. Einstein quickly realized that these two assumptions were at odds with one another, so he added the now infamous "cosmological constant" Λ to the GR field equation which essentially added a repulsive force to the Universe that could balance attractive gravity.

For the most part, cosmological models through the 1980s did not find enough cosmological evidence to include the unphysical cosmological constant. However, evidence in favor of Λ began to accumulate towards the end of the 1980s and throughout the 1990s. Large scale clustering analyses favored a matter density less than $\Omega_m < 0.5$ [42, 43], which in combination with standard inflationary cosmology predictions of a spatially flat universe indicated that a new energy component of the universe had a density parameter $1 - \Omega_m$ [44]. As cosmological simulations continued to advance, many simulation studies tested a variety of different cosmological models, including a flat-ΛCDM universe. The large-scale structure produced by these simulations was compared to observations which showed remarkable similarities between the flat-ΛCDM model and the observed universe [25, 45]. Globular clusters with ages older than a Universe with a high Hubble parameter also pointed towards a cosmological constant [46, 47, 48]. And finally in 1998 two independent studies of high redshift supernovae almost simultaneously discovered that for the last 5 billion years the universe has actually increased its expansion rate [40, 41], thus providing the astronomical community with enough evidence to accept Λ as a key component of our cosmological model.[3] And because the origin of this repulsive force is completely unknown, and in an homage to the great Fritz Zwicky and dark matter, astronomers quickly began to use the term dark energy as the source of the accelerated expansion [50].

Table 1.1: Current cosmological parameter estimates for flat-ΛCDM cosmology. These values come from a joint analysis of DES Y1 + Planck + JLA + BAO [51]. In ΛCDM the equation of state of dark energy is fixed at $w = -1$. Included here is the parameter estimate for w to show that even when this assumption is not made, the value is still close to -1

Parameter	Value	Description
h	$0.685^{+0.005}_{-0.007}$	Commonly referred to as the dimensionless Hubble Parameter, h is used to reparameterize Hubble's constant $H_0 = 100h$ km s^{-1} Mpc^{-1}.
Ω_M	$0.298^{+0.007}_{-0.007}$	Matter density parameter of the universe: $\Omega_M = \rho_M/\rho_{\rm crit}$.
Ω_b	$0.0479^{+0.0007}_{-0.0008}$	Baryonic matter density parameter.
Ω_Λ	$0.702^{+0.007}_{-0.007}$	Dark energy density parameter.
σ_8	$0.805^{+0.015}_{-0.015}$	Normalization of the matter power-spectrum at $z = 0$
n_p	$0.973^{+0.005}_{-0.004}$	Slope of primordial power-spectrum.
w	$-1.00^{+0.05}_{-0.04}$	Dark energy equation of state.

1.1.2 The Halo Mass Function

The current most widely accepted and tested cosmological model flat-ΛCDM is commonly parameterized by 5 free parameters: Ω_M, Ω_b, σ_8, h, and n_p, with two additional constraints: $\Omega_M + \Omega_\Lambda = 1$ (flat curvature) and $w = -1$ (dark energy equation of state). Table 1.1 lists and describes the parameters in ΛCDM cosmology as well as gives the current best estimates. In a flat-ΛCDM universe, adiabatic density fluctuations from the early universe grow gravitationally in a background that is undergoing accelerated expansion. The estimates for the model parameters listed in Table 1.1 are obtained from many different probes that compare analytic and semi-analytic models with simulations and observations across cosmic time. Combinations of some probes produce much tighter parameter estimates than a single probe because each probes' posteriors are orthogonally degenerate. For example, constraints on σ_8 and Ω_M from the high mass tail of the halo mass function are strongly degenerate [52], while constraints on the same two parameters from observations of the cosmic microwave background

[3] And in the two decades since these studies there has been only more evidence in support of an accelerated expansion. As David Weinberg so eloquently summarized in his review: "A wide range of observations — including larger and better calibrated supernova samples over a broader redshift span, high-precision CMB data down to small angular scales, the baryon acoustic scale in galaxy clustering, weak lensing measurements of dark matter clustering, the abundance of massive clusters in X-ray and optical surveys, the level of structure in the Lyα forest, and precise measurements of H_0 — are all consistent with an inflationary cold dark matter model with a cosmological constant" [49].

from WMAP are orthogonally degenerate [53]. Therefore, a combination analysis of both posterior distribution functions produce much tighter constraints [52]. Because of this orthogonality (as well as sensitivity to other cosmological parameters described in the coming paragraphs), the high mass tail of the halo mass function is a particularly useful cosmological probe and is one of the main methods of using galaxy clusters to constrain cosmology.

Galaxy clusters are the most massive structures in the universe; therefore, they uniquely populate the high mass tail of the halo mass function. Galaxy clusters form hierarchically starting from small density fluctuations in the early universe. These over-dense regions begin to collapse gravitationally, which decouples them from the expanding background forming the first galaxies. These early galaxies continue to accrete and merge with other galaxies forming groups of galaxies and eventually clusters of galaxies. Because of this formation history, galaxy clusters make possible a plethora of useful cosmological and astrophysical tests, but these same mergers complicate cosmological studies by creating substructures which are difficult to model (see §1.3 below). Nevertheless, cosmologists have still developed cosmological probes with galaxy clusters despite these complications. The halo mass function is one such probe which has proven to be particularly useful because of the sensitivity of the high mass tail to Ω_M, Ω_Λ, σ_8, and w (e.g. [54, 52]).

The halo mass function (HMF) is used to describe the abundances of dark matter halos as a function of mass. Spanning over 6 orders of magnitude, the HMF is populated by dwarf galaxies (the most dark matter dense structures in the universe) at the low mass end and galaxy clusters at the high mass end. Because galaxy clusters are the most massive gravitationally gravitationally bound structures in the universe, they sit on the cusp between gravitational dominance (dark matter) and repulsive expansion of the universe (dark energy) making the high mass tail particularly sensitive to parameters describing dark matter, dark energy, and the amplitude of density fluctuations in today's universe. Furthermore, a detailed study of the HMF's evolution over cosmological time is also sensitive to the equation of state of dark energy [54, 55]. In order to obtain this parameter constraints, observations of the high mass tail are compared with model predictions from cosmological simulations.

1.2 Mass Estimation Techniques for Galaxy Clusters

The high mass tail of the HMF has proven to be a powerful probe of ΛCDM cosmology; however, the efficacy of this method depends strongly on the estimates of cluster masses. Therefore, this section will detail the three most common methods for measuring masses of galaxy clusters: gravitational lensing, X-ray emission, and dynamics. Then a brief discussion on the limitations of these methods will follow.

1.2.1 Lensing Masses

As part of General Relativiy, Einstein postulated that because mass curves spacetime, and objects move along geodesics within this curved spacetime, then photons that travel through a region of strong curvature will also experience gravitational effects [56]. Known as gravitational lensing, this effect was confirmed in 1919 with observations of a lensed background star by the Sun during a solar eclipse [57]. The theory behind gravitational lensing is well studied and has been developed into a technique for probing the mass distribution of the gravitational lens. Due to their large masses, the dark matter halo of a cluster of galaxies acts as a large gravitational lens that distorts the light from background galaxies; therefore, lensing techniques provide one of the most common and successful methods for measuring cluster masses.[4]

Unlike X-ray or dynamical masses (see below), gravitational lensing provides a technique for probing the mass distribution of clusters of galaxies that is independent of the nature of dark matter or the dynamical state of the cluster. Gravitational lensing is broken into two regimes: strong and weak lensing. Strong lensing was first discussed in 1937 by Fritz Zwicky [8], and the first observations of strong lensing from a galaxy cluster were presented in 1987 [60]. Strong lensing only occurs in regions of high mass density and is therefore limited to probing the mass profile within the inner regions of galaxy clusters. Nevertheless, in combination with weak lensing, strong lensing can drastically improve calibration of projected mass maps [61, 62, for example], and strong lensing masses are in good agreement with X-ray masses [63, 64].

Although strong lensing is restricted to the inner regions of galaxy clusters, the lensing effect itself is not. At large radii, weak gravitational lensing induced by the tidal field causes a subtle change in background galaxy shapes producing a correlated alignment signal which can be studied statistically [65, 66]. Although triaxiality introduces scatter of individual mass estimates from weak lensing [67, 62], working with suitably large samples of clusters produces a nearly unbiased estimate of mean mass [68]. Large scale sky surveys such as SDSS, Dark Energy Survey (DES) [69] or Hyper-Suprime Cam (HSC) [70] have been used to calibrate mass-observable scaling relations by performing weak lensing analyses on stacked galaxy cluster samples. Furthermore, upcoming surveys such as LSST will advance these studies in the coming decades. For example Leauthaud et. al. (2010) calculated weak lensing masses for clusters in the COSMOS survey [71] and compared these masses to X-ray luminosities in order to investigate the X-ray luminosity and mass scaling relation $L_X - M$ [72]. Constraining scaling relations is a key contribution to galaxy cluster cosmology made by weak lensing analyses.

[4]The majority of the information from this section is taken from two fantastic reviews: theory [58] and application to galaxy clusters [59]

1.2.2 X-ray Masses

Although galaxy clusters are predominantly dark matter, the large majority of their baryonic matter is in the form of hot and diffuse intra-cluster gas with a temperature on the order of $T_{\rm gas} \sim 10^7 - 10^8$ K. This hot gas emits strongly in the X-ray frequencies due to thermal bremsstrahlung emission. Under the assumptions of hydrostatic equilibrium (HSE) and spherical symmetry, the measured gas density and temperatures (both derived from observations of X-ray emission from clusters) can be related to the total mass [73]. In galaxy clusters, the assumption of HSE is justified because, for large populations of galaxy clusters, the gravitational potential remains stationary, the motion of the gas is subsonic, and gas pressure and gravity are the dominant forces. In HSE the gas is treated as an isotropic fluid because collisional times for the ions and free electrons within the hot gas are much shorter than the timescales for heating and cooling [74]. The spherical symmetry argument is made in order to derive a solution for mass interior to some radius r from the hydrostatic equilibrium equation. The HSE assumption breaks down for clusters that are undergoing a major merger and in central regions of relaxed clusters with strong active galactic nuclei (AGN) feedback [75]. Recent simulations have shown that thermal gas pressure accounts for only $\sim 80\%$ of the pressure required for hydrostatic equilibrium in galaxy clusters, which could bias X-ray mass estimates at the 20% level [76].

The most common approach to deriving X-ray masses involves fitting parametric models to the observed projected surface brightness and temperature profiles, which are then directly substituted into the HSE equations to calculate a cluster mass [77, for example]. Another approach utilizes a non-parametric model for the brightness and temperature profiles, but assumes some parameterized model for the mass distribution such as the NFW profile [78]. This approach gives the added benefit of testing various dark matter mass models. Simulations have shown that for dynamically relaxed clusters, the HSE assumptions constrain X-ray masses estimates with scatter $\lesssim 10\%$ but are biased low by $\sim 10 - 15\%$ [62].

1.2.3 Dynamical Masses

Dynamical mass estimates of galaxy clusters involve optically observed spectroscopic redshifts of galaxies along the line-of-sight to the cluster center. These galaxies are treated as test particles within the gravitational potential of the dark matter halo, and so the observed velocity dispersion of these galaxies probes the underlying dark matter distribution. There are three main approaches for estimating cluster masses using galaxy dynamics: calculations of total velocity dispersion that then use the virial theorem or the $M - \sigma$ scaling relation to derive a cluster mass [8, 79], the caustic technique [80], or by solving the Jeans equation [81].

The Virial Theorem

If a galaxy cluster has not undergone a major merger within its recent history, the cluster is considered to be relaxed or virialized, in other words the virial theorem applies. The virial theorem states that for a stable, self-gravitating, spherical distribution of tracer particles (galaxies in the case of clusters), then the total kinetic energy (T) of the system is equal to $-\frac{1}{2}$ of the system's potential energy (U):

$$2T + U = 0. \tag{1.1}$$

In order to derive this relation let's begin by considering the position $\boldsymbol{x}_i$ and velocity $\boldsymbol{v}_i$ of the i-th galaxy at a specific time[5]. The momentum of this particle is $\boldsymbol{p}_i = m_i \boldsymbol{v}_i$, and

$$\frac{d}{dt}\left(\boldsymbol{p}_i \cdot \boldsymbol{x}_i\right) = \frac{d\boldsymbol{p}_i}{dt} \cdot \boldsymbol{x}_i + \boldsymbol{p}_i \cdot \frac{d\boldsymbol{x}_i}{dt} = \boldsymbol{F}_i \cdot \boldsymbol{x}_i + 2T_i, \tag{1.2}$$

where $\boldsymbol{F}_i$ and T_i are the external force and kinetic energy of the galaxy, respectively. This equation is valid for every galaxy in the system, therefore, summing over all galaxies and time averaging over a timescale τ yields

$$\frac{1}{\tau}\delta\left(\sum_i \boldsymbol{p}_i \cdot \boldsymbol{x}_i\right) = \sum_i \langle \boldsymbol{F}_i \cdot \boldsymbol{x}_i \rangle + 2\langle T \rangle \tag{1.3}$$

where angle brackets denotes a time average, T is now the total kinetic energy of the system, and the δ-notation specifies a change in this quantity over τ. The left-hand side will go to zero because this quantity is not expected to change under the assumption of a relaxed, virialized, steady-state system. For a galaxy cluster, the virial theorem describes the balance between the inward force of gravity and the motions of the galaxies; therefore, the only force considered here is gravitational:

$$\boldsymbol{F_i} = \sum_{i \neq j} G m_i \frac{m_j}{|\boldsymbol{x}_j - \boldsymbol{x}_i|^3}\left(\boldsymbol{x}_j - \boldsymbol{x}_i\right) \tag{1.4}$$

and so

$$\sum_i \boldsymbol{F}_i \cdot \boldsymbol{x}_i = \sum_i \sum_{i \neq j} G m_i \frac{m_j}{|\boldsymbol{x}_j - \boldsymbol{x}_i|^3}\left(\boldsymbol{x}_j - \boldsymbol{x}_i\right) \cdot \boldsymbol{x}_i. \tag{1.5}$$

For a particular pair of galaxies this summation reduces to

$$\frac{G m_i m_j}{|\boldsymbol{x}_j - \boldsymbol{x}_i|^3}\left[\left(\boldsymbol{x}_j - \boldsymbol{x}_i\right) \cdot \boldsymbol{x}_i + \left(\boldsymbol{x}_i - \boldsymbol{x}_j\right) \cdot \boldsymbol{x}_j\right] = -\frac{G m_i m_j}{|\boldsymbol{x}_j - \boldsymbol{x}_i|} = U_G \tag{1.6}$$

where U_G is the gravitational potential energy between the two galaxies. Putting everything together, we arrive at the virial theorem: $2\langle T \rangle + \langle U_G \rangle = 0$.

[5]This derivation assumes that each galaxy will be treated as a point particle within the cluster's potential

For a cluster each galaxy has $2T_i = m_i v_i^2$ and under the assumption that all N galaxies have the same mass then the time averaged total kinetic energy is $2\langle T\rangle = Nm\langle v^2\rangle$. The time averaged square of the velocity is known as the velocity dispersion $\sigma^2 = \langle v^2\rangle$ of the galaxies within the cluster. There are $N(N-1)/2 \approx N^2/2$ galaxy pairs each with potential energy $Gm^2/\langle R\rangle$. Therefore the virial theorem says

$$\sigma^2 \sim \frac{GM}{\langle R\rangle} \tag{1.7}$$

where M is the total mass of the cluster and $\langle R\rangle$ is some size measure of the cluster. A determination of the cluster velocity dispersion σ allows for an indirect measurement of the mass of the cluster, and this is exactly how Fritz Zwicky measured the mass of the Coma cluster in 1933 [7]. This method is still used today [82]; however, this relationship between velocity dispersion and mass suggested a power-law scaling relationship, which is the most impactful contribution of the virial theorem to cluster mass estimates [79]. This scaling relation exhibits relatively large scatter (10-15%) with $\sim 40\%$ scatter in mass at fixed velocity dispersion [83].

The Caustic Method

In the late 1980s astronomers began exploring the distribution of galaxies in rest-frame velocity vs projected radius phase space and noticed that these distributions form trumpet-like shapes now known as caustics [84, 85]. Using simulations, it was shown that the edges of these caustic surfaces actually trace out the amplitude of the escape velocity from the cluster as a function of projected radius [80, 86]. And because the escape velocity is directly related to the cluster potential, this escape velocity profile can be used to measure the mass profile of the cluster within the virialized region of the cluster and throughout the surrounding infall region. Unlike previous dynamical mass estimators, the caustic technique does not require any assumptions to be made about the dynamical state of the cluster and can measure the mass profile out to multiple times the virial radius. Over the past couple decades, the caustic technique has been used in numerous analyses with great success: samples of nearby clusters [87], clusters from SDSS [88], the HectoSpec Cluster Survey [89], and many detailed studies of individual clusters (e.g. [90, 91]).

Jeans Analysis

For galaxies within a dark matter halo of a cluster that is dynamically relaxed, the Jeans equation can be used to relate the mass profile to the galaxy distribution function. The derivation of the Jeans equation starts from the collisionless Boltzmann equation

$$\frac{\partial f}{\partial t} + \boldsymbol{v}\cdot\frac{\partial f}{\partial \boldsymbol{x}} - \frac{\partial \Phi}{\partial \boldsymbol{x}}\cdot\frac{\partial f}{\partial \boldsymbol{v}} = 0 \tag{1.8}$$

where Φ is the gravitational potential, f is the six-dimensional distribution function of position $\boldsymbol{x}$ and velocity $\boldsymbol{v}$. Integrating 1.8 over all velocities yields a "probability continuity" equation

$$\frac{\partial \nu}{\partial t} + \nabla \cdot (\nu \overline{\boldsymbol{v}}) = 0 \tag{1.9}$$

where ν is the 3D number density profile and $\overline{\boldsymbol{v}}$ is the average velocity which are related to the distribution function f via

$$\nu(\boldsymbol{x}) \equiv \int \mathrm{d}^3\boldsymbol{v} f(\boldsymbol{x}, \boldsymbol{v}), \quad \overline{\boldsymbol{v}}(\boldsymbol{x}) \equiv \frac{1}{\nu(\boldsymbol{x})} \int \mathrm{d}^3\boldsymbol{v}\boldsymbol{v} f(\boldsymbol{x}, \boldsymbol{v}). \tag{1.10}$$

Multiplying 1.8 by v_j and again integrating over all velocities gives[6]

$$\frac{\partial(\nu\overline{v_j})}{\partial t} + \frac{\partial(\nu\overline{v_i v_j})}{\partial x_i} + \nu\frac{\partial \Phi}{\partial x_j} = 0 \tag{1.11}$$

This can be simplified by subtracting from it $\overline{v_j}$ times the continuity equation (1.9) to get

$$\nu\frac{\partial \overline{v}_j}{\partial t} + \nu\overline{v}_i\frac{\partial \overline{v}_j}{\partial x_i} = -\nu\frac{\partial \Phi}{\partial x_j} - \frac{\partial(\nu\sigma_{ij}^2)}{\partial x_i} \tag{1.12}$$

where σ_{ij} is velocity-dispersion tensor which is related to f by

$$\sigma_{ij}^2(\boldsymbol{x}) \equiv \frac{1}{\nu(\boldsymbol{x})} \int \mathrm{d}^3\boldsymbol{v}(v_i - \overline{v}_i)(v_j - \overline{v}_j) f(\boldsymbol{x}, \boldsymbol{y}) = \overline{v_i v_j} - \overline{v}_i\overline{v}_j. \tag{1.13}$$

For a Newtonian gravitational potential which only has radial dependence, 1.12 reduces to a more simple form

$$\frac{\mathrm{d}(\nu\sigma_r^2)}{\mathrm{d}r} + 2\frac{\beta}{r}\nu\sigma_r^2 = -\nu\frac{\mathrm{d}\Phi}{\mathrm{d}r} \tag{1.14}$$

where we introduced the anisotropy index $\beta \equiv 1 - \frac{\sigma_\theta^2 + \sigma_\phi^2}{2\sigma_r^2}$ and σ_r is the radial velocity dispersion. For a specific choice of gravitational potential $\Phi(r) = -\frac{GM}{r}$, 1.14 reduces to its most common form used in galactic and cluster dynamics:

$$\frac{1}{\nu}\frac{\mathrm{d}}{\mathrm{d}r}(\nu\sigma_r^2) + 2\frac{\beta\sigma_r^2}{r} = -\frac{GM(r)}{r^2}. \tag{1.15}$$

When estimating dynamical masses with a Jeans analysis the general procedure works as follows: (1) a simple analytic model for the number density profile is chosen, (2) a parametric model for the mass profile (typically some variant of an NFW profile) and (3) fit the parameters of these profiles using the observed velocity dispersion profile of member galaxies. This procedure was first applied to the Coma cluster in 1987 [92] and has been used numerous times in the past few decades [93, for example].

[6] We'll now drop the vector notation and instead use conventional summation notation

1.2.4 Current Limits on Galaxy Cluster Mass Estimates

Although each method described above produces a galaxy cluster mass with varying amounts of scatter, these methods are not without their limitations. Gravitational lensing is great to use with large photometric surveys such as SDSS or the upcoming LSST; however, the method can be significantly limited by the accuracy of photometric redshifts. Lensing requires a clear understanding of the redshift distribution of the background galaxies in order to accurately measure the shear profile. Furthermore, lensing masses are limited at large radii where the signal is more susceptible to foreground contamination along the line-of-sight. X-ray and most dynamical mass estimates are under the assumption of dynamical equilibrium which limits their usefulness for recent cluster mergers. Attempts to measure X-ray masses out to large radii ($r \gtrsim r_{500}$) are difficult because X-ray emission at these radii is increasingly faint, there are increased levels of nonthermal pressure support [94], and gas clumping [95]. Dynamical methods are limited by irregular shapes of galaxy orbits, effects of contamination, and the amount of observational time needed to obtain high quality spectroscopic redshifts; although, this last point is somewhat diminished with new multi-object spectrographs such as HectoSpec and M2FS (see below for more details).

Most significant for this thesis, because galaxy clusters form hierarchically, their dark matter distributions could contain significant substructure that affect all three mass estimation techniques. Using mock observations from cosmological simulations, Old et al. (2018) tested many different dynamical mass estimators and showed that masses of low mass clusters with significant substructure were overestimated by as much as 20% [96]. Furthermore, substructure affects the comparison of observed cluster mass (regardless of technique) and cluster masses from simulations. This discrepancy arises from various definitions of a cluster's mass from simulations such as friends-of-friends (FOF) or spherical over-density (OD) masses which differ from observable masses. In clusters with significant substructure these definitions yield vastly different mass estimates for the same cluster [97]. This issue will then propagate into cosmological parameter constraints using the halo mass function which compares abundances of halos at a given mass from observations and simulations.

Dynamical mass estimators are particularly susceptible to galaxy cluster substructure. Under the assumptions made in these estimators, each galaxy is assumed to independently probe the dark matter halo; however, this assumption breaks down if these galaxies are part of sub-groups within the cluster potential. The galaxies within these sub-groups are no longer independent tracers, and if they are not treated accordingly this could significantly affect the estimate of dynamical mass. Recent work has shown that the current cutting edge of dynamical mass estimators are unable to accurately estimate cluster masses that exhibit significant substructure (upwards of 20% [96]); therefore, there is a need for an extension of these models that can robustly account for potential substructures.

1.3 Previous Substructure Analysis Techniques

Understating substructure poses significant challenges to galaxy cluster cosmology. Due to the large scale and long relaxing time ($\sim 10^{11}$ yrs [98]) of galaxy clusters, substructure is quite common. The existence of substructure can provide insights into the formation process of the cluster, unveil new information about dark matter [27], inform the galaxy-environment connection by shaping the morphology-density relation [99], and probe structure formation and expansion of the universe [100]. On the other hand, substructures can substantially affect estimates of cluster velocity dispersion and mass profiles [101, 102]. One of the main goals of this thesis is to develop a dynamical mass estimator that can account for substructures within the cluster environment, so this section will summarize the work and methods previously used to tackle this problem.

Since cluster substructures were first detected in the optical band [103], there have been numerous methods aimed at identifying and investigating these substructures. In the optical frequencies, methods to identify substructure can be classified into three broad categories: 1D tests (redshifts alone), 2D tests (positions alone), and 3D tests (both positions and redshifts). Tests that use only observed galaxy redshifts typically assume the cluster's velocity distribution to be Gaussian, and these methods search for deviations from this distribution. Kurtosis or skewness [104] and asymmetry and tail indices [105] are common 1D substructure test. The 1D DEDICA methodology [106] uses an adaptive kernel and identifies different components of the velocity distribution; if the DEDICA kernel is Gaussian, then this method reduces to a Gaussian mixture model which is another substructure test [107].

2D substructure tests use the projected positions of galaxies and are useful when spectroscopic observations are missing or incomplete. Early 2D tests focused on analyzing smoothed number density contour maps [108] with later tests explored symmetry, angular separation, and density contrasts [109] or the average two-point correlation function [110]. Two-dimensional wavelet transformations have also been used to detect and characterize substructure across a variety of scales [111]. Without the added information coming from spectroscopic redshifts, these tests are extremely susceptible to foreground or background galaxies, that when projected onto the sky could create spurious substructures.

The most commonly used 3D substructure test (and the overall most common substructure test) is widely known as the Dressler & Shectman (DS) Δ-test [112]. The Δ-test looks for deviations in the local velocity from the global velocity of the cluster by computing the mean velocity and dispersion of each galaxy with its N-nearest neighbor galaxies in position space and comparing these local values to the mean velocity and dispersion of the cluster. Other less common 3D substructure methods include 3D variants of the DEDICA procedure [113] and wavelet transformations [114]. Pinkney et. al. (1996) [102] investigated 31 substructure tests including 5 3D tests with N-body simulations in order to test the efficiency of each test as well as

their significance level of detection. All these methods (1D, 2D, and 3D tests) mainly focus on substructure detection; however, they lack the ability to identify member galaxies of subpopulations or fit profiles and estimate velocity dispersions or masses, at least not in a way that propagates uncertainties in member selection.

Most efforts to analyze the different populations of galaxies within the substructures are unfortunately not very robust. These efforts typically involve a multistep process: (1) the Δ-test is used to show that a cluster exhibits high significance of substructure, (2) the galaxy population is then segregated based on color, morphological type, spectral indices, and sky position, and (3) these subgroups of galaxies are then independently modeled to fit their profiles [115, 116, 91, for example]. Recently, a preprocessing step of the caustic technique was used to identify substructure using a binary merger tree algorithm [117, 118]. Although this method is robust in its ability to identify member galaxies of each substructure, it still lacks the ability to analyze the size and masses of the substructures concurrently as well as probabilistically determine cluster and substructure members (the algorithm only absolutely assigns membership). This thesis projects aims in part to advance substructure detection and analysis methods by addressing these two shortcomings of previous techniques.

1.4 Summary of Thesis

This thesis is comprised of the six chapters the first of which is this introduction. Chapter 2 will provide an introduction to the observational aspects of this project. In that chapter I will describe the multi-object spectrograph the Michigan/Magellan Fiber System (M2FS) that I have used exclusively throughout my tenure as a graduate student. I will describe what I learned from the nearly 30 nights that I've spent on the telescope in terms of observation subtleties. In order to aid in the reduction of observations with M2FS, I developed a data reduction pipeline with a front-end GUI which I also describe in this chapter. I finish this chapter with a discussion of how M2FS has been used in the past to observe galaxy clusters.

Chapter 3 is a copy of a published paper in AJ [119]. This chapter will detail the work we did in developing a new full spectrum fitting model that uses a simple stellar population synthesis technique. Parameter estimates describe the mean age, metallicity, chemical enrichment, internal velocity dispersion, and redshift of the stellar population are outputs from this model. We first test this model with mock spectra showing a strong ability to recover input parameters over a range of input signal-to-noise values. We then compare this model to a previously published spectral fitting model [193] and show good agreement albeit with some constant offsets that is attribute to different choices for spectral libraries. And finally, we present the spectral fits to observation of Abell 267 (A267) with M2FS.

Chapter 4 details the observational program developed to obtain spectra for the CLASH cluster M0429. This cluster is of particular interest because it was the only cluster in the CLASH sample that is observable from the southern hemisphere that

had not previously been followed-up spectroscopically. In this chapter we detail the target selection procedure and present the observed spectra. We then fit these spectra with the spectral fitting model described in Chapter 3 and present some of the results of these fits. This chapter has not been published but we plan to make the spectra and fits publicly available prior to the completion of this thesis.

Chapter 5 is an updated version of a paper we have submitted to ApJ [120]. In this chapter we detail the development of a multi-population mixture model that can be used to model the dynamics of galaxy clusters while accounting for substructure. We first test this model using mock observations generated from the dark matter only simulation MultiDark in order to determine how well this model can identify substructure, as well as determine the effect these substructures will have on the accuracy of cluster mass estimates. We then apply this model to a redshift catalog of galaxies along the line-of-sight to A267 comprised of a our observations from M2FS and the publicly available observations from HeCS [89]. We investigate the effect substructure has on properties of the cluster estimated from this model. For A267 we report a halo mass $M_{200} = 7.0 \pm 1.3 \times 10^{14} M_{\odot}/h$ and concentration $\log_{10} c_{200} = 0.71 \pm 0.38$ for a model that accounts for $N_{\rm subs} = 4$ substructures in addition to the main cluster halo.

Finally in Chapter 6 I will summarize the main results and conclusions of the thesis with an outlook to future work and impacts on cluster cosmology.

Chapter 2

Multi-object Spectroscopic Observations

Spectroscopy is an important observational tool that astronomers have been using for centuries. In the 1800s Joseph von Fraunhofer first used a glass prism to observe the solar spectrum [121]; he later combined prisms with telescopes in order observe planets in the solar system as well as bright stars such as Betelgeuse [122]. Prisms were used to disperse the incoming light throughout the 1800s; however, in order to obtain higher resolution spectra, larger prisms were needed, but this presented an engineering problem because of their large mass. In the early 1900s J. S. Plaskett developed the first gratings which quickly replaced prisms in spectrographs because they produced higher resolution spectra, could observe fainter objects, and could be rotated in order to observe different portions of the spectrum.

In the past few decades, these early single-object spectrographs have developed into multiple-object systems – both fiber-fed and multi-slit [123] – which efficiently produce high quality spectra of hundreds of objects simultaneously [124]. This chapter will detail the use of the Michigan/Magellan Fiber System (M2FS) on the Clay Magellan Telescope at Las Campanas Observatory in Chile to collect high quality galaxy spectra. §2.1 briefly describes the details of M2FS, and §2.2 details observational techniques with M2FS developed during the 25+ nights spent observing as part of the thesis project. §2.3 will explain the data reduction pipeline used to extract the spectra from a set of observations, and lastly, §2.4 will describe the observational program used for galaxy clusters Abell 267 ($z \sim 0.23$) and MACS 0429 ($z \sim 0.39$) as part of this thesis project.

2.1 The Michigan/Magellan Fiber System[1]

The Michigan/Magellan Fiber System (M2FS) is a fiber-fed multi-object spectrograph installed on the Magellan/Clay 6.5m telescope at Las Campanas Observatory in Chile. M2FS employs 256 science fibers, 8 acquisition fibers, 2 guide fiber bundles, and a Shack-Hartmann periscope used for wavefront sensing and continuous active optics control. The 256 science fibers are fed into two separate spectrographs which allows for observing the same field-of-view with two different spectroscopic set-ups (e.g. high resolution and low resolution or different wavelength coverages). One of the greatest attributes of M2FS is that it has the versatility to operate at a variety of different configurations. First, the spectrographs can operate at three resolution settings: HiRes ($R \equiv \Delta\lambda/\lambda \sim 30000$), MedRes ($R \sim 10000$), and LoRes ($R \sim 2000$, used for galaxy observations). Furthermore, there are ~ 15 different filters available which focus the spectrograph on specific regions of electromagnetic spectrum at a given resolution, and some filters allow multiple spectroscopic orders to be produced on a the CCD thus producing high resolution spectra over a much larger wavelength range. In addition to these filters and resolution setups, the spectroscopes can operate at a variety of slit widths and different tilt angles.

The Magellan/Clay 6.5 m telescope has a field-of-view of 30 arcmins in diameter. Each science fiber covers 1.2 arcsecs in diameter and there is a 12 arcsecs minimum fiber separation due to the physical size of the ferrule that house each fiber. This minimum fiber separation is better than previous and current spectrographs on similarly sized telescopes, which allows M2FS to observe dense star fields such as globular clusters. The calibration unit (MCal) is mounted near the telescope's secondary mirror and deploys a suite of calibration lamps used for wavelength and continuum calibrations. MCal includes a set of high resolution lamps: Thorium-Argon-Neon, and a set of low-resolution lamps: Neon-Mercury-Argon-Xenon.

2.2 Observations with M2FS

Over the past four years, I have spent upwards of 25 nights (spread over about a half dozen trips) on the Magellan/Clay 6.5m telescope assisting in the operation of M2FS. Only a few of these nights involved observations of targets that are of interest to this thesis (see §2.4); the majority of my time on the telescope involved collecting data for tens of different projects geared towards a variety of scientific interests. Instead of detailing all these projects, this section will focus on the observational procedures involved with the operation of M2FS.

M2FS employs 256 fibers, and each of these fibers need to be carefully placed so that the specific fiber observes the desired target. In order to accomplish this M2FS uses pre-drilled plug plates that are fabricated at the Carnegie Observatory's Machine

[1]See [125] for more details.

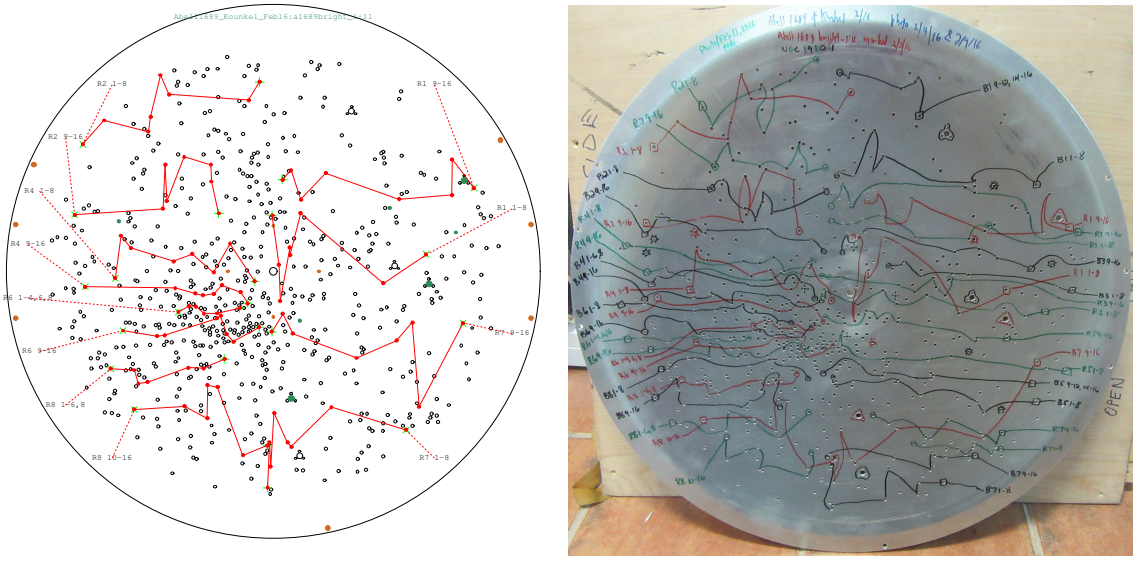

Figure 2.1: *Left*: Schematic drawing showing which fibers correlate to a given set of pre-drilled holes defining a field.
Right: The plug plate corresponding with multiple fields drawn on the plate. The red lines correlate with the schematic shown on the left. The green and black lines correlate with a different field that utilizes the same plate.

Shop and shipped to the telescope before a field is observed. An example of a plug plate is shown in the right panel of Fig. 2.1. Numerous fields are typically drilled into the same plate; therefore, prior to observing a specific field with a given plate, the plate needs to be carefully labeled such that it can be quickly and correctly plugged when installed on the instrument. The plug plate shown on the right in Fig. 2.1 has been labeled for one of the fields of the galaxy cluster Abell 1689. In the left panel of Fig. 2.1 shows the schematic for how the plate should be labeled correctly. This schematic is generated via an algorithm which seeks to optimize the fiber plugging routine in order to minimize the distance to each fiber and limit fibers crossings.

Once a plate is labelled, it must be attached to the telescope and plugged correctly. This process can range from ~ 15 minutes to ~ 1 hour depending on the complexity of the field (e.g. only specific fibers will be plugged, dense clustering of fibers) and the experience of the observers. Because the process of removing one plate and plugging a new plate typically occurs $2-4$ times per night, this procedure must be accomplished efficiently and correctly. A properly and cleanly labeled plate is faster and easier to plug correctly. During this process, acquisition and guide fibers are also plugged.

Acquiring the field is an extremely important and delicate process. If a field is not acquired correctly, some of the light from the targets will not be recorded, thus diminishing the signal-to-noise (S/N) of the data. Acquiring the field involves a multi-step, slightly iterative procedure. First, the telescope is pointed towards the pointing provided by the researcher whose field we are observing. At this point typically

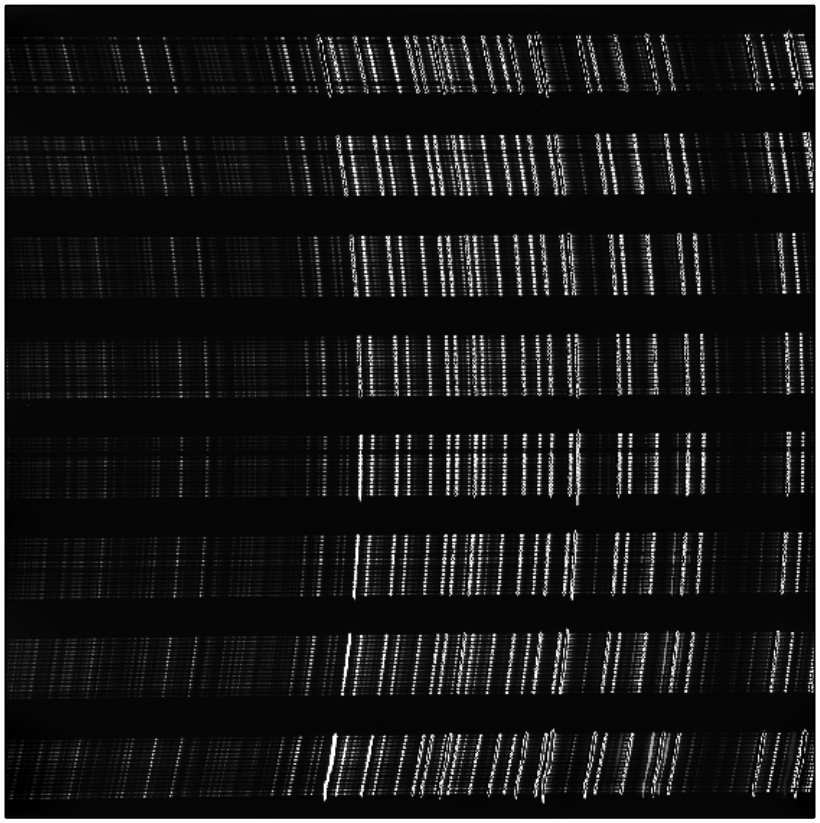

Figure 2.2: Example of wavelength calibration exposure taken with M2FS. This exposure was taken with the Thorium-Argon-Neon lamp at the low-resolution set up. Wavelength increases from left to right, and each fiber is separated vertically from top to bottom.

the two guide stars will be visible within the guider camera and maybe some of the acquisition fibers will be illuminated. If needed the telescope is moved slightly so that the guide stars are near the center of their guider camera. Next, minor rotations of the plate mount ($\sim 10^{-2}$ deg) are applied in order to align the guide stars within the guide cameras. Finally the telescope is dithered in order to maximize the illumination of the acquisition fibers. These last two steps can be repeated if needed in order to maximize the acquisition fiber counts.

Before, after, and sometimes in the middle of a set of science exposures, calibration data must be taken. Calibration images include wavelength calibration lamp exposures and quartz exposures (or flat fields). These are taken by deploying the MCal unit which houses all the wavelength calibration lamps as well as a set of LED lights used in lieu of quartz lamps. An example of a wavelength calibration exposure is shown in Fig. 2.2. These exposures are used in data reduction to generate a transformation from pixel space to wavelength space which is then applied to the science spectra. The LED lamps are used to illuminate the fibers, which is used to identify

the fiber locations on the CCD for a given exposure and extract the one-dimensional spectra (see §2.3 for more information on both calibration exposures).

Following the completion of the calibration exposures, MCal is retracted, and the telescope begins guiding on one of the guide stars. In order to determine if the fibers are plugged correctly, we take a quick test exposures ($\sim$ 120 seconds). We compare the relative brightnesses of the fibers in the test exposure with the magnitudes of the objects each fiber should be observing to verify a plate is plugged correctly. If everything looks good in the test exposure, we begin science exposures. Depending on the science goals, magnitudes of the targets, and time allocation, science fields are observed with multiple sub-exposures which range from 15 minutes to an hour. The multiple sub-exposures ensure the easy removal of cosmic rays during data reduction. Even in the middle of the Atacama Desert in Chile, there is still a significant amount of sky glow from the moon, stars, and nearby cities; therefore, estimating the amount of sky background and correcting each spectrum for this background is necessary. This is done by allocating a small subset of fibers to relatively blank areas of the sky which in essence collects a spectrum of the background sky. In data reduction these sky fibers are then used to estimate the background and subtract it off of the non-sky fibers.

Once a field is complete and all calibration exposures are taken, the telescope is returned to its standard position (pointing towards the zenith), and the observers then unplug the previous plate and plug the next plate on the schedule. The observation process then repeats for the new field. During the short nights of the summer months (November to March in Chile), M2FS will observe $2-3$ fields per night; on the other hand, during the longer winter nights, M2FS can observe upwards of five fields per night. An observer must be adequately trained in plugging fibers, acquiring the field, and collecting data in order to minimize the overhead and maximize the time spent observing each field.

The work of an observer is not limited to the night hours. As already mentioned, making sure all plates are labeled for the night is a major task completed during the afternoon. There are also four sets of calibration exposures that need to be made during non-observing hours. Bias exposures are used to estimate the bias level within each CCD chip. These exposures are obtained by reading out the pixels after a zero-second exposure without opening the shutter. Dark exposures are similar to bias exposures in the sense that the shutter is not opened; however, while bias exposures are used to estimate the bias in the CCD chip, dark exposures are used to estimate the dark current that builds up on the CCD chips during long exposures. Even though the CCD chips are cooled to 77K, it is still warm enough to build up a non-negligible amount of electrons. This dark current is strongest at the corners of the CCDs where it is held in place because these supports are much warmer than the CCD. An example of a dark exposure is shown in Fig. 2.3.

Fibermaps are taken exclusively during the day and are obtained by taking an exposure of the ambient sunlight within the dome. Fibermaps are required for each

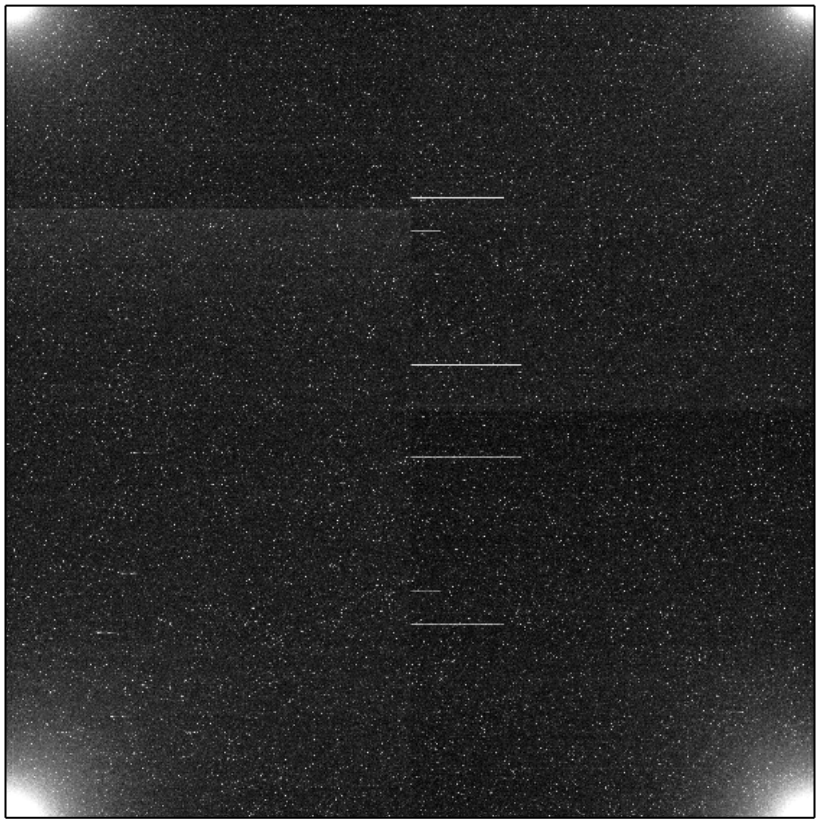

Figure 2.3: Example of dark exposure taken with M2FS. The bright spots in the corners are the dark current that builds up due to the supports that are warmer than the CCD chip.

configuration observed during a run. Similar to a quartz exposures, fibermaps are designed to illuminate each fiber more uniformly and are used to identify the fiber locations for a given configuration. The last set of calibration exposures are known as twilights and are exposures of the sky taken after sunset and before sunrise when the sky is too bright to take science exposures. Twilights are used to correct the relative differences in throughput between the fibers (see §2.3 for more details). Similar to fibermaps, every configuration that is observed during a run must have at least one set of twilight exposures.[2]

[2]A configuration has a different meaning than plugging setup. Configuration refers to the setup of spectrograph (e.g. filter, grating angle, resolution, slit width, etc.), whereas plugging setup is how and where the fibers are plugged. Different plugging setups can use the same configuration.

2.3 Data Reduction

Data reduction is the process of cleaning and correcting the raw observations (Fig. 2.6) for instrumental effects in order to produce a data set that is easier to analyze (Fig. 3.3). This process is tedious as it involves many steps that must be done for every exposure; therefore, data reduction pipelines are frequently used to expedite the process. For major surveys such as BOSS [126] and SDSS [127], the data reduction pipelines are vital components of their respective surveys. M2FS produces a particularly difficult data reduction pipeline problem to solve in the sense that there are a few dozen different configurations each with their own subtle data reduction nuances. For this reason, a simple to use and streamlined data reduction pipeline was not developed in conjunction with M2FS; instead the raw images were provided to the PI on a given project, and they were responsible for their own data reduction. As part of my thesis project, I attempted to develop a robust, generalized pipeline with a user friendly GUI front-end in order to simplify the data reduction process as well as open M2FS to a more generalized group of astronomers who might not have the necessary background required to reduce the raw images. Although, the end result is not entirely general in the sense that it cannot be applied to all existing M2FS configurations, the M2FS data reduction pipeline I developed works well for a large subset of configurations and requires only a few user-generated input files and little hands-on guidance throughout the data reduction process.

In the mid 1980s astronomers at the National Optical Astronomy Observatory (NOAO) developed a software package known as Image Reduction and Analysis Facility (IRAF) geared toward the reduction of astronomical images [128]. IRAF provides a set of packages and routines optimized for the reduction of observations collected on CCD chips. However, these routines are disjunct and need to be called successively in order to reduce a set of images. Therefore, IRAF is a commonly used backend for data reduction pipelines and is used in a similar fashion for my pipeline. Furthermore, the groundwork for an M2FS pipeline was already laid by the instrument's PI Mario Mateo, who developed a rigid M2FS pipeline that used IRAF routines. This pipeline was useful in the sense that it informed decisions on the numerous parameters needed to run each IRAF routine,[3] but it was lacking in its flexibility and user friendliness. My goal was to adapt parts of this old pipeline into an easier and more generalizable pipeline with a simplistic GUI front-end while incorporating new routines written in Python to fill in the gaps left by some inadequate or non-existent IRAF routines.

The main window of the M2FS pipeline GUI is shown in Fig. 2.4. The first few fields tell the pipeline where the raw images are located (*Root Directory*), the configuration file directory, and the locations of the pre-computed bias and dark images or the locations of the sets of exposures to make a new one. In the bottom portion of this window are the data reduction options; for a full data reduction (from

[3]IRAF is a particularly frustrating software package to use because of these numerous convoluted parameters that can drastically change the outcome for a given routine.

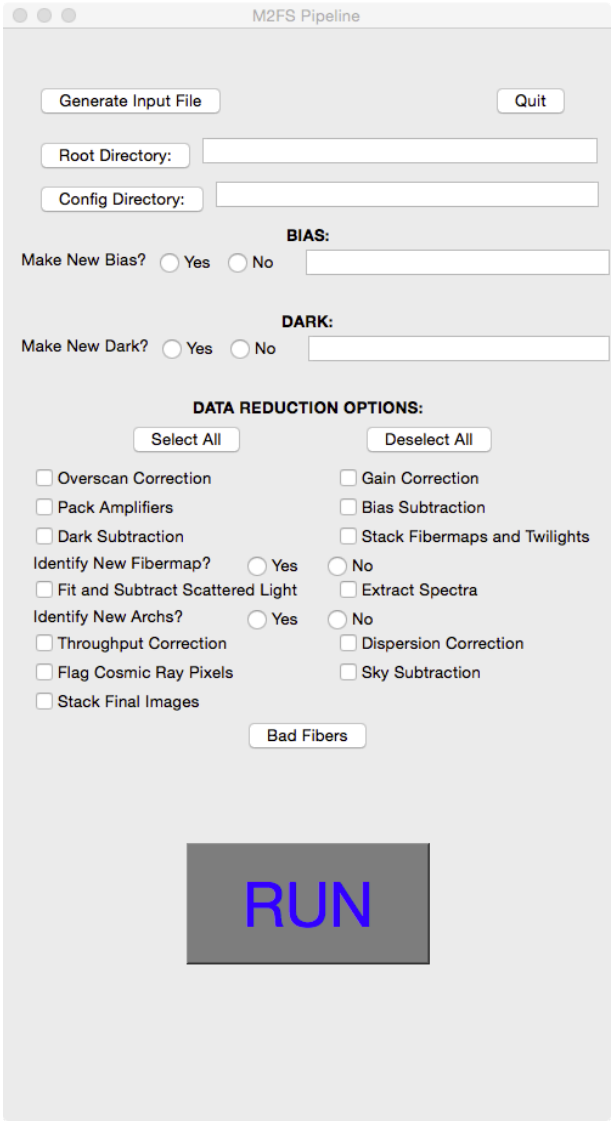

Figure 2.4: Main window of the M2FS pipeline GUI.

raw images to fully reduced spectra) all fields will be selected. If the reduction involves a new configuration that does not have the support files in the configuration directory, then *Identify New Fibermap?* and *Identify New Arcs?* must be set to *Yes* in order to generate the support files for the configuration. More on each step of the pipeline will be discussed below.

The backbone of the pipeline is a file called the input file. The input file essentially tells the pipeline which exposures to reduce, what type of exposure each image is (e.g. science, wavelength calibration, etc.), the field that each image is apart of, which calibration images to use for a specific exposure, and the configuration. This can be a complicated file, so I wrote a subroutine that generates this file in the correct

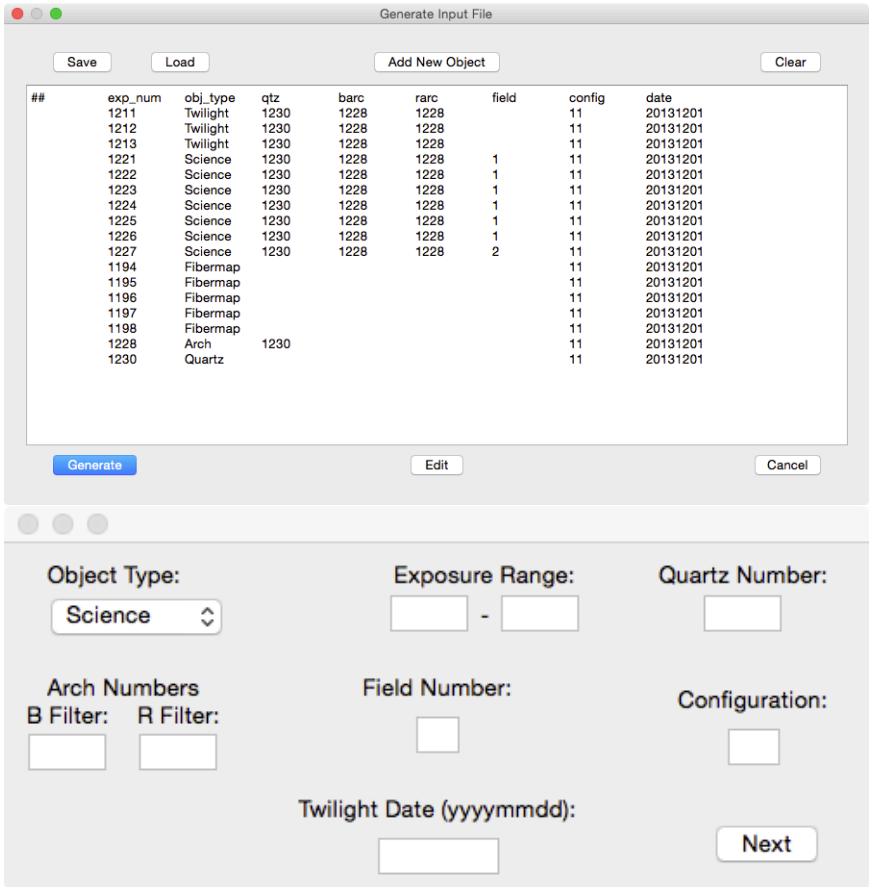

Figure 2.5: Generate input file windows for M2FS pipeline

format to be read by the pipeline. The *Generate Input File* button at the top of the main window will open the input file viewer window shown in the top panel of Fig. 2.5. From here one can load in an already generated input file, make changes to the input file, save these changes, or generate a completely new input file. In Fig. 2.5, the viewer window shows what the input file will look like as it is being generated. To add a new object to the input file, click the *Add New Object* button at the top of the window, which will open a new window shown in the bottom panel of Fig. 2.5. In this window you select the type of exposure, exposure numbers, as well as the calibration exposures that should be used with the reduction of these exposures. These exposures will then be added into the viewer window and saved to the input file when *Save* is clicked. Once the input file is setup correctly, the *Generate* button will then load the input file into the pipeline.

Once the input file is generated and all options are setup correctly, the big *RUN* button will process all the information provided and generate a .cl script which can then be run in an IRAF window. The pipeline reduces the set of images following fairly standard routines used to reduce 2D spectra similar to those produced by M2FS.

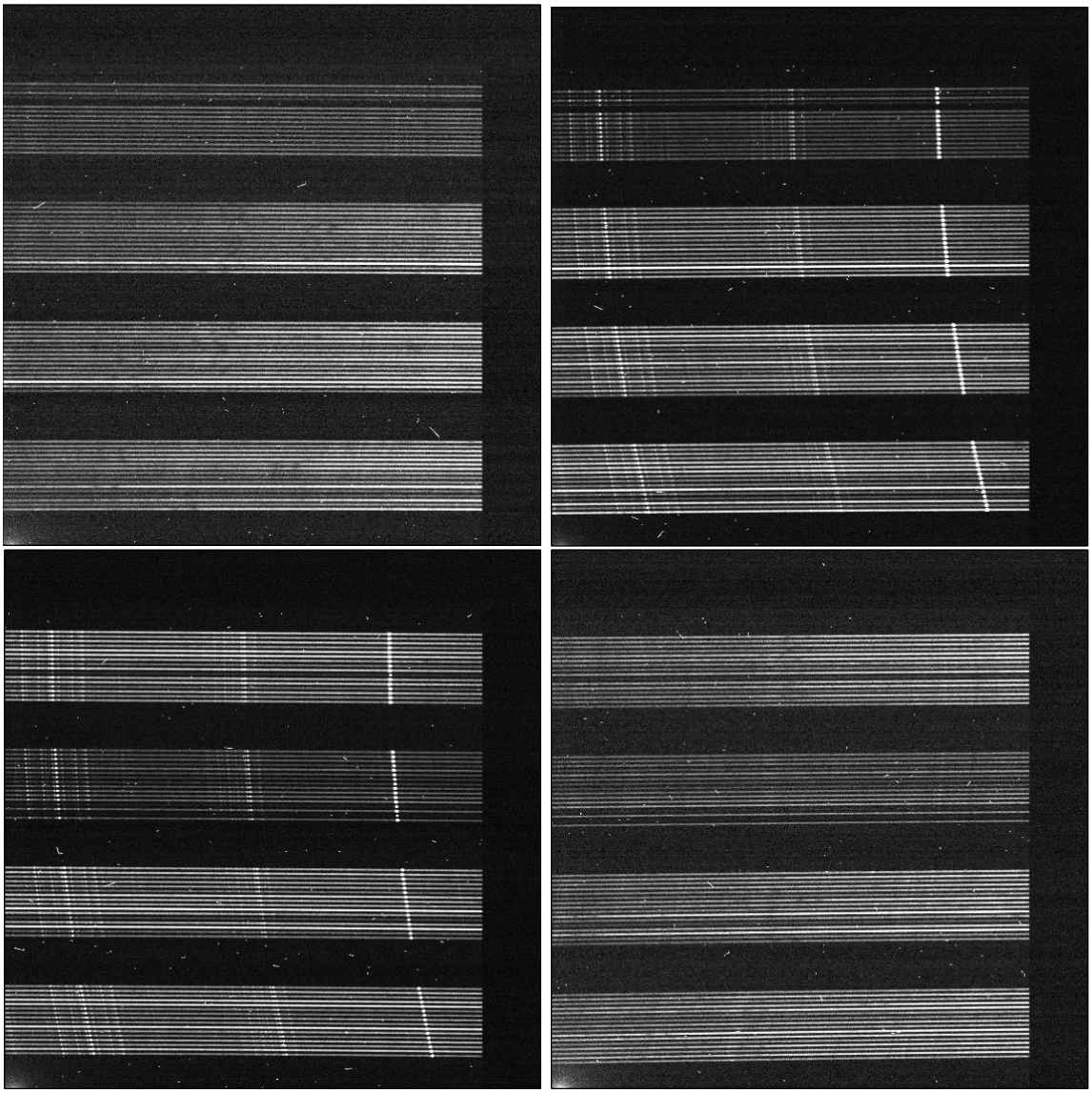

Figure 2.6: Raw images of the four amplifiers from one CCD chip. The dark regions on the right and top sides of each amplifier is the overscan region. These images need to be rotated and stitched together in order to produce an image of the complete CCD chip.

The pipeline works as follows

1. **Overscan correction**: The dual spectrographs on M2FS (referred to as the B and R sides) each have their own CCD chip and each chip has four separate amplifiers; therefore, for each exposure M2FS produces 8 images. Fig. 2.6 shows the images from the four amplifiers of one of the CCDs. The overscan region of each amplifier is essentially fake pixels that are read out by the amplifiers and are used to estimate any changes in the bias level that may have occurred in

the time between bias exposures and the current exposure. The overscan region can be seen as the dark regions along the right-edge and the top of each image. During overscan correction this portion of the CCD is subtracted off from the science portion of the CCD and then trimmed away.

2. **Bias Subtraction**: A bias is applied to the CCDs in order to ensure that no pixel is empty which can cause issues during readout. This bias level must be estimated and subtracted off properly. With M2FS we generate a master bias file during each run on the telescope which is then used to remove the bias level. This subtraction is done on a pixel by pixel basis and each amplifier for each CCD has their own master bias.

3. **Dark Subtraction**: The dark current builds up in the CCD during long exposures due to thermal energy in the CCD and the surrounding spectrograph. This current is minimized by cooling the CCDs with liquid N_2. Similar to a master bias, we generate a master dark from multiple dark exposures throughout a run. An example of a master dark is shown in Fig. 2.3. The master dark is then used to calculate the dark current in each pixel which is then rescaled based on the length of a given exposure and subtracted off.

4. **Gain Correction**: CCDs are used to measure the counts of photons that are incident onto the chip during each exposure. Because of the photoelectric effect [129], photons excite electrons in the CCD; however, CCDs are set up so that an electron is only generated after a certain energy of photons is deposited onto a pixel. Therefore, each pixel contains a certain number of electrons which must be converted back into a photon count via an amplifier's gain, which is done during the gain correction. During this step we also generate the variance image which is used for error propagation throughout the remainder of the pipeline. In other words, for every subsequent processing step we apply the correct error propagation procedure to the variance image depending on the mathematical operation done in the given step.

5. **Pack Amplifiers**: The next step is to rotate the individual images from each amplifier so that they are properly aligned and stitch them together. This process takes the images shown in Fig. 2.6 (after overscan, bias, dark, and gain corrections) and packs them together into the single image shown in Fig. 2.7.

6. **Stack Fibermaps, Twilights, and Final Images**: In this step images are stacked (combined) using a simple inverse variance weighting routine in order to increase signal-to-noise as well as remove cosmic rays. Cosmic rays are high energy particles of cosmic origin that could strike the detector thus exciting electrons in typically one pixel (if a cosmic ray is incident at a shallow enough angle it could "streak" across the detector thus illuminating multiple pixels). The isolated white pixels all over Fig. 2.7 are mostly caused by cosmic rays. In

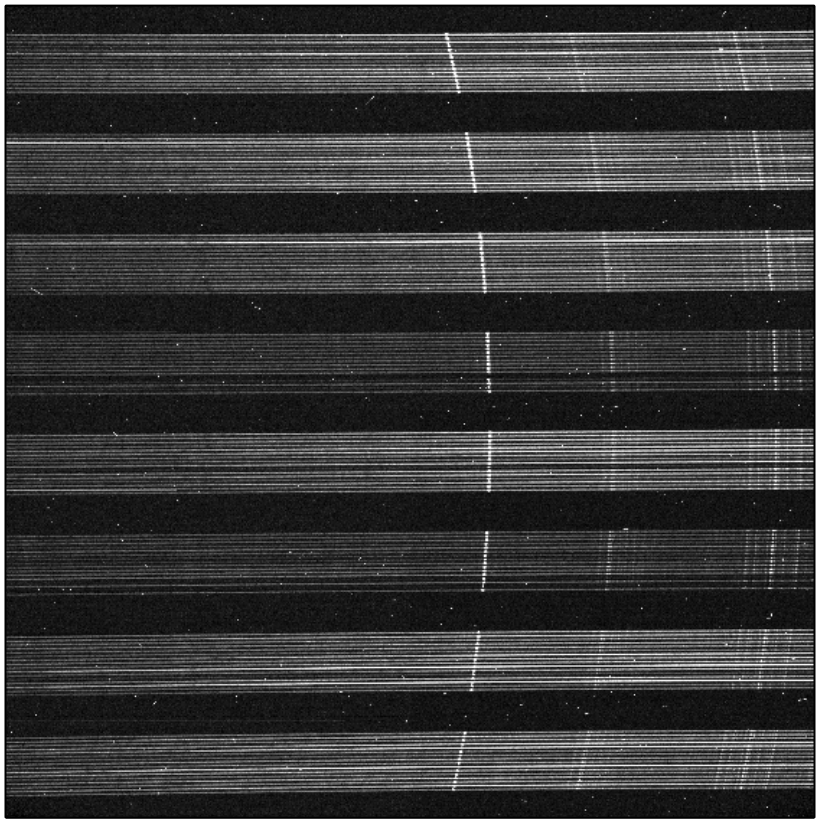

Figure 2.7: Packed image of one CCD of M2FS

order to remove them, IRAF has a routine names CRREJECT (CosmicRayREJECT), which uses multiple images to essentially smooth out the delta-function peaks caused by cosmic rays. Fig. 2.8 shows six sub exposures on the left used to generate the stacked image on the right.

7. **Identify Fibermaps**: If this is set to *No*, then a fibermap template will be pulled from the configuration directory corresponding to the correct configuration given in the input file. This routine will then use this template to identify the location of the apertures (or fibers) on the CCD. Each horizontal line seen in the CCD image corresponds to the light from one fiber, and IRAF needs to identify the center points of these apertures and fit a polynomial for the edges. These polynomials and positions are later used to collapse the 2D spectra into 1D spectra (see Extract Spectra below). If this is set to *Yes*, then the user must manually identify the location of each aperture using the IRAF package APALL, and then the newly identified fibermap will automatically be added to the configuration directory.

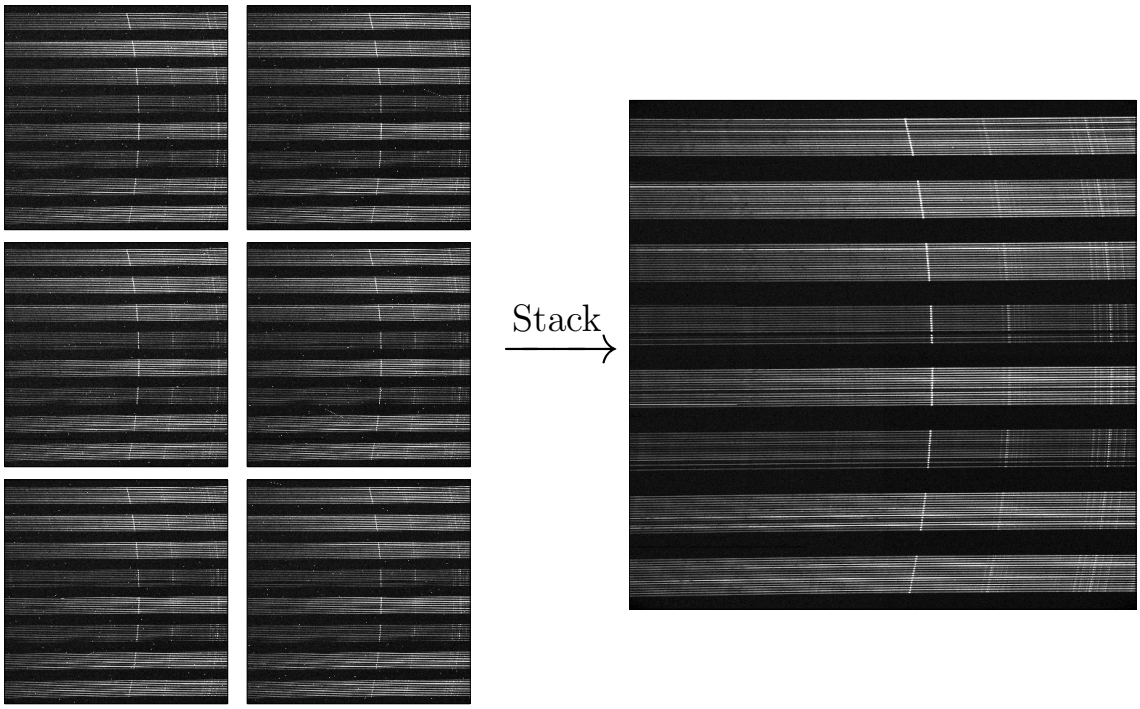

Figure 2.8: On the left, the six-15 minute sub-exposures used for Abell 267. One the right, the resultant image following the stacking routine which removes cosmic rays.

8. **Fit and Subtract Scattered Light**: Due to the optics of the system there is a non-negligable amount of light that is scattered and lands on incorrect portions of the CCD. In order to estimate the scattered light and subtract it off, the pipeline fits a surface function using the regions of the CCD without apertures. These regions are selected via the identified fibermaps which knows the location of each fiber. Although the surface function is fit using empty portions of the CCD, the function is estimated globally and subtracted from the entire CCD.

9. **Extract Spectra**: Using the identified fibermaps, the spectra from each exposure are extracted which produces a 1D spectrum. This is accomplished in a multi-step process. First the fibermaps are used to identify and extract the spectra from the quartz image by allowing a global shift in the entire aperture location. This step allows for the fact that the location of the apertures could vary up or down from the solution identified with the fibermaps from the time the fibermaps were taken to the time of science exposures. This global shift is most commonly caused by variations in temperature. This solution from the quartzs is then used with the science exposures again allowing a global shift in the aperture locations. Then using the exact location of these apertures each wavelength calibration exposure is extracted multiple times, once for each science exposure that uses that wavelength calibration.

10. **Identify Arcs**:[4] If set to *No* then a wavelength calibration template is pulled from the configuration directory corresponding to the same configuration specified in the input file. This template is then used to identify the extracted arcs from the new exposures. If set to *Yes*, then the user must manually identify a new arc which will then be automatically added to the configuration directory. By identifying an arc, IRAF determines a polynomial mapping from pixel space to wavelength by specifying the location and wavelength of a set of emission lines from the arc. At low-resolution this process can be difficult due to blending of nearby lines as well as non-uniform coverage of lines across the entire dispersion axis. Therefore, this step is typically the bottleneck of the pipeline because of the time and effort needed to properly identify an arc for a new configuration.

11. **Dispersion Correction**: After the arcs have been identified these wavelength solutions are used to map all 1D spectra from pixel space to wavelength space. The pipeline does two separate mappings: 1) keeps the pixel spacing the same so that $\Delta\lambda$ between pixels will not be constant, and 2) rebinning the data to put it on a uniform wavelength grid. Personally, I prefer option (1) because it keeps the data on its natural binning.

12. **Throughput Correction**: Each fiber has their own unique throughput which is adjusted for in this step. This is done with the twilight exposures which more uniformly illuminates all fibers compared to fibermaps and quartz exposures. Because twilights illuminate the entire focal plane uniformly with the same source, any variation in the fiber brightness is caused by variation in fiber throughput. Therefore the pipeline uses these variations to estimate each fibers relative throughput and rescales each fiber by this factor. Additionally during this step, the pipeline also fits the continuum of each spectrum and normalizes by this continuum.

13. **Sky Subtraction**: For each science field, a small subset of $\sim$ 15 fibers are allocated to relatively blank regions of the sky and are used to estimate the brightness of the background sky. This is done by rebinning each sky spectrum onto a uniform much higher sampled grid and estimating the background sky as the median value of all sky fibers at each wavelength [184]. This oversampled estimated background is then rebinned to each science fiber's unique wavelength solution and then subtracted off. This procedure has been written and executed in Python because there is no adequate IRAF routine. The sky estimation procedure is an area that I feel could be greatly improved upon, especially for low-resolution spectra of high redshift galaxies ($z \gtrsim 0.3$) where atmospheric emission lines are particularly problematic.

[4] Arcs are another term commonly used for wavelength calibration images because of the type of lamps that are used

14. **Bad Fibers**: This is not a separate step, but the pipeline has the flexibility to ignore fibers that are tagged as bad fibers. Due to the high usage of fibers (plugging and unplugging) it is common for fibers to break or go bad during a run. When this occurs, the data reduction needs to be made aware of such issues so that it can treat those bad fibers accordingly. The *Bad Fibers* button will open a new window where one can specify which if any fibers should not be used.

2.4 Observations of Galaxy Clusters with M2FS

Galaxy redshift surveys are a focal component of cosmological research which are used to probe the growth of large scale structure via the matter power spectrum [130] and galaxy clustering [131], measure redshift space distortions [132], and investigate the internal properties of groups and clusters of galaxies. Over the past few decades, multi-object spectrographs have catapulted these surveys into the era of big data by collecting hundreds of thousands of galaxy spectra out to $z \sim 1$. Surveys such as Two-degree Field (2dF) Galaxy Redshift Survey (GRS, [133]), SDSS spectroscopy (BOSS and eBOSS [134, 135, 136]), and Hectospec Cluster Survey (HeCS [89]) utilize fiber spectrographs while the Cluster And Infall Region Nearby Survey (CAIRNS [87]) and Visible MultiObject Spectrograph (VIMOS) based surveys (VVDS-Wide [137], VIPERS [138], and CLASH-VLT [139]) are multi-slit spectrographs. M2FS is another multi-fiber spectrograph with similar capabilities to its contemporaries (and at a higher resolution!) for collecting galaxy spectra thus adding to the growing galaxy redshift catalogs.

As part of my thesis I pioneered the use of M2FS for observations of distant galaxies. In November 2013, we observed one field along the line of sight to the rich galaxy cluster A267 as a pilot program to assess the capability of M2FS for observing unresolved stellar populations. The resulting observations laid the ground work for this thesis. Over the past few years I have used M2FS to observe three other clusters (Abell 1689, CL 1301, and MACS 0429) while others have generated high-redshift surveys of Lyα emitting galaxies [140, 141] and galaxy cluster spectroscopy is the focal point of a PhD thesis at the University of Michigan (A. Kremin, private communication). This section will give a brief outline of how we use M2FS for galaxy spectroscopy while in §3.2 and §4.2 more details will be laid out for the specific observation programs of A267 and M0429, respectively.

Because spectroscopy is typically follow-up observations of already identified galaxy clusters by X-ray, lensing or the SunyaevZel'dovich (SZ) effect and due to the relatively long exposure times of a limited number of objects, spectroscopic observations of galaxy clusters are most limited by target selection in which we try to select as many galaxies to observe with high probabilities of membership to the cluster. A large portion of the galaxy populations in clusters are made up of old, large, red elliptical galaxies due to hierarchical formation; therefore, our targeting program for

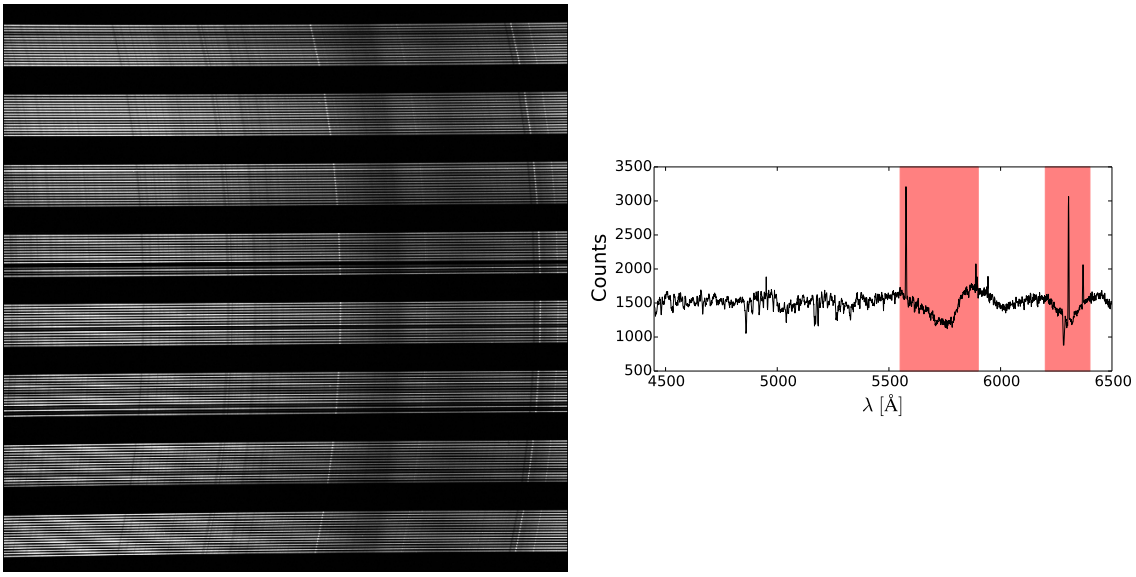

Figure 2.9: Twilight spectra collected with M2FS at a typical resolution used for galaxy cluster observations. On the left, is the stacked and scatter light corrected CCD image for twilight exposures from the A267 runs. Notice the broad darker regions in each spectrum on the right half of the CCD. These features are possibly caused by the polarization of the light. These features are more noticeable (and highlighted in red) in the extracted 1D spectrum shown on the right.

galaxy clusters involved selecting red galaxies via the red-sequence similar to previous galaxy cluster redshift surveys (see [89] for example). This selection criteria optimizes the likelihood of selecting true cluster members when photometric redshifts are not available. However, when photometric redshifts are available, we use both pieces of information (redshift and red-sequence) to optimize the target selection further.

The general procedure for target selection is as follows. First, we select all galaxies (brighter then the magnitude limit of M2FS $r \sim 21$) within some small region around the core of the cluster ($\sim 5''$). Next, we plot these selected galaxies on a color magnitude diagram in order to identify the red-sequence of the cluster. Finally, we select all galaxies that lie along the determined red-sequence that are within a certain projected radial distance of the cluster center (if only one pointing is desired then this will be the field-of-view of M2FS $30'$ in diameter, but this could be extended if multiple pointings are used). Depending on how many fields and pointing are allocated for the cluster, we select a subsample of these galaxies (weighted by photometric redshifts where available) as high priority targets. Plates are then drilled and sent down to Las Campanas Observatory in Chile.

Spectra of galaxies in clusters are essentially spectra of unresolved stellar populations, so it is best to utilize M2FS at its low-resolution setup ($R \sim 7000$). One of the most important features in red elliptical galaxies in age determination is the 4000Å break where two distinct Calcium absorption lines (Franhaufer K and H lines)

reside. Therefore, we tilt the grating so that the wavelength coverage corresponds to a rest-frame wavelength that includes the 4000Å break at the redshift of the cluster. For higher redshift clusters (see Chapter 4 below), this becomes problematic because there are a large amount of atmospheric emission lines that dominate the spectrum at $\lambda \gtrsim 6000$Å. Therefore, this procedure is best used for clusters with $z < 0.4$, but due to the decreased brightness of distant clusters, $z \lesssim 0.35$ is more recommended. Three sub-exposures are sufficient, and each sub-exposure does not need to exceed 1 hour (observations of A267 were carried out with merely six 15-minute sub-exposures). The ThArNe wavelength calibration lamps have blended emission lines at this resolution; however, they cover a much wider wavelength range and so are preferred over the NeHgArXe lamps.

Twilight spectra create a particularly difficult challenge at this resolution with M2FS. For some relatively unknown reason (though light polarization is the leading theory), low-resolution twilight spectra exhibit broad absorption features that make throughput correction difficult. For this reason, I use the fibermap exposures (which is unpolarized light because it is reflected around within the telescope dome) instead of the twilights for throughput correction. An example of the CCD chip and one extracted twilight spectrum is shown in Fig. 2.9.

I have carried out this targeting and observational procedure for four clusters observed during my tenure as a graduate student: Abell 267 ($z \sim 0.23$, Chapter 3), MACS 0429 ($z \sim 0.39$, Chapter 4), CL 1301 and Abell 1689. Observations of CL 1301 and Abell 1689 were collected for other groups, and so I do not go into detail on these clusters in subsequent chapters. The next chapter will detail the observations of A267, present a spectral fitting model, and apply the model to A267 spectra. While in chapter 4 I will present a larger set of observations for M0429 and present the spectral fitting model results for these spectra as well.

Chapter 3

Magellan/M2FS Spectroscopy of Galaxy Clusters: Stellar Population Model and Application to Abell 267

Abstract

We report the results of a pilot program to use the Magellan/M2FS spectrograph to survey the galactic populations and internal kinematics of galaxy clusters. For this initial study, we present spectroscopic measurements for 223 quiescent galaxies observed along the line of sight to the galaxy cluster Abell 267 ($z \sim 0.23$). We develop a Bayesian method for modeling the integrated light from each galaxy as a simple stellar population, with free parameters that specify redshift ($v_{\rm los}/c$) and characteristic age, metallicity ([Fe/H]), alpha-abundance ([α/Fe]), and internal velocity dispersion ($\sigma_{\rm int}$) for individual galaxies. Parameter estimates derived from our 1.5-hour observation of A267 have median random errors of $\sigma_{v_{\rm los}} = 20$ km s^{-1}, $\sigma_{\rm Age} = 1.2$ Gyr, $\sigma_{\rm [Fe/H]} = 0.11$ dex, $\sigma_{\rm [\alpha/Fe]} = 0.07$ dex, and $\sigma_{\sigma_{\rm int}} = 20$ km s^{-1}. In a companion paper, we use these results to model the structure and internal kinematics of A267.

3.1 Introduction

Galaxy clusters are the most massive gravitationally bound and collapsed structures in the Universe, and therefore they are important laboratories for observational cosmology [80, 142, 143, 144, 54, 89, 145]. Due to their high density of galaxies they are also ideal for studying galaxy interactions and the effect these interactions have on the galaxy population. Galaxy clusters are studied in a multitude of ways, from gravitational lensing, both weak and strong [146, 147, 148, 149, and references therein] to X-ray temperature measurements of hot intracluster gas [150, 151, 152] to Sunyaev-

Zeldovich effects [153, 154, 155] to optical spectroscopy [87, 89, 156, 157, 158, 159, 160, and references therein]. Many of these methods seek to measure the mass of the cluster, populating the high mass tail of the halo mass function which is sensitive to cosmological parameters such as the amplitude of the power spectrum or the evolution of matter and dark energy densities over cosmological time.

With the advancement of multi-object spectrographs, astronomers have the ability to conduct large spectroscopic surveys of galaxies in cluster environments. Multiple-object spectroscopic systems have allowed for observations of hundreds of objects simultaneously. These spectrographs provide the necessary tools to perform efficient follow up of photometrically identified galaxies over a range of redshifts. For example, the Sloan Digital Sky Survey (SDSS) produced a spectroscopic catalog of millions of galaxy spectra with up to a thousand cluster member galaxies at low redshift and less than ten member galaxies at their highest redshift $z \sim 0.8$ [126, 127]. Additionally, the new age of spectroscopic data from SDSS includes integral field unit (IFU) observations with MApping Nearby Galaxies at Apache Point Observatory (MANGA) which resolves galaxy spectra in two-dimensions on the sky. Using the 6.5m MMT and Hectospec fiber spectrograph, [89] have measured redshifts for more than 22,000 individual galaxies in 58 clusters (the HECs survey). Moreover, astronomers have used MMT/Hectospec and VLT/VIMOS to build large spectroscopic catalogs for cluster galaxies observed with the Cluster Lensing and Supernova Survey with Hubble (CLASH) [161, 162, 139, 116, for example]. Another commonly used spectrograph, The Inamori-Magellan Areal Camera and Spectrograph (IMACS) is a multi-slit, wide-field spectrograph on the Baade-Magellan Telescope in Chile, which has been used in recent years to study galaxy clusters [163, 164].

The Michigan/Magellan Fiber System (M2FS) is a multi-object fiber spectrograph consisting of 256 fibers and was installed on the 6.5m Clay-Magellan Telescope at the Las Campanas Observatory in Chile in August 2013 [125, 165]. In its highest resolution setting ($R \sim 50000$), M2FS has been used by [166] to search for exoplanets in open clusters, [167] to measure chemical abundances in globular clusters [168, 169, 170], and [171] to measure chemical abundances in dwarf spheroidal galaxies. At more moderate resolutions ($R \sim 18000$) [172, 173, 174] have used M2FS for detailed kinematic analyses of dwarf spheroidal galaxies.

In addition to cosmological constraints from cluster masses, the galaxy spectra themselves convey a multitude of information about their stellar populations. In recent years, with the development of more robust statistical techniques, there has been great progress in the fitting of galaxy spectra to extract stellar population information. These efforts have focused on building a more robust statistical framework around the early methods of stellar population synthesis [175, 176, 177] used for modeling the spectral energy distributions (SEDs) of galaxies. These early stellar population synthesis methods have been improved over the years to incorporate a more complete understanding of galactic processes [178, for a review]. In the past few years, new efforts have been made to apply Bayesian techniques to fit these stellar population

models. BayeSED [179] and BEAGLE [180] are two recently developed Bayesian models aimed at fitting SEDs of galaxies over a large wavelength coverage. However, these models are geared towards SEDs, which sample only at few band passes over a large wavelength range (from γ-rays to IR). And most recently, [181] developed a single stellar population model with Bayesian statistical techniques to fit spectra in the near-infrared.

In this paper we develop an integrated light population synthesis method for fitting galaxy spectra built upon the modeling techniques developed by [182]. We applied this method to spectra obtained in November 2013 of Abell 267 (A267) with the Michigan/Magellan Fiber System (M2FS) on the Clay-Magellan Telescope at Las Campanas Observatory in Chile. In §3.2 we describe the observations and subsequent data reduction. §3.3 describes the integrated light spectral model used to fit these spectra. §3.4 we describe how we implemented and fit this model and test it with mock spectra and previously fit galaxy spectra. And finally in §3.5 we apply the model to fit the new A267 spectra.

3.2 Observations and Data Reduction

In this section we present a pilot program for cluster spectroscopy at low resolution with M2FS and detail the reduction of these spectra.

3.2.1 Target Selection

We select targets for M2FS observations by identifying galaxies detected in Sloan Digital Sky Survey images [183] that are projected along the line of sight to Abell 267 and are likely to be quiescent cluster members. First we extract from SDSS all extended sources projected within a circle of diameter 0.5° that is centered on Abell 267 ($\alpha_{2000} = 28.174°$, $\delta_{2000} = +1.008°$); for all such objects brighter than r=23, Fig. 3.1 displays sky positions and r, r-i photometry. In the right panel of Fig. 3.1, blue markers indicate colors and magnitudes for galaxies nearest the center of Abell 267—i.e., those lying within the shaded blue circle (radius 0.05°) in the left panel of Fig. 3.1. These objects clearly trace A267's red sequence, which is enclosed by a red rectangle in the right panel of Fig. 3.1. Finally, red points in the left panel of Fig. 3.1 indicate sky positions for all galaxies lying in the red sequence selection box. We consider all objects within this selection box to be candidate members of Abell 267's red sequence. It is from this set of objects that we select M2FS targets, giving greater weight to brighter objects.

3.2.2 Observations

We observed 223 individual galaxy spectra on 30 November 2013 on the Clay Magellan Telescope using M2FS. We used the low resolution grating on M2FS and chose a

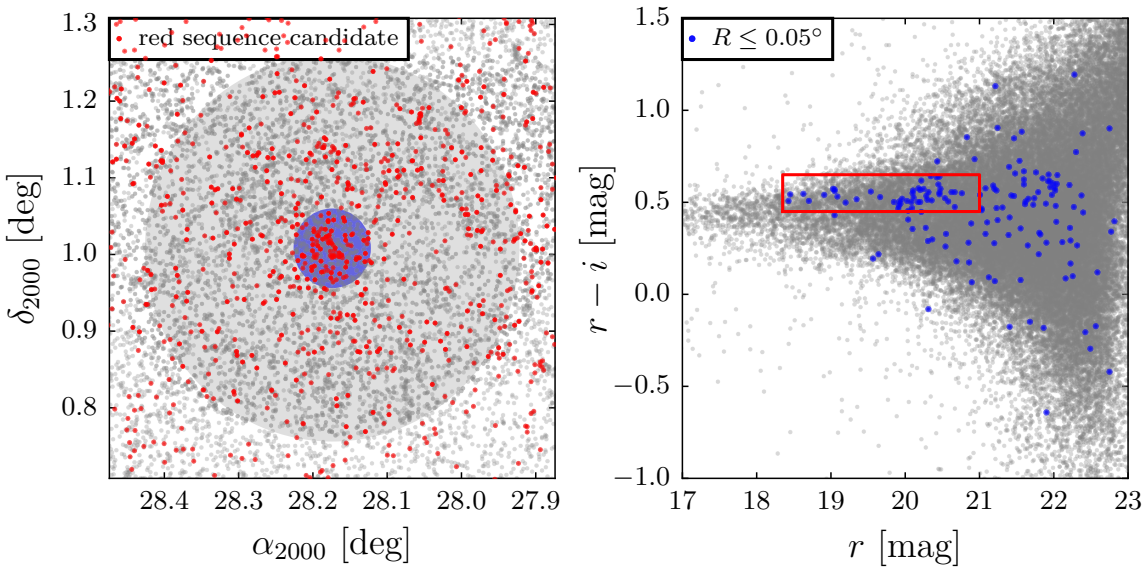

Figure 3.1: Equatorial coordinates (left) and r, $r-i$ photometry (right) for galaxies along the line of sight to Abell 267 [183]. In the right-hand panel, blue markers represent galaxies nearest the center of Abell 267 (from within the shaded blue circle in the left-hand panel). The red rectangle encloses quiescent galaxies on Abell 267's red sequence. In the left-hand panel, red points show the spatial distribution of these red sequence candidates; it is from this set of objects that we select M2FS targets. In the left-hand panel, the shaded gray circle represent the M2FS field of view.

coverage range of 4600-6400 Å with a resolution of $R \sim 2000$. Of the 256 fibers available on M2FS, we allocated 223 for science targets, leaving 33 fibers directed at relatively blank regions of sky. We observed the field over 6 sub-exposures of 15 minutes each, which we then stacked to improve signal-to-noise ratio and remove cosmic rays (see §3.2.3 below). For wavelength calibration we took Thorium-Argon-Neon lamp exposures both before and after a set of science exposures, and we took a quartz-lamp exposure immediately after the sequence of science exposures. To identify the apertures on the CCD for each fiber we took "fibermap" exposures which are high signal-to-noise (S/N) exposures of the ambient light in the dome during the daytime. For the purpose of calibration and correction for variations in fibre throughput, we also took a series of high S/N exposures (including Th-Ar-Ne and quartz calibrations) during evening twilight sky.

3.2.3 Data Reduction

The detector used with M2FS consists of two 4096 x 4112-pixel CCDs, each of which is read out through four amplifiers. We used the 2 x 2 binning setup for readout, so the output images are 2048 x 2056-pixels. The 256 fibers are organized into 16 cassettes of 16 fibers each. The cassettes are spatially separated on the CCD and within each

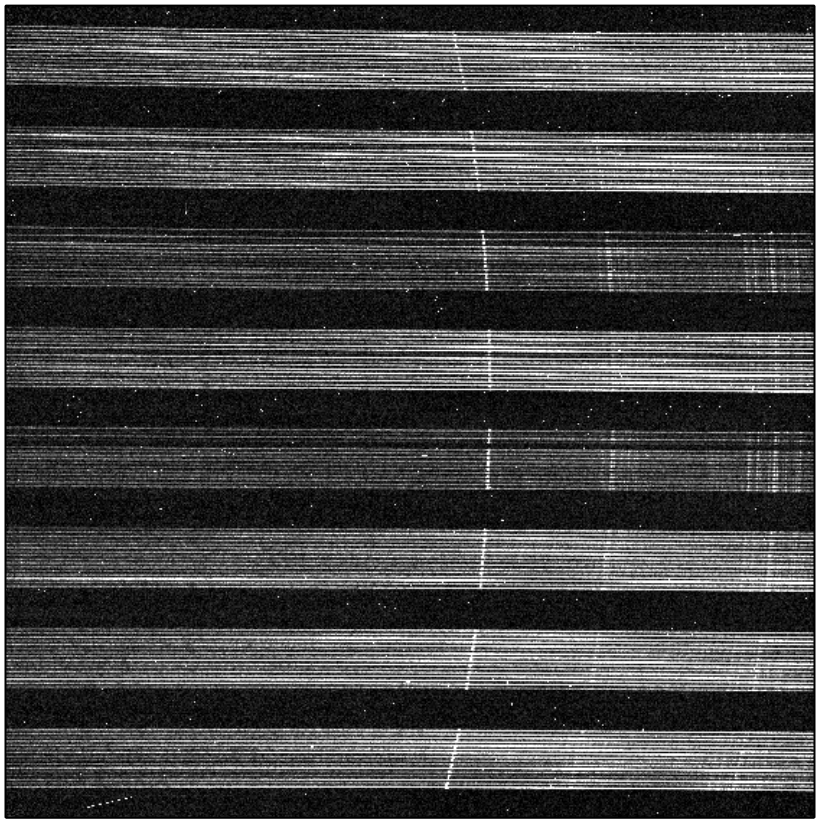

Figure 3.2: One of the two CCDs from M2FS. Each horizontal line corresponds to one of the fiber spectra. The fibers are organized into 8 cassettes (fiber bundles) of 16 fibers. The bright curved vertical feature is a bright atmospheric emission line that is observed in nearly all fibers.

cassette each individual fiber is spatially separated. Fig. 3.2 shows an example of one of the CCDs with twilight spectra obtained during the A267 observations.

We use standard IRAF routines to process the raw images, to extract the 1D spectra and to estimate the wavelength solution for each spectrum obtained in each science exposure. We also propagate the variance associated with the count level in each pixel of each image. At the outset, for every science frame (i.e. the images obtained in an individual science exposure) we generate a corresponding variance frame in which the value assigned to a given pixel in units of electrons is

$$\mathrm{Var(pix)} = C(\mathrm{pix})G + R^2 \tag{3.1}$$

where $C(\mathrm{pix})$ is the count in analog-to-digital units (ADU), $G \approx 0.68\mathrm{e}^-/\mathrm{ADU}$ is the gain of the M2FS detector and $R = 2.7\mathrm{e}^-$ is the read noise. In order to propagate variances, we process variance frames accordingly to the way that we process their corresponding science frames (see below). For example, where we combine spectra via

addition or subtraction (e.g. to combine subexposures or to subtract sky background) we compute the combined variances as the sum of the variances associated with the pixels contributing to the sum or difference. Or, where we rescale count levels in a given science exposure (e.g. to correct for the variability in the fiber throughput) we rescale the variances by the square of the same factor.

For a given frame we begin the data reduction pipeline using the IRAF package CCDPROC to perform overscan corrections independently for each amplifier. We then rescale the counts in each frame by the gain associated with each amplifier independently in order to convert ADUs to electrons. For each of the two CCDs, we combine the four amplifier images to form a continuous gain-corrected image. We then bias subtract and remove the dark current. For the dark current correction, we rescale the measured dark current by the exposure time of each individual subexposure, then subtract this rescaled dark current. During our observations of A267, there was a non-negligible dark current that builds up in the corners of the CCD and contributed $\sim 50 - 200$ counts per 15 minute exposure.

Next, we use the IRAF package APALL to identify the locations and shapes of the spectral apertures, and to extract 1D spectra for science, quartz, Th-Ar-Ne arcs, and twilight exposures and associated variance frames. We initially identify aperture locations and trace patterns in the relatively bright fibermap exposures. Fibermap exposures are obtained by taking short exposures, with all fibers plugged, of ambient sunlight in the dome during the daytime. We use fibermaps instead of quartz calibration frames to identify aperture locations because the ambient sunlight more uniformly illuminates all fibers compared to quartz exposures. After identifying the aperture locations with the fibermaps, we use the IRAF package APSCATTER to fit the scattered light in the regions of the CCD outside the apertures and subtract this fit from the regions of the CCD inside the apertures. Fixing the relative locations and shapes of the apertures according to the fibermaps, we use APALL and allow the entire aperture pattern to shift globally in order to provide the best match to the corresponding science frames. We apply exactly the same shift to define apertures and traces for the Th-Ar-Ne frames. We then use APALL to extract the spectra from each aperture by combining (adding) counts from pixels along the axis perpendicular to the dispersion direction for each science, twilight, and Th-Ar-Ne and associated variance frames.

Next we use the extracted twilight spectra to adjust for differences in fiber throughput and pixel sensitivity. We first fit a (6th-order) Legendre function to the extracted twilight spectra, which iteratively rejects counts that either exceed the fit by more than 3-times the rms of the residuals or are smaller than the fit by more that 1.75-times the rms of residuals. The lower tolerance is smaller than the upper tolerance to effectively exclude the absorption features from the fit. We then determine the median count level of the fit for each fiber and normalize each fit by the mean of these median count levels. Finally we divide the science and twilight spectra by this normalized fit per spectrum, thereby correcting for differences in throughput and

pixel sensitivity simultaneously.

Next we estimate wavelength solutions, λ(pix). For each extracted Th-Ar-Ne spectrum, we use the IRAF package IDENTIFY to fit a (5th-order) Legendre polynomial to the centroids of between 30 and 40 identified emission lines of known wavelength. Residuals of these fits typically have a root mean square (rms) scatter ~ 0.150 Å or ~ 10 km/s. We assign the same aperture-dependent wavelength solutions to the corresponding science frames. Except for extraction from 2D to 1D, each individual spectrum retains the same sampling native to the detector; therefore, the wavelength solutions generally differ from one spectrum to another and have a non-uniform $\Delta\lambda/\Delta$pix even within the same spectrum.

3.2.4 Sky Subtraction

After determining the wavelength solutions and correcting for fiber throughput and pixel sensitivity, we estimate the background sky and subtract it from our science exposures. Apart from a strong atmospheric emission feature at $\sim$ 5600Å, the main source of sky background is scattered sunlight. Following [184] we begin by taking the sky fibers (in this set of exposures $\sim$ 33) for a given frame and interpolate the individual sky spectra onto a common grid with constant spacing $\Delta\lambda'/\Delta\text{pix}' \sim 0.1$Å(oversampled by a factor of 16 with respect to the original sampling). For each discrete wavelength of the oversampled sky spectrum, we record the median count level and estimate the variance as

$$\text{Var}_{\text{sky}} = 2.198\pi \frac{\text{MAD}^2}{2N_{\text{sky}}} \tag{3.2}$$

where $N_{\text{sky}} \sim 33$ and MAD is the median absolute deviation [185]. We then interpolate the resulting spectrum of median sky level and associated variances back onto the real, irregularly-sampled wavelength solution that is unique to a given science spectrum. Lastly we subtract the sky spectrum from the science spectrum, pixel by pixel.

Following sky subtraction, we then combine sub-exposures by taking the inverse-variance weighted mean at each pixel using the IRAF package, SCOMBINE with the rejection routine CRREJECT (CosmicRayREJECT) to remove cosmic rays. Fig. 3.3 displays examples of the resulting M2FS spectra for science targets.

3.3 Integrated Light Population Synthesis Model For Galaxy Spectra

We model the galaxy spectra by generating synthetic integrated light spectra (ILS). This model is building on the procedure of [182] (hereafter W15b), but here we are extending this model from resolved stellar spectra to integrated light spectra. The

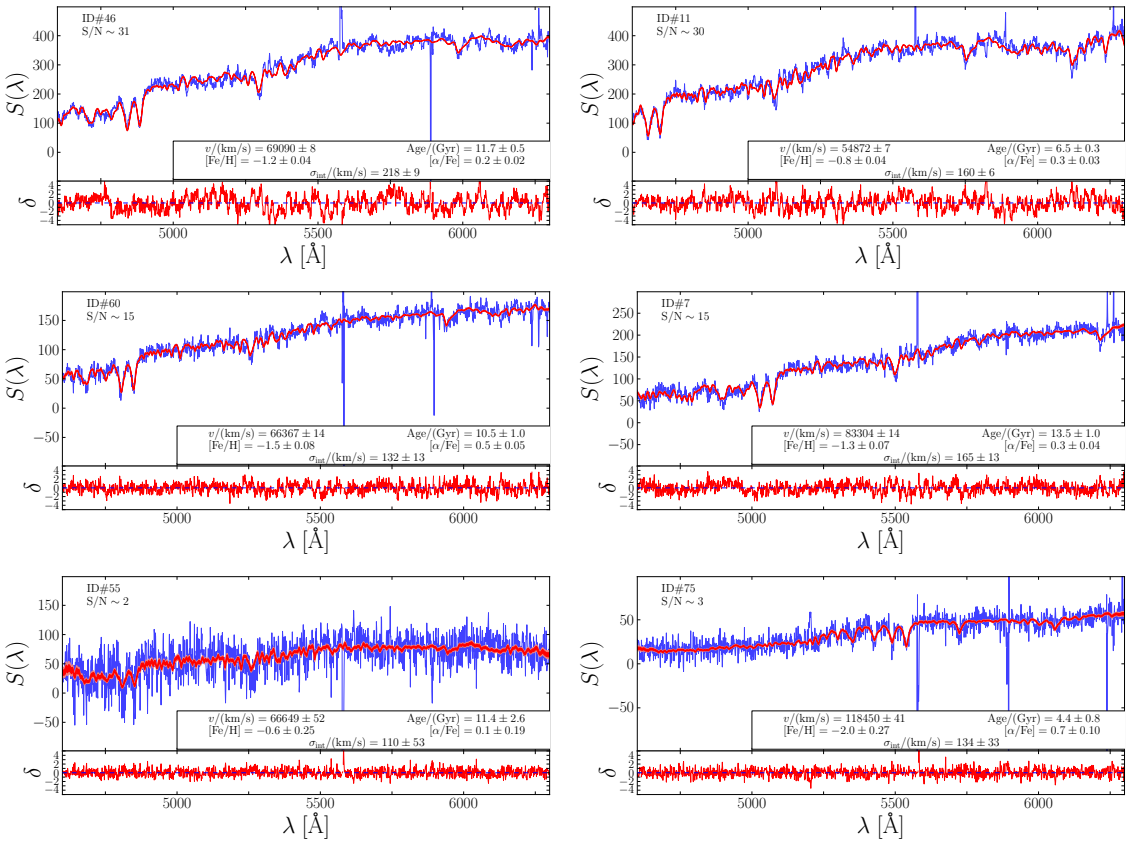

Figure 3.3: Sky-subtracted M2FS spectra (blue) for probable Abell 267 member galaxies (left-hand panels) and contamination galaxies (right-hand panel) spanning median signal-to-noise $2 \lesssim \mathrm{S/N/pixel} \lesssim 30$. The red overplotted regions show the range of spectra encompassing the central 68% and 95% (dark and lighter red, respectively) of the posterior PDFs for our spectral model (§3.3). The text in each panel lists the median S/N and our estimates of $v_{\rm los}$, Age, [Fe/H], [α/Fe], and $\sigma_{\rm int}$ as well as the ID#'s for easy reference to the data listed in Table 3.3. The bottom portion of each panel shows the residuals of these fits scaled by the variance in each pixel (Eq. 3.14).

general procedure is to build a luminosity-weighted sum of template stellar spectra that correspond to a simple stellar population of a given age, metallicity, and alpha-abundance, and then to shift and smooth that spectrum to match the redshift, internal velocity dispersion, and instrumental broadening of the spectrograph.

3.3.1 Integrated Light Spectral Library

The first component of the model is a stellar spectral library. We use the Phoenix Stellar Spectral Library [186] as the basis for building the integrated light spectra. This synthetic spectral library is computed on a regular four dimensional grid in $T_{\rm eff}$,

log g, [Fe/H], and [α/Fe] space spanning a large range in each parameter: $0 - 15$ Gyr in Age, 0 to 5 in log g, -4.0 to $+0.5$ in [Fe/H], and -0.2 to $+0.8$ in [α/Fe]. We continuum-normalize each spectrum beforehand. This library does not include rare bright stars such as carbon or asymptotic giant branch (AGB) stars and therefore they will not be included in our model. Despite their rarity, the high luminosity of these stars can contribute significantly to a galaxy's integrated light [187]. Because our model does not include the contribution of these stars, our parameter estimates are susceptible to systematic error that is not reflected in the quoted random errors.

In order to calculate an integrated light spectrum, we need to know how the stars from the stellar library contribute to the light in each stellar population; in other words we need to sum luminosity-weighted contributions along the isochrone for a given stellar population. For this we use the Dartmouth Isochrone Database [188][1]. This database consists of a three dimensional grid of isochrone lists in galactic age, mean metallicity [Fe/H], and chemical abundance [α/Fe] space. We construct a regular grid of isochrone lists with ΔAge = 0.25 Gyr, Δ[Fe/H] = 0.5 dex, and $\Delta[\alpha/\mathrm{Fe}] = 0.2$ dex. Each isochrone is a list of stellar properties (mass, effective temperature, magnitudes, surface gravity) describing the stars of a given age, metallicity, and chemical enrichment.

We first generate an integrated light spectrum for each isochrone, thus converting the isochrone database into an integrated light spectral library. For this procedure, we weight each individual library spectrum according to the luminosity function computed by [188]. For each luminosity bin in the tabulated luminosity function, we identify the isochrone having luminosity closest to the bin's central value. For the luminosity function we use a magnitude bin width of 0.1 and a Chabrier log-normal initial mass function (IMF) of the form

$$dN/dM \propto \frac{1}{M} \exp\left[-\frac{\ln\left(M/M_c\right)^2}{2\sigma^2}\right] \tag{3.3}$$

where $M_c = 0.22 M_\odot$ is the central mass and $\sigma = 0.57$ is the dispersion [189]. In principle these could be free parameters of our model as well, but for now we hold them fixed. We identify which stars listed in the isochrone fall within a given magnitude bin (from the luminosity function) and determine the stellar parameters ($T_{\rm eff}$, log g, [Fe/H], and [α/Fe]) associated with the median star within the bin. This star will be included in the integrated light spectrum with a weight that is simply the product of the number of stars in the magnitude bin calculated from the luminosity function and the luminosity of the star selected.

We denote the original spectra in the library as $L_0(\lambda, \boldsymbol{\theta}_{\rm atm})$, corresponding to stellar-atmospheric parameters $\boldsymbol{\theta}_{\rm atm} \equiv (T_{\rm eff}, \log\ g, [\mathrm{Fe/H}], [\alpha/\mathrm{Fe}])$. As described by W15b (their equations 7 and 8), we apply a smoothing kernel over the entire stellar library to obtain a unique spectrum at the specific $\boldsymbol{\theta}_{\rm atm}$ of each isochrone. We denote

[1] http://stellar.dartmouth.edu/models/

the smoothed spectra as $L_1(\lambda, \boldsymbol{\theta}_{\rm atm})$. In our case, the number of spectra in the Phoenix library is $N_L = 5566$, and we set the smoothing bandwidths equal to the grid spacing in each dimension: $h_{T_{\rm eff}} = 200$ K, $h_{\log\ g} = 0.5$ dex, $h_{\rm [Fe/H]} = 0.5$ dex, and $h_{[\alpha/{\rm Fe}]} = 0.2$ dex.

After generating each individual stellar spectrum $L_{1,i}\left(\lambda, \boldsymbol{\theta}_{{\rm atm},i}\right)$ corresponding to each isochrone, we weight and sum these spectra as described above, which produces an integrated light spectrum given by:

$$L_{\rm ILS}\left(\lambda, \boldsymbol{\theta}_{\rm gal}\right) = \sum_{i}^{N_\phi} L_{1,i}\left(\lambda, \boldsymbol{\theta}_{{\rm atm},i}\right) w_i. \tag{3.4}$$

The weight given to each spectrum is $w_i \equiv n_i \phi_i$, where n_i is the number of stars in the given magnitude bin and ϕ_i is the luminosity of the star specified in the isochrone; N_ϕ is the number of magnitude bins in the luminosity function and $\boldsymbol{\theta}_{\rm gal} \equiv ({\rm Age}, [{\rm Fe/H}], [\alpha/{\rm Fe}])$ are the galactic parameters specific to each isochrone. We do this for the entire isochrone database, thus generating an integrated light spectral library covering the parameter space defined by $\boldsymbol{\theta}_{\rm gal}$.

When fitting the galactic spectra there are two processes that broaden the absorption features: instrumental line spread function (LSF) and internal motions (i.e. redshift distribution, internal velocity dispersion, galaxy rotations, and so on). The instrumental LSF must be measured independently to break its inherent degeneracy with internal velocity dispersion (see §3.3.2 below). To mimic broadening, we add another dimension to our integrated light spectral library: a smoothing parameter h_0. Following the same procedure described by W15b to broaden the spectra over a range of smoothing bandwidths, we apply Eqs. 5 and 6 from W15b to each $L_{\rm ILS}\left(\lambda, \boldsymbol{\theta}_{\rm gal}\right)$. We generate six versions of each integrated light spectrum using smoothing bandwidths $h_0 = 0, 2, 4, 6, 8, 10$ Å. This range of smoothing bandwidths was chosen so as to cover the broadening associated with the range of internal velocity dispersions we expect to measure in our galaxy sample (up to ~ 550 km s^{-1} at 5500 Å).

3.3.2 Spectral Model

Following [190], [184], and W15b, we fit each individual galaxy spectrum with a spectral model of the form

$$M(\lambda) = \max\left[S\left(\lambda\right)\right] P_l(\lambda) T\left(\lambda\left[1 + \frac{v_{\rm los}}{c}\right]\right) \tag{3.5}$$

where c is the speed of light and $\max\left[S\left(\lambda\right)\right]$ is the maximum count level of a science spectrum. Eq. 3.5 is the same as Eq. 2 in W15b, except we chose to not include the polynomial $Q_m(\lambda)$ which is a wavelength-dependent redshift. We noticed from fitting the A267 spectra that the parameters needed for this polynomial are unconstrained in our low resolution integrated light spectra, but relatively well constrained by the

Table 3.1: Free parameters and priors for Integrated Light Population Synthesis Model

Parameter	Prior	Description
$v_{\rm los}/\,({\rm km\ s^{-1}})$	Uniform between 0 and 138000	Line-of-sight velocity ($z = v_{\rm los}/c$)
Age/Gyr	Uniform between 0 and 15	Age of simple stellar population
[Fe/H]	Uniform between -4 and $+0.5$	Metallicity of simple stellar population
[α/Fe]	Uniform between -0.2 and $+0.8$	Chemical abundance of simple stellar population
$\sigma_{\rm int}/\,({\rm km\ s^{-1}})$	Uniform between 0 and 500	Internal velocity dispersion of simple stellar population
h_0/Å	Uniform between 0 and 4	Polynomial coefficient (line spread function: Eq. 3.6)
h_1/Å	Uniform between -2 and $+2$	Polynomial coefficient (line spread function: Eq. 3.6)
h_2/Å	Uniform between -4 and $+4$	Polynomial coefficient (line spread function: Eq. 3.6)
p_0	Uniform between -2 and $+2$	Polynomial coefficient (continuum: Eq. 3 from W15b)
p_1	Uniform between -2 and $+2$	Polynomial coefficient (continuum: Eq. 3 from W15b)
p_2	Uniform between -2 and $+2$	Polynomial coefficient (continuum: Eq. 3 from W15b)
p_3	Uniform between -2 and $+2$	Polynomial coefficient (continuum: Eq. 3 from W15b)
p_4	Uniform between -2 and $+2$	Polynomial coefficient (continuum: Eq. 3 from W15b)
p_5	Uniform between -2 and $+2$	Polynomial coefficient (continuum: Eq. 3 from W15b)

high-resolution, resolved stellar spectra of W15b. We still included in this model the same form for the polynomial $P_l(\lambda)$ given by W15b's Eqs. 3, which fits the continuum of the observed spectra.

Because we are modeling a population of stars, we build into our model a way of measuring the internal velocity dispersion of this population. The velocity dispersion will manifest itself as a broadening of the absorption features in each spectrum. However, this broadening will be degenerate with the line spread function (LSF) of the spectrograph, so care must be taken to break this degeneracy between the two sources of broadening. To do this, we first measure the LSF with twilight spectra and then broaden the model spectra according to the LSF in addition to the broadening associated with the velocity dispersion of the stars. In order to allow for a wavelength dependent LSF, we introduce another polynomial for the smoothing bandwidth, $H_n(\lambda)$, which we allow to vary with wavelength according to

$$H_n(\lambda) = h_0 + h_1\left[\frac{\lambda-\lambda_0}{\lambda_s}\right] + h_2\left[\frac{\lambda-\lambda_0}{\lambda_s}\right]^2 + ... + h_n\left[\frac{\lambda-\lambda_0}{\lambda_s}\right]^n. \tag{3.6}$$

Given that the broadening related to velocity dispersion $\sigma_{\rm int}$ is given by $\sigma_{\rm int}/c = \Delta\lambda/\lambda$ where c is the speed of light, the total broadening associated with both the LSF and the internal velocity dispersion of the population of stars is given by

$$h^2(\lambda) = \left(\frac{\sigma_{\rm int}}{c}\lambda\right)^2 + H_n^2(\lambda). \tag{3.7}$$

This method introduces $n+2$ new free parameters: one for internal velocity dispersion and the other $n+1$ are from the h_n coefficients. However, when fitting twilight spectra, we assume that $\sigma_{\rm int} = 0$ because the "stellar population" consists of only the sun, and so we only fit the $n+1$ parameters associated with the LSF. On the other hand, when fitting science spectra we use the previously measured $n+1$ LSF parameters from the twilight fits, and so we fit only for $\sigma_{\rm int}$.

In order to let the spectral model vary continuously despite the library's coarse gridding in galactic parameter space and the discrete values of the smoothing bandwidth, we apply another wavelength-dependent smoothing over the entire collection of library spectra. Specifically, for any choice of galactic parameters $\boldsymbol{\theta}_{\rm gal}$ and smoothing bandwidth $h(\lambda)$, we obtain a unique template

$$T(\lambda) = \frac{\sum_i^{N_{\rm ILS}} L_{\rm ILS}\left(\lambda, \boldsymbol{\theta}_{{\rm gal}_i}, h_{0_i}\right) K_3\left(\lambda, \frac{\boldsymbol{\theta}_{{\rm gal}_i} - \boldsymbol{\theta}_{\rm gal}}{\boldsymbol{h}_{\rm gal}}, \frac{h_{0_i} - h(\lambda)}{h_h}\right)}{\sum_i^{N_\lambda} K_3\left(\lambda, \frac{\boldsymbol{\theta}_{{\rm gal}_i} - \boldsymbol{\theta}_{\rm gal}}{\boldsymbol{h}_{\rm gal}}, \frac{h_{0_i} - h(\lambda)}{h_h}\right)} \tag{3.8}$$

where $N_{\rm ILS} = 14202$ is the number of ILS library spectra and the kernel is

$$K_3\left(\lambda, \frac{\boldsymbol{\theta}_{{\rm gal}_i} - \boldsymbol{\theta}_{\rm gal}}{\boldsymbol{h}_{\rm gal}}, \frac{h_{0_i} - h(\lambda)}{h_h}\right) = \exp\left[-\frac{1}{2}\left(\frac{\left({\rm Age}_i - {\rm Age}\right)^2}{h_{\rm Age}^2} + \frac{\left([{\rm Fe/H}]_i - [{\rm Fe/H}]\right)^2}{h_{[{\rm Fe/H}]}^2} + \frac{\left([\alpha/{\rm Fe}]_i - [\alpha/{\rm Fe}]\right)^2}{h_{[\alpha/{\rm Fe}]}^2} + \frac{\left(h_{0_i} - h(\lambda)\right)^2}{h_h^2}\right)\right]. \tag{3.9}$$

We set the galactic smoothing bandwidths $\boldsymbol{h}_{\rm gal}$ equal to the grid spacing in each dimension: $h_{\rm Age} = 0.25$ GYr, $h_{[{\rm Fe/H}]} = 0.5$ dex, $h_{[\alpha/{\rm Fe}]} = 0.2$ dex, $h_h = 1$Å. We found that setting the smoothing bandwidth $h_h = 2$Å (the grid spacing of the library) results in our model favoring a larger broadening parameter, thus over-smoothing the spectral fit; therefore, we decreased the smoothing bandwidth to $h_h = 1$Å, which solved this issue. This smoothing procedure gives posterior probability distributions that are approximately Gaussian and tend not to cluster near the library's grid points.

3.4 Analysis of Spectra

We now apply this model for fitting spectra and estimating model parameters.

3.4.1 Likelihood function and free parameters

Given the spectral model $M(\lambda)$, we assume that the observed spectrum $S(\lambda)$ has likelihood

$$\mathcal{L}\left(S(\lambda)|\boldsymbol{\theta}\right) = \prod_{i=1}^{N_\lambda} \frac{1}{\sqrt{2\pi \mathrm{Var}\left[S(\lambda_i)\right]}} \exp\left[-\frac{1}{2}\frac{\left(S(\lambda_i) - M(\lambda_i)\right)^2}{\mathrm{Var}\left[S(\lambda_i)\right]}\right]. \tag{3.10}$$

In practice the value of $M(\lambda_i)$ that we use in Eq. 3.10 is the linear interpolation, at observed wavelength λ_i, of the discrete model we calculate from Eq. 3.5. This interpolation is necessary because a given template spectrum $T(\lambda)$ retains the discrete wavelength sampling of the synthetic library, which generally differs from those of the observed spectra.

Following W15b in order to define the polynomials in Eqs. 3.5 and 3.6, we chose $l = 5$ and $n = 2$, respectively. These choices give sufficient flexibility to fit the continuum shape and to apply low-order corrections to the wavelength solution. We adopt scale parameters λ_0 and λ_s such that $-1 \leq (\lambda - \lambda_0)/\lambda_s \leq 1$ over the entire wavelength range considered in a fit.

With these choices the spectral model $M(\lambda)$ is fully specified by a vector of 14 free parameters:

$$\boldsymbol{\theta} = (v_{\rm los},\ \mathrm{Age},\ [\mathrm{Fe/H}],\ [\alpha/\mathrm{Fe}],\ \sigma_{\rm int},\ h_0,\ h_1,\ h_2,\ p_0,\ p_1,\ p_2,\ p_3,\ p_4,\ p_5). \tag{3.11}$$

The first five have physical meaning and the rest are nuisance parameters. Table 3.1 lists all parameters and identifies the adopted priors, all of which are uniform over the specified range of values and zero outside that range.

3.4.2 Parameter Estimation

From Bayes' theorem, given the observed spectrum $S(\lambda)$, the model has a posterior probability distribution function (PDF)

$$p\Big(\boldsymbol{\theta}|S(\lambda)\Big) = \frac{\mathcal{L}\Big(S(\lambda)|\boldsymbol{\theta}\Big)p(\boldsymbol{\theta})}{p\Big(S(\lambda)\Big)} \tag{3.12}$$

where $\mathcal{L}\Big(S(\lambda)|,\boldsymbol{\theta}\Big)$ is the likelihood from Eq. 3.10, $p(\boldsymbol{\theta})$ is the prior and

$$p\Big(S(\lambda)\Big) = \int \mathcal{L}\Big(S(\lambda)|\boldsymbol{\theta}\Big)p(\boldsymbol{\theta})\mathrm{d}\boldsymbol{\theta}\mathrm{d}s_1\mathrm{d}s_2 \tag{3.13}$$

is the marginal likelihood, or 'evidence'.

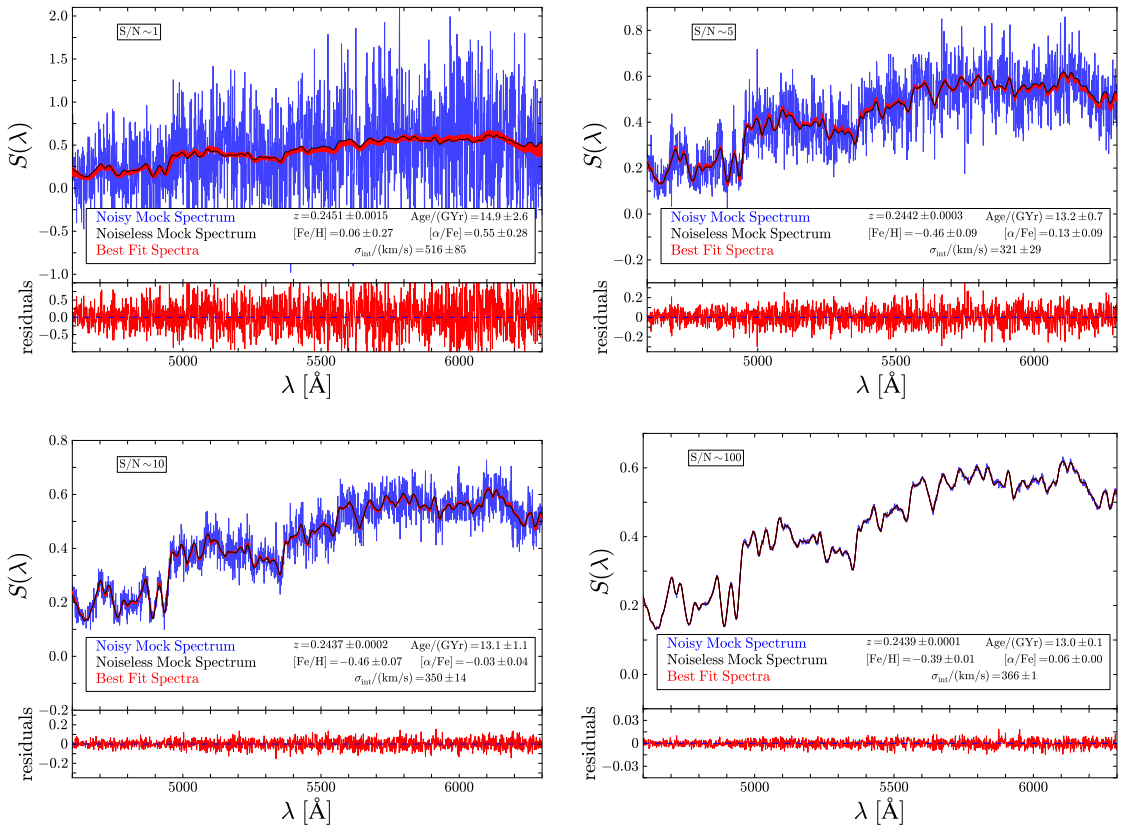

Figure 3.4: Mock spectra (blue) for different values of median S/N per pixel, which is identified in the top left of each panel. The original, noiseless mock spectrum is plotted in each panel in black. Over plotted in red in the top portion of each panel is the range of spectra encompassing 68% of the posterior distribution of the spectral fit. Also in each panel we list the best fit parameters with uncertainties. For $v_{\rm los}$ we show redshift z instead. In the bottom portion of each panel, we show the residual difference between the noisy mock spectrum and the best fit spectrum from the model.

In order to evaluate the posterior PDF, we must scan the 14D parameter space. For this task, we use the software package MULTINEST[2] [191, 192]. MULTINEST implements a nested-sampling Monte Carlo algorithm that is designed to calculate the evidence (Eq. 3.13) and simultaneously to sample the posterior PDF (Eq. 3.12). [191] and [192] demonstrate that MULTINEST performs well even when the posterior is multimodal and has strong curving degeneracies, circumstances that can present problems for standard Markov Chain Monte Carlo techniques.

Table 3.2: Input physical parameters for the mock spectral catalog.

$v_{\rm los}$	Age	[Fe/H]	[α/Fe]	$\sigma_{\rm int}$
km s^{-1}	Gyr	dex	dex	km s^{-1}
69579	10.9	0.39	-0.03	540
74406	5.8	-0.52	0.68	472
71331	9.0	-2.11	0.79	194
70380	10.8	-0.12	0.24	149
73100	13.2	-0.39	0.06	367
73851	14.9	-1.38	0.02	271
67592	0.2	-0.64	0.32	466
73442	2.8	-0.92	0.27	256
67467	3.1	-1.86	0.13	489
72545	7.9	-0.42	0.17	296
69134	8.7	0.60	-0.15	535
69698	1.4	-0.36	-0.10	204
68629	7.9	0.36	0.08	287
68724	14.4	0.36	0.20	519
71461	12.5	-2.38	0.63	507
68701	13.5	-0.38	0.58	534
73772	13.8	0.35	0.09	319
67092	1.4	-1.60	0.68	144
65444	3.2	-2.13	-0.04	365
67506	12.0	-2.13	0.51	364

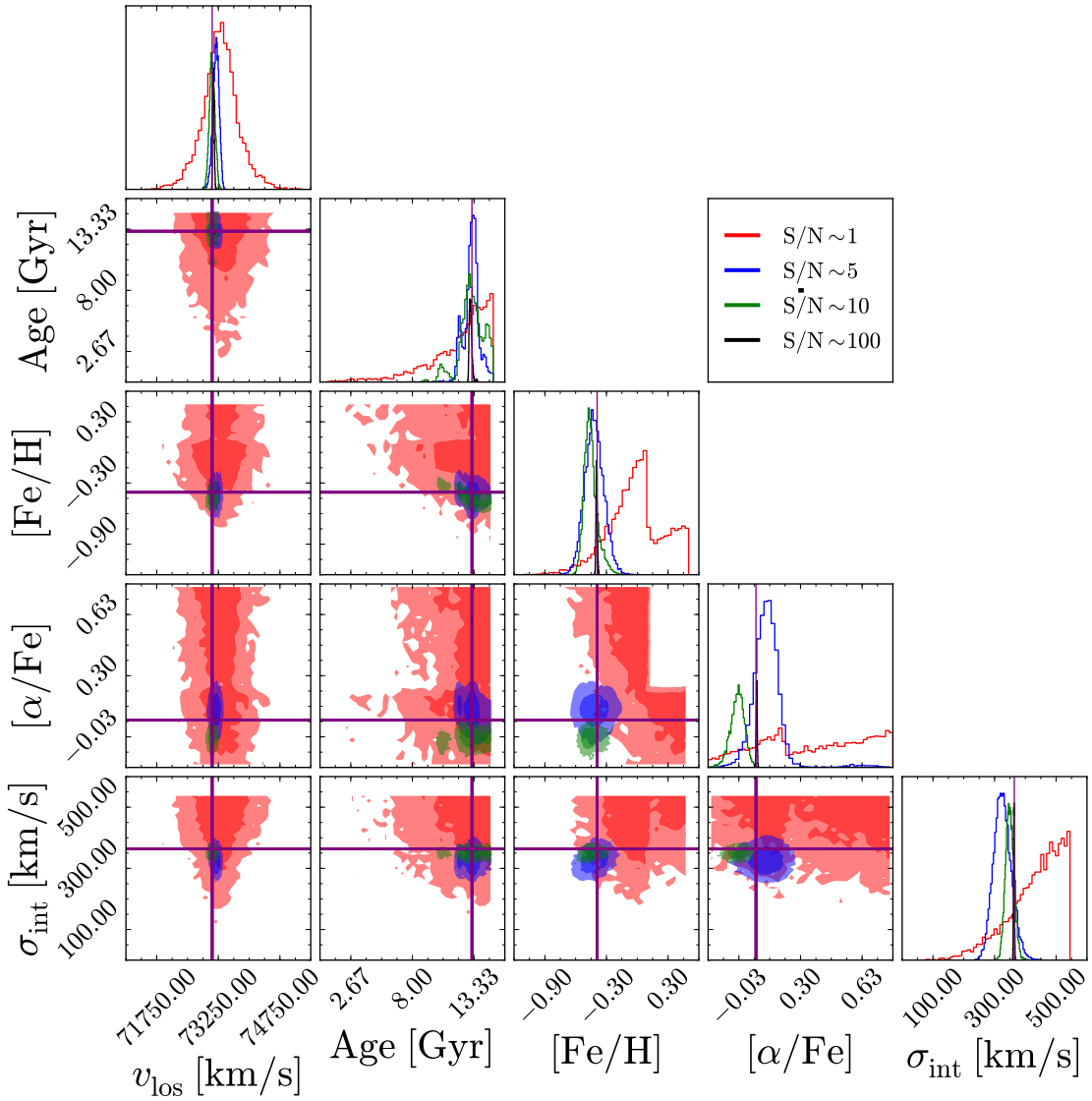

Figure 3.5: Marginal posterior probability distributions for the five galactic parameters corresponding to the fits to mock spectra shown in Fig. 3.4. Each S/N value is represented with a different color as indicated in the top right panel. For the 2D posteriors, we show the the 1σ and 2σ regions of these distributions as the darker and lighter regions respectively. Above each column is the marginalized 1D posterior PDFs for each of the five parameters. Also shown in each panel in purple is the input value of the parameters used in generating this noiseless mock spectrum.

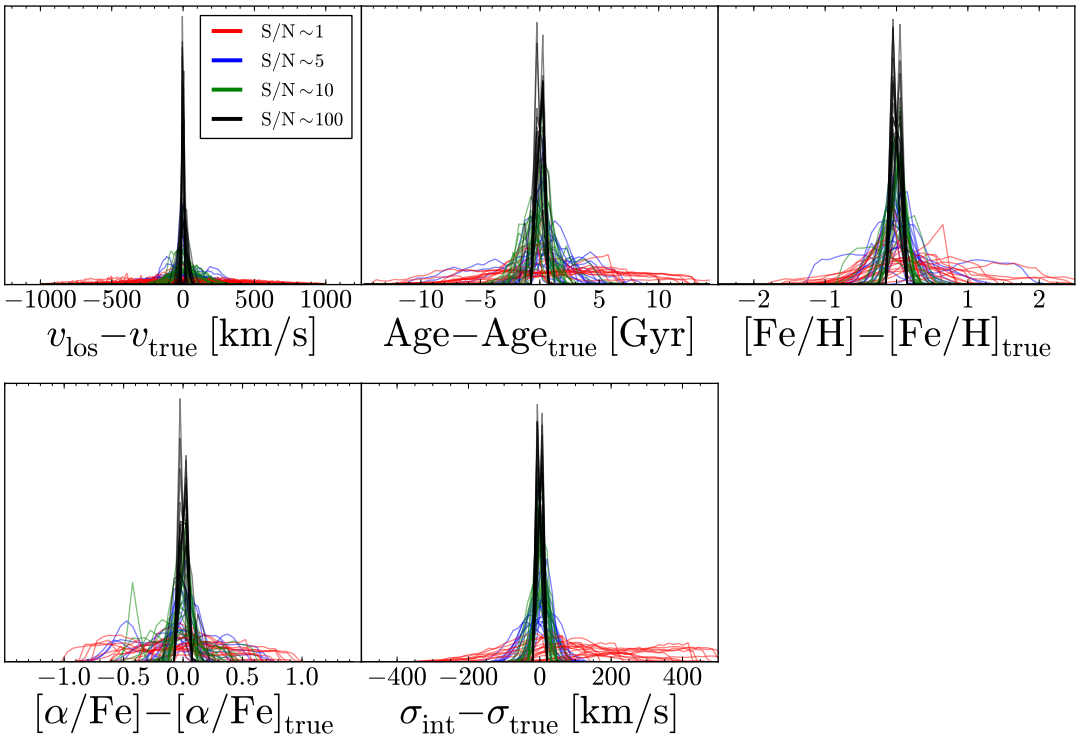

Figure 3.6: Difference between all posterior PDFs and the true input values (subscript true) for the five physical parameters for all mock spectra. Each PDF is colored by the median pixel S/N as shown in the top left panel.

3.4.3 Tests with Mock Spectra

As a first test of the accuracy of our model, we generated and fit mock spectra over a range of S/N values. We first generated a noiseless mock spectrum, for a given set of Age, [Fe/H], [α/Fe], and $\sigma_{\rm int}$, using the pre-calculated spectral library (see §3.3.1) and the spectral model described in §3.3.2. Table 3.2 shows the 20 sets of input galactic parameters we used to generate each noiseless mock spectrum. In order to also analyze the performance of our model at different S/N levels, we added noise such that the median S/N of each mock spectrum had values $\sim 1, 5, 10, 100$. Therefore, each noiseless mock spectrum produced four noisy spectra which we fit with our model. Each spectrum shown in Fig. 3.4 was generated from the same noiseless mock spectrum (the input parameters for the mock spectra shown in Fig. 3.4 are given in the first row in Table 3.2).

Plotted over each mock spectrum in Fig. 3.4 is the best-fitting model spectrum. We show in red the range of spectra attributed to central 68% of the posterior distribution estimated by MULTINEST at each pixel. For high S/N levels, these red regions

[2]Available at ccpforge.cse.rl.ac.uk/gf/project/multinest

look just like single curves because the fits are tightly constrained; however, for low S/N, one can see the width of these distributions (top left panel of Fig. 3.4). In the bottom portion of each panel, we show the residual difference between the best fitting spectrum (most likely set of parameters) and the mock spectrum. The text within each panel indicates estimates of physical parameters redshift z, Age, [Fe/H], [α/Fe], and internal velocity dispersion $\sigma_{\rm int}$.

In the text of Fig. 3.4, along with the best fit values of the galactic parameters, we also list their respective uncertainties. These uncertainties enclose the central 68% of the posterior PDF for each parameter. Therefore, in Fig. 3.5 we show the marginal posterior PDFs for the five galactic parameters, which better quantifies the distribution of each parameter. The posteriors shown in Fig. 3.5 correspond to the spectral fits shown in Fig. 3.4. Each color in the 1D and 2D posteriors corresponds to a different median pixel S/N. The darker and lighter regions in the 2D posteriors show the 1σ and 2σ contours of these distributions, respectively. For increasing S/N, the posterior distributions become more Gaussian in shape (which is expected considering we use a Gaussian likelihood function Eq. 3.10) and the 2D posteriors are much better constrained. Furthermore, we also show the true input values of each of these parameters in purple. We can easily see how the posteriors converge on the true values as S/N increases. Additionally we can see that some parameters are better constrained about the true values at lower S/N ($v_{\rm los}$ for example) while other parameters ([α/Fe]) have difficulty at low S/N.

We repeated this test for 20 sets of input parameters (Table 3.2), and thus a total of 80 mock spectra. Fig. 3.6 shows a summary of our results for the mock catalog. In each panel of Fig. 3.6, we show the difference between the true input value for each mock spectrum and the posterior PDFs for each of the five galactic parameters. Each panel corresponds to a different parameter and the colors show how these distributions vary with S/N. As expected, with increasing S/N, these posteriors become more constrained and are more centered on zero deviation (in other words centered on the true input value for the mock spectrum).

These tests establish good statistical properties for our model. However, they leave our estimates susceptible to systematic errors due to the choice of spectral library (e.g incomplete line list) and isochrone databases (e.g. IMF). W15b found that there is a significant dependence on choice of spectral library, such that estimates of [Fe/H] and [α/Fe] can suffer systematic errors of up to $\sim$ 0.5dex. In order to gauge the magnitude of these errors, we compare results obtained from our procedure to those obtained by others using different methods.

3.4.4 External Tests

As a final test of our model, we compared our model estimates with previously published results. The spectra for this test were generously provided by I. Chilingarian (private communications) and we compared our results to those in [193] (hereafter

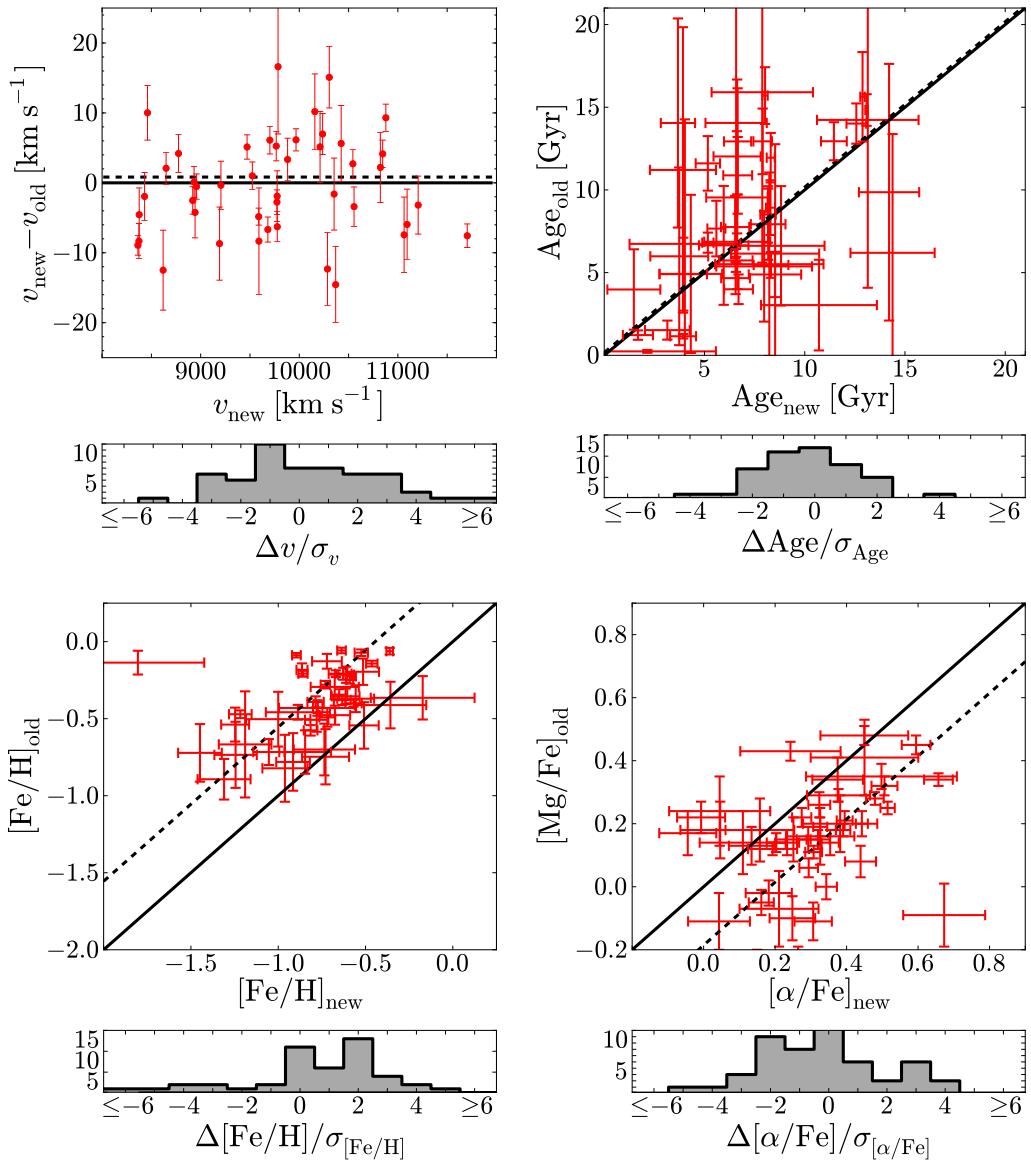

Figure 3.7: We compare our results (subscript "new") to those cited in [193] (subscript "old") for the Abell 496 cluster. Each group of plots corresponds to one of the galactic parameters. The solid black line guides the eye to a one-to-one correlation between the two sets of results. The dashed black line is a fit to the correlation keeping the slope set to one but allowing a constant systematic offset between the two sets. For the velocity panel we show the difference between the measurements in order to more clearly show their uncertainties. The histograms in the bottom panels of each plot show the difference between our measured value and the previous value after applying this constant systematic offset and scaling by the total variance in the two results.

C08). These spectra were observed on the ESO Very Large Telescope using the FLAMES/Giraffe instrument at a resolution of $R \sim 6300$ in the wavelength range $5010 - 5831$Å. Following the method outlined in [194], their spectral fitting method is built upon the PEGASE.HR synthetic spectra [195]. Using a Salpeter IMF, they generated a template spectrum from a linear combination of synthetic spectra at a given age and metallicity similar to our procedure. Using a multidimensional χ^2 minimization procedure, they first fit the kinematics and continuum for each spectrum at a set of fixed values for age and metallicity. Finally they obtained a map of minimal χ^2 in age-metallicity space for each spectrum, from which they estimate age and metallicity for the given stellar population. Therefore, they estimated the stellar population parameters of age and mean metallicity along with line-of-sight velocity and internal velocity dispersion, all of which we compare to the output from our model. Furthermore, they measured Lick indices to compute magnesium abundance ratios [Mg/Fe] which we compare to our estimates of chemical enrichment [α/Fe].

Before fitting the spectra, we noticed from manual inspection that one spectrum had strong emission lines, which we masked by setting the variance in those pixels to large values (10^9). We did this because our syntethic library does not include processes that would cause emission lines such as star formation or active galactic nuclei (AGN). Fig. 3.7 compares the results between the two models: our results are on the x-axis (with subscripts *new*) while C08 results are on the y-axis (with subscripts *old*). The solid black line over plotted in each panel guides the eye to a one-to-one relationship. For the velocity panel, we show the difference between measured velocities in order to more clearly show the distribution. We also fit a linear least squares line to these distributions while fixing the slope to unity so that we can quantify any systematic differences between the two models. These fits are shown as the dashed black lines in each panel. In the bottom plot of each panel we, show histograms of the differences between the two models, incorporating this systematic offset, and scaled by the total uncertainty in the measurements. In the bottom left panel we compare our measurements of chemical abundance [α/Fe] to their measurement of [Mg/Fe]; therefore, this systematic offset partially correlates to the abundance of elements other than magnesium in the stellar population. The systematic offsets between our results and theirs is most likely due to differences in the choice of spectral libraries. We discussed above in §3.4.3 that different library spectra can affect the stellar property estimates by up to 0.5 dex. We caution the reader to understand that our estimates are susceptible to such systematic offsets.

The histograms show that our measured model parameters are mostly within ~ 2 standard deviations of those measured in C08. There are a few outliers (one most notable in [Fe/H] space) which differ by $\gtrsim 3\sigma$ from the values cited in C08 after accounting for systematic offsets. These outliers are fits to low S/N spectra, and our model still produces good fits to the data even though our best fitting parameters differ from C08. Nevertheless, it is not surprising to see one or two 3σ outliers in a sample of ~ 50. The distribution of the age comparisons appears to show little

Table 3.3: Results for fitting of A267 spectra. For full data table see A.1

ID	α_{2000} (hh:mm:ss)	δ_{2000} (°:′:″)	r [mag]	i [mag]	S/N	$\overline{v_{\rm los}}$ (km s^{-1})	$\overline{\rm Age}$ (Gyr)	$\overline{\rm [Fe/H]}$ (dex)	$\overline{\rm [\alpha/Fe]}$ (dex)	$\overline{\sigma_{\rm int}}$ (km s^{-1})
1	01:53:13.48	+01:00:48.6	20.38	19.86	10.1	114156 ± 16	5.5 ± 0.6	-0.72 ± 0.10	0.05 ± 0.05	193.3 ± 12.2
2	01:53:20.26	+01:01:17.0	20.52	20.06	9.3	114059 ± 18	6.5 ± 0.4	-2.54 ± 0.05	0.48 ± 0.09	71.6 ± 24.5
7	01:53:18.66	+01:05:8.6	20.12	19.64	15.5	83304 ± 14	13.5 ± 1.0	-1.32 ± 0.07	0.34 ± 0.04	165.1 ± 13.0
11	01:53:28.58	+01:01:57.6	19.27	18.79	30.7	54872 ± 7	6.5 ± 0.3	-0.80 ± 0.04	0.31 ± 0.03	160.3 ± 6.1
13	01:53:36.88	+01:03:50.8	20.13	19.63	5.0	66669 ± 104	11.8 ± 2.4	-1.29 ± 0.25	0.34 ± 0.18	298.6 ± 84.3
19	01:52:59.68	+01:14:9.4	19.79	19.27	19.8	69207 ± 11	11.4 ± 0.8	-1.13 ± 0.06	0.20 ± 0.04	151.8 ± 10.0
46	01:52:48.44	+00:58:44.8	19.43	18.91	31.2	69090 ± 8	11.7 ± 0.5	-1.19 ± 0.04	0.16 ± 0.02	218.2 ± 9.4
55	01:52:31.17	+01:00:6.2	20.42	19.84	2.2	66649 ± 52	11.4 ± 2.6	-0.59 ± 0.25	0.13 ± 0.19	110.5 ± 52.6
60	01:52:37.42	+00:59:2.2	19.62	19.06	15.8	66367 ± 14	10.5 ± 1.0	-1.53 ± 0.08	0.47 ± 0.05	132.0 ± 12.5
75	01:52:20.13	+00:54:18.7	20.73	20.26	3.9	118450 ± 41	4.4 ± 0.8	-2.04 ± 0.27	0.67 ± 0.10	133.8 ± 33.3

correlation; however, the histogram in that panel shows that our results are consistent with C08 given the cited uncertainties. We would like to note that lacking the twilight spectra that would be necessary to estimate the instrumental LSF of C08, we do not compare $\sigma_{\rm int}$ for their spectra.

3.5 Results for Abell 267

As a first application of our model, we fit new data of the cluster A267. In order to measure the LSF of M2FS, we first fit a set of twilight spectra. In doing so, we estimate the posterior probability distribution of each of the 3 h_n parameters (see §3.3.2). Because we observed one twilight spectrum for each of the 256 fibers of M2FS, we quantify the posterior PDFs of the LSF for each fiber independently. Then, when fitting each of the science spectra, we sample the PDFs of the LSF that corresponds to the fiber that the science spectrum was observed. This technique quantifies the LSF and allows our fitting routine to break the degeneracy between the LSF and $\sigma_{\rm int}$; furthermore, it also naturally propagates the uncertainty in each of the h_n parameters into $\sigma_{\rm int}$ for each galaxy spectrum. Fig. 3.8 shows the resolving power $R = \Delta\lambda/\lambda$ for all fibers used in this analysis. For each fiber we used the central 68% of the LSF covered by the PDFs determined by MULTINEST to calculate R, which we plotted in Fig. 3.8. The two colors in Fig. 3.8 correspond to the separate spectrographs that are used in M2FS. There is a clear dichotomy between the spectrographs with the "blue" channel giving a systematically higher resolution; nonetheless, R is roughly centered around the theoretical resolving power of M2FS at the low-resolution configuration of ~ 2200.

After fitting all twilight spectra, we then fit the sky-subtracted science spectra using the technique described in §3.4 above. Table 3.3 shows the results of these

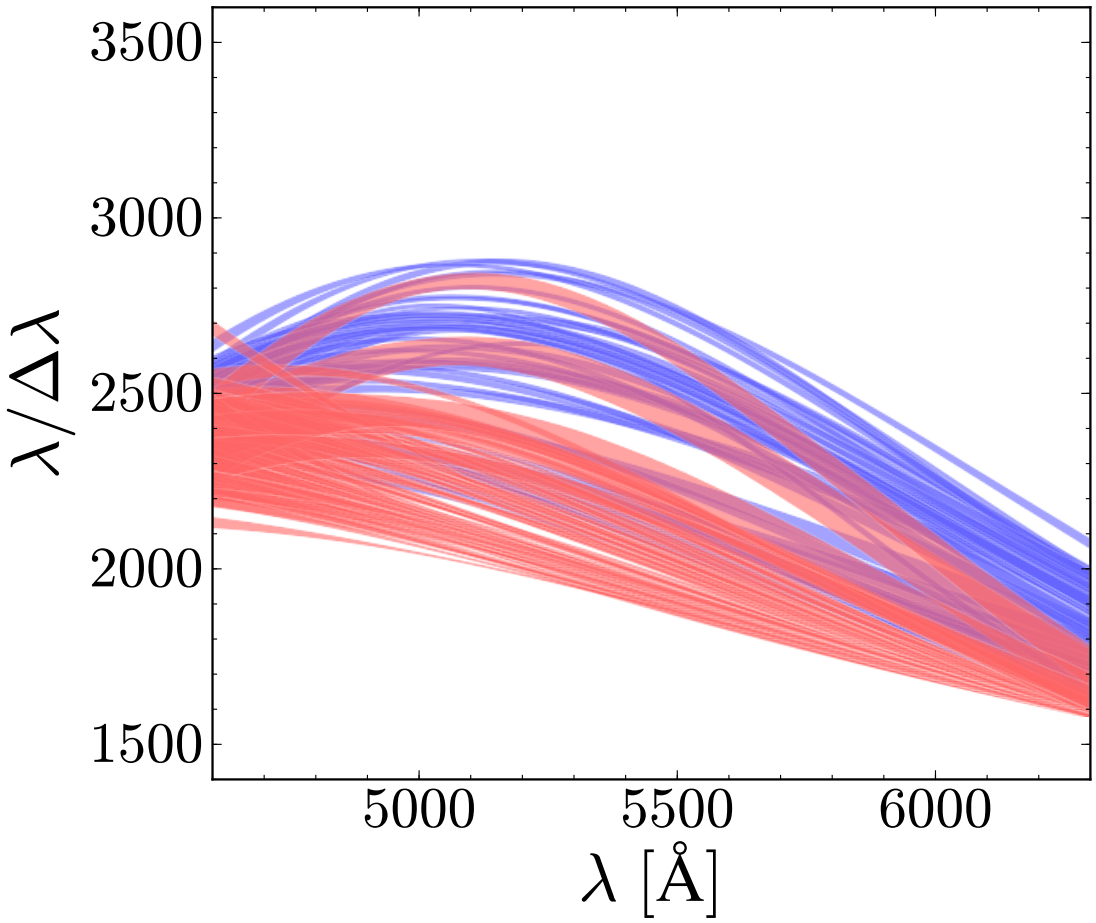

Figure 3.8: All line-spread functions measured from fitting the twilight spectra. Each curve corresponds to the LSF measured for that given fiber. The two colors differentiate between the two spectrographs that the fibers feed into on M2FS. Instead of plotting a single curve for each fiber's LSF, we show the 68% spread of each LSF as predicted by their respective posterior PDF.

fits for the galactic parameters. The parameter estimations are multidimensional posterior PDFs. Therefore, in Table 3.3 we give the mean value of the marginal PDFs for each parameter as well as the width of these distributions (central 68%) shown as an error.

Fig. 3.3 shows a series of sky-subtracted A267 spectra plotted in blue. Over plotted in red is the range of model fits covering the central 68% of the posterior probability distribution. Essentially, the red regions (thick red lines) shows the width of the posterior PDF converted into a spectrum. The bottom panel of each plot shows the residuals scaled by the variance in each pixel. Here we are only showing the residuals for the spectrum corresponding to the set of best fit parameters. The

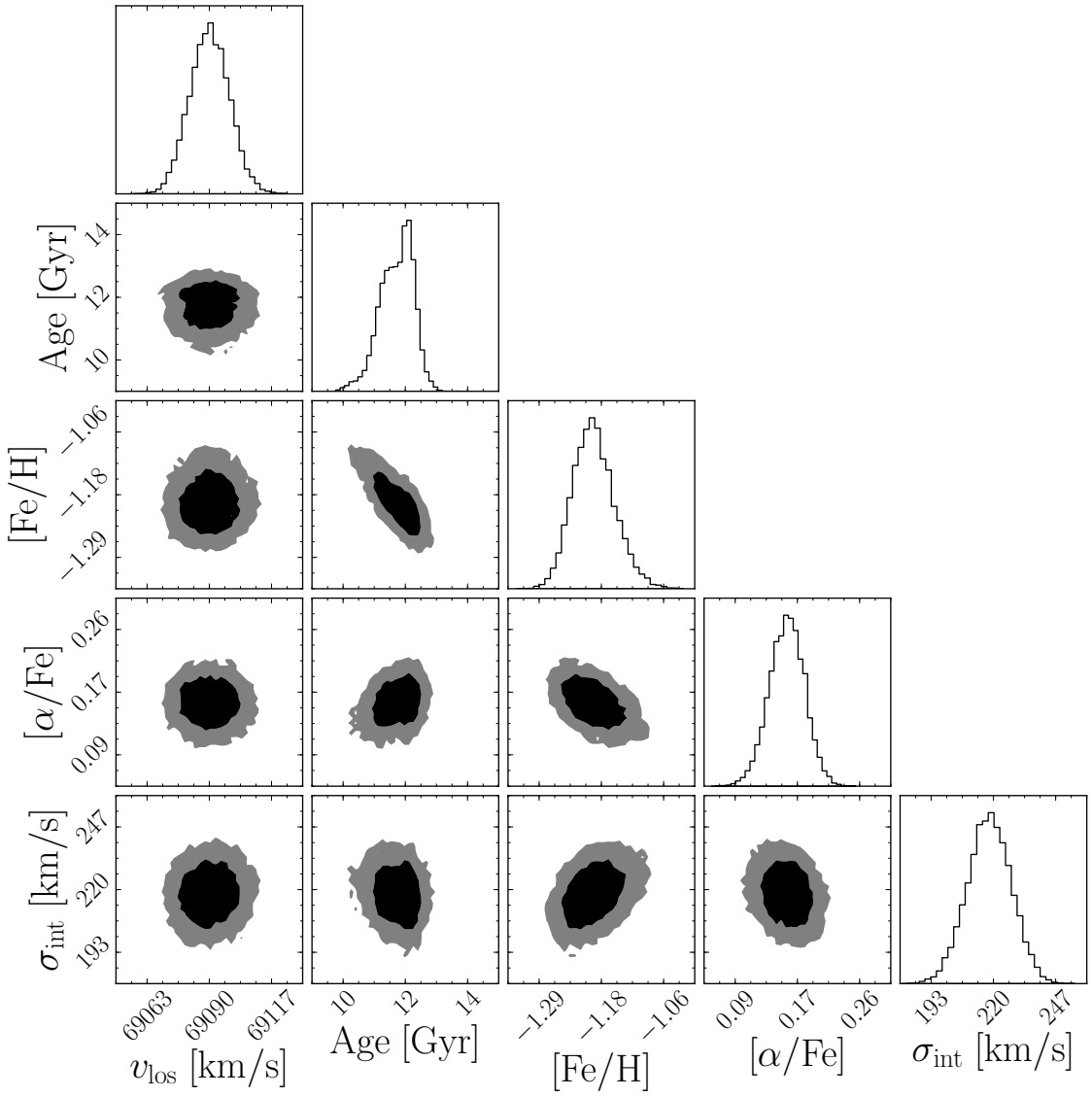

Figure 3.9: 1D and 2D posterior probability distribution functions for the five galactic parameters estimated for one of our A267 science targets (ID#46 in Table 3.3): line-of-sight velocity $v_{\rm los}$, age, metallicity [Fe/H], chemical abundance [α/Fe], and internal velocity dispersion $\sigma_{\rm int}$ of the simple stellar population. The dark and lighter shaded regions show the 1σ and 2σ widths of the 2D marginal posterior PDFs, respectively.

residuals scaled by the variance in each pixel is given by

$$\delta(\lambda) = \frac{S(\lambda) - M(\lambda)}{\sqrt{\mathrm{Var}[S(\lambda)]}} \tag{3.14}$$

where $S(\lambda)$ is the sky-subtracted science spectrum, $M(\lambda)$ is the best fit model, and $\mathrm{Var}[S(\lambda)]$ is the measured variance in the science spectrum. Also shown in each plot

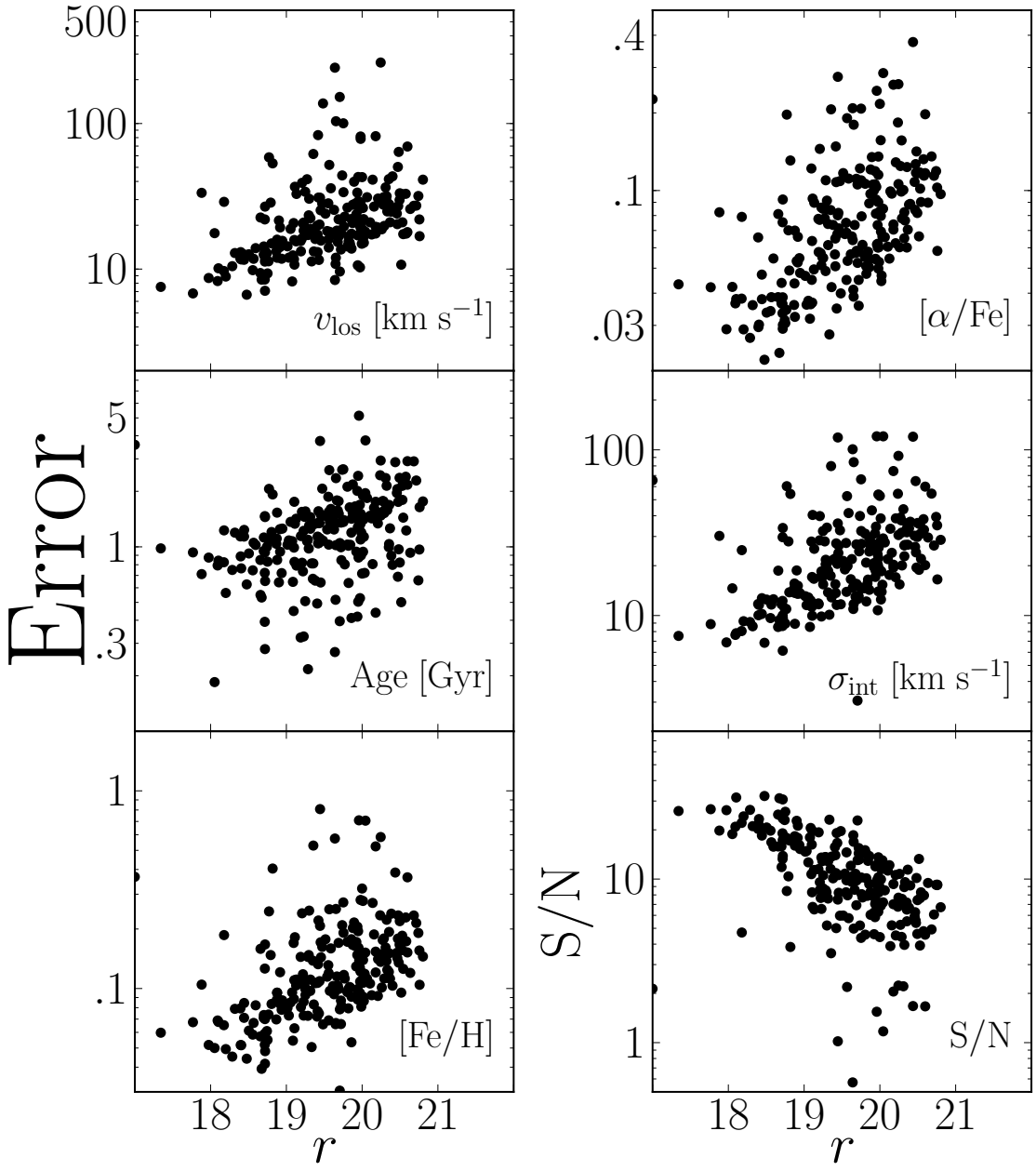

Figure 3.10: Errors in the five galactic parameters as a function of r-band magnitude and median pixel S/N as a function of r-band magnitude (each panel is labeled in the bottom right corner).

are the best fit galactic parameters along with their uncertainties, which are equal to the widths of their 1D posterior PDFs. To show the effectiveness of our model as a function of S/N, we arranged the plots with high median S/N per pixel in the top two panels (S/N $\sim$ 30) to mid-level S/N in the middle ($\sim$ 15) to low S/N in the bottom

(~ 2). Furthermore, the set of plots in the left column are for spectra with a high probability of membership to A267, while the spectra on the right are foreground and background galaxies.

In each of the plots in Fig. 3.3, we show the set of values for the galactic parameters corresponding to the best fit (highest likelihood) of the model to the data along with their uncertainties. We display the multi-dimensional posterior PDF of the five physical galactic parameters in Fig. 3.9. Here, one can more easily see the effectiveness of our model to constrain the physical parameters of interest. For the 2D marginal PDFs, we once again show the 1σ and 2σ contours as the dark and lighter shaded regions, respectively, in each panel. Most of the PDFs in Fig. 3.9 are Gaussian in shape and therefore can be easily quantified by a mean (or a highest likelihood value) and a variance; however, some parameters (i.e. Age in Fig. 3.9) have some non-Gaussian features. Because of this non-Gaussianity, it is better to describe the best fit parameters by a PDF instead of a single value and a variance. Having said that, we can still see in Fig. 3.9 that the highest likelihood parameter values still estimate the mean of the posterior PDFs effectively and the variance in these values still gives a good approximation of the width of these distributions.

Fig. 3.10 shows the error for each of the five galactic parameters labeled in the top right of each panel and median pixel S/N as a function of r-band magnitude. We notice usual behavior for our observations: for fainter objects, median pixel S/N decreases while errors in measured quantities increase. Parameter estimates of A267 have median random errors of $\sigma_{v_{\rm los}} = 20$ km s^{-1}, $\sigma_{\rm Age} = 1.2$ Gyr, $\sigma_{\rm [Fe/H]} = 0.11$ dex, $\sigma_{\rm [\alpha/Fe]} = 0.07$ dex, and $\sigma_{\sigma_{\rm int}} = 20$ km s^{-1}.

All raw spectra, our spectral fits, and all posteriors attributed to these fits are fully available online at the Zenodo database: https://doi.org/10.5281/zenodo.831784.

3.5.1 Comparison to previous redshift results

In order to discuss the accuracy of our A267 fits, we compare our redshifts to those measured previously by [89]. In their paper they measured redshifts for over 22,000 galaxies from The Hectospec Cluster Survey (HeCS), they cite 226 galaxy members to A267, and we re-observe 114 of those. In Fig. 3.11 we compare our measured redshifts ($z_{\rm M2FS}$) to theirs. In the top panel of Fig. 3.11, for added clarity, we only show galaxies that are approximately at the redshift of A267 ($z \sim 0.23$); on the other hand, the histograms in the bottom two panels show the distribution for all 196 repeat observed galaxies (separation $< 5 \times 10^{-5}$deg). The top histogram panel shows the difference in the measured line-of-sight velocity $\Delta v_{\rm los}$, while the bottom most panel shows this difference scaled by the combined uncertainties in the measured redshifts σ_v. The histograms show that our redshift measurements are in good agreement with those measured by [89].

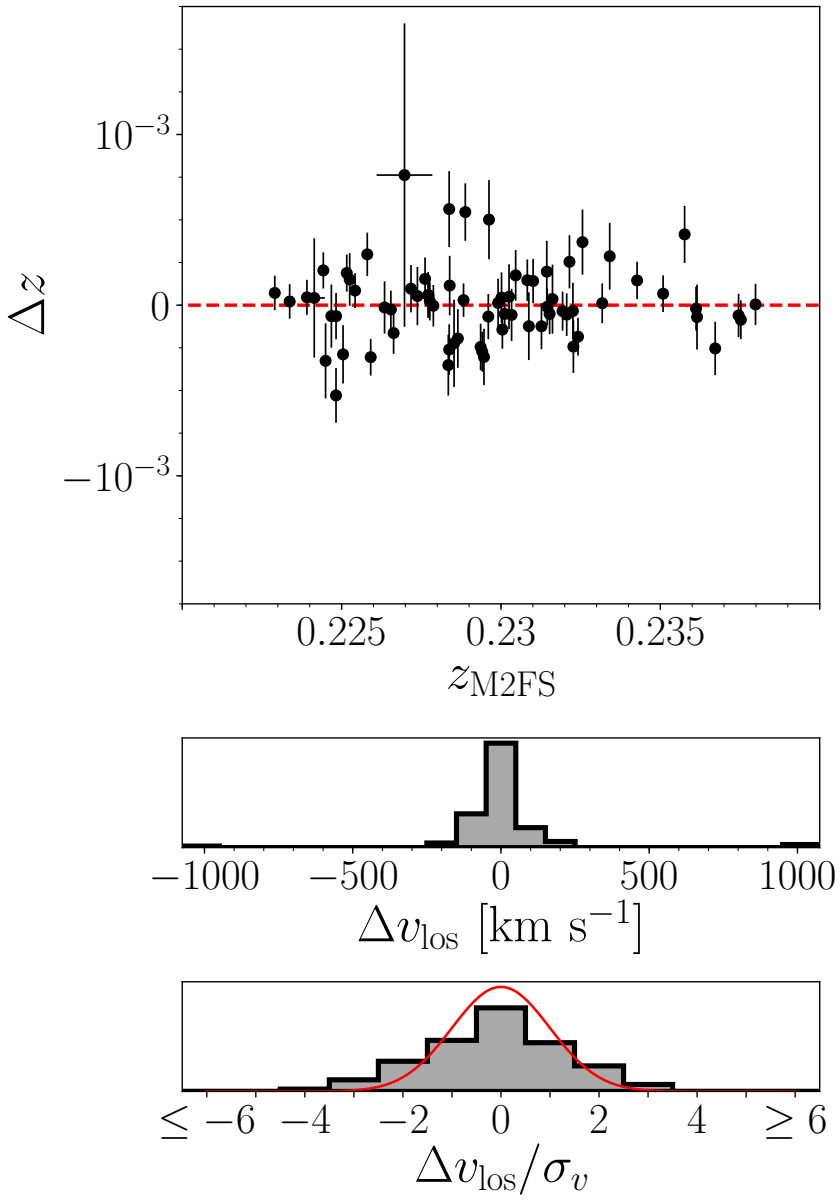

Figure 3.11: Comparing the measured redshifts of each galaxy from our analysis z_{M2FS} to previously published results in [89]. For clarity in the top panel we only show galaxies with measured redshifts around that of A267 $z \sim 0.23$; however, the bottom two panels show the distribution for all overlap observations with [89]. The bottom two panels shows the distribution in differences of redshifts, the bottom most is scaled by the combined uncertainties in the two measurements.

3.6 Conclusions

We have introduced a new model for fitting galaxy spectra using a Bayesian approach and integrated light spectra. We chose to produce a new integrated light model for a few important reasons, which we highlight in the paper. The main reason is that we wish to implement this modeling in the Bayesian statistical framework offered by MultiNest, which allows us to fully quantify the covariances of all free parameters. Furthermore, our new model gives us the flexibility to alter any aspect of the model from pre-calculated isochrones, to choices of synthetic spectral libraries, to complexity of stellar populations, which would be difficult to implement in the previous population synthesis techniques. In §3.4.4, we showed that this model is able to adequately reproduce the results of previous stellar populations fits to A496 spectra, while increasing flexibility for measuring the internal velocity dispersion of the stellar population. Lastly, this model robustly incorporates a wavelength dependence fit for the line-spread-function without the use of Hermite-Gaussian polynomials, which are typically used.

We outlined the process we used to generate an integrated light spectral library from a pre-calculated database of isochrones (Dartmouth Isochrones) and a library of synthetic stellar spectra (Phoenix Spectral Library). For this calculation, we assumed a Chabrier log-normal IMF with fixed scaling parameters, but the choice of IMF can be changed to incorporate different stellar evolution theories as well as allowing the parameters or the model be free. Furthermore, the choice of isochrones and stellar library can vary and one could use a library of real stellar spectra instead. We then discussed the model used to fit the galaxy operations and how we fit this model using the Bayesian nested sampling algorithm MultiNest.

In order to test the statistical power of the model, we generated and fit a mock catalog of galaxy spectra thus quantifying the accuracy of the model. This showed that for increasing S/N, the model performs better; however, even for low S/N$\sim$ 5, we are still able to reproduce the input galactic parameters with some level of precision. Furthermore, some of the galactic parameters are more easily estimated at lower S/N. For example, the velocity of the galaxy $v_{\rm los}$ can be estimated from our model with a high degree of certainty over the full range of S/N tested with the mock catalogs; however, we achieved similar precision for the galactic age parameter at only high S/N values.

Following the analysis of the mock catalog, we applied the integrated light spectral model to new spectral data acquired from M2FS on the Clay Magellan Telescope. We fit these spectra and estimated the posterior probability distribution for five galactic parameters: $v_{\rm los}$, Age, [Fe/H] [α/Fe], and $\sigma_{\rm int}$. We compared the estimates of $v_{\rm los}$ to previously published measurements from [89], which shows much agreement between the two measured redshifts.

In a Ch. 5, we use our spectroscopic measurements to model the internal dynamics and galaxy populations of A267. In the companion paper we will apply a

multi-population Dynamical Jeans Analysis. This model will simultaneously fit the dark matter and light distributions within the cluster while identifying contamination galaxies, substructure within the cluster environment and any overall cluster rotation.

Acknowledgements

We thank Margaret Geller and Ken Rines for helpful discussions that improved the quality of this work. We thank Charlie Conroy and Ben Johnson for useful discussions on incorporating wavelength dependence into the line-spread-function of the model. E.T. and M.G.W. are supported by National Science Foundation grants AST-1313045 and AST-1412999. M.M. is supported by NSF grant AST-1312997. E.W.O. is supported by NSF grant AST-1313006. We would also like to thank the anonymous referee for their helpful comments in improving this paper.

Chapter 4

Magellan/M2FS Spectroscopy of MACS 0429: Observations and Spectral Fits

4.1 Introduction

The Cluster Lensing and Supernova survey with Hubble (CLASH) is a 524-orbit Multi-Cycle Treasury (MST) Program of 20 X-ray selected clusters and 5 strong lens clusters. As one of the three MST programs selected, CLASH had four main goals during its near three-year long observational program [196]:

1. Measure the profiles and substructures of dark matter in galaxy clusters with unprecedented precision and resolution.

2. Detect Type Ia supernovae (SNe Ia) out to redshift $z \sim 2.5$ to measure the time dependence of the dark energy equation of state and potential evolutionary effects in the SNe themselves.

3. Detect and characterize some of the most distant galaxies yet discovered at $z > 7$.

4. Study the internal structure and evolution of the galaxies in and behind these clusters.

Over the years since the survey began, there have been numerous papers highlighting scientific discoveries that touch on all of the objectives listed above (for high redshift supernovae see [197, 198, 199, 200], the most distant observed galaxy see [201]).

As for their first objective, the combination of X-ray observations with the lensing mass maps derived from the CLASH observations does indeed produce an unprecedented view of profiles and dark matter substructures [202, 203, 204, 205, for example]. However, a complete spectroscopic follow-up survey of the CLASH clusters

adds more precise redshift measurements to these studies thus producing more precise constraints on mass profiles and substructures. Using the VIMOS spectrograph on the VLT in Chile, the CLASH-VLT program [139] was designed to obtain between $400 - 600$ cluster member galaxy spectra for the 14 CLASH clusters visible in the southern sky. The CLASH-VLT survey was carried out over 225 hours and obtained ~ 30000 galaxy spectra of which ~ 7000 are cluster members at 95% completeness. Their aim was to add to the legacy of the CLASH observations by providing deep spectroscopic followup out to at least two virial radii as well as measure redshifts for over 200 lensed background galaxies out to $z \sim 7$. The program is a large success and there have been numerous papers that combine lensing maps with CLASH-VLT spectra to deeply probe the mass distributions in galaxy clusters [162, 206, 116, 207, 208], constrain theories of gravity and dark matter [209, 210, 211], probe the environmental properties of the cluster populations [212, 213, 214, 215], and confirm the distances to strongly lensed high-redshift galaxies [216].

However, of the 14 CLASH clusters observable from the south, CLASH-VLT failed to observe one cluster, MACSJ0429-0253 (M0429), due to an oversubscription of VLT targets at that right ascension. In order to add to the legacy of CLASH-VLT, we obtained time on the Clay-Magellan 6.5m telescope to observe M0429 with M2FS. Our program aimed to generate a catalog of galaxies with similar completeness to CLASH-VLT while attempting to obtain spectra for strongly lensed background galaxies as well as $\sim 400 - 600$ member galaxies. Fortunately, M2FS operates at a much higher resolution than VIMOS thus producing more detailed spectra ripe for analyses of the unresolved stellar populations within each galaxy. In this chapter I will detail the observational program used to collect spectra of the CLASH cluster M0429 with M2FS as well as the application of the spectral fitting model detailed in chapter 3. §4.2 will detail the target selection and observations of M0429. §4.3 will present the spectra and detail the results of the spectral fitting model.

4.2 Observations

4.2.1 Target Selection

Target selection of M0429 was carried out in a similar fashion to A267 (§3.2.1) in the sense that we utilized the red sequence of M0429. For the photometry, we use Subaru Supreme-Cam galaxy catalogs [217, 218] which provides positions and three photometric bands: V, Rc, and Ic. In order to identify the red sequence we first selected all galaxies within the central 0.05° (~ 1.3 Mpc at the redshift of M0429 $z \sim 0.399$) of the X-ray identified center of M0429. This region is shown in blue in the left panel of Fig. 4.1. We then plot the color magnitude diagram for these central galaxies, shown as the blue points in the right panel of Fig. 4.1. These galaxies are used to identify the red sequence of M0429, which we highlight as the red box in Fig. 4.1. We then select all galaxies within this region of the color

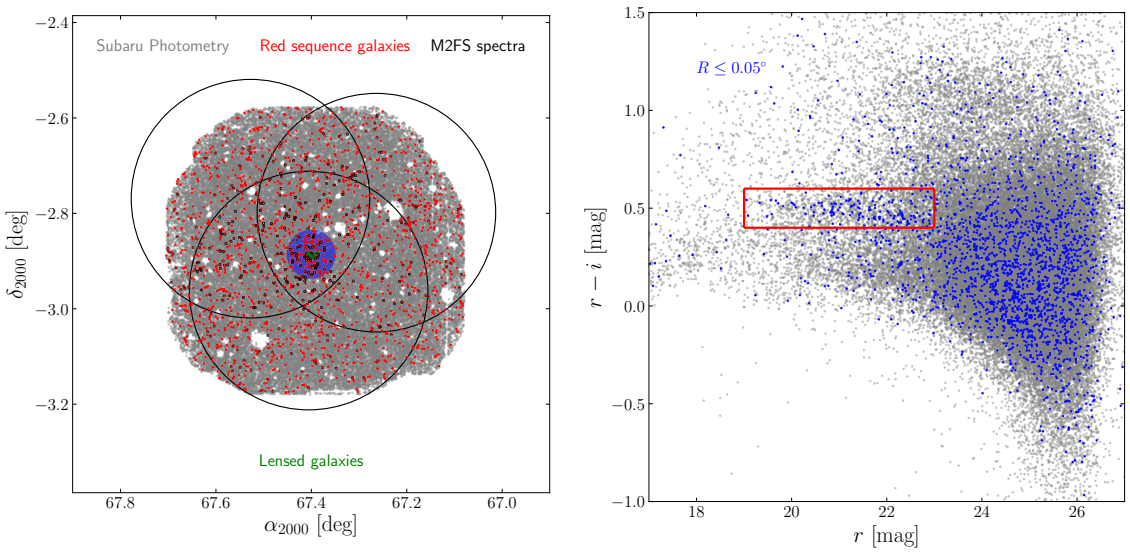

Figure 4.1: We show the sky positions (*left*) and $r - i$ vs r color-magnitude diagram (*right*) for all galaxies from the Subaru Suprime-Cam galaxy catalog. The blue shaded region on the left shows the central $\leq 0.05°$ of M0429. The galaxies within this shaded region are shown in blue on the right, and are used to identify the red sequence of M0429 which is boxed in red. The galaxies within this cut in color and magnitude are labeled as red sequence candidate galaxies and are shown in the red on the left. These galaxies are then targeted for observation with higher weight going to brighter galaxies. The galaxies observed with M2FS are lined in black and the three M2FS pointings are the big circles. The green stars on the left are targeted strongly lensed background galaxies.

magnitude diagram as red sequence candidate galaxies for M0429. We target red-sequence galaxies because this selection criteria has the highest efficiency of cluster membership efficiency relative to other target selection methods. These red sequence candidate galaxies are shown in red in the left panel of Fig. 4.1. These galaxies form the basis of our fiber allocation algorithm, which selects a subset of these galaxies, weighted by brightness (gives greater weight to brighter galaxies) and assigns them to a fiber. In addition to these red sequence galaxies, we also targeted 24 strongly lensed background galaxies which are shown in green in Fig. 4.1.

4.2.2 M2FS Spectroscopy

We utilized three separate pointing for M0429 and each pointing had two independent fields totaling ~ 1400 galaxies selected for M2FS spectroscopy. These three pointings along with their fields of view are shown as the large black circles in Fig. 4.1. Unfortunately, due to instrumental overhead and weather, only three of these fields were observed (one at each pointing) totaling 700 galaxy spectra observed. We observed two of the fields in November 2017 and the third field in February 2018. Due to the

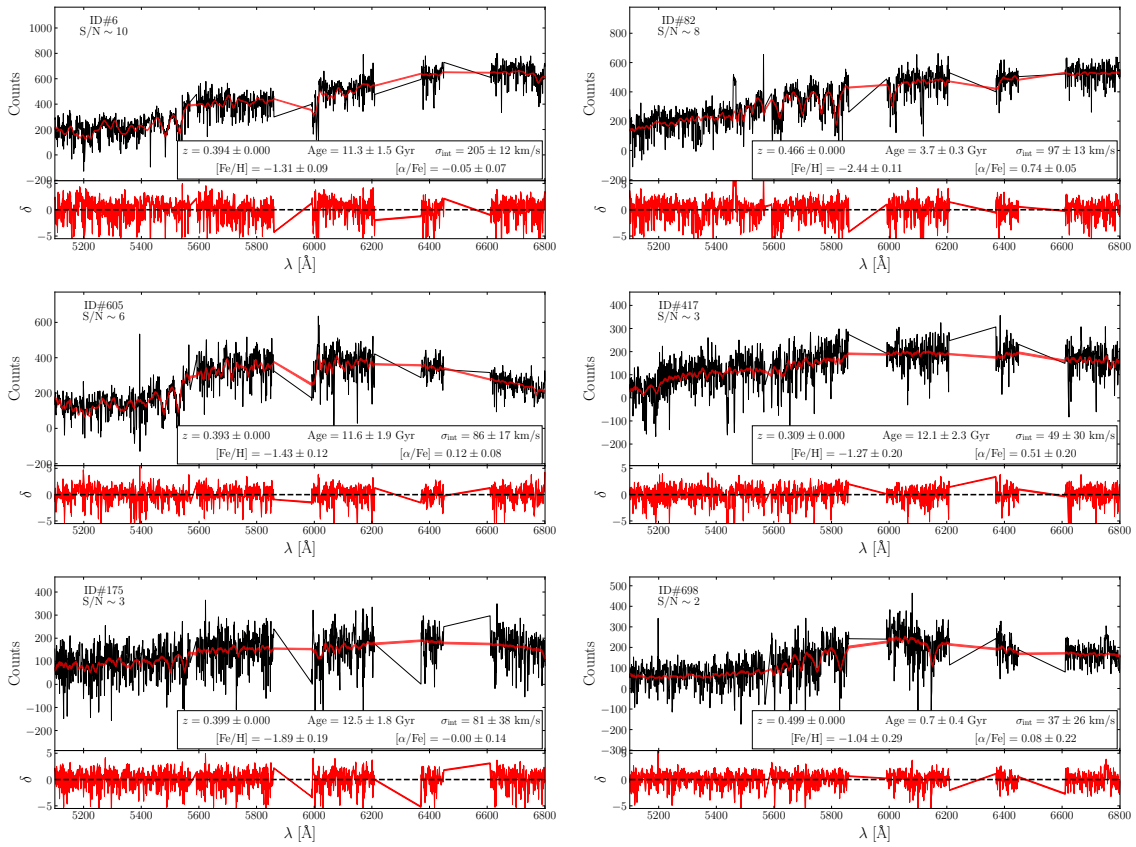

Figure 4.2: Six sky subtracted spectra (black) taken from the M2FS sample. Over-plotted in red are the central 68% of each model's posterior distribution converted into a spectrum. The scaled residuals are plotted in the bottom panels. The insert lists the stellar population parameters fit to each spectrum. The spectra are organized by decreasing S/N from top to bottom and the galaxies in the left column are highly probable cluster members.

faintness of the galaxies, these spectra were allocated time when the moon was not up. Each field was observed for nearly 3 hours with 3-50 minute sub-exposures per field.

These spectra were reduced with the data reduction pipeline detailed in §2.3. For these observations we angled the grating so that the spectra covered a wavelength range from $5100-6800$Å. At the red end of this wavelength range, there are significant atmospheric emission lines that dominate the sky spectrum and their residuals are still dominate even after applying our sky subtraction procedure. In the future, a more sophisticated sky-subtraction procedure should be implemented that better handles these emission lines. Nonetheless, during the spectral fitting detailed in §4.3 below, we masked out these emission line regions. In Fig. 4.2 we show an example of six spectra (at different S/N) from these observations.

In the core of the cluster we observed multiple galaxies in all three fields (the

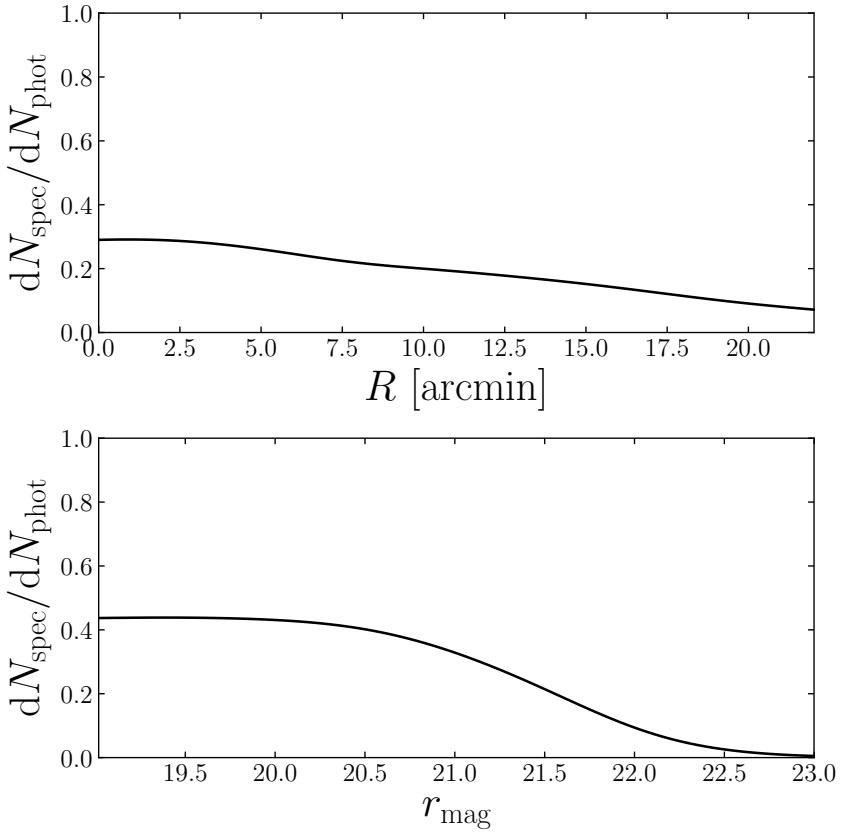

Figure 4.3: Completeness of the M0429 spectroscopic sample as a function of projected radius (top) and Subaru r-band magnitude (bottom). Both distributions are skewed low because of repeat observations, however, this effect is stronger in the cluster center because that is the region that the repeat observations were made.

overlapped region in Fig. 4.1). Therefore, of the 700 spectra obtained with M2FS, we only observed $\sim$ 360 individual galaxies. Fig. 4.3 shows the completeness of this spectroscopic sample as a function of projected radius (top) and Subaru r-band magnitude (bottom). The repeat measurements of multiple galaxies provides an opportunity to quantify the systematic uncertainties in the spectral fitting model which will be discussed in §4.3.3 below.

As part of the program, we also observed 23 strongly lensed background galaxies.[1] These galaxies are of particular interest because the gravitational lens of M0429 should magnify each galaxy thus increases its brightness making for an observation of distant galaxies more feasible. Unfortunately, the majority of these galaxies are still too faint for M2FS spectroscopy, thus the resultant spectra are of poor quality.

[1]We targeted 24 galaxies, but one of them fell on a bad fiber unfortunately.

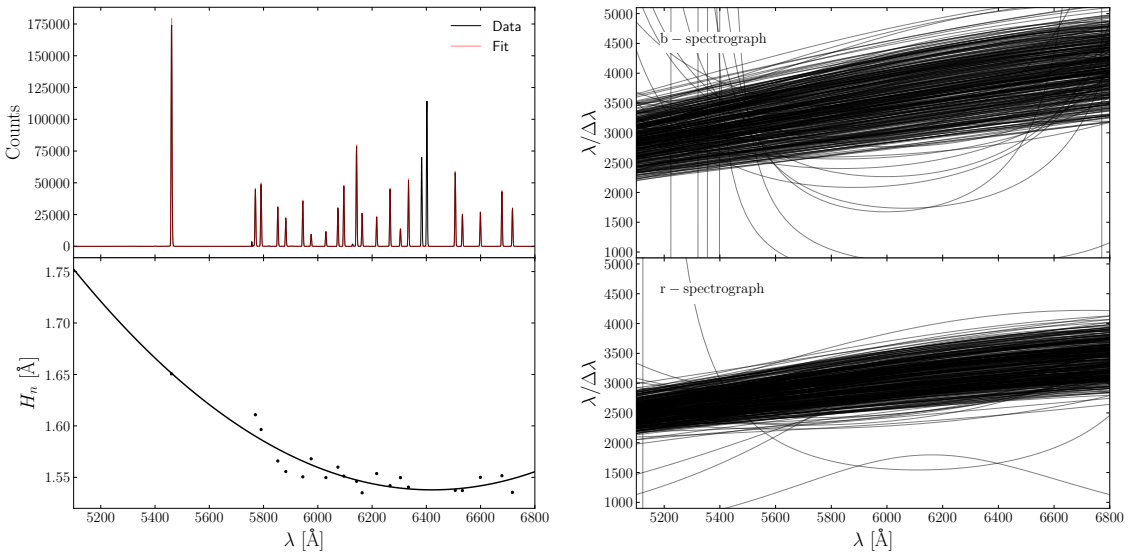

Figure 4.4: Line spread function fitting procedure utilized for M0429 observations. We fit individual gaussians to each emission line in a given NeHgArXe lamp spectrum. An example of one of these spectra as well as the fit are shown in the top left panel in black and red, respectively. The widths of these gaussians as a function of wavelength are then fit by a second order polynomial as shown in the lower left panel. This is the LSF for one fiber. On the right side we show all LSFs fit for the M0429 observations.

4.3 Spectral Fits

4.3.1 Line Spread Function

Because the measurement of internal velocity dispersion of each stellar population is degenerate with the intrinsic line spread function (LSF) of the spectrograph, we must first properly determine the LSF prior to fitting each individual spectrum. Furthermore, the LSF varies from fiber to fiber, so we fit the LSF for each fiber independently. The most commonly used procedure is to use the twilight spectra to determine the LSF function for each fiber because a twilight spectrum is essentially a solar spectrum and so any broadening of its absorption features are due to instrumental broadening. However, at the low resolution setup for M2FS, the twilight spectra exhibit broad absorption features that are likely due to polarization (see Fig. 2.9) which complicates the determination of the LSF. For A267, we utilized the fibermap exposures instead of the twilights to determine the LSF. Using the fibermaps has two major drawbacks: (1) the fibermaps could be collected days away from science exposures which is not ideal and (2) the fibermaps are collected during the day when the temperature is typically higher which affects the LSF of the spectrograph. For these two reasons, we implemented a new procedure with the M0429 spectra.

We utilized the NeHgArXe wavelength calibration exposures to determine the

Table 4.1: Results for fitting of M0429 spectra. For full table see A.2

M2FS ID	Subaru ID	$N_{\rm obs}$	α_{2000} deg	δ_{2000} deg	r [mag]	S/N	$\overline{v_{\rm los}}$ (km s^{-1})	$\overline{\rm Age}$ (Gyr)	$\overline{\rm [Fe/H]}$ (dex)	$\overline{\rm [\alpha/Fe]}$ (dex)	$\overline{\sigma_{\rm int}}$ (km s^{-1})
82	85	1	67.51	-3.09	19.94	8.9	139577 ± 24	3.7 ± 0.3	-2.44 ± 0.11	0.74 ± 0.05	97 ± 13
417	124	1	67.41	-3.16	20.09	3.9	92527 ± 34	12.1 ± 2.3	-1.27 ± 0.20	0.51 ± 0.20	49 ± 30
6	137	3	67.37	-2.88	20.31	10.9	118160 ± 21	11.3 ± 1.5	-1.31 ± 0.09	-0.05 ± 0.07	205 ± 12
605	203	3	67.43	-2.86	20.64	6.3	117750 ± 26	11.6 ± 1.9	-1.43 ± 0.12	0.12 ± 0.08	86 ± 17
698	276	1	67.09	-2.79	21.89	2.8	149702 ± 48	0.7 ± 0.4	-1.04 ± 0.29	0.08 ± 0.22	37 ± 26
175	367	3	67.41	-2.89	21.93	3.5	119474 ± 45	12.5 ± 1.8	-1.89 ± 0.19	-0.00 ± 0.14	81 ± 38

LSF for each fiber. Even at the low resolution setup, the majority of the emission features of this lamp are not blended; therefore, in theory each emission line is a delta function and any broadening of the unblended lines is due to the intrinsic broadening of the spectrograph. We fit a subset of the emission lines with a gaussian distribution and use the mean and variance of the distribution to describe the line spread at the location of each emission line. We then fit a 2nd order polynomial (Eq. 3.6) through these fits to determine the LSF of the given fiber. Fig. 4.4 shows an example of this procedure. In the upper left panel, we show an example of a typical NeHgArXe spectrum along with a spectral fit that utilizes individual gaussians for each emission line. The bottom left panel shows the widths of each of these gaussians as well as the 2nd order polynomial fit through these points. This fit is the LSF for this specific fiber which is then used for that same fiber when fitting science spectra. In the two right-hand panels, we show the LSFs (converted into resolving power $R \equiv \lambda/\Delta\lambda$) for all fibers and separated by the two spectrographs (top and bottom panels). This shows the that b-spectrograph operates at a slightly higher resolution albeit with larger scatter. The few lines in the right panels of Fig. 4.4 that vary drastically from the general trend are bad fibers and are excluded from the spectral fitting of science fibers.

4.3.2 M0429 Spectral Fits

In order to fit the observed spectra of M0429, we follow a similar prescription described in detail in §3.3 and §3.4. Fig. 4.2 shows an example of six spectra along with their spectral fits and derived stellar population parameters. These spectra are organized by decreasing S/N from top to bottom and in the left column are highly probable cluster member galaxies. At $z \sim 0.399$ the 4000Å break is redshifted to ~ 5500Å which is clearly visible at this wavelength in the left column. The four masked regions (three are clearly visible and the fourth is at ~ 5570Å) are dominated by atmospheric emission lines which affects the spectral fits. The absorption features in the spectra of the foreground and background galaxies shown in the right hand column are clearly

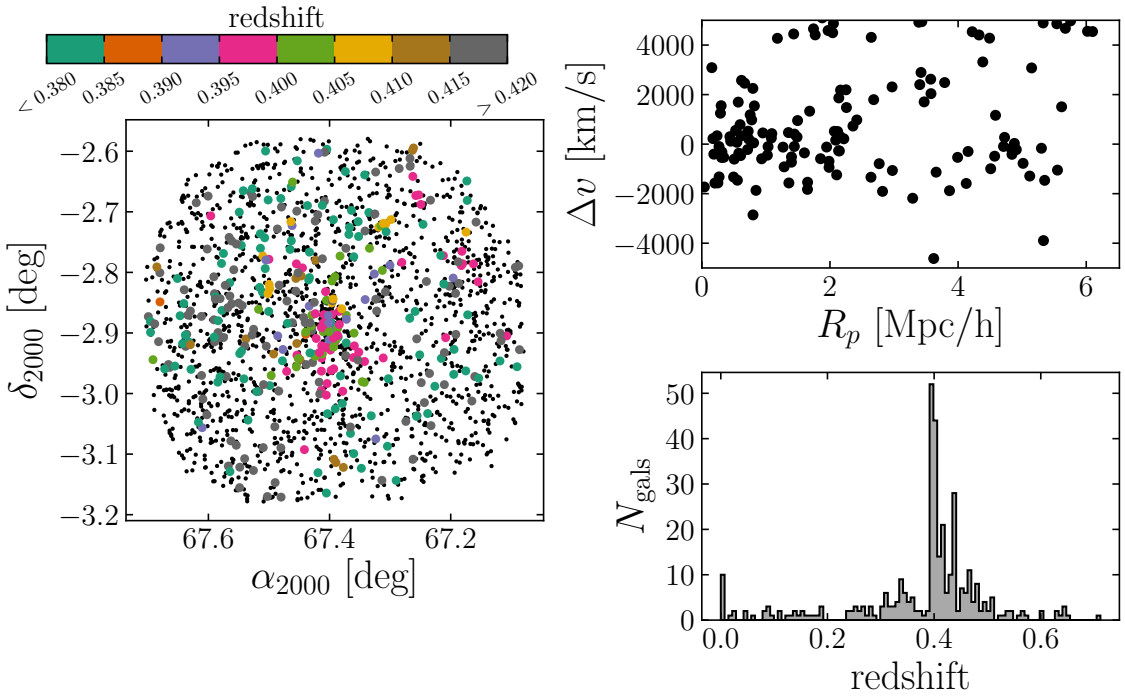

Figure 4.5: The panel on the left shows the sky positions of the red sequence candidate galaxies. The galaxies with M2FS spectra are larger and colored by their redshift. The top left panel shows velocity difference vs project cluster centric radius phase space around M0429. The bottom right panel shows the full redshift distribution for the M2FS sample.

different from the probable members' features. Table 4.1 shows a summary of the spectral fitting results for the spectra displayed in Fig. 4.2; the full table for all spectra will be available online.

In the left panel of Fig. 4.5 we show the sky positions of the red sequence selected galaxies. The larger colored points show the galaxies we select for spectroscopy and each color corresponds to the measured spectroscopic redshift. The cluster core is clearly visible with a strong clustering of galaxies with redshifts in the two bins closest to the X-ray redshift of M0429. The trumpet-shaped caustic for M0429 is easily seen in the velocity difference vs projected cluster centric radius phase space which is shown in the top right panel of Fig. 4.5. And in the bottom right panel, we show the full redshift distribution of the M0429 spectroscopic sample.

Fig. 4.6 shows the distributions of the five stellar population parameters as a function of projected radius for the spectroscopic sample. From top to bottom these parameters are redshift z, Age, metallicity [Fe/H], chemical enrichment [α/Fe], and internal velocity dispersion $\sigma_{\rm int}$. Using a broad redshift cut $0.38 \leq z \leq 0.42$, we identify galaxies that are highly probable members to M0429 and show those galaxies in red. From these cut, it is easy to see that a large portion of the centrally located galaxies ($R_p \lesssim 10$ arcmin) are highly probable cluster members as well. Using the

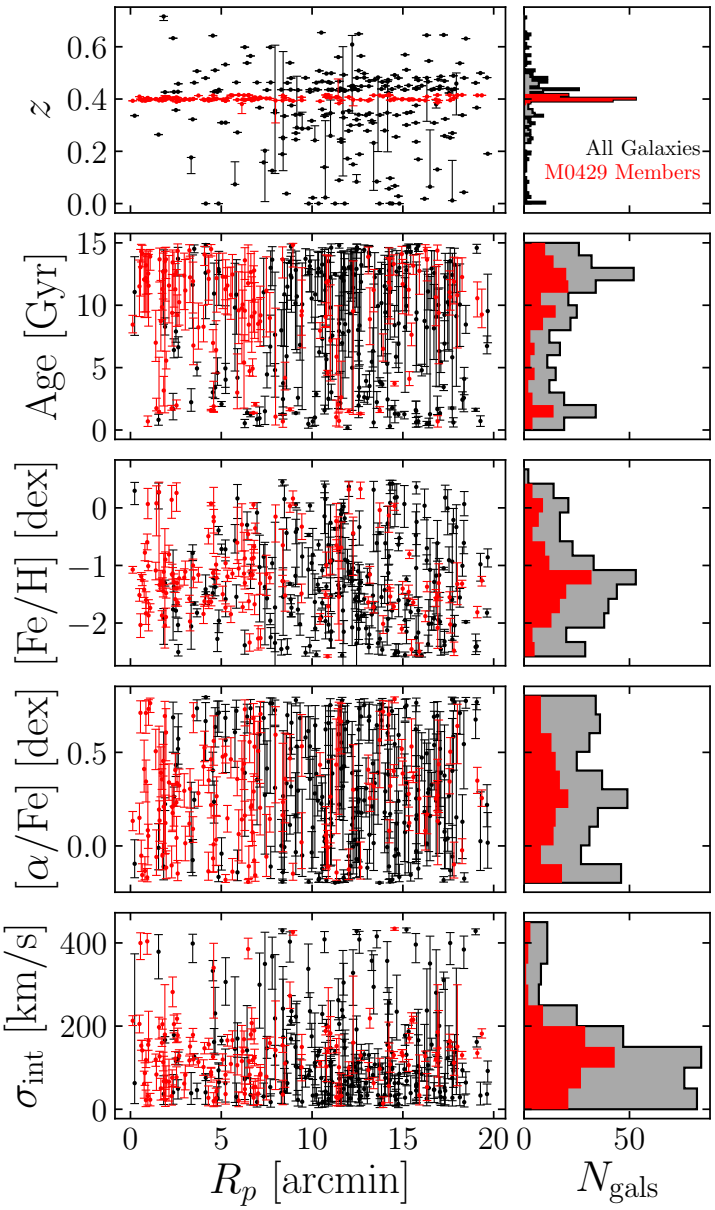

Figure 4.6: The distribution of stellar population parameters as a function of projected radius of the M0429 sample. The black points and histograms show the distributions for all galaxies in the sample, while the red points and histograms show the galaxies with measured redshifts around M0429 $0.38 \leq z \leq 0.42$.

one-dimensional projected histograms shown in the right-hand columns, we can look for any over-densities of member galaxies in each population parameter. In the Age distributions there appears to be a multimodal distribution of member galaxies with a larger peak at $\sim 11 - 12$ Gyr with a secondary peak centered at ~ 2 Gyr. While

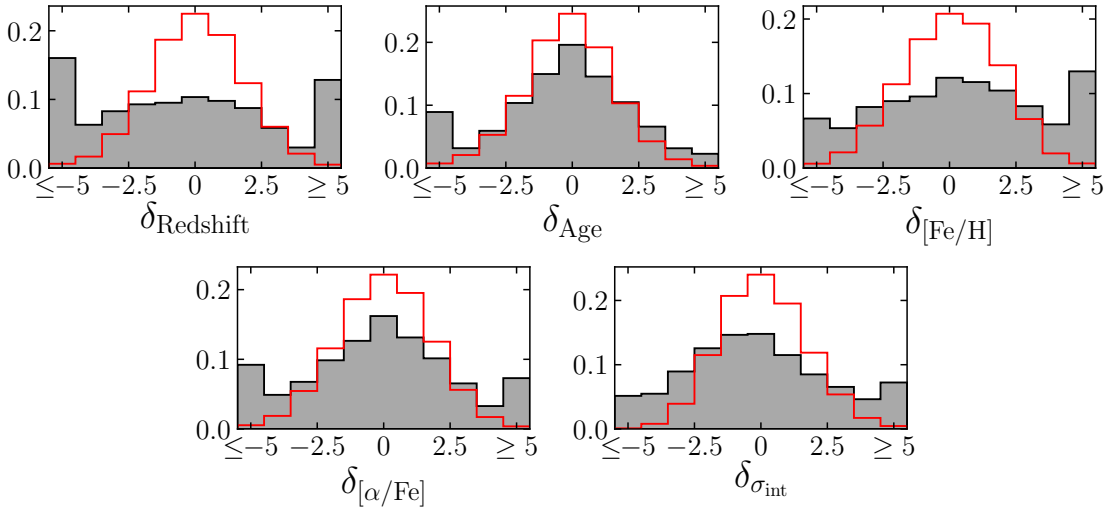

Figure 4.7: Distribution of differences between repeat observations of the same galaxy for each parameter scaled by the combined uncertainties in each measurement (Eq. 4.1)

there is not a strong over-density in the [α/Fe], there appears to be a peak in the metallically distribution around [Fe/H] ~ -1.25. And the internal velocity dispersion distribution for probable members has a peak at ~ 150 km/s.

4.3.3 Comparison of repeat observations

We selected a subset of galaxies that were observed multiple times across the three fields. Although this drastically decreased the total number of galaxies we observed (especially in the central core of the cluster), these repeat observations provide an opportunity to test the precision of the spectral fitting model. In Fig. 4.7, we show the distribution of the difference between repeat measurements of each parameter scaled by their combined uncertainty:

$$\delta_{\text{x}} = \frac{x_1 - x_2}{\sqrt{\sigma_{x_1}^2 - \sigma_{x_2}^2}} \tag{4.1}$$

where $x \in \{\text{Redshift}, \text{Age}, [\text{Fe/H}], [\alpha/\text{Fe}], \sigma_{\text{int}}\}$. In theory, if all uncertainties are properly estimated then each distribution should be centered on 0 with unit standard deviation. For the most part, each distribution is centered close to 0; however, the width of the distributions is closer to ~ 2 instead of unity. The fact that the distributions are broader than one suggests that the purely random variances calculated from the width of the posterior distributions from each spectral fit does not adequately describe the true uncertainty in the measurement.

If we apply quality control on the spectra, more specifically exclude spectra with non-Gaussian higher moments of the velocity posteriors (i.e. kurtosis or skewness that

deviate from 0), then some of the 5σ outliers are removed. This quality control is appropriate because we are assuming the posteriors are Gaussian in this comparison and if they are in fact non-Gaussian then it will affect the results. However, there are still some 5σ outliers that pass the quality control standards. These deviations suggest that the random uncertainties associated with the width of the posterior distributions are still underestimated. If we include an additional $\sim$ 65km/s of uncertainties in this analysis then the velocity distribution closely follows the theoretical red distribution shown in Fig. 4.7. About 30% of this additional error could be due to the wavelength solution which exhibits $\sim$ 0.3Å RMS scatter. Additional sources of noise likely originate from instrumental effects or observational conditions (e.g. clouds, winds, moon brightness). These variations would then result in changes in measured redshift as well as potential variations in other population parameters that are more convoluted to quantify.

4.4 Conclusions

We developed and presented an observational program to observe the galaxy cluster MACSJ0429-0253 with M2FS in an effort to complete the CLASH-VLT galaxy spectroscopic survey which observed 13 out of the 14 CLASH clusters visible from the Southern Hemisphere. The main goals of this program were to (a) obtain $\sim 400-500$ cluster member galaxy spectra out to $\sim 3R_{200}$, (b) measure stellar population parameters of these galaxies describing their mean redshift, age, metallicity, chemical enrichment, and internal velocity dispersion, and (c) obtain $\gtrsim 20$ spectra of strongly lensed background galaxies. Unfortunately, the program did not go as well as planned, however, we still hit some of these targets as well as developed good feedback to aid in future observational programs similar in scope.

We were not able to hit the observed cluster member target of $\sim 400-500$ galaxies, but we did measure galaxies out to $\gtrsim 3R_{200}$. The failure to hit this member target was due to two issues. First, we identified 6 fields of galaxies ($\sim$ 1400 targets), but were only able to observe half of those fields due to weather and instrumental overhead. Second, there was an issue during fiber allocation which resulted in the multiple observations of galaxies located in the cluster core (see the overlap region of Fig. 4.1). Despite these issues we still obtained at least one spectrum for 351 unique galaxies, $\sim$ 100 have high probability of cluster membership, and these galaxies were observed out to $\sim$ 6 Mpc/h from the cluster center.

In total we obtained 700 spectra of 351 different galaxies and estimated stellar population parameters from these spectra using the population synthesis spectral fitting model described in detail in §3.3. We showed a sample of these spectra in Fig. 4.2 along with the spectral fits and parameter estimates. These spectra are organized from top to bottom by signal-to-noise, showing how the spectral fits perform at different signal-to-noise levels. Probable cluster members are on the left showing that the the 4000Åbreak has been redshifted to $\sim$ 5500Å. We summarize the results

of these spectral fits by showing the redshift distribution in Fig. 4.5 and distribution of all stellar population parameters in Fig. 4.6. The redshift distribution shows a strong peak at the X-ray measured redshift of the cluster ($z \sim 0.399$), and the phase space shows the trumpet-like caustics typical of galaxy clusters. The stellar population parameter distributions show some over-densities in Age and metallicity for high probability cluster members, something that could be explored in more detail with a substructure analysis.

As for the last point, we did obtain spectra of 23 strongly lensed background galaxies. However, the majority of these galaxies are faint (Subaru r-band < 22) which produced low quality spectra. Nevertheless, these spectra along with all other spectra obtained during this program will be made publicly available online.

Lastly, even though the issue with fiber allocation decreased the number of galaxies we observed, it provides a unique opportunity to test the estimation of uncertainties of stellar population parameters derived from the spectral fits. From the distribution of the differences in estimated parameters between two repeat observations of the same galaxy scaled by the uncertainty derived from each parameters' posterior distribution, it is easy to see that we are underestimating the total uncertainty in each stellar population parameter (Fig. 4.7). Furthermore, the cited uncertainties in redshift are the most underestimated most likely due to a lack of consideration for the errors that arise during the wavelength calibration step of data reduction. Additional sources of noise should be considered in order to improve the error analysis of this spectral fitting technique.

Chapter 5

Galaxy Cluster Mass Estimates in the Presence of Substructure

Abstract

We develop and implement a model to analyze the internal kinematics of galaxy clusters that may contain subpopulations of galaxies that do not independently trace the cluster potential. The model allows for substructures within the cluster environment, disentangles cluster members from contaminating foreground and background galaxies, and includes an overall cluster rotation term as part of the cluster kinematics. We estimate the cluster velocity dispersion and/or mass while marginalizing over uncertainties in all of the above complexities. In a first application to our published data for Abell 267 (A267), we identify up to four distinct galaxy subpopulations. We use these results to explore the sensitivity of inferred cluster properties to the treatment of substructure. Compared to a model that assumes no substructure, our substructure model reduces the dynamical mass of A267 by $\sim 22\%$ and shifts the cluster mean velocity by ~ 100 km s^{-1}, approximately doubling the offset with respect to the velocity of A267's brightest cluster galaxy. Embedding the spherical Jeans equation within this framework, we infer for A267 a halo mass $M_{200} = 7.0 \pm 1.3 \times 10^{14} M_{\odot}/h$ and concentration $\log_{10} c_{200} = 0.71 \pm 0.38$, consistent with the mass-concentration relation found in cosmological simulations.

5.1 Introduction

Galaxy clusters are the most massive gravitationally bound and relaxed structures in the Universe, thereby representing important laboratories for observational cosmology [87, 143, 144, 54, 145, 89, 160]. Due to their high density of galaxies they are also ideal for studying galaxy interactions and the effect these interactions have on the galaxy population. Galaxy clusters are studied in a multitude of ways, from gravitational lensing both weak and strong [146, 196, 147, 149, 148, and references therein],

to X-ray temperature measurements of hot intracluster gas [150, 151, 152, 219] to Sunyaev-Zeldovich effects [153, 220], to spectroscopic velocity measurements of cluster members [87, 161, 156, 221, 157, 159, for example]. All of these methods can provide mass estimates, thus constraining the high-mass end of the halo mass function, thereby constraining cosmological parameters such as the amplitude of the power spectrum or the evolution of dark matter and dark energy density parameters.

When calculating cluster masses using the velocities of cluster members, it is common to assume that the cluster is a relaxed system with a gravitational potential and kinematics that satisfy the viral theorem. However, such assumptions neglect recent galaxy accretion that could alter the distribution of galaxies in phase space [85, 222, 80, 87]. Residual angular momentum during formation, as well as the presence of in-falling groups, could contribute a rotational velocity to the cluster [223, 224, 225]. [226] suggests that any global rotation of the universe could provide angular momentum to galaxy clusters during their formation. Additionally, even in systems that appear relaxed, these mergers can generate residual substructure within the cluster environment such that individual galaxies are not necessarily independent tracers of the gravitational potential [112, 115, 116]. These factors have the potential to impact dynamical mass measurements, leading to systematic errors which will then propagate into cosmological inferences.

Early efforts were made to detect rotations in galaxy clusters; however, this proved difficult without distinguishing between closely interacting groups [227, 228, for example]. More recently the effects of recent mergers and close interactions have been accounted for and some authors have started exploring galaxy rotation in more depth. Some have used large surveys such as SDSS to look for galaxy rotation in relaxed systems and report evidence of rotating clusters [229, 224]. Multiple analyses of Abell 2107 have concluded that it is rotating [228, 230]. Through X-ray observations some groups have studied the rotation of the intracluster medium (ICM) [231, for example]. And most recently [225] applied a model for determining whether a cluster rotates and, if it does, information about its rotational dynamics.

Additionally, recent efforts have been made to identify substructure within galaxy clusters. There are many 3D, 2D, and 1D tests for substructure that have been developed in the past few decades [112, 109, 104, 232, 233]. [102] compared and discussed the validity of some of the earlier tests while others have applied them to SDSS clusters [234]. Recent efforts in substructure analysis have focused on identifying subpopulations based on galaxy morphological types [115, 235, 236, 116, e.g.]. Accounting for such substructure when measuring dynamical masses is vital in achieving accurate estimates. For example, [96] has shown that almost all dynamical mass estimators overestimate cluster masses for clusters with significant dynamical substructure compared to estimates for clusters without substructure.

Furthermore, the identification and proper modeling of substructure may be important for distinguishing among competing models for the nature of dark matter. For example, under the standard cold dark matter (CDM) paradigm, dense 'cusps'

form at the centers of dark matter halos [237, 238, 239]. In galaxy cluster halos, CDM cusps will tend to bind the brightest cluster galaxy (BCG) near the halo center. However, recent simulations suggest that if the dark matter undergoes significant self-interactions, the subsequent unbinding of central cusps (particularly in response to major mergers) would allow BCGs to 'wobble' about the cluster center [240, 241]. Such wobbles could be detected as offsets between clusters and their BCGs in the projected phase-space. Substructure can affect the detection of such offsets, as the elements within a given substructure do not independently sample a phase space that is representative of the cluster itself.

Clearly both rotation and substructure can affect inferences about the internal dynamics of galaxy clusters. Here we devise a framework that can account for both affects simultaneously. This allows us to study the impacts of both phenomena on cluster mass estimates, and to marginalize over uncertainties in rotation and substructure. In this paper we apply this model to our own published spectroscopic observations of Abell 267 (A267, [119]), combined with measurements from the redshift catalogue HectoSpec [89] to achieve a large sample. We summarize these data sets in §5.4.1. In §5.2 we describe the dynamical model, and we then apply the model to A267 assuming a uniform velocity dispersion (§5.4.3) and a dark matter halo model (§5.4.4). Throughout the paper we use $H_0 = 100\ h^{-1}$km/s/Mpc and mass density $\Omega_m = 0.3$.

5.2 Galaxy Cluster Mixture Model

In this section we describe the mixture model for galaxy cluster substructure analysis.

We model the observed distribution of galaxy positions and redshifts as a random sample from several distinct galaxy populations. We define the populations as: the main cluster population, a set of subpopulations of galaxies within the cluster, and a contamination population including both foreground and background galaxies. Because spectroscopic observations are used as follow-up to already identified clusters with good photometry, the model incorporates into the likelihood function the sky positions from a full photometric catalog as well as spectroscopic line-of-sight velocity measurements of a subset of these galaxies. Therefore, we define the likelihood function that, given a set of model parameters $\boldsymbol{\theta}$, describes the observed position and velocity distribution as

$$\mathcal{L} = \mathcal{L}_{\rm phot}\mathcal{L}_{\rm spec} \tag{5.1}$$

where $\mathcal{L}_{\rm phot}$ is the likelihood function associated with the photometric dataset and $\mathcal{L}_{\rm spec}$ is associated with the spectroscopic dataset.

We model the discrete photometric sample of galaxies as being drawn independently from an underlying surface brightness profile $I(\mathbf{R})$. Therefore, the likelihood

for the observed photometric sample is [243]

$$\mathcal{L}_{\rm phot} \propto \exp\left[-\int_{\mathcal{R}} I\left(\boldsymbol{R}\right) \mathbf{d^2}\boldsymbol{R}\right] \prod_{i}^{N_{\rm gal}} I\left(\boldsymbol{r}_i\right) \tag{5.2}$$

where $\mathcal{R}$ is the field-of-view (FOV), $I\left(\boldsymbol{R}\right)$ is the surface brightness profile, $N_{\rm gal}$ is the number of galaxies observed in the photometric dataset, and $\boldsymbol{r}_i$ is the position on the sky of each galaxy. The constant of proportionality here does not depend on the model. For a multi population model, the surface brightness profile is the sum of the profiles for each individual population:

$$I\left(\boldsymbol{R}\right) = \sum_{M=1}^{N_p} I_M\left(\boldsymbol{R}\right) \tag{5.3}$$

where N_p is the number of populations in the model. For the purposes of this paper we assume all profiles (main cluster halo and substructures) are dark matter dominated and therefore follow a Navarro, Frenk, and White (NFW) profile [238]:

$$I_{\rm NFW}\left(\boldsymbol{R}\right) = 2\int_R^\infty \nu_{\rm NFW}(r)\frac{r}{\sqrt{r^2-R^2}}{\rm d}r = 2\nu_s r_s \int_R^\infty \frac{{\rm d}r}{\left(1+r/r_s\right)^2\sqrt{r^2-R^2}} \tag{5.4}$$

where ν_s and r_s are the scale density and radius of an NFW profile, respectively. Eq. 5.4 simply projects the three dimensional light profile $\nu_{\rm NFW}$ onto the plane of the sky yielding the two dimensional light profile $I_{\rm NFW}$. Luckily this projection is analytic for an NFW profile and is given by

$$I_{\rm NFW}\left(x\right) = \frac{2\nu_s r_s}{x^2-1}\begin{cases} 1-\frac{2}{\sqrt{x^2-1}}\arctan\sqrt{\frac{x-1}{x+1}} & x>1 \\ 1-\frac{2}{\sqrt{1-x^2}}\arctan\sqrt{\frac{1-x}{1+x}} & x<1 \\ 0 & x=1 \end{cases} \tag{5.5}$$

where $x = r/r_s$ [244].

The spectroscopic likelihood function used to describe the velocity distribution is

$$\mathcal{L}_{\rm spec} = \prod_{i}^{N_{\rm spec}} P\left(v_i|\boldsymbol{r}_i,\boldsymbol{\theta}\right) \tag{5.6}$$

where $N_{\rm spec}$ is the number of galaxies from the photometric catalog with spectroscopic derived line-of-sight velocities v_i and $P\left(v_i|\boldsymbol{r}_i,\boldsymbol{\theta}\right)$ is the probability distribution of measured line-of-sight velocity v_i, given position $\boldsymbol{r}_i$ and model parameters $\boldsymbol{\theta}$. We can then marginalize this distribution over the N_p populations M and invoke Bayes' Rule to write

$$P\left(v_i|\boldsymbol{r}_i,\boldsymbol{\theta}\right) = \sum_{M=1}^{N_p} P\left(v_i|M,\boldsymbol{r}_i,\boldsymbol{\theta}\right)\frac{P\left(M|\boldsymbol{\theta}\right)P\left(\boldsymbol{r}_i|M,\boldsymbol{\theta}\right)}{P\left(\boldsymbol{r}_i|\boldsymbol{\theta}\right)}. \tag{5.7}$$

The first term in the numerator is simply the number fraction of galaxies within that population: $P(M|\boldsymbol{\theta}) = F_M = N_M/N_{\rm tot}$. The second term in the numerator, $P(\boldsymbol{r}_i|M,\boldsymbol{\theta})$, is the probability for a galaxy at position $\boldsymbol{r}_i$ given the population M and the model $\boldsymbol{\theta}$, which is directly proportional to the surface brightness profile of the population: $P(\boldsymbol{r}_i|M,\boldsymbol{\theta}) = 2\pi r_i I_M(\boldsymbol{r}_i)/N_M$. The denominator we can again marginalize over the populations so that $P(\boldsymbol{r}_i|\boldsymbol{\theta}) = \sum_Q^{N_p} P(\boldsymbol{r}_i|Q,\boldsymbol{\theta})\,P(Q|\boldsymbol{\theta})$. And so we can re write Eq. 5.7 as

$$P(v_i|\boldsymbol{r}_i,\boldsymbol{\theta}) = \frac{\sum_M^{N_p} P(v_i|M,\boldsymbol{r}_i,\boldsymbol{\theta})\,I_M(\boldsymbol{r}_i)}{\sum_Q^{N_p} I_Q(\boldsymbol{r}_i)}. \tag{5.8}$$

The final probability distribution in Eq. 5.8 describes the velocity distribution for a given population M and position $\boldsymbol{r}_i$. The modeling framework is flexible in the sense that any choice of a velocity distribution function can be used here. Although it is not the most physically motivated model, we use a Gaussian velocity distribution similar to [81] because it is easy to implement numerically and is a fairly good approximation for the observed profile of galaxy clusters:

$$P(v_i|M,\boldsymbol{r}_i,\boldsymbol{\theta}) = \frac{\exp\left[-\frac{1}{2}\frac{\left(v_i-\langle V\rangle_M - V(\boldsymbol{r}_i)_{{\rm rot},M}\right)}{\left(\delta_i^2+\sigma(\boldsymbol{r}_i)_M^2\right)}\right]}{\sqrt{2\pi\left(\delta_i^2+\sigma(\boldsymbol{r}_i)_M^2\right)}} \tag{5.9}$$

where δ_i is the measurement uncertainty in line-of-sight velocity v_i, $\sigma(\boldsymbol{r}_i)_M$ is the projected velocity dispersion profile of the M-th population evaluated at the sky position of each galaxy $\boldsymbol{r}_i$, $\langle V\rangle_M$ is the average velocity of the M-th population, and $V(\boldsymbol{r}_i)_{{\rm rot},M}$ is the rotational velocity of the M-th population. Once again the modeling framework is flexible to a variety of choices of projected velocity dispersion profile and rotational velocity. In §5.3 and §5.4.3, we apply a uniform velocity dispersion $\sigma(\boldsymbol{r})_M = \sigma_M$ for both the main cluster halo and all sub-populations, whereas in §5.4.4 we assume the velocity dispersion of the main cluster halo follows a dark matter halo such that it is radial symmetric $\sigma(\boldsymbol{r})_{M={\rm main}} = \sigma(r)_{\rm main}$ and can be evaluated using a Jeans Analysis.

For real observations from galaxy redshift catalogs, the contamination population of galaxies is typically dominated by foreground and background clusters that happen to lie along the line-of-sight to the cluster of interest. For this reason, extra care must be taken when choosing a physically motivated contamination model. We discuss the specific choices made for contamination models in §5.3.3 and §5.4.2 below.

For every model $\boldsymbol{\theta}$, we can evaluate the probability that each galaxy is a member of the various populations. Given a galaxies velocity v_i and position $\boldsymbol{r}_i$, the probability that it is a member of population M is

$$\mathcal{P}_M = P(M|v_i,\boldsymbol{r}_i,\boldsymbol{\theta}) = \frac{P(M|\boldsymbol{\theta})\,P(v_i,\boldsymbol{r}_i|M,\boldsymbol{\theta})}{P(v_i,\boldsymbol{r}_i|\boldsymbol{\theta})} = \frac{P(v_i|\boldsymbol{r}_i,M,\boldsymbol{\theta})\,I_M(\boldsymbol{r}_i)}{\sum_Q P(v_i|\boldsymbol{r}_i,Q,\boldsymbol{\theta})\,I_Q(\boldsymbol{r}_i)}. \tag{5.10}$$

In the following sections we will use "probability of membership to the cluster" to refer to the probability that an individual galaxy belongs to either the main population or any subpopulation, and we define this membership probability as $\mathcal{P}_{\rm mem} = 1 - \mathcal{P}_{M=\rm contam}$.

In order to fit this model, we use the nested sampling algorithm MultiNest [192], which simultaneously calculates the Bayesian evidence, used for model selection, and generates random samples from the posterior probability distribution. We will use the bayesian evidence as a metric to select the optimal number of subpopulations for a given data set.

5.3 Tests with Mock Observations from Simulations

The main goal of this modeling framework is to produce more accurate estimates of cluster masses by accounting for substructure of the cluster. Therefore, as a first test of this modeling framework, we use mock galaxy cluster redshift catalogs produced from the MultiDark Planck 2 N-body simulation (MDPL2, [245]).

5.3.1 The MultiDark Simulation

We conduct this analysis with mock observations generated from a publicly available snapshot from MDPL2 simulation[1]. MDPL2 is an N-body dark matter only simulation with 3840^3 particles in a box of length 1 Gpc/h and a mass resolution of 1.51×10^9 $M_\odot$/h. The simulation is executed using L-GADGET-2 [246] and uses a Planck ΛCDM cosmology [247]: $\Omega_\Lambda = 0.693$, $\Omega_m = 0.307$, $h = 0.678$, $n = 0.96$, $\sigma_8 = 0.8828$.

Halos and subhalos are identified from simulation data using the ROCKSTAR halo finder [248] which performs a clustering algorithm in the six-dimensional phase space (three positions and three velocities) of dark matter particles. Subhalos are then populated by galaxies using the galaxy assignment procedure UniverseMachine [249]. Unlike other galaxy assignment procedures, UniverseMachine is able to track the gravitational evolution of each galaxy's subhalo even below the resolution limit of ROCKSTAR, thus increasing the total number of simulated galaxies. The resulting catalogs provide information on the cluster mass and size as well as 6D phase space information on each galaxy: comoving position and proper velocity information.

5.3.2 Mock Observations

Mock observations are generated from these galaxy cluster catalogs using the prescription described in detail in the appendix of [250]. The general procedure is as follows. First a large cylindrical cut about the center of each cluster is made in projected

[1] https://www.cosmosim.org/

phase space with radius of 10 Mpc/h and length $\pm 6 \times 10^3$ km/s oriented along the line-of-sight. This large cut will include the infall region of the cluster and include contamination galaxies that could fall along the line-of-sight to the cluster. Each galaxy that falls within this cylinder (and has a mass at accretion $M_{\rm acc} \geq 10^{11}$ $\mathrm{M}_\odot$/h) will be projected along the line-of-sight, thus producing a catalog of simulated observations of sky positions and line-of-sight velocities. For each cluster, we follow this procedure for three separate orthogonal pointings thus producing three mock observation catalogs for a given cluster which (for statistical purposes) we treat as independent clusters.

We select clusters into a low and high mass sample. The low mass sample has a mass range from 0.72×10^{14} $\mathrm{M}_\odot$/h to 0.96×10^{14} $\mathrm{M}_\odot$/h with a median 0.86×10^{14} $\mathrm{M}_\odot$/h; and the massive sample ranges from 0.63×10^{15} $\mathrm{M}_\odot$/h to 2.04×10^{15} $\mathrm{M}_\odot$/h with median 0.98×10^{15} $\mathrm{M}_\odot$/h. All mass values listed here and for the remainder of this section are M_{200c} and defined as the mass enclosed by a spherical over-density 200 times the critical density of the MDPL2 simulation, and these masses are calculated using all dark matter particles belonging to the clusters ROCKSTAR halo that fall within the spherical over-density. We used the $z = 0.117$ snapshot and placed the observer at $z = 0$. Furthermore, the mock observation generation does not include observational effects such as obstructions or lensing.

Fig. 5.1 shows two sets of mock cluster observations. The top set is of one of the low mass clusters, while the bottom is for a high mass cluster. In total our galaxy cluster sample includes 92 unique clusters from the simulation volume (half in the high mass bin), projected along three orthogonal pointings, totaling 276 mock galaxy cluster redshift catalogs. For each redshift catalog, we use all sky positions of galaxies as our photometric data set, but we select a subset of these galaxies (80%) to produce the spectroscopic catalog which includes the line-of-sight velocities. We produce 10 random samplings of each galaxy cluster redshift catalog.

5.3.3 Model Setup

For each mock cluster catalog we fit four multi-population models with $N_{\rm subs} \in \{0, 1, 2, 3\}$. For each model we assume a uniform velocity dispersion for the main cluster halo and all substructures: $\sigma(\boldsymbol{r})_M = \sigma_M$. For the contamination model, we assume a uniform distribution of galaxies on the sky as well as a uniform velocity distribution:

$$I(\boldsymbol{r})_{M=\rm contam} = \Sigma_0, \;\; P(v_i|M = \rm contam, \boldsymbol{r}_i, \boldsymbol{\theta}) = \frac{1}{v_{\rm max} - v_{\rm min}} \tag{5.11}$$

where Σ_0 is a free parameter in the model, while $v_{\rm max}$ and $v_{\rm min}$ are set by the range of velocities in the data set. We also assumed no overall cluster rotation $V(\boldsymbol{r})_{{\rm rot},M} = 0$. Therefore, each model in total includes two free parameters for the contamination model, five free parameters for the main halo, and six free parameters for each sub-

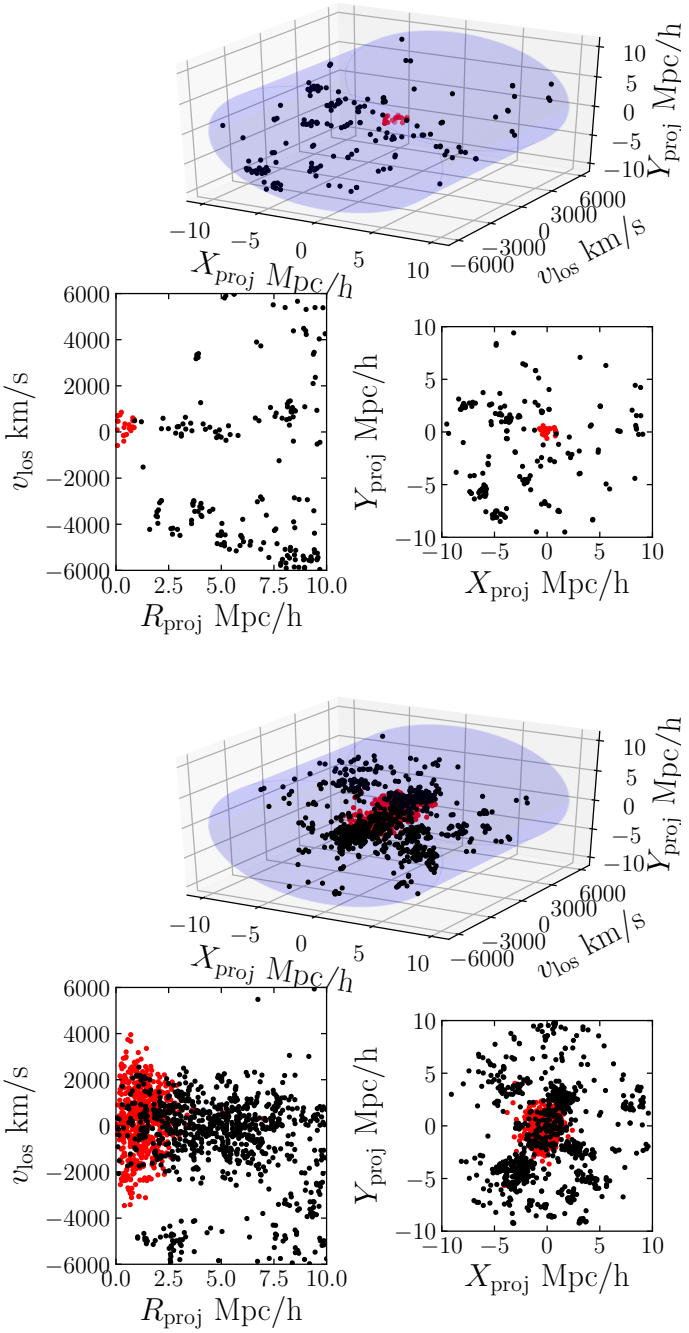

Figure 5.1: Two example mock observations of clusters produced from MDPL2. The top cluster is part of the low mass sample, while the bottom is from the high mass bin. The red points are galaxies that are members of the ROCKSTAR cluster halo.

population. All free parameters, the chosen prior, and description are listed in Table

Table 5.1: Free parameters and priors for MultiDark mock observation models

Parameter	Prior	Description
$\log_{10}[\Sigma_0/(\text{Mpc } h^{-1})^{-2}]$	Uniform between -5 and 5	Uniform contamination light profile
f_{contam}	Uniform between 0 and 1	Number fraction of contamination galaxies
$\log_{10}[r_{s,\text{main}}/R_{\text{max}}]$	Uniform between -3 and 0	NFW scale radius of main halo light profile
$\log_{10}[r_{c,\text{main}}/(\text{Mpc } h^{-1})]$	Uniform between -6 and -1	Radial offset of center of main halo
$\theta_{c,\text{main}}$	Uniform between 0 and 2π	Angular location of center of main halo
z_{main}	Uniform between 0.1 and 0.15	Redshift of main halo $z_{\text{main}} = \langle V\rangle_{\text{main}}/c$
$\log_{10}(\sigma_{\text{main}}/\text{km s}^{-1})$	Uniform between 0 and 3.5	Velocity dispersion of main halo
$\log_{10}[r_{s,\text{sub},i}/R_{\text{max}}]$	Uniform between -3 and 0	NFW scale radius of i-th substructure light profile
$\log_{10}[r_{c,\text{sub},i}/R_{\text{max}}]$	Uniform between -3 and 0	Radial offset of center of i-th substructure
$\theta_{c,\text{sub},i}$	Uniform between 0 and 2π	Angular location of center of i-th substructure
$\langle V\rangle_{\text{sub},i}$	See Eq. 5.12	Velocity of the i-th substructure
$\sigma_{\text{sub},i}/\sigma_{\text{main}}$	Uniform between 0 and 1	Velocity dispersion of i-th substructure
f_i	Uniform between 0 and 1	Number fraction hyperparameter

5.1.

Most free parameters listed in Table 5.1 have uniform prior distributions; however, we use a non-uniform prior to determine the mean velocities of the substructures. The prior choice was made after considering two related issues with the modeling. First, we need to invoke an identifiability requirement so that the Bayesian sampling algorithm (MultiNest) can differentiate between the various populations; we do this by requiring the substructures to have decreasing velocity (i.e. $\langle V\rangle_{\text{sub},1} > \langle V\rangle_{\text{sub},2} > \langle V\rangle_{\text{sub},3}$). If we implemented this requirement using uniform priors with a maximum value specified by the $i-1$ velocity, then the true prior distribution would have significantly more prior weight to low velocity values. Instead we use a prior that is uniform in the hyper-triangle defined by $v_{\text{max}} > \langle V\rangle_{\text{sub},1} > ... > v_{\text{min}}$ and zero elsewhere [251]:

$$\pi(\langle V\rangle_{\text{sub}}) = \begin{cases} \frac{1}{N_{\text{subs}}!(v_{\text{max}}-v_{\text{min}})^{N_{\text{subs}}}} & v_{\text{max}} > \langle V\rangle_{\text{sub},1} > ... > v_{\text{min}} \\ 0 & \text{otherwise} \end{cases} \tag{5.12}$$

where v_{max} and v_{min} are defined relative to the main halo velocity $\langle V\rangle_{\text{main}} \pm 5000$ km/s, respectively. This prior essentially mimics a distribution generated by sampling a uniform prior for each velocity parameter and then reordering them from greatest to least.

The number fraction of galaxies in each population F_M are defined by the hper-parameters f_i. The transformation of these hyperparameters to the true member

fractions is

$$
\begin{aligned}
F_{\rm contam} &= f_{\rm contam} \\
F_{\rm main} &= (1 - f_{\rm contam}) \prod_{i=1}^{N_{\rm subs}} f_i \\
F_{{\rm sub},i} &= (1 - f_{\rm contam})(1 - f_i) \prod_{j=i}^{N_{\rm subs}} f_j .
\end{aligned} \tag{5.13}
$$

This prescription guarantees that $\sum_M F_M = 1$. In order to insure that the main halo corresponds to the largest halo in the model, we further restrict that $F_{\rm main} > F_{{\rm sub},i}$.

5.3.4 Results

Most of the mock observations of galaxies generated from MDPL2 include some amount of 3D substructures. We define a 3D substructure as any ROCKSTAR halo with at least 10 member galaxies within the field-of-view that is gravitationally bound to the cluster. These 3D substructures could be an infalling group of galaxies or a distinct subpopulation associated in some way with the cluster. The multipopulation models identify substructures from the projected sky position and velocity of each galaxy, therefore, we will refer to substructures identified with these models as 2D substructures. An example of the 3D and 2D substructures are shown in Fig. 5.2. In the top set of panels each point is colored by the 3D substructure the galaxy belongs to with red points showing the main cluster and black points showing galaxies that are not members of a 3D substructure. In the bottom portion of Fig. 5.2 we show the results of the $N_{\rm subs} = 3$ model for this cluster by coloring the galaxies depending on their membership to the 2D substructures. Clearly there is correlation between the green 2D substructure with the true 3D substructures. The misidentified 2D substructures are likely 3D substructures that are unbound to the cluster and are therefore not shown in the top portion of Fig. 5.2.

As is obvious in Fig. 5.2, each 2D substructure could include members from different 3D substructures or none, so we quantify the success rate of a 3D substructure identification. We also compare these results to a recent substructure identification method that utilizes the caustic technique [117, hereafter Y15]. The method detailed in Y15 uses a preprocessing step of the caustic method which builds a binary tree based on the projected binding energy between galaxies and groups of galaxies and then cuts the tree to identify substructures. They tested their methodology using the Coupled Dark Energy Cosmological Simulation [252], and they report that 49% of their identified 2D substructures contain at least one member of a 3D substructure and 51% of the 2D substructures with at least one 3D member have 80% of their members belonging to the same 3D substructure. Here we will use the same metric they developed to compare our identification with theirs.

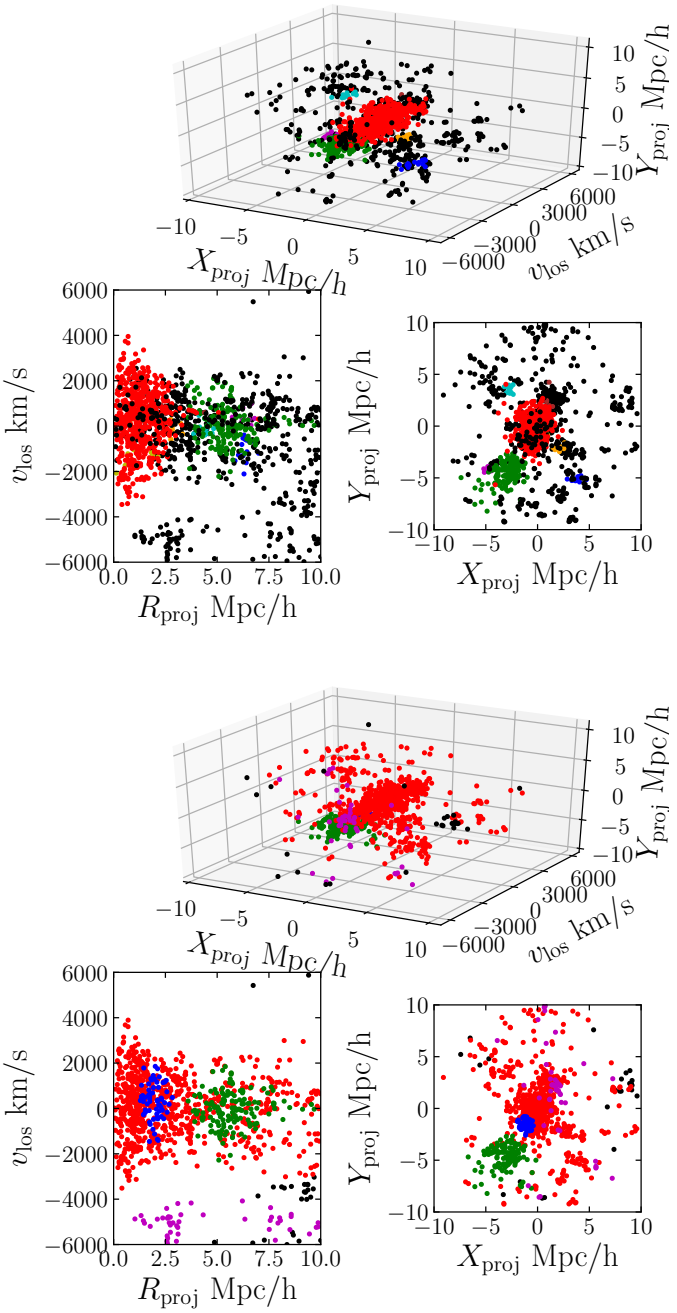

Figure 5.2: The same massive cluster shown in Fig. 5.1 but now the galaxies are colored based on their membership to true 3D substructures (*top*) and 2D substructures identified by the $N_{\rm subs} = 3$ model (*bottom*). The true 3D substructures are identified as any ROCKSTAR halo gravitationally bound to the cluster that falls within the field-of-view of the cylindrical cut and has at least 10 galaxies.

There are a few caveats we wanted to address before our discussion of the results. First, Y15 tested their substructure identification on dark matter particles in the simulation instead of galaxies painted onto subhalos as we do. Second, although our model is interested in identifying substructure, this is merely a secondary feature not the main focus of our modeling framework. And finally, our model is restricted to a preset number of substructures while the caustic method allows for any number of substructures; therefore, the substructures identified with our model are more likely to be larger and include galaxies from multiple 3D substructures. Despite these caveats, we will quantify the comparison between these two methods because the caustic technique substructure identifier is by far the most robust substructure identification model presented in the literature.

For each 2D substructure with at least one galaxy that is also a member of a 3D substructure, Y15 defines f_{3D} as the largest fraction of its members that are also members of the same 3D substructure. Because our substructure model calculates probability of membership posterior distributions for each galaxy for each 2D substructure, we identify the member galaxies of each 2D substructure with two methods. The first method (SUBMEM1) draws $N_{\rm samples} = 10000$ samples from each galaxy's membership probability posterior distributions and assigns a membership to the 2D substructure with the highest probability of membership. Then for each galaxy we take the mode of these samples to determine their final 2D substructure membership. This method will generate a 2D substructure membership for each galaxy. The second method (SUBMEM2) is more selective and only assigns a 2D substructure membership if the galaxy has a probability of membership $\mathcal{P}_M \geq 0.9$ (Eq. 5.10).

Using the SUBMEM1 method for substructure member identification 59% of 2D substructures have at least one member of a 3D substructure. Compared to Y15's method (47%), the substructures identified with our modeling are more likely to have at least one member of a 3D substructure; however, this is a bit misleading. Because we fix the number of 2D substructures per model (and only allow upwards of 3 substructures), the 2D substructures are more likely to be large and include many 3D substructures. This will inflate this percentage. This effect is best realized in the distribution of f_{3D} which is shown in Fig. 5.3. Because each 2D substructure is large and could contain many 3D substructures there are very few 2D substructures with large f_{3D} values when using the SUBMEM1 method for membership identification. The black curve in Fig. 5.3 shows the cumulative distribution of f_{3D} showing that our models have a median value ~ 0.40, whereas, compared to Y15 (shown in red), the caustic technique has a median value 0.77. In other words, 50% of the 2D substructures identified using SUBMEM1 have only $\sim 40\%$ of their member galaxies that are also members of the same bound 3D substructure. However, some of these galaxies included in each 2D substructure could have low probability of memberships which might be skewing this distribution. If this is the case, then SUBMEM2 (which only includes highly probable substructure members) should perform much better.

For 2D substructure members identified by SUBMEM2, 53% of 2D substructures

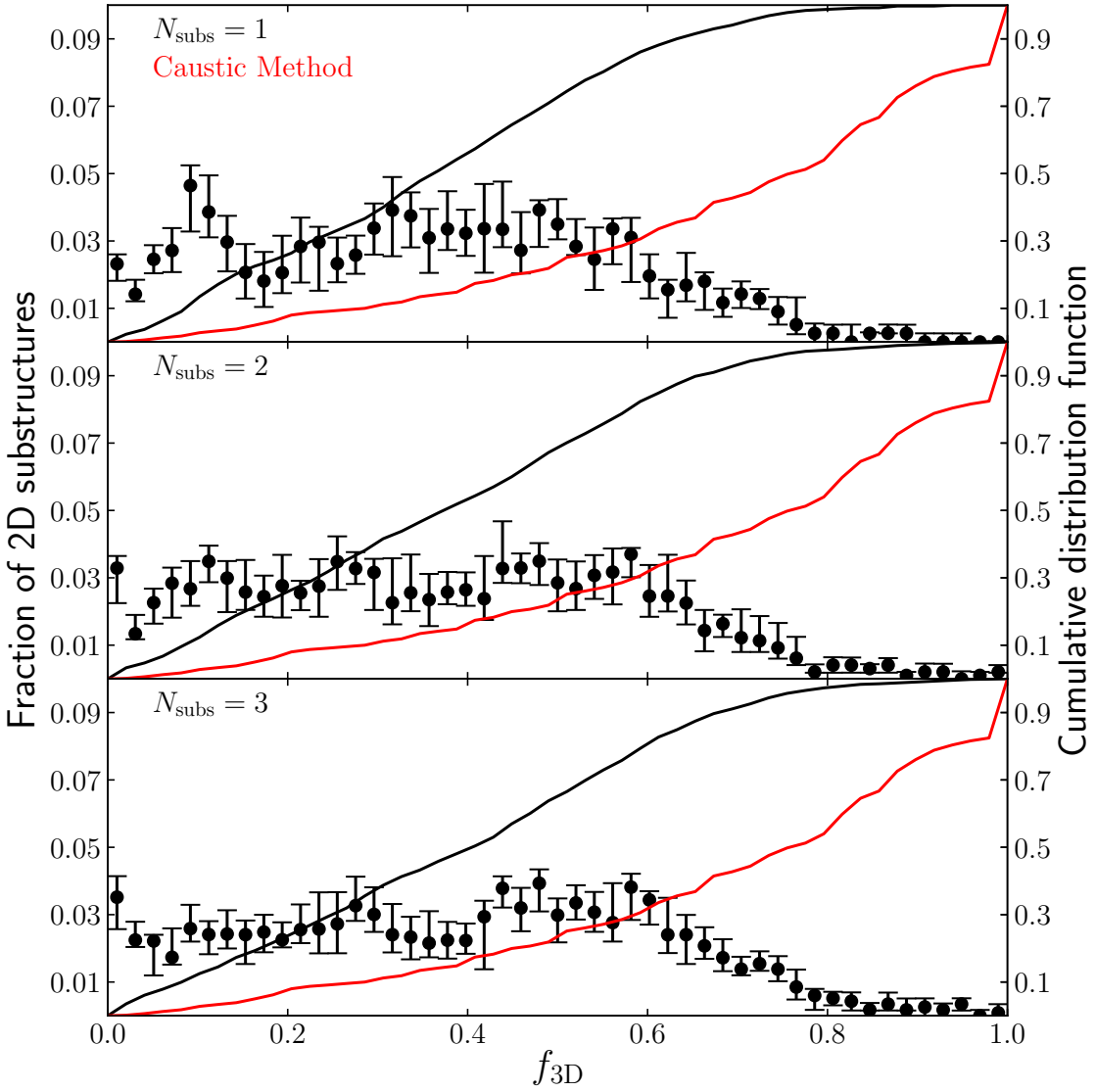

Figure 5.3: Distribution of f_{3D}, the largest fraction of the total number of members of a 2D substructure that are also members of a single 3D substructure. Member galaxies of each 2D substructure were determined via the SUBMEM1 method. The panels are organized by the number of subpopulations allowed in each model. The error bars show the 10% and 90% limits derived from the 10 random samplings of each mock observation. The black line shows the cumulative distribution function of this distribution, while the red line shows the cumulative distribution function for f_{3D} using the caustic technique outlined in Y15.

have at least one member of a 3D substructure. Furthermore, for these 2D substructures, 50% have $f_{3D} \geq 0.79$ for the $N_{\rm subs} = 3$ models, which is a slight improvement over Y15. The full distribution of f_{3D} for SUBMEM2 is shown in Fig. 5.4. For

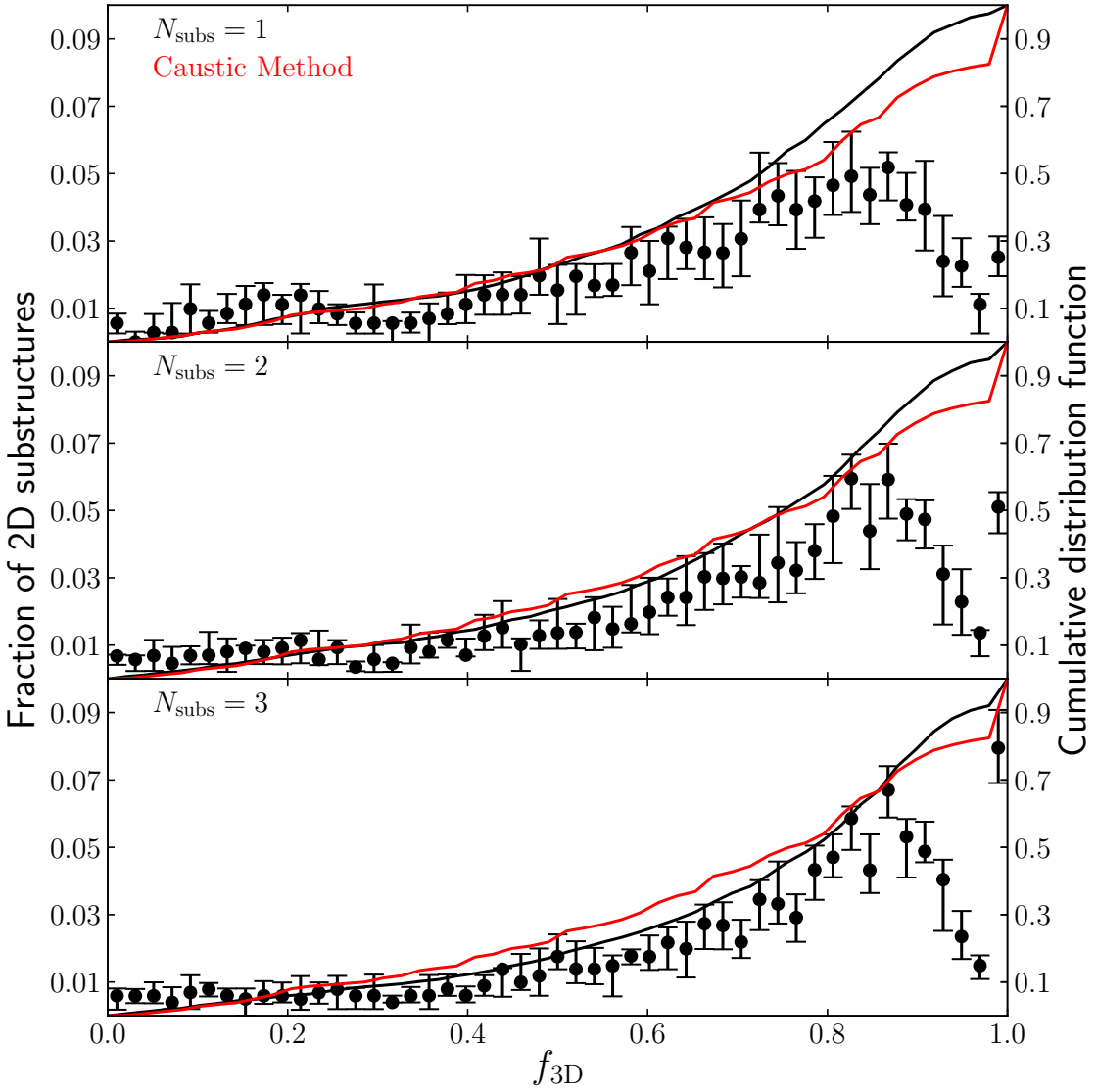

Figure 5.4: Same as Fig. 5.3 except we use the SUBMEM2 method to identify 2D substructure members.

$N_{\rm subs} = 1, 2$ our model is slightly outperformed by Y15, but the $N_{\rm subs} = 3$ model has a small advantage over Y15. This clearly shows that, especially for the highly probable 2D substructure member galaxies, the 2D substructures identified in this model correlate with the true bound 3D substructures of the cluster.

Identifying substructure is merely an added bonus of the modeling framework, the main purpose is to measure more precise cluster masses while simultaneously accounting for substructure. In §5.4.4 we implement a dark matter halo model to fit real observations of A267 in order to fit the underlying dark matter mass profile

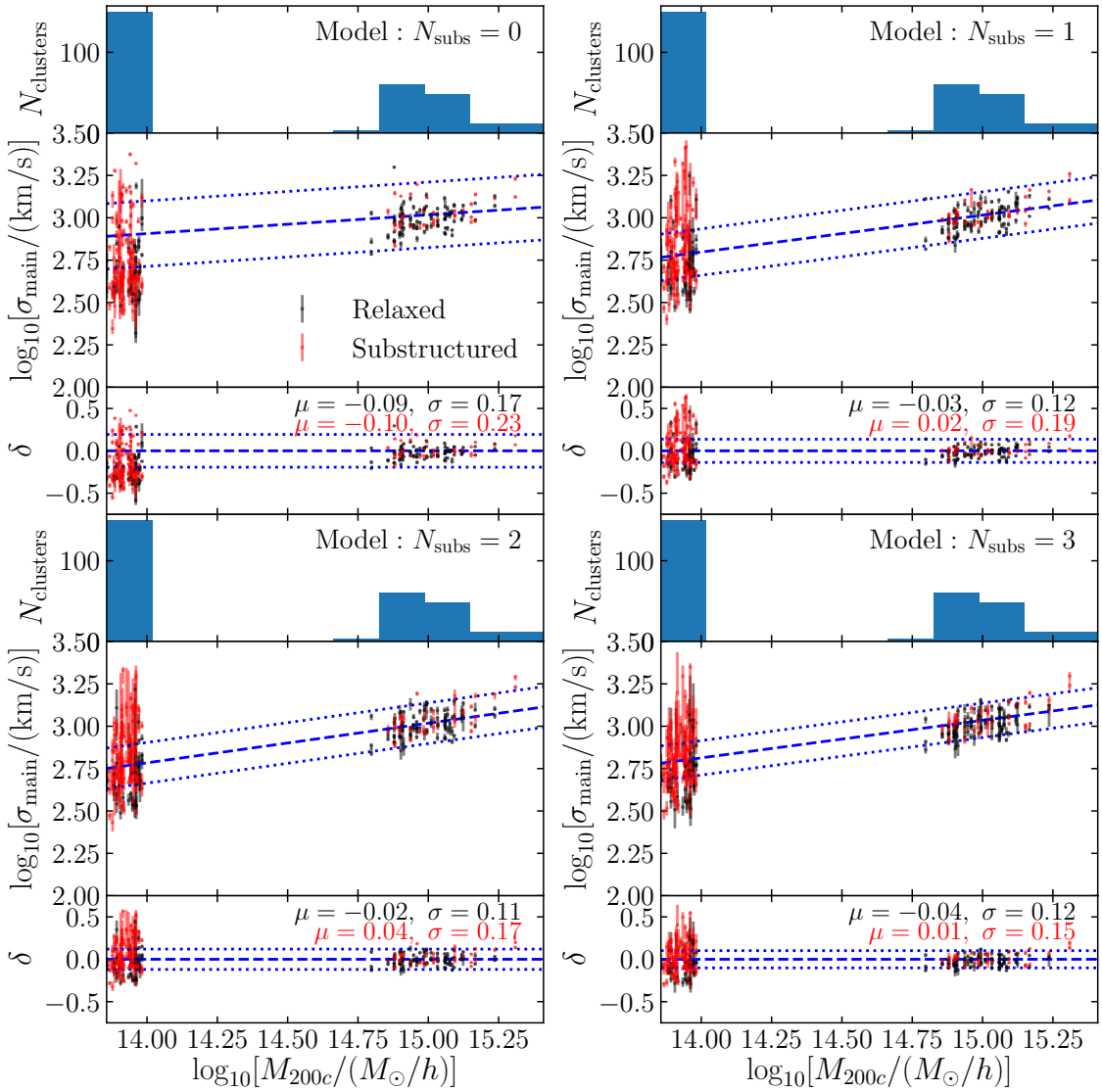

Figure 5.5: Velocity dispersion of the main cluster halo $\sigma_{\rm main}$ as a function of true cluster mass M_{200c} from the MDPL2. Each column corresponds to the number of subpopulations $N_{\rm subs}$ allowed in each model. The topmost panels show the distribution of galaxies, clearly showing the high mass and low mass sample. Each point is colored depending on if the cluster is relaxed (i.e. little to no signifiant substructure) or substructured. The error bars show the 10% and 90% ranges from the ten random samplings of each cluster. Because there is a power-law relationship between velocity dispersion and mass, we fit a power-law (blue dashed lines) with scatter (blue dotted lines). In the bottom panels we show the residuals, and quantify the scatter of these residuals for the relaxed and substructured clusters, independently. As the number of subpopulations in the model increases, the fit scatter in the power-law decreases as does the residual scatter of substructured clusters.

of the cluster; however, this calculation is expensive, and would be unfeasible to run over a large amount of mock observations. Therefore, here we will discuss the uniform velocity dispersion $\sigma_{\rm main}$ as a proxy for cluster mass. Fig. 5.5 shows the distribution $\sigma_{\rm main}$ as a function of true cluster mass M_{200c} for all clusters. There is a well established power law scaling relationship between velocity dispersion and mass that dates back to Fritz Zwicky [7] and is still commonly used today [82, for example]. This relationship is due to the virial theorem $\sigma \propto M^{1/3}$, but the power law index is commonly a free parameter fit from data. The value of the power law index is easy to fit; however, the scatter about the power-law relationship is of greater importance [253].

In Fig. 5.5 we fit a power-law through the derived cluster velocity dispersion $\sigma_{\rm main}$ as a function of true cluster mass M_{200c} along with the scatter about this relationship. The power-law is shown as the blue dashed lines while the width of the fit scatter is the blue dotted lines. Clearly, as we increase the number of subpopulations $N_{\rm subs}$ the scatter decreases drastically. Furthermore, we separate the cluster sample into two groupings, relaxed and substructured, depending on the amount of bound 3D substructures each cluster has. In the bottom panel, we show the residuals as well as the mean and standard deviation of the residual distributions for each groupings. This shows that the scatter in the residuals of the substructured cluster sample decreases by nearly 35% from the $N_{\rm subs} = 0$ model to the $N_{\rm subs} = 3$ model.

5.4 Application to A267

In this section we will apply the multi-population model outlined in §5.2 above to spectroscopic observations of the galaxy cluster Abell 267 (A267, $z \sim 0.23$). In §5.4.1, I will describe the data set; §5.4.3 will describe and present the results for the modeling assuming a uniform velocity dispersion for the main cluster halo; and in §5.4.4 we apply a dark matter halo model in order to fit the mass profile of A267.

5.4.1 Observational Dataset

The A267 data are drawn from three separate catalogues. The spectroscopic observations are a combination of over 1000 measured redshifts by HectoSpec (HeCS [89]) and 223 galaxies with the Michigan/Magellan Fiber System (M2FS). For galaxies that were observed in both data sets, we used a weighted (by inverse variance of redshift) mean of the measured redshifts. The combination of these included 1219 galaxy redshifts with a median error of 32km/s.

The observations, data reduction, and spectral fitting model for the M2FS spectroscopy is described in detail in [119]. We fit these spectra using a population synthesis integrated light model, that estimates line-of-sight velocity, $v_{\rm los}$, along with stellar population parameters mean age, metallicity [Fe/H], chemical abundance [α/Fe], and internal velocity dispersion $\sigma_{\rm int}$. A summary of these results can be found in Table

3.3 and the full data product, including sky-subtracted spectra with variances, best fitting model, and samples from the posterior distribution, can be found online at https://doi.org/10.5281/zenodo.831784.

The HeCS catalog is described in detail by [89] and contains redshifts for over 22,000 galaxies in over 50 different clusters. Compared to the M2FS sample, the HeCS sample for A267 is much larger and provides wider coverage. The M2FS sample, while smaller, provides extra dimensions of information, including mean ages and metallicities.

Both spectroscopic data sets were selected via the galaxy red sequence described in §3.2.1 and shown in Fig. 3.1. We applied this same selection criteria to obtain a photometric galaxy sample from the Sloan Digital Sky Survey (SDSS) of 1675 galaxies. The galaxies contained in the spectroscopic sample are a subset of those in the photometric sample. Fig. 5.10 shows the positions of all galaxies used in this analysis. The black points are galaxies with only photometric observations, while the colored markers are galaxies with spectroscopically measured redshifts. Fig. 5.11 shows the redshift distribution of galaxies used in this analysis.

Because we select galaxies via the red sequence, our inferences on cluster substructure and kinematics are biased to the quiescent galaxy population. We note that the velocity dispersion of quiescent galaxy members has been shown in the past to be smaller than the velocity dispersion of blue members [242, for example].

The spectroscopic completeness as a function of radial distance and r-band magnitude are shown in Fig. 5.6. The majority of the galaxies targeted via the red sequence lie between magnitudes 18 and 21.

5.4.2 Contamination Model

The grey histograms in Fig. 5.11 show the velocity distribution of the A267 spectroscopic sample. The contamination population of galaxies (the numerous sub peaks throughout the distribution) is dominated by foreground and background groups and clusters of galaxies, therefore, extra care must be taken in determining the contamination model. To this end, we implement a modified version of the multi-population model with the aim to fit a fixed number of these contamination clusters as well as some uniform component on the sky. We fit the contamination model in advance using only galaxies without spectroscopic redshifts and galaxies with spectroscopic redshifts that are obvious contaminants (i.e. galaxies with line-of-sight velocities $|v_i - cz_{267}| > 5000$ km/s).

The contamination model is of the same form of the multi-population mixture model described in detail §5.2 with a few minor changes. This model will be made up of $N_{\text{contam}} + 1$ populations. The first population will be used to describe the field galaxies that will not be fit into a clustered population. Therefore, we assume that these galaxies will be uniformly distributed on the sky $I(\boldsymbol{r})_{M=\text{contam}_0} = \Sigma_0$ with a

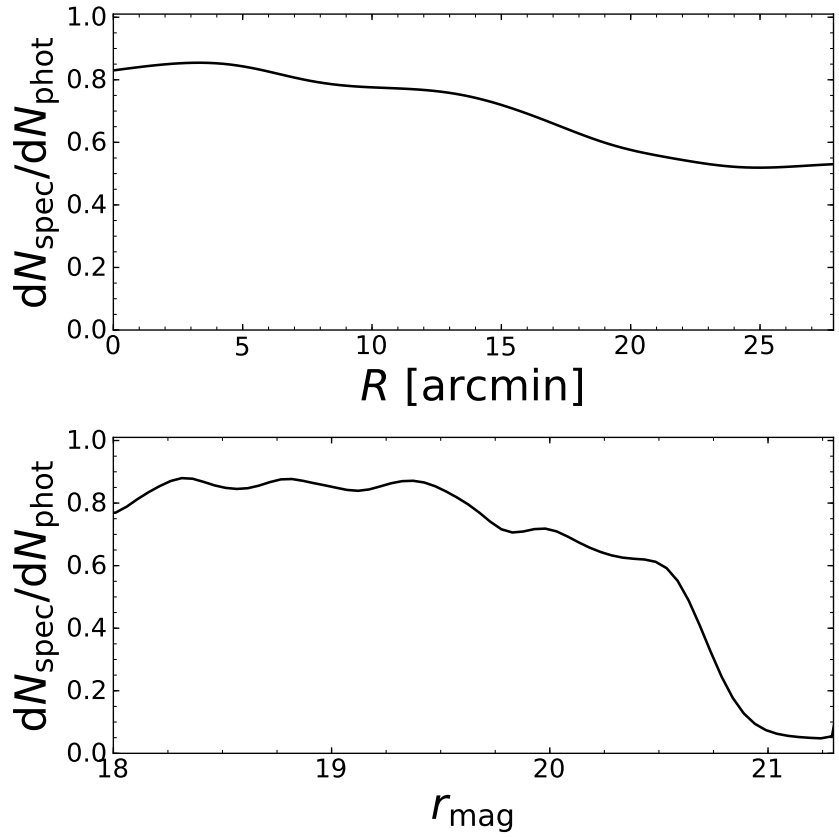

Figure 5.6: Spectroscopic completeness as a function of radial distance (*top*) and SDSS r-band magnitude (*bottom*).

generalized gamma distribution used to describe the velocity distribution:

$$P(v_i|M = \mathrm{contam}_0, \boldsymbol{r}_i, \boldsymbol{\theta}) = \frac{(p/a^d)v_i^{d-1}\exp[-(v_i/a)^p]}{\Gamma(d/p)} \tag{5.14}$$

where p, a, and d are free parameters and Γ is the gamma function. This distribution was chosen for its flexibility to handle the redshift distribution of field galaxies in our sample; however, there is no physical motivation for the Gamma distribution. We do not include observational errors in this velocity distribution because the distribution covers a large range in redshift space and so the relatively small velocity errors will have little effect on the underlying distribution. The remaining N_{contam} populations are described by NFW light profiles with gaussian velocity distributions. The free parameters used in for this contamination model are listed and described in the top portion of Table 5.2.

For the same reasons discussed in §5.3.3, we use a non-uniform prior on the red-

Table 5.2: Free parameters and priors for uniform velocity dispersion model of A267. The first set of parameters (first 10 rows) are for the contamination model and are fit ahead of time using only obvious contamination galaxies. For the contamination model we use one uniform population and five NFW populations. The remaining free parameters are used to describe the kinematics of the cluster.

Parameter	Prior	Description
$\log_{10}\left[\Sigma_0/\text{radians}^{-2}\right]$	Uniform between -2 and 15	Light profile for uniform component of contamination model
$\log_{10} a$	Uniform between -6 and 6	Parameter of gamma distribution Eq. 5.14
$\log_{10} d$	Uniform between -6 and 1	Parameter of gamma distribution Eq. 5.14
$\log_{10} p$	Uniform between -6 and 6	Parameter of gamma distribution Eq. 5.14
$\log_{10}\left[r_{s,\text{contam},i}/R_{\max}\right]$	Uniform between -3 and 0	NFW scale radius of i-th contamination population
$\log_{10}\left[r_{c,\text{contam},i}/R_{\max}\right]$	Uniform between -3 and 0	Radial offset of center of i-th contamination population
$\theta_{\text{c,contam,i}}$	Uniform between 0 and 2π	Angular location of center of i-th contamination population
$z_{\text{contam,i}}$	see Eq. 5.15	Redshift of i-th contamination population
$\log_{10}\left(\sigma_{\text{contam},i}/\text{km s}^{-1}\right)$	Uniform between 0 and 3.5	Velocity dispersion of i-th contamination population
$f_{\text{contam},i}$	Uniform between 0 and 1	Number fraction hyperparameters for contamination model
$\log_{10}\left[\Sigma_{rs}/\text{radians}^{-2}\right]$	Uniform between -1 and 1	Rescale uniform component of contamination model
f_{contam}	Uniform between 0 and 1	Number fraction of all contamination population
$\log_{10}\left[r_{s,\text{main}}/R_{\max}\right]$	Uniform between -3 and 0	NFW scale radius of main halo light profile
$\log_{10}\left[r_{c,\text{main}}/R_{\max}\right]$	Uniform between -3 and 0	Radial offset of center of main halo
$\theta_{c,\text{main}}$	Uniform between 0 and 2π	Angular location of center of main halo
z_{main}	Uniform between 0.22 and 0.245	Redshift of main halo $z_{\text{main}} = \langle V\rangle_{\text{main}}/c$
$\log_{10}\left(\sigma_{\text{main}}/\text{km s}^{-1}\right)$	Uniform between 0 and 3.5	Velocity dispersion of main halo
$\log_{10}\left[r_{s,\text{sub},i}/R_{\max}\right]$	Uniform between -3 and 0	NFW scale radius of i-th substructure light profile
$\log_{10}\left[r_{c,\text{sub},i}/R_{\max}\right]$	Uniform between -3 and 0	Radial offset of center of i-th substructure
$\theta_{c,\text{sub},i}$	Uniform between 0 and 2π	Angular location of center of i-th substructure
$\langle V\rangle_{\text{sub},i}$	See Eq. 5.12	Velocity of the i-th substructure
$\sigma_{\text{sub},i}/\sigma_{\text{main}}$	Uniform between 0 and 1	Velocity dispersion of i-th substructure
f_i	Uniform between 0 and 1	Number fraction hyperparameter

shifts of the contamination populations:

$$\pi(z_{\text{contam}}) = \begin{cases} \frac{1}{N_{\text{contam}}!(z_{\max}-z_{\min})^{N_{\text{contam}}}} & z_{\max} > z_{\text{contam},1} > \ldots > z_{\min} \\ 0 & \text{otherwise} \end{cases} \tag{5.15}$$

where $z_{\min}$ and $z_{\max}$ are set by the full range of redshifts in our sample.

For this model we fit $N_{\text{contam}} = 5$ contamination populations. These 5 populations are clearly visible in the velocity distribution of our sample (grey histograms) as well as the model fit in Fig. 5.11. Although there are clearly more peaks in the velocity distribution that the model does not properly account for, it is unfeasible to fit those distributions because MultiNest becomes increasingly inefficient at sampling high-dimensional posteriors. In order to fit this model, we required $\sim 1.25 \times 10^9$ likelihood

evaluations with a sampling acceptance rate of 1.8×10^{-4} which took over 1.6×10^4 CPU hours to fully sample the posterior distributions.

In order to cut down on the number of free parameters, we fit the contamination model beforehand and feed this fit model into the analysis described below. We originally sampled the posterior of the contamination model; however, this also drastically decreased the sampling efficiency, so instead we use the highest likelihood model from the fit instead. We've seen there is no dependence on the resulting posterior distribution in spite of this choice.

5.4.3 Uniform Velocity Dispersion Profile

In this section, we use a simple kinematic model in order to explore how inferences on the kinematics of A267 depend on the number of subpopulations allowed. We do this by running five separate model fits, each model allowing an additional subpopulation (from zero to four). The free parameters and their prior ranges used in these models are given in Table 5.2.

Model Setup

The model setup is similar to the setup described in §5.3.3 with a few minor differences mainly pertaining to the contamination model. We use the pre-fit contamination model described in §5.4.2 which drastically reduces computation time and increases computation efficiency. Although the contamination model is already fit, we do allow there to be a rescaling of the uniform contamination component Σ_{rs}. The remaining free parameters are discussed in detail §5.3.3. We again use the same prior on the line-of-sight velocities of the subpopulations in order to preserve prior probability mass and solve the identifiability issue (Eq. 5.12). The transformation from the number fraction hyperparameters to the true number fractions are given by:

$$
\begin{aligned}
F_{\mathrm{contam},0} &= f_{\mathrm{contam}} \prod_{i=1}^{N_{\mathrm{contam}}} f_{\mathrm{contam},i} \\
F_{\mathrm{contam},i} &= f_{\mathrm{contam}}(1 - f_{\mathrm{contam},i}) \prod_{j=i}^{N_{\mathrm{contam}}} f_{\mathrm{contam},j} \\
F_{\mathrm{main}} &= (1 - f_{\mathrm{contam}}) \prod_{i=1}^{N_{\mathrm{subs}}} f_i \\
F_{\mathrm{sub},i} &= (1 - f_{\mathrm{contam}})(1 - f_i) \prod_{j=i}^{N_{\mathrm{subs}}} f_j.
\end{aligned}
\tag{5.16}
$$

In total these models are described by $2 + 5 + 6N_{\mathrm{subs}}$ free parameters. For the A267 sample we include $N_{\mathrm{gal}} = 1675$ galaxies in the photometric sample with $N_{\mathrm{spec}} = 1121$ of these galaxies with spectroscopically measured line-of-sight velocities.

Substructures in A267

As discussed in [96], the presence of substructure can have a significant effect on dynamical mass measurements of galaxy clusters. In order to understand this effect on mass estimates, we first assume a simple uniform velocity dispersion profile to explore how substructure influences these measurements. We fit a set of five models, with each model allowing an additional subpopulation within the cluster environment (the largest number of subpopulations we fit are $N_{\rm subs} = 4$).

Fig. 5.7 shows a summary of the main results from this analysis in black. In the top panel we show the evolution of the change in the log evidence for each model relative to the $N_{\rm subs} - 1$ model. This value is frequently referred to as the Bayes factor, and it is commonly used for model selection. The larger the Bayes factor, the more significant the evidence is that new model is "better" than the previous model, accounting for differences in model complexity. According to [254], a Bayes factor ($\Delta \log(\mathrm{Ev})$) between 3 and 5 indicates "strong" evidence and if this factor exceeds 5, then the new model is very strongly favored. The Bayes factor is consistently > 5 for the $N_{\rm subs} = 1$, 2, and 3 models, which indicates that each of these models is strongly favored over the model with one less subpopulation ($N_{\rm subs} = 0$, 1, and 2 respectively). However, the $N_{\rm subs} = 4$ model (with Bayes factors < 3) is only "slightly positive" or "not worth more than a bare mention" compared to the $N_{\rm subs} = 3$ model.

The second panel in Fig. 5.7 shows the number of likelihood evaluations needed to adequately sample the posterior PDF of each model. As expected for models with increasing number of free parameters, the required number of likelihood evaluations increases exponentially, rendering the computation of increasing numbers of subpopulations $N_{\rm subs} > 4$ expensive.

The third panel in Fig. 5.7 shows the number fraction of galaxies in all subpopulations. This panel gives an idea of how many galaxies are added to the subpopulations with increasing number of subpopulations.

In the next three panels of Fig. 5.7 we show the evolution of free parameters describing the main cluster: NFW scale radius $r_{s,\rm main}$, mean cluster redshift $z_{\rm main}$, and uniform velocity dispersion $\sigma_{\rm main}$. The second from the bottom panel ($\sigma_{\rm main}$) shows the evolution of velocity dispersion, a proxy for cluster mass. For comparison, we include the velocity dispersion for A267 measured by [89], which is calculated by first identifying cluster members via the Caustic technique [80] and calculating the dispersion of the members about the mean cluster redshift (also determined via the Caustic method). The Caustic method does not explicitly consider the effects of substructure (unless it is evident in the plane of $v_{\rm los} - R$), so we compare it to to our measurement assuming $N_{\rm subs} = 0$, finding good agreement. As the number of subpopulations increases, the velocity dispersion trends downwards decreases; furthermore, the velocity dispersion decreases by ~ 400 km/s from $N_{\rm subs} = 3$ to $N_{\rm subs} = 4$ (see below for more details on this drop off).

The inflation of velocity dispersion due to the presence of substructure is not a new result. [255] studied the dynamics Abell 98, and showed that the cluster was

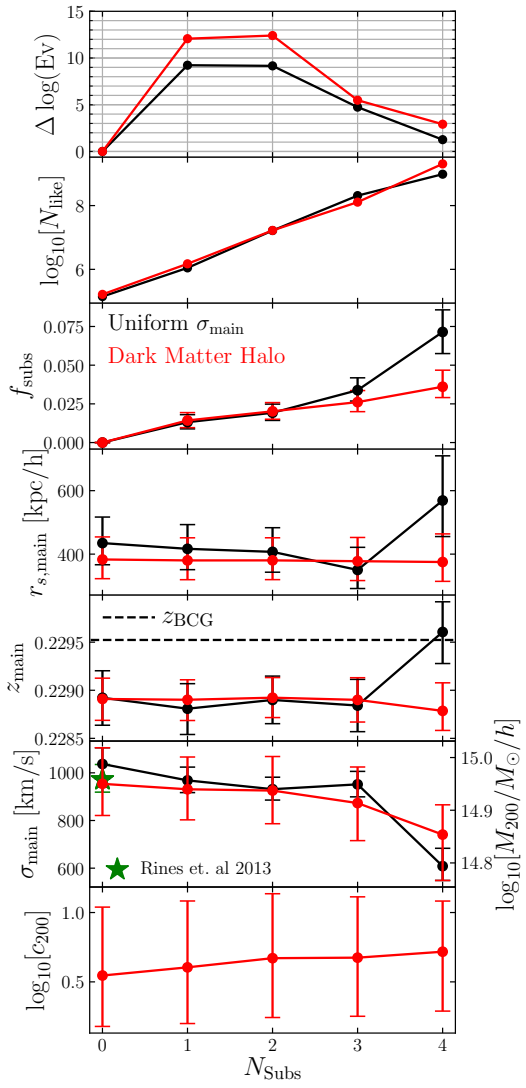

Figure 5.7: Summary plot of the subpopulation analysis with the black curves showing the progression for the uniform velocity dispersion models while red is for the dark matter halo models. The first panel from the top shows the evolution of the change in Bayesian evidence relative to a model with one fewer subpopulations, which is commonly known as the Bayes factor. The second panel shows the number of likelihood evaluations required to adequately sample the posterior PDF of each model. Next is the number fraction of galaxies within all subpopulations. The bottom four panels are the model parameters used to describe the main cluster populations: NFW scale radius $r_{s,\mathrm{main}}$, mean cluster redshift z_{main}, velocity dispersion σ_{main}, and mass M_{200} and concatenation c_{200} for the dark matter model. The dashed line in the 5th panel shows the measured redshift of the BCG for A267. In the second from the bottom panel, the green star shows the velocity dispersion of A267 as measured by [89].

sub-structured with two distinct components. Furthermore, by using a two component model to fit the cluster dynamics, they showed that failure to recognize this substructure inflates the velocity dispersion and hence the mass-to-light ratio of the cluster. [256] obtain a similar result for the Cancer Cluster. What is new here is the ability to evaluate the number of substructures and estimate cluster mass while marginalizing over uncertainty in the substructure parameters.

As the number of subpopulations increases, the scale radius $r_{s,\mathrm{main}}$ decreases for the most part. This trend is consistent with the mass of the main cluster also decreasing. While the redshift of the cluster stays roughly constant throughout most of the models, it is significantly lower than the redshift of the BCG of A267, which is shown as the black dashed line in Fig. 5.7. This offset is on the order of ~ 100 km/s and could be interesting in regards to tests of a "wobbling" BCG as predicted by SIDM [240, 241].

There is clearly something different happening from $N_{\mathrm{subs}} = 3$ to $N_{\mathrm{subs}} = 4$, so let's look more into that now. Fig. 5.8 shows the distributions of galaxies on the sky as well as in phase space. Each galaxy is colored by their memberships to a given population. The galaxy members were determined via the SUBMEM2 method discussed above which assigns membership to a population if a galaxy has a probability of membership that exceeds 0.9. If a galaxy's probability of membership is below this threshold for all populations then it is labeled as a contamination galaxy. We showed in §5.3.4 that this prescription for identifying substructure members yields a strong correlation to the true 3D substructures for mock observations from simulations.

In the $N_{\mathrm{subs}} = 0$ panels, the cluster and its trumpet-shaped caustic are clearly visible. The first substructure the model fits is an elongated grouping of galaxies with a center $x \sim -15$ arcmins and velocity offset $\sim +4000$ km/s relative to the cluster. The second substructure found is a small localized group of galaxies that also has a large velocity offset relative to the cluster (~ -4000 km/s). An important feature to note is that the subpopulation identified in the $N_{\mathrm{subs}} = 1$ model is still identified as a distinct substructure in the $N_{\mathrm{subs}} = 2$ model. This is important because each model is independent of the previous, there is no guarantee that the identification of the substructure will be consistent. The third subpopulation identified a localized group of galaxies at large projected radius ~ 5 Mpc/h yet a similar redshift of the cluster. These galaxies are likely an infalling group of galaxies to A267. Once this substructure is modeled accordingly the cluster lightly profile is more compact, yet the velocity dispersion increases slightly.

The $N_{\mathrm{subs}} = 4$ model yields an odd result that is actually expected once the assumptions of the model are considered. With the added complexity of the fourth substructure, and the requirement that the velocity dispersion of the cluster is constant, the model essentially over fits the distributions. This can easily be seen in the stripped pattern in the $N_{\mathrm{subs}} = 4$ phase space panel of Fig. 5.8. The cluster's light profile is much larger now and the velocity dispersion is much smaller because the model can easily fit a small uniform dispersion profile while accepting for the

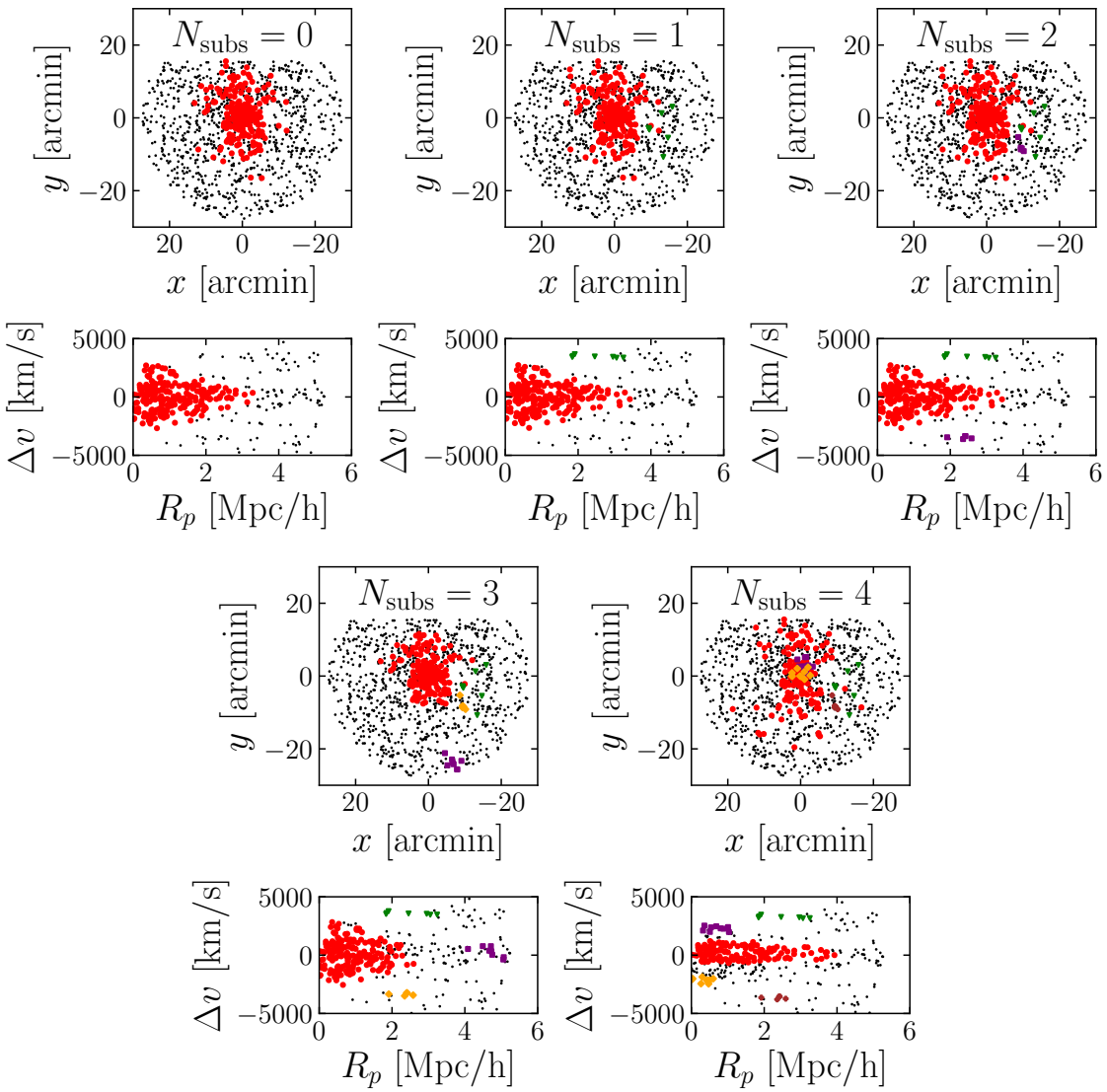

Figure 5.8: Sky position and phase space diagrams for the A267 sample from the uniform velocity dispersion models. Each galaxy is colored based off of their membership to each substructure. Black galaxies are contamination galaxies, red are main cluster halo galaxies, and green, purple, orange, and brown are the four substructures fit in the models. The panels are organized by increasing number of substructures accounted for in the model.

tails as independent substructures. There are now sets of galaxies that were once highly probable members of the main cluster that are now no longer highly probable members to any population. The bayesian evidence (top most panel of Fig. 5.7) does not favor this model over the $N_{\rm subs} = 3$ model; however, this could change once we incorporate a more realistic velocity dispersion profile as will be discussed in §5.4.4

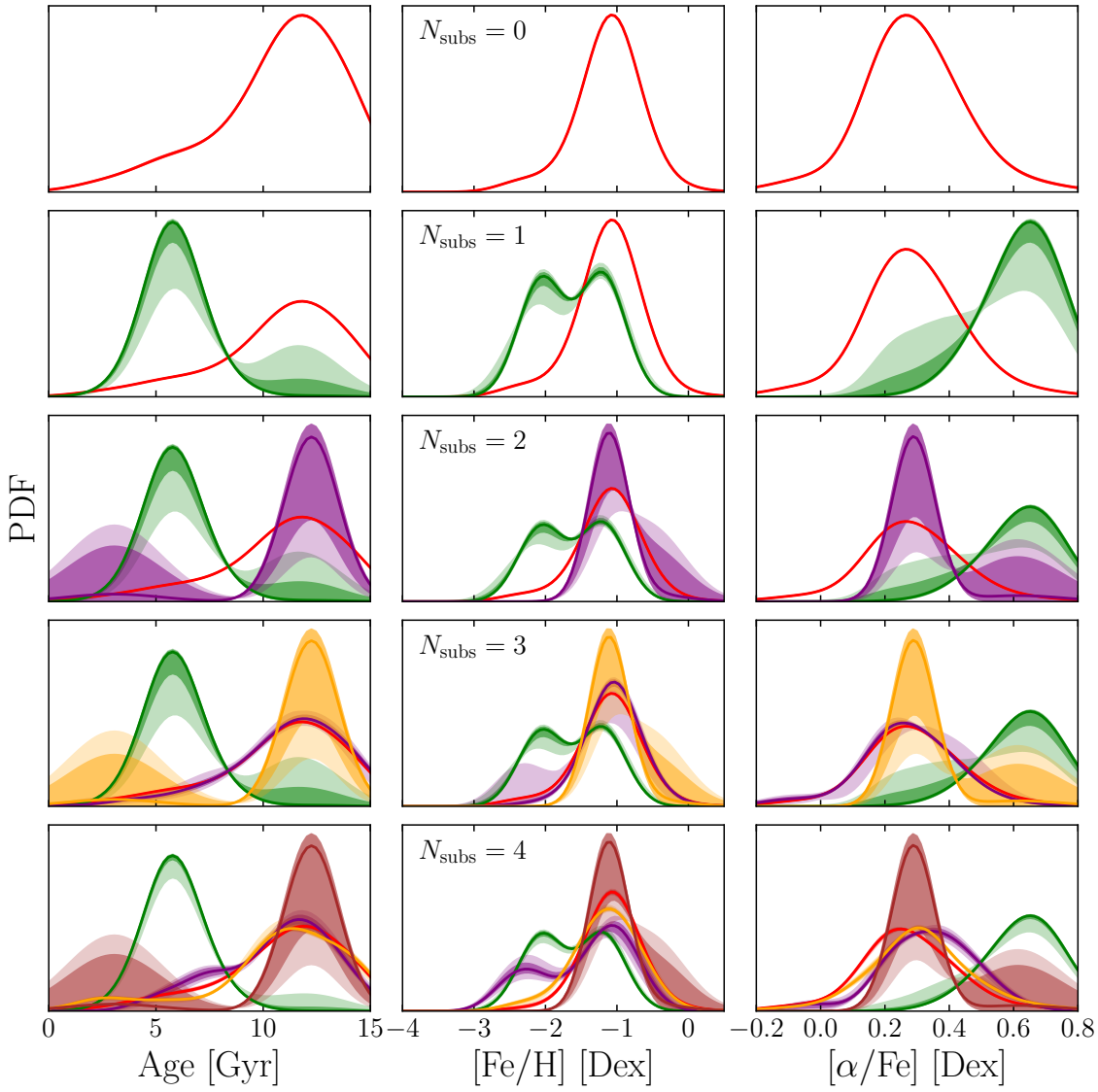

Figure 5.9: Distribution of stellar-population parameters for substructures from A267 sample. The stellar population parameters are obtained from the spectral fits described in Ch. 3. Each curves color corresponds to a different subpopulation and these colors are consistent with the substructures shown in Fig. 5.8. From top to bottom, we show the results of the models with increasing number of substructures.

below.

For the 223 galaxies observed with M2FS, we have estimates of the parameters describing the mean age, metallicity, and chemical enrichment of each galaxy's stellar population. In Fig. 5.9 we show the distribution of these galaxy's stellar parameters, weighted by their probability of membership to each substructure. The colors

Table 5.3: Mean values and standard deviations of 1D posterior PDFs for A267 free parameters in the uniform velocity dispersion $N_{\rm subs} = 3$ model.

	r_s/kpc h^{-1}	α_{2000}/deg	δ_{2000}/deg	z	$\sigma_{\rm disp}$/km s^{-1}	$f_{\rm mem}$	$N_{\rm mem}$
Main	357 ± 68	28.174 ± 0.001	0.999 ± 0.001	0.2288 ± 0.0003	951 ± 56	0.199 ± 0.012	183 ± 22
Sub1	930 ± 692	27.964 ± 0.048	0.944 ± 0.075	0.2403 ± 0.0004	229 ± 96	0.014 ± 0.005	8 ± 3
Sub2	247 ± 269	28.070 ± 0.032	0.625 ± 0.105	0.2297 ± 0.0016	429 ± 124	0.015 ± 0.006	7 ± 3
Sub3	54 ± 189	28.022 ± 0.057	0.864 ± 0.042	0.2173 ± 0.0003	131 ± 74	0.006 ± 0.002	5 ± 1

of each curve in Fig. 5.9 correspond to the same colored substructures shown in Fig. 5.8. Although most substructures have a similar age and metallicity, there is a clear difference in the mean age of the cluster ~ 12 Gyrs and the age of the high velocity substructure (green). A more in-depth analysis of these distributions is limited by the fact that we incorporate more than 1100 galaxy redshifts in the kinematic model, but only have stellar population parameters for roughly 1/6th of these galaxies. Therefore, we have not incorporated these stellar-population parameters into the model framework, because we only have these parameter estimates for a small sub-sample of the galaxies included in this analysis. However, including these parameters within the multi-population mixture model would potentially give more power to separate subpopulations, and would enable more detailed studies of galaxy evolution within the cluster environment.

Table 5.3 gives a summary of the results for the $N_{\rm subs} = 3$ model. The parameters describing the main cluster halo all have strong constraints; furthermore, the center of the main halo's light profile is offset from the BCG of A267 by 89.9 ± 14.2 kpc/h. The scale radii of the substructures are relatively unconstrained mainly due to the low number of galaxies in each population. The scale radius of the 1st subpopulation is completely unconstrained. This is likely due to that fact that the galaxies in this population (see Fig. 5.10) are elongated on the sky and therefore are not fit well by the radially symmetric NFW profile. Despite the poor fits to the light profile, the central locations, redshifts, and velocity dispersions of the substructures are relatively well constrained.

Fig 5.10 shows a more in-depth look at the sky positions of the galaxies labeled by their most likely substructure membership for $N_{\rm subs} = 3$ model. In the upper left panel, we show just the sky position of our sample. Galaxies with colors and various shapes are ones with spectroscopic redshifts and colored based off of their membership. The black points are galaxies without spectra which were used to constrain the light profiles in the model. The contours show the light profile fit from the model of all populations (contamination + main cluster + substructures). The other two panels show an overlay image of our analysis (the colored circles and white contours) with the SDSS mosaic [127], the weak lensing signal in blue [257], and X-ray luminosity in pink (XMM-Newton objid 0084230401). The bottom most panel is a zoom-in on the central core of A267.

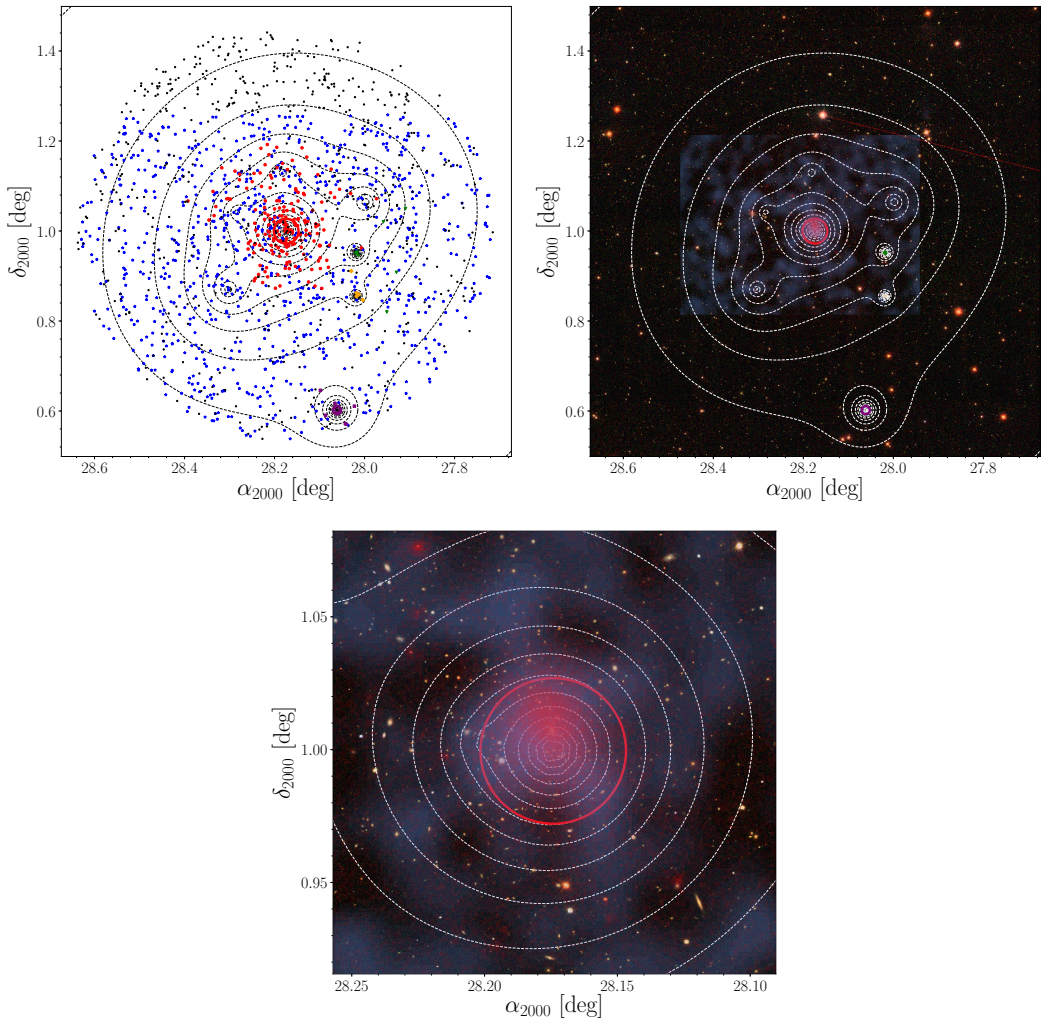

Figure 5.10: Top left shows the positions of galaxies on the sky. Each galaxy is colored and shaped based on which population the galaxy has the highest probability of membership: red circles are the main cluster population, green triangles, purple squares, and orange diamonds are for the three subpopulations, and blue stars are either foreground or background contamination galaxies. The solid red circle shows the scale radius of the main cluster population $r_{s,\mathrm{main}}$ centered on A267. The other colored circles show the scale radius $r_{s,\mathrm{sub},i}$ of their respective subpopulations centered on the measured center of the population. The dashed black curves show contours of equal density from the highest likelihood number density profile to the data ($\sum_M^{N_p} I_M(\boldsymbol{r})$). In the other two panels, we overplot these contours as well as the scale radii of the populations on top of the SDSS image center on A267, the x-ray luminosity (shown as a pink hue), and the weak-lensing signal [257, shown in light blue]. The bottom panel is a zoom-in on the center of A267.

In Fig. 5.11 we show the velocity distribution of our sample. We overplot the velocity distributions fit to the data for the $N_{\mathrm{subs}} = 3$ model. The darker and lighter

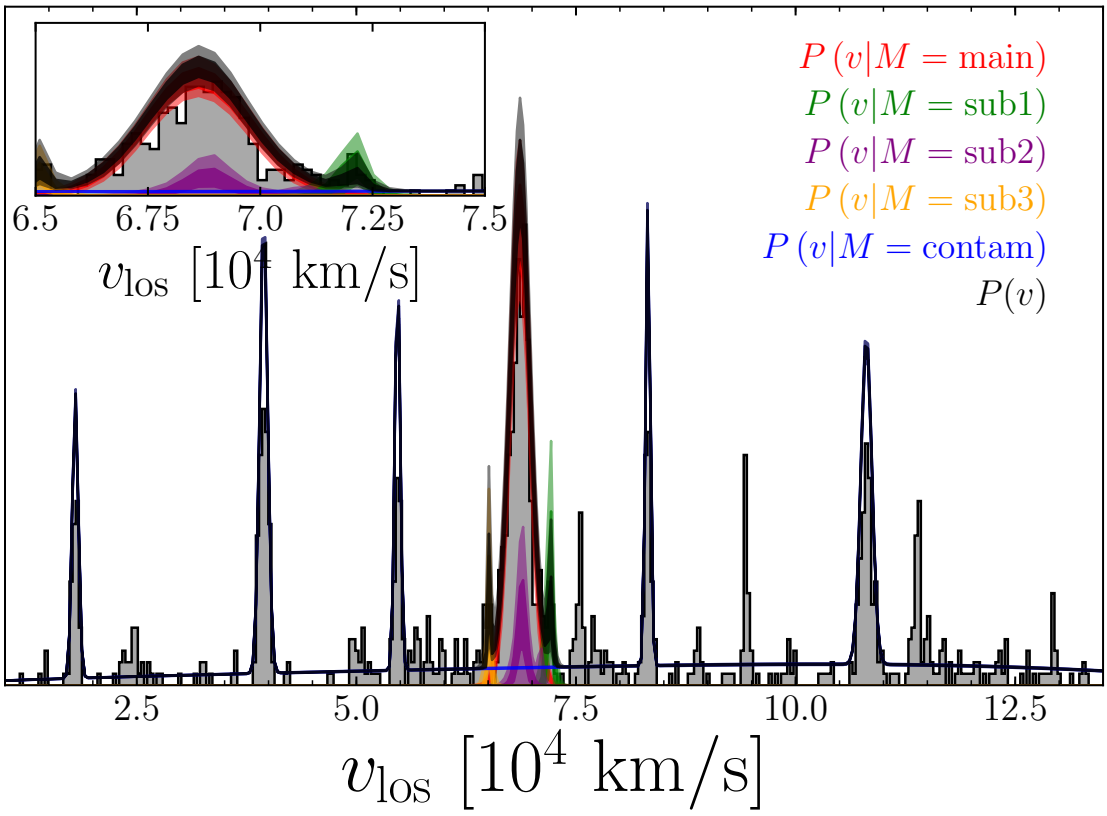

Figure 5.11: The velocity distribution profile. The grey histograms show the profile of the galaxy redshift sample (HeCS *plus* M2FS). The red curve is the profile for the main cluster population, the green, purple, orange, brown, and cyan are for the five subpopulations, and the blue is for the contamination population. The black curve is the sum of all of these profiles. The insert in the upper left corner shows the distribution zoomed-in on the region of redshift space around A267.

regions of these distributions show the inner 68% and 95% limits of the posterior distributions, respectively. The contamination model (blue) fits the five strongest sub peaks in this distribution with the gamma distribution doing a good job fitting the broad distribution of field galaxies. The insert in the upper left corner shows a zoom-in of the distribution around the mean redshift of A267 which shows in greater detail the velocity distributions of the main halo and substructures.

Comparison to other test for substructures

A commonly used statistical test for substructure is known as the Δ-statistic and was developed by [112]. The Δ-statistic looks for deviations in the local velocity from the global velocity of the cluster. First, for each galaxy one calculates the mean

local velocity $v_{\rm local}$ and local dispersion $\sigma_{\rm local}$ of the n nearest neighbors to the galaxy, where typically $n \sim \sqrt{N_{\rm tot}}$. This local velocity and dispersion is compared to the global velocity $\langle V \rangle_{267}$ and dispersion $\sigma_{\rm main}$ of the cluster quantified by

$$\delta_i^2 = (n+1)\left[\left(v_{\rm local} - \langle V \rangle_{267}\right)^2 + \left(\sigma_{\rm local} - \sigma_{\rm main}\right)^2\right]/\sigma_{\rm main}^2. \tag{5.17}$$

The full Δ-statistic is the sum of δ_i over all galaxies $N_{\rm tot}$.

The Δ-statistic is used to test whether or not there is considerable substructure within the cluster's environment. According to [112], for a relaxed cluster without signifiant substructure $\Delta \sim N_{\rm tot}$. Fig 5.12 shows a "Bubble Plot", a commonly used representation of the Δ-statistic. Each galaxy's "bubble" is sized by that galaxy's δ_i value given by Eq. 5.17. In each panel we show the progression of this plot for increasing number of subpopulations. We use the SUBMEM2 method of cluster member identification by applying a hard cut on the probability of membership to the main cluster $\mathcal{P}_{\rm main}$ and only show galaxies with $\mathcal{P}_{\rm main} > 0.9$. In the upper left corner we also show the ratio $\Delta/N_{\rm tot}$ in order to show a quantitative comparison between the two methods. As the number of substructures increases to $N_{\rm subs} = 3$ the ratio of $\Delta/N_{\rm tot}$ is slightly closer to one, yet it is still larger suggesting there may be additional substructures. This is also noticeable qualitatively by the overall decrease in size of the δ-bubbles. However, this ratio increases to its largest value for the $N_{\rm subs} = 4$ model suggesting the substructures identified by this model are likely not real as already discussed above. The main takeaway from this comparison is that our model is improving the Δ-statistic; however, it is limited by the uniform velocity dispersion profile which affects the identification of additional substructures for the $N_{\rm subs} = 4$ model.

We also make a qualitative comparison of the substructures identified with the $N_{\rm subs} = 3$ model to the binary tree algorithm of [117]. The sky-positions and phase-space diagrams for both sets of substructures are shown in Fig. 5.13. There is some agreement between the main cluster halos (red circles) and the purple substructure. The main cluster identified with the $N_{\rm subs} = 3$ model has a more concentrated distribution albeit with a broader velocity dispersion. The purple substructure identified by the binary tree method is more extended on the sky compared to a similar substructure identified by the $N_{\rm subs} = 3$ model. Interestingly, the cyan and orange substructures from the binary tree method do have some overlap with two of the substructures from the $N_{\rm subs} = 4$ model (see Fig. 5.8). We will revisit this comparison below while discussing the results of the model using a radial velocity dispersion profile as opposed to a uniform profile used here.

5.4.4 Dark Matter Halo Model

Thus far we have assumed that A267's velocity distribution is independent of radius. In the following subsections, we describe our procedure and results for fitting a dark matter halo model and corresponding velocity dispersion profile to the main cluster

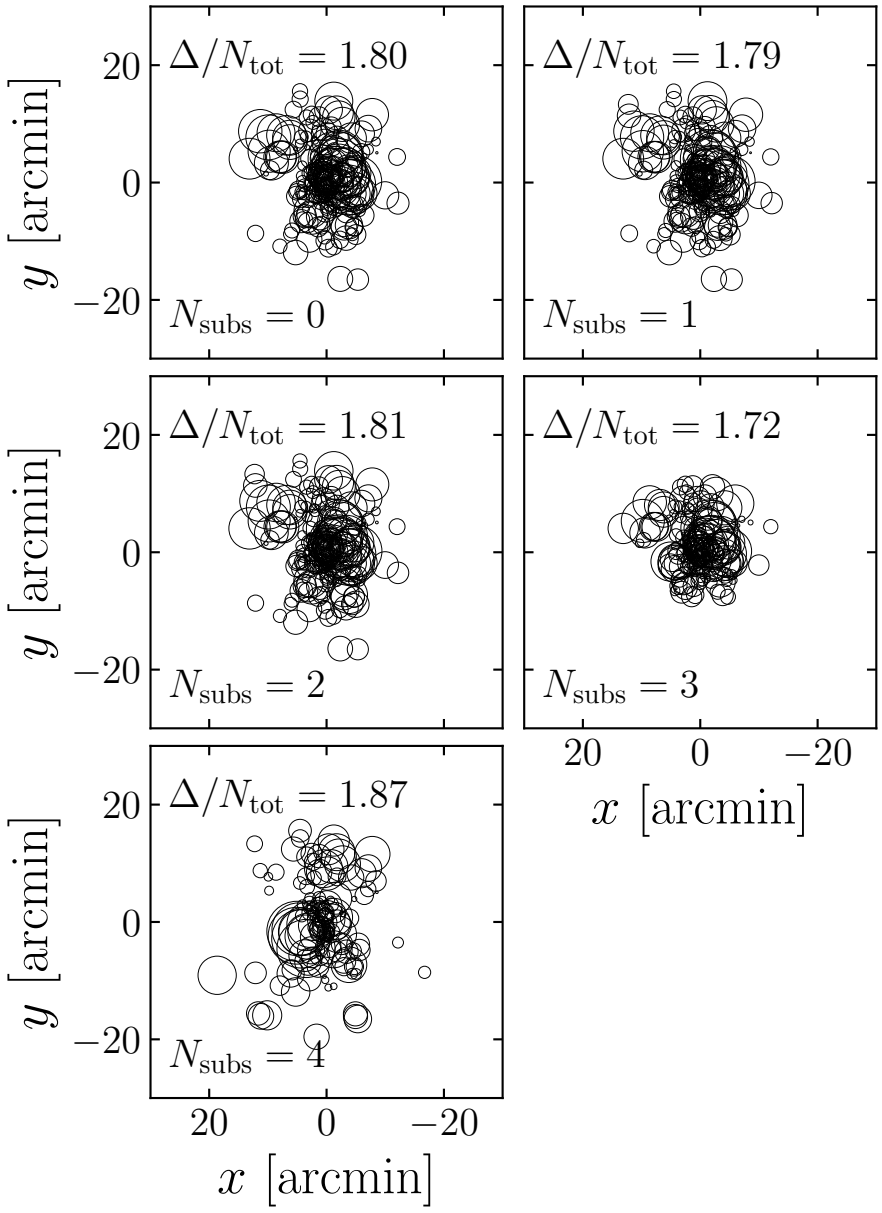

Figure 5.12: "Bubble plot" for the Δ-statistic. Each member galaxy is plotted with a circle whose size is proportional to δ_i (Eq. 5.17). Regions of large circles show areas with high probability of substructure. From left to right and top to bottom we increase the number of subpopulations which is given in the bottom left of each panel.

population of A267 ($\sigma_{\rm main}(\boldsymbol{r}) = \sigma_{\rm main}(r)$). We will first describe the theoretical framework for calculating the velocity dispersion profile as a proxy for cluster mass using the spherical Jeans equation, and then how we implement this technique for A267.

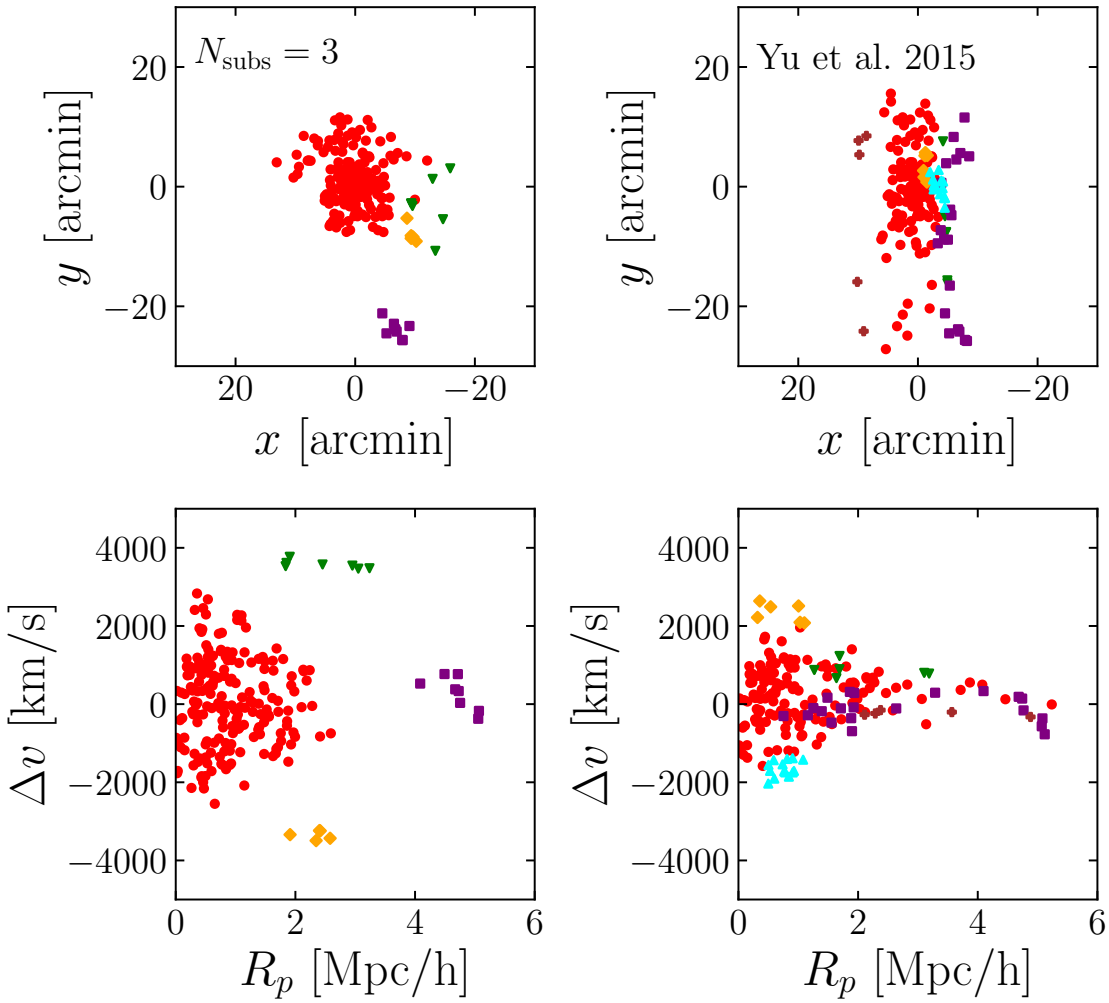

Figure 5.13: Comparison of the $N_{\rm subs} = 3$ model's substructures (*left*) with those identified by the binary tree method [117] (*right*). The top panels show the sky positions of the galaxies, while the bottom panels show the phase-space diagrams.

Jeans Analysis

In order to measure cluster mass, we assume that the galaxies within the main cluster population sample a single, pressure-supported halo that is dynamically relaxed and traces an underlying dark matter dominated gravitational potential. With the additional assumption of spherical symmetry, the mass profile, $M(r)$, of the dark matter halo relates to the galaxy distribution function via the Jeans equation:

$$\frac{1}{\nu}\frac{d}{dr}\left(\nu\sigma_r^2\right) + 2\frac{\beta\sigma_r^2}{r} = -\frac{GM(r)}{r^2} \tag{5.18}$$

where $\nu(r)$ is the three-dimensional galaxy number density, $\sigma_r^2(r)$ is the radial velocity dispersion, and $\beta \equiv 1 - \sigma_\theta^2/\sigma_r^2$ is the orbital anisotropy. Using cosmological dark matter only simulations, [258] showed that the velocity anisotropy for cluster-sized halos ($10^{14} - 10^{15} h^{-1} M_\odot$) is roughly constant with radius at a value $\beta \sim 0.4$. According to [98], for the special case of constant, non-zero anisotropy, the Jeans equation has the simple solution:

$$\nu\sigma_r^2 = Gr^{-2\beta} \int_r^\infty s^{2\beta-2} \nu(s) M(s) ds. \tag{5.19}$$

And by projecting along the line of sight, we can relate the mass profile to the observable profiles of the projected galaxy number density $I(R)$ and velocity dispersion profile $\sigma_p(R)$ by

$$\sigma_p^2(R) = \frac{2}{I(R)} \int_R^\infty \left(1 - \beta \frac{R^2}{r^2}\right) \frac{\nu\sigma_r^2 r}{\sqrt{r^2 - R^2}} dr. \tag{5.20}$$

And so, by plugging Eq. 5.19 into Eq. 5.20, specifying an underlying dark matter halo model $M(R)$, and adopting a profile for $I(R)$, we can determine the velocity dispersion and mass profiles of the cluster.

For simple anisotropy profiles, we can rewrite the combination of Eq. 5.19 and 5.20 as

$$\sigma_p^2(R) = \frac{2G}{I(R)} \int_R^\infty K\left(\frac{r}{R}, \frac{r_a}{R}\right) \nu(r) M(r) \frac{dr}{r} \tag{5.21}$$

where the kernel K depends on the choice of anisotropy, and are given for five anisotropy models in Appendix 2 of [259]. For A267, we used a constant anisotropy model. Although it is not the most physically motivated model, we use a Gaussian velocity distribution similar to [81] because it is easy to implement numerically and is a fairly good approximation for the observed profile of galaxy clusters.

Model Setup

The modeling setup for the radial velocity dispersion profile is similar to the uniform dispersion setup especially in terms of the contamination model and substructures. Similar to before we still assume the number density profile of the main cluster halo follows an NFW profile, but now there is an underlying dark matter halo which we also assume is NFW in shape. These profiles will have the same centers but could have different scale radii. For the dark matter halo, the dark matter NFW profile $\rho(r)$ is related to the mass profile by $M(R) = 4\pi \int_0^R r^2 \rho(r) dr$.

The dark matter halo is parameterized by two free parameters: $M_{200} = M(r_{200})$ and $c_{200} = r_{200}/r_s$, where r_{200} is the radius at which the mean density falls to 200 times the critical density of the universe. For the Jeans analysis, we parametrize the model by the velocity anisotropy index β which we assume to be uniform. The anisotropy index varies from $-\infty$ for completely tangential orbits to $+1$ for purely

Table 5.4: Free parameters and priors for dark matter halo model of A267. The first set of parameters (first 10 rows) are for the contamination model and are fit ahead of time using only obvious contamination galaxies. For the contamination model we use one uniform population and five NFW populations. The remaining free parameters are used to describe the kinematics of the cluster.

Parameter	Prior	Description
$\log_{10}\left[\Sigma_0/\text{radians}^{-2}\right]$	Uniform between -2 and 15	Light profile for uniform component of contamination model
$\log_{10} a$	Uniform between -6 and 6	Parameter of gamma distribution Eq. 5.14
$\log_{10} d$	Uniform between -6 and 1	Parameter of gamma distribution Eq. 5.14
$\log_{10} p$	Uniform between -6 and 6	Parameter of gamma distribution Eq. 5.14
$\log_{10}\left[r_{s,\text{contam},i}/R_{\max}\right]$	Uniform between -3 and 0	NFW scale radius of i-th contamination population
$\log_{10}\left[r_{c,\text{contam},i}/R_{\max}\right]$	Uniform between -3 and 0	Radial offset of center of i-th contamination population
$\theta_{\text{c,contam,i}}$	Uniform between 0 and 2π	Angular location of center of i-th contamination population
$z_{\text{contam,i}}$	see Eq. 5.15	Redshift of i-th contamination population
$\log_{10}\left(\sigma_{\text{contam},i}/\text{km s}^{-1}\right)$	Uniform between 0 and 3.5	Velocity dispersion of i-th contamination population
$f_{\text{contam},i}$	Uniform between 0 and 1	Number fraction hyperparameters for contamination model
$\log_{10}\left[\Sigma_{rs}/\text{radians}^{-2}\right]$	Uniform between -1 and 1	Rescale uniform component of contamination model
f_{contam}	Uniform between 0 and 1	Number fraction of all contamination population
$\log_{10}\left[r_{s,\text{main}}/R_{\max}\right]$	Uniform between -3 and 0	NFW scale radius of main halo light profile
$\log_{10}\left[r_{c,\text{main}}/R_{\max}\right]$	Uniform between -3 and 0	Radial offset of center of main halo
$\theta_{c,\text{main}}$	Uniform between 0 and 2π	Angular location of center of main halo
z_{main}	Uniform between 0.22 and 0.245	Redshift of main halo $z_{\text{main}} = \langle V\rangle_{\text{main}}/c$
$\log_{10}[M_{200}/M_\odot\ h^{-1}]$	Uniform between 13 and 16	Mass of cluster interior to r_{200}
$\log_{10}[c_{200}]$	Uniform between 0 and 2	Concentration of dark matter halo: $c_{200} = r_{200}/r_{s,DM}$
$-\log_{10}[1-\beta]$	Uniform between -1 and $+1$	Anisotropy index β of velocity dispersion profile
$\log_{10}\left[r_{s,\text{sub},i}/R_{\max}\right]$	Uniform between -3 and 0	NFW scale radius of i-th substructure light profile
$\log_{10}\left[r_{c,\text{sub},i}/R_{\max}\right]$	Uniform between -3 and 0	Radial offset of center of i-th substructure
$\theta_{c,\text{sub},i}$	Uniform between 0 and 2π	Angular location of center of i-th substructure
$\langle V\rangle_{\text{sub},i}$	See Eq. 5.12	Velocity of the i-th substructure
$\log_{10}[\sigma_{\text{sub},i}/\text{km s}^{-1}]$	Uniform between 0 and 3	Velocity dispersion of i-th substructure
f_i	Uniform between 0 and 1	Number fraction hyperparameter

radial orbits. Because of this large parameter space we re-parameterize the anisotropy index so that $\beta' = -\log_{10}(1-\beta)$ which we constrain to vary between $-1 < \beta' < +1$.

All together this model will include 2 free parameters for the contamination model (in addition to the pre-fit contamination model described in §5.4.2), 7 free parameters for the main cluster halo and 6 free parameters for each substructure. All free parameters and the adopted priors are listed in Table 5.4. Similar to before the transformation from the number fraction hyperparamters to the number fractions of each population is given by Eq. 5.16.

Results for A267

The red curves in Fig. 5.7 shows the progression of model parameters as the number of substructers is increased from $N_{\rm subs} = 0$ to $N_{\rm subs} = 4$. There is a similar behavior for this set of modeling compared to the uniform velocity dispersion models. From $N_{\rm subs} = 0$ to $N_{\rm subs} = 1$ the Bayes factor (top most panel) increases considerably which indicates that the $N_{\rm subs} = 1$ model is favored between the two. This trend continues with the $N_{\rm subs} = 2$ model, and although the Bayes factor is not quite as large for the $N_{\rm subs} = 3$ model, it still exceeds 5 providing strong evidence in favor of this model over models with fewer substructures. Unlike the uniform velocity dispersion models, which do not favor the $N_{\rm subs} = 4$ model, there is strong evidence in support of the $N_{\rm subs} = 4$ model with a dark matter halo.

The remainder of the parameters follow a similar trend to the uniform dispersion analysis except for the $N_{\rm subs} = 4$ models. In the dark matter halo model when $N_{\rm subs} = 4$, the results are more consistent with the results from the models with fewer substructures. Furthermore, the mass of the cluster (2nd from the bottom panel) decreases continuously and at a relatively steady rate as the number of substructures increase. The velocity offset from the BCG of A267 to mean redshift of the cluster remains roughly constant at ~ 150 km/s; however, the mean velocity of the cluster decreases slightly for the $N_{\rm subs} = 4$ model, mainly due to the fact that the mean velocity of the additional substructure identified populates the high velocity tail of the cluster's distribution.

Fig. 5.14 shows the progression of substructure membership for increasing number of substructures. This figure is similar to Fig. 5.8 except for the choice of velocity dispersion profile. Both dispersion profiles yield two similar substructures, the green and purple populations seen in the $N_{\rm subs} = 2$ panels of both figures. One signifiant difference is that, with the radial dispersion profile used here, there are now main halo members beyond 4 Mpc/h unlike the uniform dispersion models. In the $N_{\rm subs} = 3$ and 4 panels, there is one fewer substructure identified then the model allows. This is due to the fact that posterior distribution for the additional substructure is highly multimodal and so the procedure we use to identify cluster members essential finds no members to these populations. If instead of sampling the posterior, we used just one sample, then there would be the proper number of substructures in all panels of Fig. 5.14.

Fig. 5.15 shows the 1D and 2D posterior distributions for three parameters describing the subpopulations in the $N_{\rm subs} = 3$ (*left*) and $N_{\rm subs} = 4$ models (*right*). The colors of each posterior correspond to the colors of the substructures shown in Fig. 5.14. The purple and yellow posteriors in the $N_{\rm subs} = 3$ and 4 panels, respectively, are unconstrained which is why there are no member galaxies identified to these substructures in Fig. 5.14. This multimodal behavior is typically indicative of at least one additional substructure that the model does not have the flexibility to fit because the number of substructures are fixed for each model. Nevertheless, the main goal of this modeling framework is to measure cluster masses while marginalizing over potential

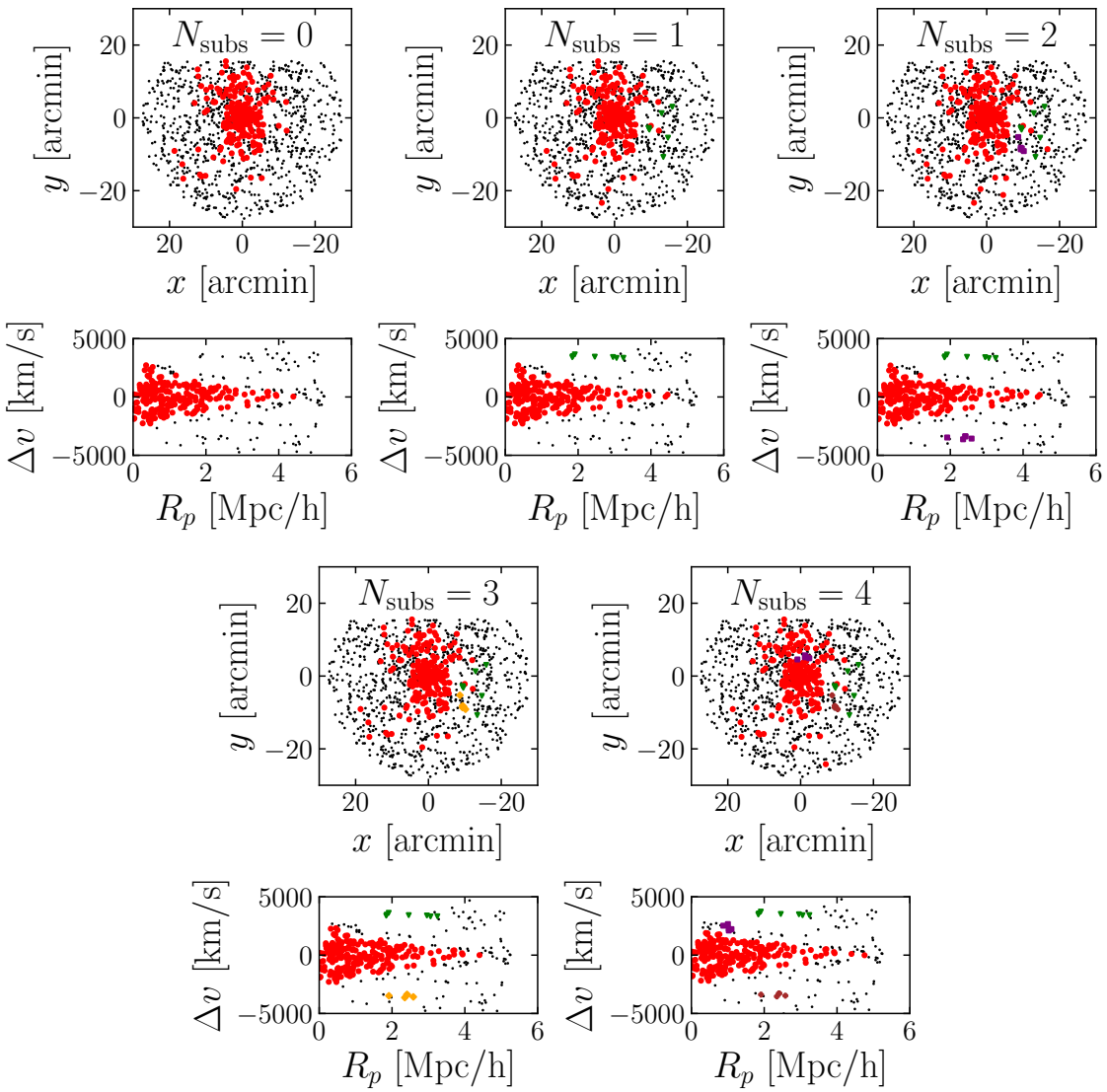

Figure 5.14: Same as Fig. 5.8 except now for the dark matter halo models.

Table 5.5: Mean values and standard deviations of 1D posterior PDFs for A267 free parameters in the dark matter halo $N_{\rm subs} = 4$ model.

	r_s/kpc h^{-1}	α_{2000}/deg	δ_{2000}/deg	z	$\sigma_{\rm disp}$/km s^{-1}	$M_{200}/10^{14} M_\odot\ h^{-1}$	$\log_{10} c_{200}$	β	$f_{\rm mem}$	$N_{\rm mem}$
Main	388 ± 87	28.174 ± 0.001	0.999 ± 0.001	0.2288 ± 0.0003		7.0 ± 1.3	0.71 ± 0.38	-1.3 ± 2.1	0.192 ± 0.013	194 ± 24
Sub1	790 ± 703	27.974 ± 0.047	0.949 ± 0.061	0.2404 ± 0.0003	188 ± 72				0.013 ± 0.004	8 ± 3
Sub2	110 ± 202	28.150 ± 0.016	1.066 ± 0.028	0.2363 ± 0.0020	235 ± 97				0.009 ± 0.004	5 ± 2
Sub3	198 ± 404	28.115 ± 0.204	0.865 ± 0.204	0.2241 ± 0.0045	339 ± 224				0.011 ± 0.007	4 ± 3
Sub4	34 ± 43	28.016 ± 0.003	0.859 ± 0.003	0.2173 ± 0.0002	100 ± 36				0.006 ± 0.002	5 ± 0

substructure which is still achieved even though these parameters are unconstrained.

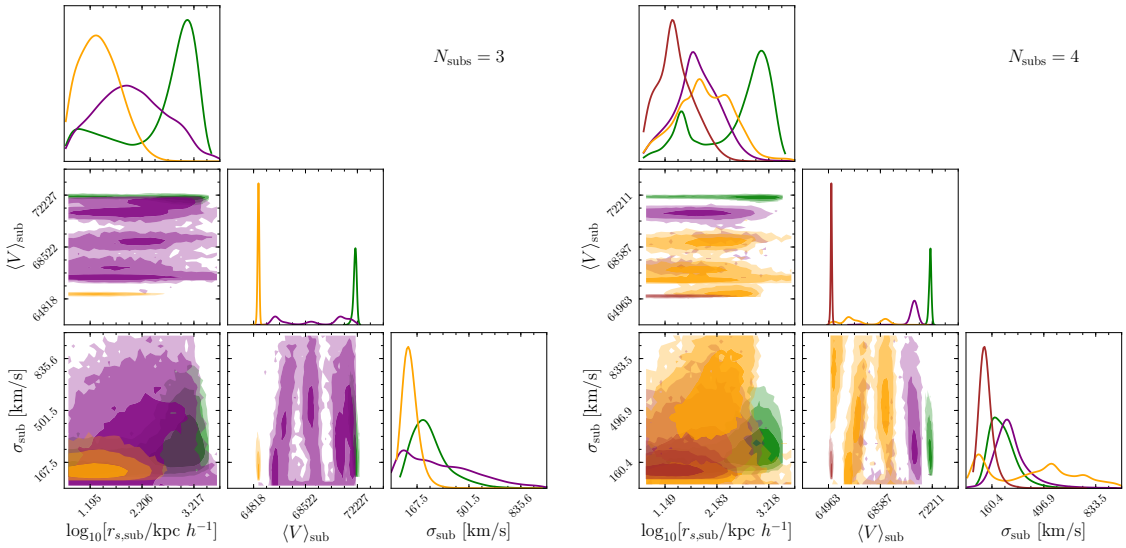

Figure 5.15: 2D and 1D posterior distributions for subpopulations inferred from the $N_{\rm subs} = 3$ (*left*) and $N_{\rm subs} = 4$ (*right*) models. The colors of each distribution correlate to the colors of the substructures shown in Fig. 5.14.

Fig. 5.16 shows the 1D and 2D posterior distributions for the parameters that define the main cluster population in the $N_{\rm subs} = 4$ model. The main cluster halo parameters are all reasonably well constrained. Table 5.5 lists a summary of the results for these parameters as well as the parameters describing the substructures. It is clear from this table that Sub3 (the yellow distributions in Fig. 5.15) is largely unconstrained. Furthermore, as is the case for the uniform dispersion models, the estimates on the NFW scale radii of the substructures' light profiles is largely uncertain due to the few number of highly probable members to these populations.

In Fig. 5.16, there is a strong $c_{200} - \beta$ degeneracy, and a weaker $M_{200} - c_{200}$ degeneracy. The $M_{200} - c_{200}$ relation is a usefully cosmological scaling relation that exhibits relatively low scatter. In Fig. 5.17 we zoom-in on the $M_{200} - c_{200}$ panel and compare the results from the dark matter halo models with predictions of the $M_{200} - c_{200}$ relation derived from N-body simulations [260]. Even though the mass of the dark matter halo decreases with increasing number of subpopulations and the posterior for c_{200} is relatively less constrained, we still recover a mean concentration in accordance with [260].

Fig. 5.18 shows the velocity dispersion profile $\sigma_{\rm main}(r)$ inferred from the Jeans analysis of A267. The dark and light shaded regions show the 68% and 95% confidence intervals of the posterior PDFs, respectively, while the black curve show the median posterior velocity dispersion profile. In red we compare the fit velocity dispersion profile to the binned velocity dispersion calculated with highly probable member galaxies ($\mathcal{P}_{\rm main} > 0.9$). In the infall region of A267 ($R_p \gtrsim 2$ Mpc/h), the fit dispersion profile exceeds the binned data. This is likely due to an inhomogeneity of the

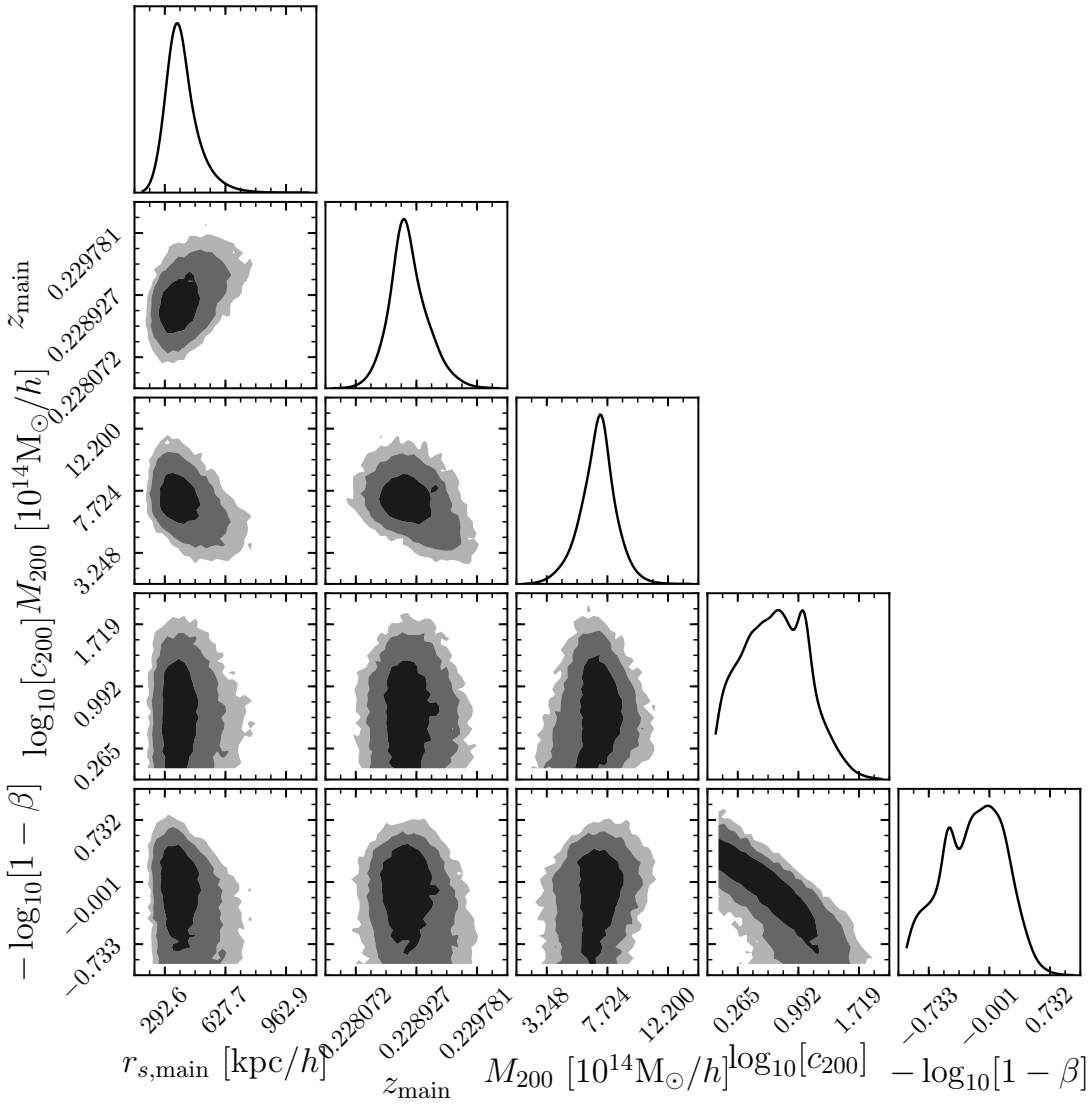

Figure 5.16: Posterior PDFs of parameters specifying the dark matter halo of A267, using the Jeans Equation analysis described in §5.4.4. We show the scale radius of the NFW light profile $r_{s,\mathrm{main}}$, mean cluster redshift z_{main}, virial mass and concentration of the dark matter halo M_{200} and c_{200}, and velocity anisotropy β. We also show the 1, 2, and 3σ contours for the 2D posteriors.

galaxy distribution in the cluster outskirts [262, 263]. The assumptions made when conducting a Jeans analysis breaks down at these radii thus yielding a poor fit.

In order to qualitatively show any potential bias in calculating a binned velocity dispersion, we check the binning procedure using mock data generated from halo models sampled from the posterior. At each sample of the posterior, a catalog of

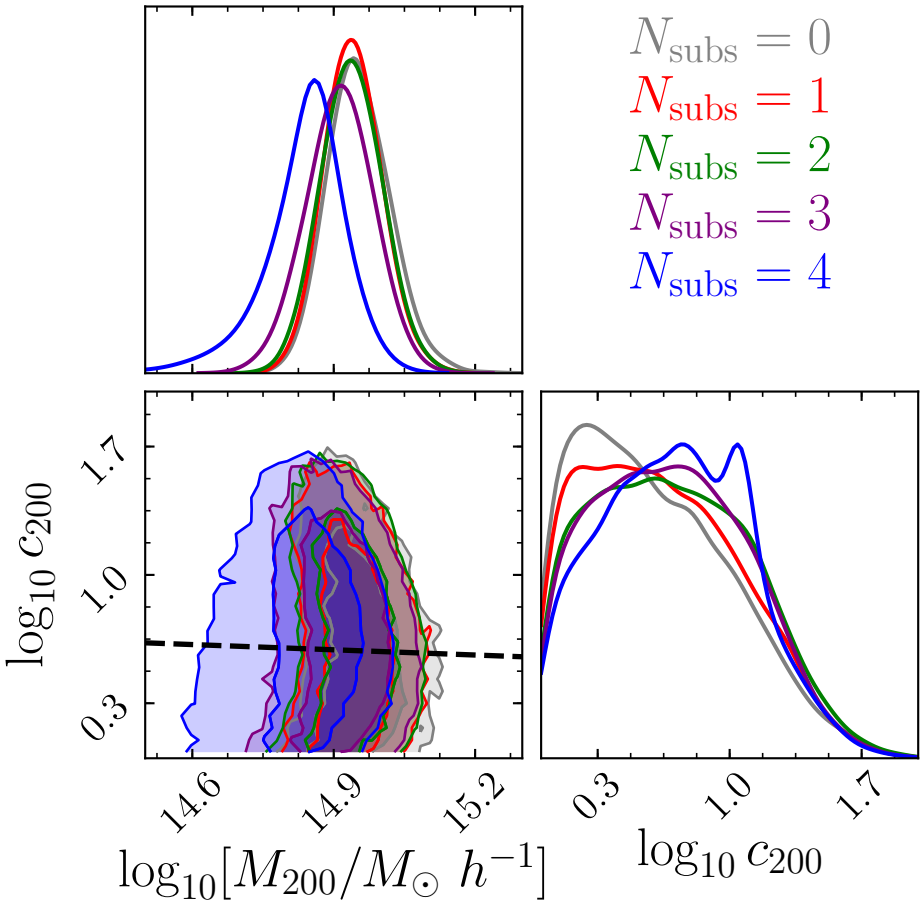

Figure 5.17: Mass-concentration posteriors from the dark matter halo models. Each color represents a model that allows for a different number of subpopulations. The dashed black curve shows the $M_{200} - c_{200}$ relation from [260, 261].

galaxies is generated. These galaxies are then binned and a velocity dispersion is calculated in the same way as the real data. The blue points show the results of this posterior predictive check. The error bars are calculated from the scatter of the velocity dispersion within each bin across the sampled posterior. The posterior predictive check shows almost no bias in the binned dispersion; however, there is considerably larger scatter within each bin than would be expected from the 1σ and 2σ widths of the posterior.

Fig. 5.19 shows the mass profile of the dark matter halo for A267. Like previous plots, the dark and light regions show the 68% and 95% confidence intervals of the PDFs, and the solid black curve shows the median posterior. For comparison we include previous mass measurements of A267 from a variety of different techniques: in green the weak lensing mass $M_{200}^{\rm WL}$ [264], in red and purple the caustic mass $M_{200}^{\rm Caustic}$

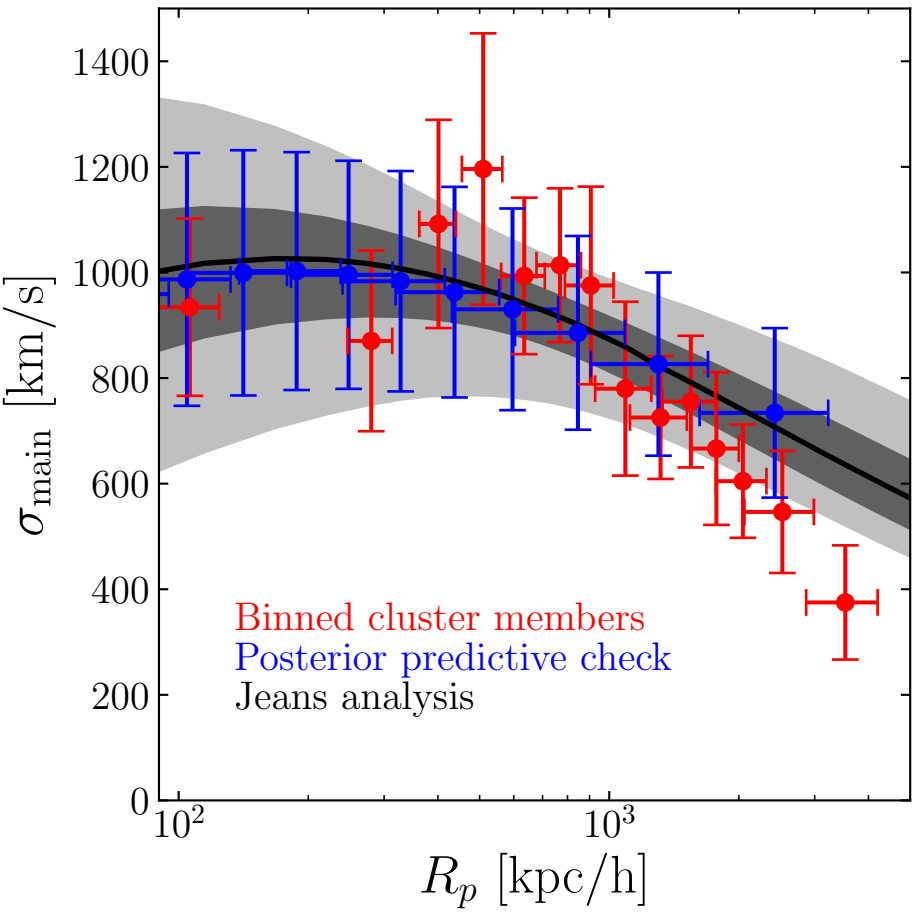

Figure 5.18: Line-of-sight velocity dispersion profile for A267 with the $N_{\rm subs} = 4$ model. The dark and lighter regions correspond to 1σ and 2σ of the posterior, respectively. The solid black line is the median posterior curve. The red points show the velocity dispersion of binned member galaxies. The blue points show the binned velocity dispersion calculated with simulated data generated from sampling the posterior distribution.

and viral mass calculated with velocity dispersion of cluster members $M_{vir}^{\rm Dispersion}$, respectively [89], and in blue we show the X-ray derived mass M_{500}^{X} [265]. Our results are consistent with M_{500}^{X}, $M_{200}^{\rm Caustic}$, and $M_{200}^{\rm WL}$, but we measure a significantly smaller mass than $M_{vir}^{\rm Dispersion}$ because the mass estimate derived from the velocity dispersion is more susceptible to substructure. Also shown in Fig. 5.19 are the median posterior curves of the mass profile from the models with fewer substructures. For A267 as the number of substructures increases the mass of the cluster decreases.

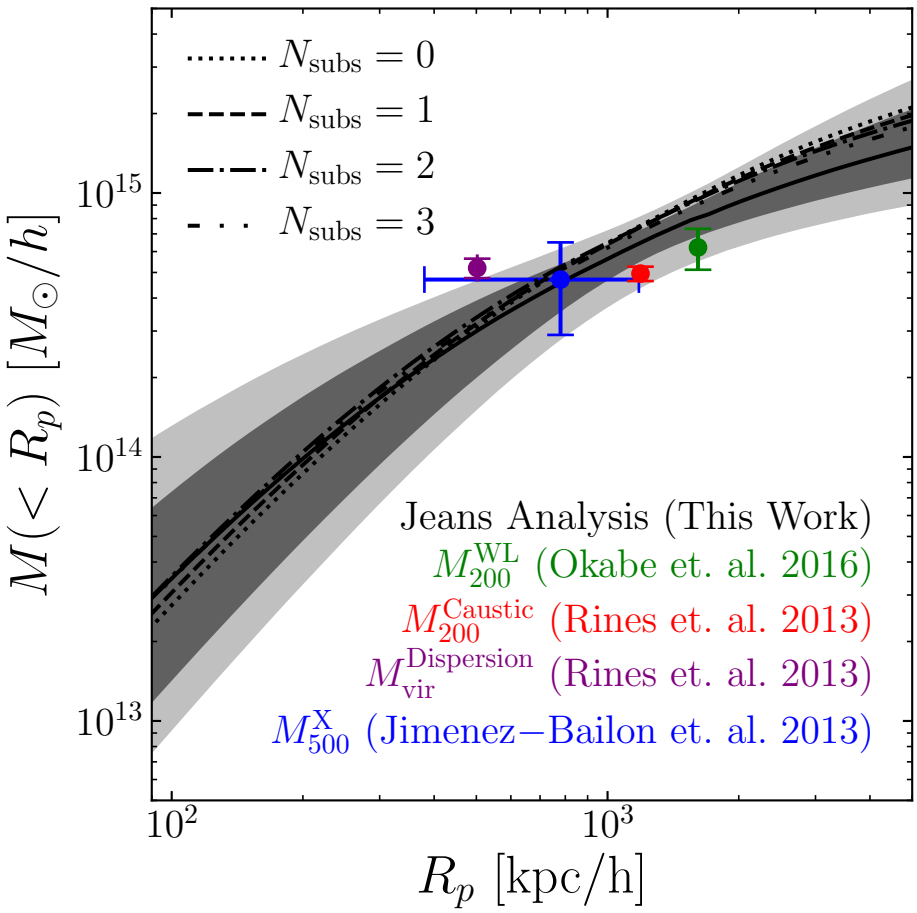

Figure 5.19: Projected radial mass profile for A267 with the $N_{\rm subs} = 4$ model. The darker and lighter regions correspond to 1σ and 2σ of the posteriors, respectively. The solid black line is the median posterior curve. The colored points show 4 different mass estimates of A267 from weak lensing [264, green], caustic [89, red], velocity dispersion [89, purple], and X-ray [265, blue]. Also shown, as the non solid black curves, are the mass profiles for the models with fewer substructures.

5.5 Conclusions

We have developed a muli-population mixture model in order to simultaneously model the internal kinematics and substructure of A267. We included in this model the ability to fit $N_{\rm subs}$ subpopulations, as well as cluster parameters such as NFW scale radius, mean cluster redshift and velocity dispersion. Although we did not implement an overall cluster rotation turn in the modeling here, such a term can be incorporated in the velocity distribution function in the future. We embedded this model in a full Bayesian framework, such that we quantify posteriors of all free parameters as well as parameter covariances. In the application of this model to A267, we considered two

alternative models that differ in how the cluster velocity dispersion is treated. We first assumed a simple uniform velocity dispersion profile to analyze the dependence of the internal kinematics on the arbitrary choice of the number of subpopulations. We then solved the spherical Jeans Equation in order to fit a dark matter halo to A267, thus inferring the enclosed mass profile while allowing the velocity dispersion to vary with radius.

Prior to the work with A267, we tested the uniform velocity dispersion model with mock redshift observations from the dark matter only simulation MultiDark (MDPL2, [245]). This allowed a comparison of the identified 2D substructures from this model with the true 3D substructures within the cluster environment known from the simulation. By comparing galaxies identified by the models as highly probable members to the 2D substructures, we report that 53% of the 2D substructures have at least one member galaxy that is also a member of a true 3D substructure. Furthermore, 51% of these 2D substructures have $f_{3D} > 0.79$ (the largest fraction of the total number of members of a 2D substructure that are also members of a single 3D substructure). Both these values are on par with the current most robust cluster substructure identification algorithm [117, 118]; furthermore, our modeling framework simultaneously fits light and mass profiles of the cluster which is lacking in the caustic methods.

The main focus of this modeling framework is to estimate more accurate cluster masses while accounting for the potential of substructure. To this end we showed with the mock observations from MDPL2 that there is significantly less scatter in the $M_{200c}-\sigma$ power-law relation when accounting for 3 additional substructures compared to a similar model that does not account for substructure (Fig. 5.5). Furthermore, the majority of the decrease in scatter can be attribute to the clusters that exhibit significant amounts of true 3D substructures.

For A267, we investigated the dependence of the internal kinematics on the number of subpopulations. We showed that as the number of subpopulations increases, the inferred scale radius and velocity dispersion of the cluster both decrease, with significant consequences for cluster mass estimates (Fig. 5.7). For the uniform velocity dispersion model the Bayes factor shows the largest evidence in favor of the $N_{\rm subs} = 3$ model; however, for the dark matter set of models $N_{\rm subs} = 4$ is most favored. Comparing the preferred dark matter model $N_{\rm subs} = 4$ to a dark matter model without substructure, we infer a dynamical mass that is $\sim 22\%$ smaller than the model that neglects substructures. Furthermore, we found that the mean redshift of the cluster is also sensitive to the presence and treatment of subpopulations. This demonstrates how accounting for substructure can have significant implications for detecting "wobble" of the BCG around the cluster core, as predicted by self-interacting dark matter models [241, 240].

We compared the substructure identification of this model to two other substructure methods: the Dressler-Shectman Δ-test [112] and the binary tree caustic algorithm [117]. We showed that the Δ-statistic decreased as increased numbers of substructures identified by our model were removed from the cluster environment

which is an indication that these substructures influence the Δ-statistic (Fig. 5.12). We also made a qualitative comparison between the substructures identified in the $N_{\rm subs} = 3$ uniform velocity dispersion model with the substructures identified by the binary tree algorithm (Fig. 5.13). At least one substructure in both methods overlap with each other; furthermore, there is also a correlation with one of the substructures identified in the $N_{\rm subs} = 4$ dark matter model.

Most previous work in regards to substructure has focused on substructure detection; in other words, they are formulated to state how likely a cluster exhibits substructure. More recent work has focused on algorithms for identifying they substructures as well as the galaxy members; however, these methods have focused on a binary assignment to each galaxy (either a member or not). Here we take the next step forward: first our algorithm provides the statistical framework to assign a probability of membership to the cluster and each subpopulation within the cluster. Furthermore, unlike previous substructure methods, this model simultaneously fits the light and dark matter profiles of the cluster while accounting for these substructures. Although the fitting of the model is inefficient for large numbers of substructures, the advantages of this modeling framework is a step in the right direction in regards to dynamical mass estimators and substructure.

Finally we embedded our mixture model within a dynamical model that relates the dark matter halo potential to cluster kinematics. From this analysis, allowing for up to $N_{\rm subs} = 4$ sub-populations, we infer for A267 a halo mass $M_{200} = 7.0 \pm 1.3 \times 10^{14} M_{\odot}/h$ and concentration $\log_{10} c_{200} = 0.71 \pm 0.38$ with velocity dispersion anisotropy $\beta = -1.3 \pm 2.1$. The mass and concentration posteriors are consistent with the well established $M_{200} - c_{200}$ relation derived from N-body simulations (Fig. 5.17, [260]). The corresponding mass profile (Figure 5.19) is in good agreement with previously measured masses of A267 from X-ray and weak-lensing measurements [265, 257], as well as the dynamical estimate based on the caustic technique [89]. Interestingly, the dynamical mass previously estimated directly from the galaxy velocity dispersion (assuming no sub-substructure; [89]) is larger than we infer when we allow for $N_{\rm subs} = 4$ sub-populations, but in better agreement with the mass profile we obtain if we restrict our Jeans model to $N_{\rm subs} = 0$ sub-populations.

Although, the largest number of substructures we fit are $N_{\rm subs} = 4$, in the dark matter halo models there is evidence from the posterior distributions that there could be at least one other substructure (Fig. 5.15). The multimodal behavior of the posterior distributions for the set of parameters describing one of the subpopulations suggests that there could be an additional substructure still unaccounted for. Unfortunately, due to the inefficiency of the sampling of MultiNest for high dimensionality parameter spaces (required over 10^9 likelihood evaluations for $N_{\rm subs} = 4$ model), it is computational unfeasible to fit an $N_{\rm subs} = 5$ model with MultiNest and the current modeling framework. However, recent work has been done to develop sampling algorithms that are ideal for problems like this where the number of populations is a free parameter in the model [266]. Future work should be done to investigate the efficacy

of using a diffusive sampling algorithm to sample the posterior distributions instead of MultiNest.

In summary, we have developed a dynamical mixture model to account for substructure within galaxy clusters. Our first application, to Abell 267, illustrates the sensitivity of important dynamical results—mean redshift, scale radius, internal velocity dispersion, and dynamical mass—to the presence and modeling of substructure. This work adds to mounting evidence that, given the widespread interest in using galaxy clusters for both cosmology and tests of dark matter models, it is necessary to account for such substructure when modeling galaxy kinematic data. In future work, we will extend this analysis to other galaxy clusters with similarly large and high-quality data sets.

Acknowledgements

We thank Margaret Geller for her comments and suggestions that greatly improved the quality of this paper. We thank Nobu Okabe for generously providing the weak lensing map. We also thank Kaustuv Basu and Martin Sommer for reducing the radio observations of A267. We'd like to thank Michelle Ntampaka and Matt Ho for generously helping to generate mock observations from the MultiDark simulation. We thank the anonymous referee for their constructive and thoughtful comments that significantly improved the quality of this work. M.G.W. is supported by National Science Foundation grants AST-1313045, AST-1412999 and AST-1813881. M.M. is supported by NSF grant AST-1312997 and AST-1815403. E.W.O. is supported by NSF grant AST-1313006 and AST-1815767.

Chapter 6

Conclusions and Future Outlook

Clusters of galaxies are the most massive gravitationally bound structures in the Universe. Because of their large size and high mass, galaxy clusters live on the cusp between gravitational attraction dominated by dark matter and cosmic expansion. Therefore, the properties of galaxy clusters are used as cosmological probes in order to gain insights into dark matter and dark energy. As cosmological probes, clusters of galaxies populate the high mass tail of the halo mass function which is particularly sensitive to many cosmological parameters [54, 52]. Therefore, their success in cosmology is directly tied to the accuracy of halo mass estimates derived from X-ray luminosity, lensing effects, and dynamical analyses. Of these three mass estimators, dynamical masses provide a unique and detailed glimpse into the mass profile of individual halos; however, the complex formation histories of galaxy clusters muddy the water in terms of the accuracy of the estimated masses. Furthermore, dynamical analyses are limited by the number of galaxies with spectroscopically measured redshifts because spectroscopic follow-up observations are relatively time expensive. This thesis aimed to to take a few steps in the right direction to solve some of these issues in order to further cement the importance of galaxy clusters as cosmological probes.

In the first part of the thesis, I detailed an observational program for observing galaxies along the line-of-sight to galaxy clusters using the Michigan/Magellan Fiber System (M2FS) on the 6.5m Clay/Magellan Telescope at Las Campanas Observatory in Chile. Like other multi-object spectrographs, M2FS provides the instrumentation to efficiently observe hundreds of galaxies at the same time. As a proof of concept, I observed one pointing to the rich cluster Abell 267 (A267, $z \sim 0.23$) using only six exposures of 15 minutes in length. I then obtained time to conduct a much larger program to observe MACSJ0429-0253 (M0429, $z \sim 0.399$). I aimed to observe a total of six separate fields ($\sim$ 3 hours per field) in order to obtain upwards of 1400 galaxy spectra ($\sim$ 500 of which are cluster members) as well as a couple dozen strongly lensed background galaxies. Unfortunately, even though this program was not a complete success, I still obtained over 300 unique galaxy spectra with $\sim$ 100 cluster members.

Nevertheless, the successes and failures of this program taught me how a similar program should be better conducted in the future.

Also part of this thesis, I developed a data reduction pipeline of raw images from M2FS. Although the pipeline works well, the observations of M0429 showed that there is still much work that needs to be done in order to improve the pipeline. First off, because I targeted for observation quiescent galaxies that live along the red-sequence the portion of the spectrum most useful for spectral fitting covers the rest-frame 4000Å break. For clusters with redshifts $z \gtrsim 0.35$, this coverage is redshifted to a wavelength range that includes a large number of atmospheric emission lines. The currently used sky-subtraction procedure implemented in the data reduction pipeline proved to be inadequate at removing these sky lines from the spectra. Therefore, I had to mask out the regions where the residuals of the sky lines dominated, which drastically decreased the number of pixels in each spectrum. In the future, a better prescription for sky-subtraction should be implemented that would remove these sky lines so that the entire spectrum can be used for spectral fitting. For the reduction of spectra of high redshift galaxies, the DEEP2 team uses B-splines ("basis splines") to model the night sky emission and then remove it from their spectra [267]. The DEEP2 spectra are from a multi-slit spectrograph, so work would need to be done to implement a similar procedure with fiber spectra, which do no so easily allow for separating sky from target spectra.

The observations of M0429 provided multiple spectra for some galaxies. Although this decreased the total number of galaxies observed, the repeat observations provided an opportunity to quantify the precision of stellar population parameters estimated from the spectral fits. This analysis showed that the statistical errors estimated from the widths of each parameter's posterior distribution underestimates the true uncertainty. This is most notable in the precision of the spectroscopic redshift estimates; therefore, another improvement in the data reduction pipeline needs to focus on a more accurate estimation of the wavelength solution for the detector. Furthermore, the error in the wavelength solution needs to be incorporated into the spectral fitting model in the future. As of now, the model assumes that the wavelength of each pixel determined from the data reduction pipeline has no uncertainty which results in underestimates on the error in the redshift estimate. Future work should be made to both improve the accuracy of the wavelength solution as well as incorporate any uncertainties in this solution into the spectral fitting model.

The second part of my thesis focused on the estimation of stellar population parameters derived from fitting the observed galaxy spectra. The model is similar to previously published full spectrum population synthesis models in the sense that it utilized a set of precomputed synthetic spectra; however, I implemented the model in a Bayesian framework allowing for the quantification of the posterior distributions of each parameter along with their associated covariances. I first developed the spectral fitting model and tested it with mock spectra which displayed the ability of the model to recover the input parameters of the mock spectra over a range of signal-

to-noise. Using previously measured and fit spectroscopic observations of the galaxy cluster Abell 496 (A496), I showed that parameter estimates from this new model are consistent with estimates from other models. Some parameter estimates do exhibit a roughly constant offset compared to previous measurements from the same spectrum which is likely due to differences in synthetical spectra library utilized by each model. Lastly, I fit the A267 and M0429 spectra and summarized the results from these spectral fits.

Although I have shown in this thesis that the methods and techniques developed for the integrated light model reproduces input parameters of mock spectra, agrees well with parameter estimates derived from other models (albeit with some offsets attributable to variations in synthetic libraries), and qualitatively fits the observed spectra well, there is still plenty of room for improvement. First, the model currently assumes a simple stellar population (i.e. all stars in the population are the same age and metallicity); however, the true stellar population, even in the central regions of quiescent galaxies, is likely composed of a more complex star formation history which is neglected in the current model. Developing a framework that allows for a more complex stellar population would improve the inferences from the model and allow for a marginalization over some of these complex parameters which are difficult to model. The most recent full spectrum fitting stellar population models still assume a simple stellar population; however, recent work in fitting SEDs has shown promise in regards to including more complex star formation histories as well as other sources such as AGN or active star formation (see [180] for example). Future work should be done to extend these SED modeling features to full spectrum fitting models.

Currently, the modeling framework detailed in this thesis relies on a library of precomputed synthetic galaxy spectra situated on an evenly spaced grid in stellar population parameter space. When the model is fit a galaxy spectra must be generated by interpolating between grid points within the library. Not only is this relatively computationally expensive it can also lead to biases in the parameters estimated from the model. Therefore, future work should be done to develop a synthetic galaxy spectra emulator. A neural network could be trained with the synthetic spectra such that after the training is complete, the network would be able to generate a synthetic spectra given a set of input parameters describing the stellar population. This network would be pre-fit and then incorporated into the modeling framework detailed in this thesis in lieu of the synthetic spectral library. This type of emulator would drastically decrease computation time necessary for each likelihood evaluation.

The Bayesian approach utilized here to fit galaxy spectra is useful because of its ability to sample each parameter's posterior distribution and marginalize over any nuisance parameters incorporated into the model; however, the sampling of the posterior is slow, requiring large amounts of computational resources when fitting a large dataset of observations. Because dynamical analyses require thousands of galaxies with spectroscopical measured redshifts, many spectral fitting models merely fit the redshift and ignore the wealth of other information that is encoded in each galaxy

spectrum. This model is developed to extract this extra information; unfortunately, fitting thousands of galaxies in this way is unfeasible without large dedicated computational resources. Therefore, a new approach utilizing deep learning techniques can be developed to quickly and efficiently fit thousands of galaxy spectra without sacrificing the extraction of stellar population parameters. In the past few years there has been much work done with fitting stellar spectra with deep convolutional neural networks [268] and autoencoders [269, 270], so an extension of these models can be made with galaxy spectral. The models would be trained using synthetic galaxy spectra and would be able to predict stellar population parameters from observed galaxy spectra.

The third and final part of my thesis focused on developing a flexible model to estimate galaxy cluster dynamical masses while marginalizing over substructure. With the plethora of multi-object spectrographs installed on some of the largest telescopes in the world, it is relatively easy to obtain thousands of galaxy spectra which produce large spectroscopic redshift catalogs ideal for detailed kinematic analyses. These analyses are ideal because they produce a much more detailed look at the cluster mass profile compared to X-ray and lensing mass estimators. However, most current techniques fail to account for substructure which could drastically affect the estimated dynamical mass [96]. I developed a multi-population Gaussian mixture model which allows for substructures within the cluster environment, disentangles cluster members from contaminating foreground and background galaxies, and estimates the cluster velocity dispersion and/or mass while marginalizing over uncertainties in these complexities. Unlike previous cluster kinematic models, this model detects substructure and estimates a probability of membership for each galaxy while simultaneously fitting the light profiles of the substructures.

With mock redshift catalogs generated from cosmological simulations, I showed that on average 77% of the highly probable member galaxies of the 2D substructures identified by this model correspond to the same true 3D substructures bound to the cluster. However, using a probabilistic approach (i.e. using each galaxies probability of membership as a weight) this correlation drops to only 40%. This drop off is most attributed to one of the major shortcomings of this model. In the model's present form, the number of substructures to be identified needs to be specified before the model can be fit. When I fit the simulated data, the largest of number of substructures allowed was three; therefore, these substructures are typically large and included many true 3D substructures thus lowering the cited percentage. It is currently computationally expensive to increase the number of substructures beyond three, so I was unable to test if this issue would be resolved when fitting a model with a larger number of subpopulations. MultiNest is inefficient at sampling high dimensional parameter spaces; however, recent work has been done on developing Bayesian sampling algorithms that could help to solve this issue. Specifically, diffusive nested sampling (e.g. DNest4 [266]) has not only been shown to be more efficient at sampling high dimensional posteriors, but also has the necessary framework to allow the number of

substructures to be a free parameter fit by the model.

Substructures can affect dynamical mass estimates which will then propagate into cosmological parameter constraints derived from the high mass tail of the halo mass function; therefore, understanding the accuracy of the mass estimates from this model is a key component of this thesis. The most ideal test would be to directly compare mass estimates with the true cluster mass known from the simulation; however, dynamical masses estimated via the Jeans equation are computationally expensive and unfeasible when fitting the large number of mock cluster catalogs involved in this analysis. Instead, I fit a uniform velocity dispersion profile and use this velocity dispersion as a proxy for mass. Mass and velocity dispersion are known to follow a power-law relationship, so I fit this power-law with scatter for the fit velocity dispersion vs true cluster mass distribution. I showed that as the number of substructures included in the model increases from zero to three, the scatter in this relationship decreases by nearly 35%. This shows that the models that include substructures produce a more accurate velocity dispersion (or mass) compared to models that neglect substructure.

Following the analysis with mock observations, I analyzed the kinematics of A267. I looked into the effect the number of subpopulations has on the derived properties of the main cluster halo. I showed that not only does the mass (or velocity dispersion) of the cluster depend on the number of substructures fit in the model, but the light profile and redshift of the cluster are also affected.

Although I used a detailed model describing the contamination model of galaxies in the sample, I believe further care needs to be taken. The first two substructures identified in the modeling of A267 appear to be dynamically distinct groups of galaxies that have no gravitational association with the cluster. This assessment is due to the fact that both groups have a rest frame line-of-sight velocity difference of ~ 4000 km/s as well as a projected radial offset of ~ 2 Mpc/h. In theory this is a non-issue because the model identifies these structures and models them accordingly (regardless if they are included in the contamination model or as one of the substructures); however, in practice this issue is problematic. Because each additional substructure requires 6 additional free parameters, the sampling becomes inefficient as the model approaches four substructures. Therefore, if two of these limited number of substructures are allocated to objects that are not associated with the cluster, the model fails to fit the maximum number of actual substructures associated with the cluster.

I showed that for the dark matter halo model with $N_{\rm subs} = 4$ that the posteriors for one of the substructures was multimodal which typically indicates that there is a high probability of at least one additional substructure. The number of likelihood evaluations required to sample the $N_{\rm subs} = 4$ model ($> 10^9$) indicates it would be unfeasible to fit a model with one additional substructure in a timely manner. However, if those two dynamically distinct substructures were included in the contamination model instead of as substructures, then it would be easy to fit one or two additional substructures. Therefore, a better treatment of the contamination model is needed in order to remedy this issue. At the moment, I apply a hard redshift cut to identify

the obvious contaminants and then model those galaxies as a multi population distribution. An obvious next step would be to apply a two dimensional cut (redshift and project radius) instead, and then model those galaxies in a similar fashion.

I briefly touched upon the possibility of including the stellar population parameters from the spectral fits in my discussion of the results of A267. The quick analysis I included showed the potential for estimating distinct populations of galaxies in age and metallicity for the substructures identified in the model. A more robust approach would be to include these parameters in the multipopulation model and fit these distributions concurrently with the kinematics. I could not do this for A267 because only $\sim$ 200 galaxies in the sample had stellar population parameters derived from M2FS observations. However, in the future with a larger sample of M2FS spectra such a model should be developed. The distribution of ages and metallicities of the galaxies in a given subpopulation could yield important insights into the formation history of the galaxy cluster.

One of the main features of the multipopulation mixture model presented here is the flexibility in the choice of light profiles and velocity distributions. Here I only consider NFW light profiles and Gaussian velocity distributions; however, other choices such as Plummer or King light profiles can be easily incorporated. I also mentioned in the presentation of the model that a rotational velocity term can be easily included in the velocity distribution for the main cluster halo. Although I did not include a rotational velocity term in the analyses presented in this thesis, there is current active research in searching for and measuring galaxy clusters that are rotating and this modeling framework could be used in these studies.

This modeling framework could also be used to test alternate theories of dark matter. Self-interacting dark matter predicts that the brightest cluster galaxy (BCG) of a galaxy clusters could wobble about the center of the cluster. This wobbling effect would manifest itself as an offset from the center of cluster in phase space, which this model is sensitive to. Furthermore, I showed that the inferences on the redshift and center of the cluster depend on the number of subpopulations accounted for which could have an effect on any detections of a wobbling BCG.

All in all there are many applications and future work to be done with the models and results presented in this thesis. In regards to cosmology, the main impact of this thesis is in estimating more accurate cluster dynamical masses by accounting for substructure within the cluster environment. These improvements are made necessary because of the high quality spectra efficiently produced by the new age of multi-object spectrographs like M2FS. Furthermore, improvements of the models presented in this thesis can give further insights on cluster formation processes as well as probe alternate theories of dark matter. The universe is dark and mysterious but step-by-step together we can decode the cosmos and gain new insights into the formation and evolution of the universe.

Appendix A

Data Tables

Table A.1: Results for fitting of A267 spectra.

ID	α_{2000} (hh:mm:ss)	δ_{2000} (°:′:″)	r [mag]	i [mag]	S/N	$\overline{v_{\rm los}}$ (km s^{-1})	$\overline{\rm Age}$ (Gyr)	$\overline{\rm [Fe/H]}$ (dex)	$\overline{[\alpha/{\rm Fe}]}$ (dex)	$\overline{\sigma_{\rm int}}$ (km s^{-1})
1	01:53:13.48	+01:00:48.6	20.38	19.86	10.1	114156 ± 16	5.5 ± 0.6	-0.72 ± 0.10	0.05 ± 0.05	193.3 ± 12.2
2	01:53:20.26	+01:01:17.0	20.52	20.06	9.3	114059 ± 18	6.5 ± 0.4	-2.54 ± 0.05	0.48 ± 0.09	71.6 ± 24.5
3	01:53:16.28	+01:01:52.3	20.25	19.84	14.1	54204 ± 14	6.3 ± 0.7	-1.67 ± 0.14	0.43 ± 0.10	88.3 ± 28.6
4	01:53:16.37	+01:04:1.2	20.32	19.82	10.9	54561 ± 83	7.5 ± 1.0	-2.44 ± 0.13	0.52 ± 0.15	426.1 ± 13.7
5	01:53:20.59	+01:04:2.5	19.84	19.33	19.3	55088 ± 13	11.0 ± 1.1	-1.44 ± 0.08	0.51 ± 0.06	150.1 ± 11.7
6	01:53:19.68	+01:05:3.0	19.72	19.19	14.8	83185 ± 12	11.6 ± 1.1	-1.02 ± 0.07	0.25 ± 0.04	148.8 ± 11.5
7	01:53:18.66	+01:05:8.6	20.12	19.64	15.5	83304 ± 14	13.5 ± 1.0	-1.32 ± 0.07	0.34 ± 0.04	165.1 ± 13.0
8	01:53:13.90	+01:05:9.6	20.54	19.98	9.1	83296 ± 21	11.9 ± 1.5	-1.19 ± 0.11	0.31 ± 0.06	140.2 ± 20.2
9	01:53:28.43	+00:57:3.2	20.44	19.92	6.3	83271 ± 28	12.9 ± 1.5	-1.21 ± 0.12	0.24 ± 0.09	107.1 ± 27.2
10	01:53:31.90	+00:58:23.9	19.89	19.34	8.4	39343 ± 59	7.0 ± 2.1	-1.64 ± 0.25	0.46 ± 0.20	245.2 ± 60.6
11	01:53:28.58	+01:01:57.6	19.27	18.79	30.7	54872 ± 7	6.5 ± 0.3	-0.80 ± 0.04	0.31 ± 0.03	160.3 ± 6.1
12	01:53:30.05	+01:03:29.4	20.79	20.31	6.5	113890 ± 27	12.7 ± 1.0	-2.72 ± 0.19	0.39 ± 0.06	59.7 ± 31.7
13	01:53:36.88	+01:03:50.8	20.13	19.63	5.0	66669 ± 104	11.8 ± 2.4	-1.29 ± 0.25	0.34 ± 0.18	298.6 ± 84.3
14	01:53:35.06	+01:04:33.0	19.47	18.92	20.1	54993 ± 12	11.9 ± 1.1	-1.16 ± 0.07	0.46 ± 0.05	154.5 ± 10.3
15	01:53:29.86	+01:04:48.5	21.03	20.52	7.4	67019 ± 33	5.3 ± 0.8	-2.23 ± 0.22	0.64 ± 0.12	65.5 ± 36.2

16	01:53:20.85	+01:05:16.2	19.90	19.38	19.6	68669 ± 138	13.5 ± 1.1	-1.00 ± 0.07	0.21 ± 0.04	245.7 ± 11.7
17	01:52:59.79	+01:15:29.5	20.24	19.66	9.8	68840 ± 16	10.4 ± 1.6	-1.12 ± 0.12	0.25 ± 0.07	110.5 ± 19.7
18	01:53:5.29	+01:15:19.2	20.55	20.02	9.8	90258 ± 26	6.5 ± 1.3	-0.44 ± 0.14	0.02 ± 0.06	271.3 ± 21.1
19	01:52:59.68	+01:14:9.4	19.79	19.27	19.8	69207 ± 11	11.4 ± 0.8	-1.13 ± 0.06	0.20 ± 0.04	151.8 ± 10.0
20	01:53:7.34	+01:07:42.6	20.42	19.84	11.5	82938 ± 22	12.5 ± 1.4	-1.01 ± 0.09	0.27 ± 0.04	250.5 ± 18.4
21	01:53:2.61	+01:07:35.6	19.51	19.01	17.3	66623 ± 11	10.6 ± 0.9	-1.17 ± 0.07	0.30 ± 0.04	138.4 ± 10.0
22	01:53:6.70	+01:06:49.7	20.51	20.05	6.0	67745 ± 28	8.6 ± 2.2	-1.08 ± 0.20	0.30 ± 0.12	110.1 ± 28.0
23	01:53:2.87	+01:05:41.7	20.00	19.43	13.5	68063 ± 18	12.5 ± 1.2	-1.31 ± 0.09	0.33 ± 0.05	187.0 ± 18.5
24	01:52:59.21	+01:02:35.6	20.60	20.11	10.3	54433 ± 78	8.5 ± 1.4	-2.47 ± 0.12	0.54 ± 0.14	424.3 ± 14.0
25	01:52:56.23	+01:13:42.6	19.32	18.79	22.0	55214 ± 10	7.9 ± 0.8	-0.98 ± 0.07	0.44 ± 0.04	150.7 ± 8.0
26	01:52:53.85	+01:12:15.5	19.68	19.22	13.3	55017 ± 22	10.7 ± 1.5	-1.54 ± 0.13	0.43 ± 0.08	195.4 ± 29.8
27	01:52:55.26	+01:11:1.5	20.62	20.12	7.2	69112 ± 18	10.0 ± 2.0	-1.00 ± 0.15	0.27 ± 0.09	68.1 ± 29.3
28	01:52:55.69	+01:07:44.2	19.88	19.33	13.6	68685 ± 18	13.4 ± 1.1	-1.12 ± 0.07	0.23 ± 0.05	211.7 ± 20.4
29	01:52:58.25	+01:04:47.2	19.65	19.15	17.9	54498 ± 14	11.2 ± 1.2	-1.30 ± 0.08	0.45 ± 0.05	165.4 ± 13.5
30	01:52:54.05	+01:04:34.6	20.68	20.13	22.8	33390 ± 152	14.5 ± 0.4	-2.57 ± 0.03	0.24 ± 0.11	437.6 ± 3.1
31	01:52:53.56	+01:03:36.5	19.45	18.98	17.9	58094 ± 11	10.3 ± 1.1	-0.66 ± 0.07	0.14 ± 0.03	184.8 ± 10.9
32	01:52:58.18	+01:02:49.4	20.85	20.37	5.5	69830 ± 28	12.7 ± 1.7	-1.09 ± 0.15	0.19 ± 0.12	110.0 ± 36.0
33	01:52:47.53	+00:52:22.0	20.05	19.54	6.5	69766 ± 33	14.1 ± 0.8	-0.85 ± 0.11	0.27 ± 0.09	198.1 ± 25.3
34	01:52:46.25	+00:54:10.2	20.03	19.53	9.6	68559 ± 26	13.4 ± 1.2	-1.17 ± 0.09	0.28 ± 0.07	207.0 ± 21.8
35	01:52:47.33	+00:58:2.7	20.42	19.88	10.8	68884 ± 15	11.4 ± 1.6	-0.82 ± 0.10	0.24 ± 0.06	137.9 ± 13.0
36	01:52:48.44	+00:59:0.9	20.58	20.14	7.7	68550 ± 29	13.0 ± 1.5	-1.29 ± 0.14	0.52 ± 0.11	175.0 ± 30.6
37	01:52:46.61	+00:59:59.4	20.63	20.12	6.7	69240 ± 25	4.6 ± 0.9	-1.70 ± 0.24	0.69 ± 0.09	109.9 ± 33.6

38	01:52:48.19	+01:00:18.0	19.80	19.26	11.8	83569 ± 14	13.2 ± 1.1	-1.25 ± 0.07	0.28 ± 0.04	152.3 ± 11.8
39	01:52:46.24	+01:01:45.5	20.04	19.55	11.5	82954 ± 19	8.2 ± 0.7	-2.36 ± 0.14	0.47 ± 0.08	133.5 ± 17.4
40	01:52:47.83	+01:01:48.4	20.72	20.19	8.3	68252 ± 17	12.7 ± 1.4	-1.49 ± 0.13	0.43 ± 0.09	98.2 ± 22.0
41	01:52:51.68	+00:53:53.0	20.99	20.49	5.9	68829 ± 24	11.9 ± 2.0	-0.96 ± 0.15	0.41 ± 0.11	101.4 ± 30.4
42	01:52:52.38	+00:57:22.6	20.12	19.57	7.7	108444 ± 20	4.9 ± 0.7	-0.50 ± 0.12	0.12 ± 0.06	206.8 ± 17.0
43	01:52:49.49	+00:57:24.2	20.58	20.12	6.9	68383 ± 22	7.5 ± 1.8	-1.13 ± 0.17	0.52 ± 0.11	46.7 ± 26.9
44	01:52:49.88	+00:58:5.0	20.13	19.61	8.3	67584 ± 28	11.7 ± 1.9	-0.87 ± 0.13	0.25 ± 0.07	205.8 ± 27.4
45	01:52:53.05	+00:58:11.4	19.91	19.35	11.4	83143 ± 15	10.8 ± 1.4	-0.84 ± 0.10	0.13 ± 0.05	170.9 ± 16.7
46	01:52:48.44	+00:58:44.8	19.43	18.91	31.2	69090 ± 8	11.7 ± 0.5	-1.19 ± 0.04	0.16 ± 0.02	218.2 ± 9.4
47	01:52:52.94	+00:59:33.1	20.72	20.15	7.6	69725 ± 20	12.7 ± 1.5	-0.92 ± 0.11	0.38 ± 0.08	95.6 ± 20.0
48	01:52:51.40	+00:59:58.5	20.49	19.95	12.1	66524 ± 11	12.1 ± 1.3	-1.25 ± 0.09	0.32 ± 0.05	74.5 ± 18.7
49	01:52:32.90	+00:52:22.8	20.45	19.94	4.6	83024 ± 26	11.1 ± 2.1	-0.55 ± 0.17	0.10 ± 0.11	100.5 ± 31.3
50	01:52:34.49	+00:54:51.1	20.98	20.52	4.6	68195 ± 30	9.5 ± 2.4	-0.29 ± 0.17	-0.08 ± 0.08	119.7 ± 29.9
51	01:52:31.17	+00:56:11.8	20.46	19.98	9.8	69858 ± 17	12.5 ± 1.5	-0.96 ± 0.10	0.28 ± 0.06	134.7 ± 15.6
52	01:52:33.75	+00:57:49.8	20.96	20.44	1.7	44269 ± 45300	11.9 ± 2.9	-0.27 ± 0.39	0.48 ± 0.38	274.7 ± 120.1
53	01:52:31.24	+00:59:28.4	20.19	19.63	12.1	67159 ± 17	11.2 ± 1.4	-1.03 ± 0.10	0.29 ± 0.06	154.9 ± 16.5
54	01:52:34.11	+00:59:37.2	20.77	20.22	9.3	68057 ± 18	10.8 ± 1.6	-1.20 ± 0.12	0.37 ± 0.07	124.3 ± 19.4
55	01:52:31.17	+01:00:6.2	20.42	19.84	2.2	66649 ± 52	11.4 ± 2.6	-0.59 ± 0.25	0.13 ± 0.19	110.5 ± 52.6
56	01:52:30.31	+01:01:15.3	20.35	19.86	10.5	69507 ± 18	12.2 ± 1.6	-1.06 ± 0.09	0.30 ± 0.05	142.2 ± 15.4
57	01:52:34.96	+00:53:15.1	20.16	19.67	3.8	64449 ± 54	3.1 ± 1.9	-0.55 ± 0.41	0.61 ± 0.13	135.1 ± 54.2
58	01:52:35.09	+00:55:15.0	20.52	20.01	7.9	82961 ± 15	12.3 ± 1.6	-0.64 ± 0.10	0.19 ± 0.06	105.4 ± 15.6
59	01:52:36.90	+00:55:16.6	20.02	19.54	13.7	69093 ± 13	11.5 ± 1.3	-0.76 ± 0.08	0.18 ± 0.04	172.3 ± 12.8

60	01:52:37.42	+00:59:2.2	19.62	19.06	15.8	66367 ± 14	10.5 ± 1.0	-1.53 ± 0.08	0.47 ± 0.05	132.0 ± 12.5
61	01:52:35.69	+01:00:42.4	20.88	20.47	6.3	70923 ± 20	9.7 ± 2.1	-0.81 ± 0.14	0.36 ± 0.08	80.3 ± 26.0
62	01:52:36.74	+01:00:45.7	20.59	20.03	10.8	68862 ± 19	11.3 ± 1.5	-1.07 ± 0.10	0.30 ± 0.06	148.0 ± 15.4
63	01:52:37.57	+01:01:7.5	20.70	20.20	9.0	66945 ± 15	12.6 ± 1.5	-1.27 ± 0.11	0.49 ± 0.08	67.3 ± 27.5
64	01:52:35.28	+01:01:39.3	20.39	19.90	11.9	70432 ± 17	10.9 ± 1.4	-0.93 ± 0.10	0.24 ± 0.05	179.1 ± 17.1
65	01:52:4.37	+00:57:8.8	20.07	19.61	6.0	72091 ± 24	6.0 ± 1.5	-1.20 ± 0.18	0.58 ± 0.12	109.9 ± 21.3
66	01:52:1.76	+00:57:45.3	20.28	19.90	3.5	67424 ± 62	2.0 ± 0.8	-1.17 ± 0.53	0.48 ± 0.21	141.0 ± 79.8
67	01:52:6.52	+01:00:42.6	18.85	18.42	26.1	39373 ± 8	11.9 ± 1.0	-1.27 ± 0.06	0.47 ± 0.04	144.3 ± 7.5
68	01:51:49.92	+01:01:14.0	20.07	19.64	10.6	72039 ± 25	5.7 ± 0.6	-2.06 ± 0.17	0.68 ± 0.08	159.4 ± 23.9
69	01:51:57.88	+01:02:2.2	20.68	20.15	2.1	107895 ± 82	0.8 ± 0.4	-1.79 ± 0.52	0.42 ± 0.26	140.3 ± 74.1
70	01:51:59.91	+01:03:34.1	20.00	19.38	6.6	107393 ± 21	3.7 ± 0.3	0.41 ± 0.07	-0.01 ± 0.09	229.6 ± 9.9
71	01:52:3.42	+01:04:16.5	18.91	18.45	26.7	38889 ± 7	9.1 ± 0.9	-1.32 ± 0.07	0.33 ± 0.04	142.3 ± 8.8
72	01:51:53.61	+01:04:17.8	20.14	19.66	8.6	67685 ± 18	12.3 ± 1.8	-0.82 ± 0.12	0.24 ± 0.07	145.2 ± 15.6
73	01:52:17.61	+00:53:20.5	19.85	19.44	11.5	109266 ± 16	4.6 ± 0.3	-2.30 ± 0.14	0.67 ± 0.08	119.5 ± 11.8
74	01:52:16.79	+00:53:56.8	19.42	18.90	15.8	75170 ± 13	9.8 ± 1.0	-0.94 ± 0.07	0.27 ± 0.04	182.3 ± 9.7
75	01:52:20.13	+00:54:18.7	20.73	20.26	3.9	118450 ± 41	4.4 ± 0.8	-2.04 ± 0.27	0.67 ± 0.10	133.8 ± 33.3
76	01:52:18.68	+00:58:5.5	20.04	19.56	7.6	67997 ± 19	13.1 ± 1.5	-0.53 ± 0.10	0.08 ± 0.07	139.0 ± 13.9
77	01:52:20.42	+00:58:27.9	19.96	19.50	10.4	83740 ± 29	11.7 ± 1.1	-2.60 ± 0.15	0.39 ± 0.07	179.4 ± 27.8
78	01:52:20.63	+01:02:39.4	20.91	20.40	5.2	114067 ± 27	10.8 ± 1.6	-1.84 ± 0.19	-0.05 ± 0.10	88.7 ± 23.9
79	01:52:13.32	+01:05:33.3	20.57	20.09	10.0	68594 ± 16	10.2 ± 1.4	-1.09 ± 0.11	0.19 ± 0.07	132.5 ± 12.5
80	01:52:7.39	+01:05:48.2	20.50	20.08	7.0	107777 ± 21	3.3 ± 0.4	-1.95 ± 0.20	0.60 ± 0.12	99.5 ± 26.1
81	01:52:28.63	+01:14:19.3	20.99	20.41	4.4	117074 ± 31	9.4 ± 1.6	-2.38 ± 0.18	0.40 ± 0.16	78.7 ± 31.7

82	01:52:33.36	+01:11:5.1	20.31	19.80	13.1	69357 ± 10	11.1 ± 1.0	-1.38 ± 0.08	0.31 ± 0.05	95.5 ± 12.6
83	01:52:30.85	+01:09:50.8	20.31	19.80	10.4	69232 ± 8	11.2 ± 1.3	-1.38 ± 0.10	0.38 ± 0.06	90.6 ± 14.7
84	01:52:34.57	+01:07:37.5	20.35	19.94	12.3	69608 ± 10	4.9 ± 0.5	-1.05 ± 0.09	0.42 ± 0.06	104.9 ± 10.7
85	01:52:24.92	+01:07:30.6	21.08	20.61	6.1	69386 ± 27	8.9 ± 2.3	-1.16 ± 0.21	0.35 ± 0.11	108.4 ± 26.5
86	01:52:25.95	+01:07:14.5	21.00	20.52	10.2	54883 ± 64	7.5 ± 1.0	-2.44 ± 0.14	0.45 ± 0.14	426.3 ± 19.5
87	01:52:34.03	+01:06:31.7	19.04	18.53	26.4	54118 ± 9	12.1 ± 0.9	-1.14 ± 0.05	0.40 ± 0.03	189.2 ± 6.9
88	01:52:32.17	+01:04:49.9	20.55	19.93	7.9	70612 ± 40	12.7 ± 1.5	-1.97 ± 0.22	0.37 ± 0.13	216.2 ± 43.2
89	01:52:19.90	+01:11:23.4	20.10	19.61	9.6	56636 ± 39	6.1 ± 0.8	-2.14 ± 0.24	0.41 ± 0.14	242.5 ± 40.0
90	01:52:16.30	+01:11:8.3	20.60	20.06	5.0	107222 ± 31	5.2 ± 1.6	-0.59 ± 0.22	0.10 ± 0.11	179.2 ± 27.4
91	01:52:20.59	+01:08:40.4	20.79	20.25	6.2	88587 ± 23	12.8 ± 1.6	-1.26 ± 0.13	0.10 ± 0.10	119.5 ± 19.8
92	01:52:17.81	+01:08:14.7	19.29	18.75	21.1	68995 ± 13	10.7 ± 1.2	-0.64 ± 0.08	0.18 ± 0.04	263.7 ± 8.6
93	01:52:22.47	+01:07:45.1	19.75	19.17	16.0	88418 ± 12	6.4 ± 0.8	-0.34 ± 0.10	0.05 ± 0.03	224.8 ± 9.0
94	01:52:15.87	+01:07:20.8	20.37	19.68	7.7	107952 ± 23	5.1 ± 0.8	-0.37 ± 0.11	-0.10 ± 0.06	230.7 ± 14.6
95	01:52:23.55	+01:06:34.2	20.44	19.98	13.0	58078 ± 18	5.6 ± 0.7	-1.01 ± 0.12	0.28 ± 0.07	173.3 ± 15.4
96	01:52:20.84	+01:06:33.9	21.06	20.59	5.4	108357 ± 27	6.8 ± 1.8	-1.29 ± 0.23	0.51 ± 0.12	126.5 ± 24.1
97	01:52:58.87	+00:53:21.4	19.45	18.94	19.0	69673 ± 38	14.0 ± 0.9	-1.02 ± 0.05	0.28 ± 0.04	179.4 ± 12.2
98	01:52:58.14	+00:53:42.7	20.33	19.82	1.5	72457 ± 2467	7.1 ± 5.2	-0.55 ± 0.73	0.14 ± 0.25	198.5 ± 121.2
99	01:52:54.46	+00:55:20.0	20.98	20.47	7.9	83212 ± 68	7.7 ± 1.3	-1.59 ± 0.17	0.15 ± 0.11	58.7 ± 33.5
100	01:52:55.95	+00:58:5.2	19.31	18.83	20.9	70098 ± 31	8.7 ± 0.8	-0.90 ± 0.07	0.20 ± 0.04	132.2 ± 7.5
101	01:52:58.71	+00:58:10.7	20.88	20.41	13.3	69767 ± 41	5.2 ± 0.5	-1.24 ± 0.10	0.43 ± 0.07	75.8 ± 19.5
102	01:52:53.96	+00:58:50.2	20.50	19.92	11.7	83663 ± 56	10.6 ± 1.1	-1.17 ± 0.09	0.38 ± 0.05	138.7 ± 14.1
103	01:52:54.57	+01:00:8.8	20.14	19.59	15.7	83406 ± 71	14.5 ± 0.5	-1.82 ± 0.07	0.12 ± 0.06	249.0 ± 21.2

104	01:52:53.35	+01:01:32.1	20.01	19.51	12.9	69247 ± 60	10.2 ± 1.5	-0.61 ± 0.10	0.20 ± 0.05	224.5 ± 16.7
105	01:53:4.04	+00:56:12.1	19.48	18.98	18.3	40159 ± 24	10.4 ± 1.5	-1.44 ± 0.10	0.43 ± 0.07	161.5 ± 14.0
106	01:53:2.11	+00:57:35.5	19.07	18.51	31.5	69892 ± 38	10.2 ± 0.7	-0.78 ± 0.06	0.16 ± 0.03	265.9 ± 7.6
107	01:53:1.95	+00:58:20.9	20.06	19.59	10.7	69338 ± 82	3.5 ± 0.4	-1.56 ± 0.17	0.52 ± 0.12	130.9 ± 26.4
108	01:53:0.85	+00:58:39.9	20.72	20.22	10.6	68653 ± 58	12.9 ± 1.4	-1.21 ± 0.09	0.31 ± 0.06	131.8 ± 16.7
109	01:53:7.59	+01:01:11.8	20.74	20.20	6.4	113876 ± 101	13.9 ± 0.9	-2.33 ± 0.16	0.46 ± 0.10	137.8 ± 26.8
110	01:53:4.33	+01:01:28.6	19.77	19.29	13.8	54899 ± 46	12.2 ± 1.4	-1.98 ± 0.16	0.44 ± 0.09	190.2 ± 33.7
111	01:53:11.53	+01:04:15.3	20.63	20.14	4.4	67375 ± 204	6.3 ± 2.6	-1.11 ± 0.27	0.14 ± 0.21	291.8 ± 68.3
112	01:53:12.73	+01:04:19.5	21.10	20.61	9.2	67580 ± 73	13.7 ± 1.1	-1.89 ± 0.15	0.42 ± 0.10	102.8 ± 33.2
113	01:53:30.74	+01:13:15.3	20.55	20.09	8.5	68677 ± 72	11.6 ± 1.9	-0.74 ± 0.12	-0.10 ± 0.07	216.0 ± 29.9
114	01:53:29.37	+01:09:31.1	20.38	19.90	8.0	83010 ± 80	8.6 ± 1.2	-2.31 ± 0.18	0.74 ± 0.05	56.6 ± 30.0
115	01:53:30.35	+01:08:46.1	20.35	19.92	5.2	83253 ± 145	6.5 ± 1.3	-2.04 ± 0.25	0.68 ± 0.09	50.9 ± 33.9
116	01:53:38.98	+01:08:28.8	20.91	20.36	3.9	76939 ± 75	11.6 ± 2.2	-0.55 ± 0.18	0.30 ± 0.12	78.6 ± 35.2
117	01:53:36.94	+01:08:9.3	20.63	20.10	4.6	115700 ± 88	5.2 ± 0.9	-1.23 ± 0.17	0.33 ± 0.10	28.7 ± 20.3
118	01:53:37.06	+01:07:20.7	20.82	20.20	4.0	115314 ± 85	6.5 ± 2.2	-0.07 ± 0.23	0.08 ± 0.08	190.7 ± 22.0
119	01:53:38.46	+01:06:54.3	20.36	19.76	4.7	115349 ± 99	4.7 ± 1.2	-0.25 ± 0.19	-0.07 ± 0.08	178.4 ± 24.3
120	01:53:30.39	+01:05:52.6	20.51	19.94	8.1	54634 ± 45	6.4 ± 1.7	-0.73 ± 0.16	0.02 ± 0.11	173.7 ± 27.9
121	01:53:20.93	+01:15:11.1	20.76	20.20	2.2	68279 ± 239	4.2 ± 2.8	-0.66 ± 0.58	0.19 ± 0.25	327.3 ± 91.0
122	01:53:19.22	+01:15:10.7	20.09	19.70	6.8	50056 ± 50	4.2 ± 1.3	-1.10 ± 0.18	0.68 ± 0.09	144.6 ± 40.4
123	01:53:8.28	+01:11:59.6	20.72	20.34	9.1	83600 ± 121	7.9 ± 0.9	-2.51 ± 0.11	0.66 ± 0.10	258.8 ± 41.5
124	01:53:26.90	+01:08:41.1	20.89	20.37	7.0	68697 ± 76	9.9 ± 1.9	-1.93 ± 0.28	0.26 ± 0.16	77.9 ± 39.4
125	01:53:16.13	+01:08:25.3	20.46	20.02	6.0	68694 ± 73	11.1 ± 2.2	-0.96 ± 0.16	0.45 ± 0.11	132.2 ± 29.8

126	01:53:9.10	+01:07:59.1	19.61	19.06	17.2	68039 ± 50	11.0 ± 1.1	-1.03 ± 0.08	0.15 ± 0.05	206.6 ± 13.6
127	01:53:21.37	+01:07:38.1	20.92	20.39	7.6	68781 ± 65	10.8 ± 1.8	-1.47 ± 0.16	0.38 ± 0.10	80.0 ± 32.2
128	01:53:7.40	+01:05:55.3	19.91	19.50	1.0	53217 ± 29035	8.1 ± 3.7	-0.69 ± 0.79	0.27 ± 0.27	261.2 ± 116.7
129	01:52:42.29	+00:55:1.1	19.52	19.05	18.4	67792 ± 40	10.5 ± 1.2	-0.72 ± 0.08	0.25 ± 0.04	200.5 ± 12.4
130	01:52:42.17	+00:55:18.3	19.23	18.73	19.8	40032 ± 50	6.2 ± 0.7	-1.45 ± 0.11	0.38 ± 0.08	318.5 ± 33.9
131	01:52:42.28	+00:58:9.2	20.92	20.38	5.2	68556 ± 102	12.4 ± 1.8	-1.19 ± 0.18	0.36 ± 0.12	104.0 ± 41.5
132	01:52:42.40	+00:59:56.6	19.66	19.12	15.3	66989 ± 49	10.2 ± 1.2	-0.65 ± 0.09	0.13 ± 0.05	217.2 ± 13.7
133	01:52:42.42	+01:00:15.8	20.44	19.93	11.6	68353 ± 46	11.5 ± 1.4	-1.17 ± 0.10	0.36 ± 0.06	136.5 ± 15.6
134	01:52:43.89	+01:01:23.4	19.70	19.13	18.0	107972 ± 40	9.4 ± 1.3	-1.25 ± 0.11	0.19 ± 0.03	140.8 ± 9.0
135	01:52:42.86	+01:01:31.6	20.85	20.31	9.6	68922 ± 63	11.4 ± 1.6	-1.14 ± 0.12	0.24 ± 0.08	165.4 ± 23.7
136	01:52:44.01	+01:02:0.1	19.59	19.08	23.0	67366 ± 47	13.0 ± 1.0	-1.36 ± 0.06	0.32 ± 0.03	228.9 ± 10.9
137	01:52:45.12	+00:52:40.5	20.22	19.66	8.6	68039 ± 47	12.2 ± 1.6	-1.18 ± 0.11	0.22 ± 0.08	59.0 ± 28.6
138	01:52:45.42	+00:56:39.0	20.39	19.85	15.0	67826 ± 48	13.1 ± 1.1	-1.60 ± 0.10	0.36 ± 0.06	139.8 ± 13.5
139	01:52:44.38	+00:57:22.3	20.57	20.03	8.8	67784 ± 98	14.4 ± 0.5	-1.56 ± 0.10	0.36 ± 0.09	216.5 ± 28.4
140	01:52:46.04	+00:57:45.6	20.44	20.00	10.1	71169 ± 49	5.1 ± 0.6	-1.09 ± 0.10	0.41 ± 0.08	49.5 ± 26.5
141	01:52:45.20	+00:58:38.6	19.81	19.28	23.1	68591 ± 42	12.0 ± 0.7	-1.09 ± 0.05	0.24 ± 0.03	217.1 ± 10.3
142	01:52:45.48	+00:59:29.8	20.16	19.62	16.9	69514 ± 42	12.0 ± 1.0	-1.13 ± 0.07	0.23 ± 0.04	161.8 ± 11.4
143	01:52:45.57	+01:00:25.1	20.92	20.37	8.9	83794 ± 87	8.8 ± 1.6	-1.16 ± 0.14	0.40 ± 0.06	232.5 ± 24.0
144	01:52:44.97	+01:01:12.9	20.51	19.96	12.2	69127 ± 53	11.9 ± 1.5	-0.99 ± 0.10	0.20 ± 0.06	169.8 ± 17.9
145	01:52:53.45	+01:13:35.6	19.23	18.80	20.3	39023 ± 17	10.4 ± 1.1	-1.27 ± 0.08	0.52 ± 0.06	150.8 ± 11.7
146	01:52:50.84	+01:13:12.0	19.59	19.12	21.2	55542 ± 47	10.0 ± 0.9	-2.10 ± 0.12	0.52 ± 0.06	246.8 ± 15.0
147	01:52:51.87	+01:11:31.6	20.73	20.26	11.4	69615 ± 57	9.0 ± 1.2	-1.49 ± 0.11	0.27 ± 0.07	121.4 ± 22.7

148	01:52:50.99	+01:10:10.8	20.88	20.41	4.5	68864 ± 71	13.3 ± 1.4	-0.85 ± 0.14	0.16 ± 0.13	61.8 ± 37.3
149	01:52:53.04	+01:08:49.7	19.45	18.95	19.8	67826 ± 36	9.7 ± 0.8	-1.08 ± 0.06	0.21 ± 0.03	151.4 ± 9.6
150	01:52:53.34	+01:03:6.5	20.32	19.80	5.2	69427 ± 114	10.1 ± 2.7	-0.39 ± 0.21	0.10 ± 0.13	217.4 ± 39.6
151	01:52:53.13	+01:02:23.0	20.40	19.84	12.0	68824 ± 63	13.2 ± 1.3	-1.01 ± 0.08	0.23 ± 0.05	224.0 ± 19.8
152	01:52:51.46	+01:02:6.7	19.28	18.82	23.8	69262 ± 38	5.8 ± 0.4	-0.86 ± 0.07	0.12 ± 0.03	162.1 ± 8.9
153	01:52:46.81	+01:11:9.6	19.44	18.94	23.4	69654 ± 41	11.6 ± 0.7	-1.08 ± 0.05	0.20 ± 0.03	234.5 ± 9.4
154	01:52:48.22	+01:10:40.5	20.69	20.09	7.0	98277 ± 74	7.6 ± 1.6	-0.53 ± 0.15	-0.01 ± 0.07	138.3 ± 18.7
155	01:52:49.42	+01:09:56.0	19.31	18.75	23.3	64914 ± 36	11.9 ± 0.7	-1.09 ± 0.05	0.28 ± 0.03	215.4 ± 11.8
156	01:52:48.44	+01:07:47.6	20.64	20.19	7.4	86767 ± 85	8.7 ± 2.4	-0.96 ± 0.21	0.40 ± 0.08	182.9 ± 24.7
157	01:52:50.15	+01:07:25.3	19.98	19.49	14.0	69164 ± 39	10.9 ± 1.1	-1.12 ± 0.08	0.11 ± 0.05	115.1 ± 15.5
158	01:52:50.35	+01:05:46.0	19.69	19.19	16.1	70813 ± 35	6.9 ± 0.6	-0.56 ± 0.07	-0.01 ± 0.05	163.3 ± 11.7
159	01:52:45.42	+01:04:1.1	19.05	18.54	24.2	68152 ± 37	8.6 ± 0.6	-0.62 ± 0.05	0.13 ± 0.03	193.0 ± 9.4
160	01:52:39.86	+00:53:6.9	19.92	19.38	12.7	83304 ± 66	11.4 ± 1.4	-0.87 ± 0.09	0.26 ± 0.04	232.1 ± 12.7
161	01:52:40.18	+00:53:53.2	20.30	19.82	8.2	83264 ± 65	8.0 ± 1.5	-1.21 ± 0.14	0.34 ± 0.07	46.3 ± 26.1
162	01:52:40.17	+00:54:59.1	20.39	19.83	5.8	69829 ± 91	12.7 ± 1.6	-1.27 ± 0.16	-0.01 ± 0.11	152.7 ± 44.4
163	01:52:38.22	+00:58:12.6	20.41	19.85	14.3	69112 ± 52	11.6 ± 1.0	-1.33 ± 0.08	0.24 ± 0.05	163.6 ± 18.1
164	01:52:39.41	+00:58:29.7	20.92	20.39	4.8	69636 ± 68	6.5 ± 2.2	-0.52 ± 0.23	0.33 ± 0.13	74.1 ± 38.0
165	01:52:38.59	+00:59:45.2	21.03	20.47	6.7	69033 ± 97	12.2 ± 1.8	-0.94 ± 0.15	0.36 ± 0.10	234.2 ± 28.4
166	01:52:39.53	+01:00:8.3	20.72	20.23	7.2	68328 ± 68	11.9 ± 1.8	-1.36 ± 0.15	0.27 ± 0.10	133.3 ± 38.0
167	01:52:37.63	+01:01:31.4	19.39	18.85	20.7	71644 ± 45	12.3 ± 0.8	-1.38 ± 0.06	0.37 ± 0.03	203.6 ± 12.3
168	01:52:41.34	+00:55:47.6	19.82	19.34	14.7	68308 ± 41	9.7 ± 1.0	-0.89 ± 0.08	0.17 ± 0.05	164.1 ± 13.3
169	01:52:40.42	+00:58:2.4	20.17	19.62	13.2	68519 ± 65	13.9 ± 0.9	-1.45 ± 0.08	0.37 ± 0.06	219.3 ± 23.6

170	01:52:42.02	+00:58:35.9	20.41	19.86	13.6	69280 ± 61	10.7 ± 1.1	-1.20 ± 0.09	0.23 ± 0.05	202.0 ± 21.3
171	01:52:41.58	+00:58:58.5	19.72	19.23	16.2	69929 ± 42	7.4 ± 0.8	-0.82 ± 0.08	0.28 ± 0.04	161.6 ± 11.8
172	01:52:40.83	+00:59:53.6	20.59	20.06	4.6	67585 ± 53	11.4 ± 2.2	-0.73 ± 0.15	0.26 ± 0.12	28.0 ± 20.3
173	01:52:41.02	+01:00:20.6	20.59	20.10	9.2	67592 ± 47	11.7 ± 1.7	-0.84 ± 0.11	0.26 ± 0.06	114.9 ± 16.5
174	01:52:41.47	+01:00:43.0	20.38	19.93	4.4	67489 ± 134	2.6 ± 0.7	-1.35 ± 0.33	0.41 ± 0.22	114.4 ± 54.1
175	01:52:42.02	+01:01:51.1	20.94	20.48	9.5	69908 ± 77	13.8 ± 1.0	-1.64 ± 0.12	0.22 ± 0.09	165.8 ± 31.9
176	01:52:42.62	+01:13:42.6	20.74	20.15	8.3	126781 ± 90	9.6 ± 1.0	-2.40 ± 0.14	0.40 ± 0.08	131.7 ± 20.4
177	01:52:43.79	+01:09:0.6	19.72	19.17	16.9	68609 ± 57	10.6 ± 1.1	-1.01 ± 0.09	0.25 ± 0.04	220.8 ± 14.7
178	01:52:44.89	+01:08:20.8	20.45	20.12	8.3	82572 ± 75	10.0 ± 1.6	-2.00 ± 0.17	0.60 ± 0.10	36.6 ± 23.3
179	01:52:42.35	+01:08:0.8	20.32	19.81	13.8	55335 ± 28	11.9 ± 1.4	-1.24 ± 0.09	0.44 ± 0.05	125.0 ± 14.1
180	01:52:43.96	+01:07:39.1	19.49	19.01	25.8	54846 ± 17	11.4 ± 0.8	-1.11 ± 0.05	0.40 ± 0.03	161.2 ± 8.3
181	01:52:45.19	+01:04:29.6	19.74	19.22	15.8	71626 ± 44	7.5 ± 0.5	-2.32 ± 0.15	0.46 ± 0.08	215.4 ± 20.6
182	01:52:38.94	+01:03:39.4	19.65	19.14	18.0	69411 ± 48	11.5 ± 1.0	-0.98 ± 0.07	0.25 ± 0.04	206.7 ± 14.5
183	01:52:43.15	+01:02:40.0	19.92	19.38	12.8	69787 ± 62	9.1 ± 1.3	-0.77 ± 0.11	0.13 ± 0.06	259.6 ± 18.3
184	01:52:34.77	+01:12:9.8	20.47	19.90	8.3	83670 ± 76	13.8 ± 1.0	-1.11 ± 0.09	0.41 ± 0.06	145.3 ± 23.7
185	01:52:37.54	+01:08:32.2	19.47	18.97	24.8	55005 ± 14	10.8 ± 0.9	-1.00 ± 0.06	0.54 ± 0.04	163.5 ± 7.9
186	01:52:36.71	+01:05:37.7	20.15	19.62	14.4	71109 ± 55	11.9 ± 1.3	-0.98 ± 0.09	0.29 ± 0.04	215.7 ± 15.2
187	01:52:35.43	+01:05:9.0	20.37	19.86	10.2	71299 ± 76	12.7 ± 1.3	-2.24 ± 0.19	0.54 ± 0.11	203.6 ± 35.2
188	01:52:36.99	+01:05:6.8	20.53	20.05	11.3	71497 ± 63	11.5 ± 1.5	-1.08 ± 0.11	0.26 ± 0.06	177.1 ± 21.5
189	01:52:35.46	+01:03:59.3	19.31	18.79	21.7	68508 ± 48	13.7 ± 1.0	-1.08 ± 0.05	0.34 ± 0.03	242.7 ± 10.0
190	01:52:38.11	+01:02:53.0	20.20	19.73	10.5	69002 ± 47	11.2 ± 1.3	-1.33 ± 0.11	0.39 ± 0.06	95.9 ± 22.4
191	01:52:37.91	+01:02:37.2	19.78	19.23	20.5	71585 ± 44	10.3 ± 0.7	-1.39 ± 0.06	0.21 ± 0.04	200.6 ± 12.1

192	01:52:22.81	+00:52:21.0	20.45	20.02	5.9	70052 ± 80	11.9 ± 2.0	-0.81 ± 0.15	0.38 ± 0.11	118.1 ± 33.0
193	01:52:23.58	+00:54:59.6	20.10	19.62	8.3	69787 ± 41	11.4 ± 1.7	-0.52 ± 0.11	0.18 ± 0.06	100.8 ± 17.9
194	01:52:24.57	+00:55:59.9	20.68	20.23	9.1	70842 ± 56	10.0 ± 1.7	-1.07 ± 0.13	0.44 ± 0.07	99.4 ± 25.0
195	01:52:24.10	+00:58:1.5	19.80	19.29	19.1	67208 ± 44	9.9 ± 1.0	-0.95 ± 0.07	0.35 ± 0.03	168.4 ± 11.4
196	01:52:21.69	+01:00:8.0	19.38	18.84	18.8	68362 ± 40	14.8 ± 0.2	-1.53 ± 0.05	0.47 ± 0.04	228.0 ± 13.9
197	01:52:22.51	+01:01:34.6	19.69	19.20	22.7	68283 ± 30	11.0 ± 0.6	-2.44 ± 0.08	0.42 ± 0.05	285.0 ± 15.3
198	01:52:24.82	+01:05:37.5	20.28	19.69	8.5	118121 ± 80	2.5 ± 0.2	-1.80 ± 0.14	0.54 ± 0.11	28.0 ± 19.1
199	01:52:20.61	+01:06:3.6	20.61	20.11	7.5	107817 ± 114	12.4 ± 1.1	-2.85 ± 0.20	0.37 ± 0.07	71.3 ± 36.6
200	01:52:29.78	+00:52:19.3	20.32	19.82	8.1	69082 ± 48	12.9 ± 1.5	-0.81 ± 0.12	0.36 ± 0.08	86.6 ± 26.2
201	01:52:26.44	+00:52:39.4	20.12	19.62	14.6	68427 ± 43	13.6 ± 1.1	-1.11 ± 0.07	0.32 ± 0.05	145.9 ± 14.2
202	01:52:28.70	+00:56:33.0	19.10	18.59	2.1	18031 ± 110	8.9 ± 3.6	-0.45 ± 0.38	0.09 ± 0.22	92.0 ± 65.3
203	01:52:29.15	+00:59:22.5	20.82	20.28	6.2	11012 ± 45	2.4 ± 0.5	0.39 ± 0.09	-0.06 ± 0.09	294.8 ± 34.2
204	01:52:29.27	+00:59:40.6	19.31	18.78	26.5	67501 ± 41	13.9 ± 0.9	-1.04 ± 0.05	0.29 ± 0.03	223.7 ± 9.1
205	01:52:28.28	+01:02:32.1	20.10	19.59	13.6	71629 ± 70	11.7 ± 1.1	-2.58 ± 0.13	0.46 ± 0.07	321.6 ± 29.5
206	01:52:25.81	+01:05:3.0	20.40	19.79	8.0	107750 ± 76	11.1 ± 1.3	-1.31 ± 0.10	0.34 ± 0.05	95.4 ± 20.3
207	01:52:25.31	+01:06:25.9	19.19	18.73	32.2	58251 ± 13	12.0 ± 0.6	-0.98 ± 0.04	0.36 ± 0.02	152.8 ± 6.3
208	01:52:7.83	+01:12:52.0	21.07	20.63	4.9	24148 ± 32	7.5 ± 2.9	-0.17 ± 0.23	-0.03 ± 0.13	103.1 ± 53.2
209	01:52:10.53	+01:11:29.7	19.68	19.18	16.8	68885 ± 39	11.6 ± 1.0	-1.24 ± 0.07	0.37 ± 0.04	120.9 ± 11.8
210	01:52:13.26	+01:10:50.0	20.64	20.05	1.2	69718 ± 34035	7.7 ± 3.8	-0.41 ± 0.62	0.31 ± 0.29	194.5 ± 118.8
211	01:52:14.65	+01:10:14.0	20.89	20.39	7.2	133103 ± 159	11.3 ± 1.0	-3.39 ± 0.12	0.40 ± 0.01	178.2 ± 30.2
212	01:52:13.17	+01:09:7.3	20.08	19.58	10.8	69520 ± 52	7.2 ± 1.2	-1.00 ± 0.11	0.41 ± 0.07	114.8 ± 19.0
213	01:52:14.84	+01:08:4.0	20.78	20.27	7.2	55257 ± 70	6.2 ± 1.4	-2.05 ± 0.28	0.65 ± 0.11	196.4 ± 62.2

214	01:52:8.04	+01:06:54.6	20.38	19.93	12.9	69252 ± 46	7.1 ± 0.9	-0.98 ± 0.10	0.25 ± 0.06	109.9 ± 15.6
215	01:52:14.30	+01:06:36.5	21.08	20.58	1.7	91688 ± 150	11.0 ± 3.0	-0.80 ± 0.37	0.09 ± 0.20	63.6 ± 58.1
216	01:51:58.41	+01:13:32.8	20.89	20.32	2.2	109077 ± 110	10.3 ± 2.3	0.29 ± 0.16	0.13 ± 0.10	79.2 ± 43.4
217	01:52:7.15	+01:13:12.3	21.02	20.59	9.2	83133 ± 73	6.0 ± 0.6	-2.33 ± 0.17	0.53 ± 0.12	101.9 ± 36.2
218	01:51:53.79	+01:08:23.0	20.97	20.49	5.6	103504 ± 173	4.7 ± 0.7	-2.37 ± 0.18	0.63 ± 0.12	180.2 ± 65.4
219	01:52:3.40	+01:08:22.6	20.60	20.10	6.9	104370 ± 68	4.9 ± 0.9	-0.54 ± 0.14	0.02 ± 0.08	65.4 ± 28.3
220	01:51:58.75	+01:07:36.1	20.04	19.61	18.5	70416 ± 36	6.6 ± 0.5	-0.88 ± 0.06	0.23 ± 0.04	131.4 ± 10.9
221	01:52:5.53	+01:07:28.6	20.76	20.24	6.8	55287 ± 4140	10.2 ± 2.1	-2.51 ± 0.23	0.47 ± 0.17	365.8 ± 51.5
222	01:51:53.85	+01:06:35.2	20.55	20.02	0.6	107614 ± 177	0.4 ± 0.3	-1.54 ± 0.62	0.06 ± 0.20	106.5 ± 85.1
223	01:51:57.14	+01:06:15.0	20.08	19.60	16.6	62773 ± 47	12.1 ± 1.4	-1.74 ± 0.11	0.53 ± 0.07	177.6 ± 22.3

Table A.2: Results for fitting of M0429 spectra

M2FS ID	Subaru ID	$N_{\rm obs}$	α_{2000} deg	δ_{2000} deg	r [mag]	S/N	$\overline{v_{\rm los}}$ (km s^{-1})	$\overline{\rm Age}$ (Gyr)	$\overline{\rm [Fe/H]}$ (dex)	$\overline{[\alpha/{\rm Fe}]}$ (dex)	$\overline{\sigma_{\rm int}}$ (km s^{-1})
672	2	1	67.18	-2.79	21.39	5.7	118624 ± 29	11.3 ± 2.1	-1.54 ± 0.15	0.32 ± 0.09	106 ± 19
139	6	2	67.39	-2.91	21.04	4.7	79308 ± 1652	1.2 ± 2.1	0.18 ± 0.33	-0.00 ± 0.11	369 ± 49
660	6	2	67.39	-2.91	21.04	4.9	119967 ± 37	13.2 ± 1.4	-1.23 ± 0.10	-0.05 ± 0.09	112 ± 32
683	7	1	67.20	-2.82	21.05	5.1	144193 ± 24	14.6 ± 0.4	-1.87 ± 0.08	0.30 ± 0.11	89 ± 26
687	8	1	67.23	-2.97	21.23	3.5	149543 ± 48	3.0 ± 0.6	-2.13 ± 0.27	0.17 ± 0.26	69 ± 46
498	9	1	67.62	-2.69	20.41	3.3	131403 ± 55	12.8 ± 1.8	-2.05 ± 0.19	0.76 ± 0.04	139 ± 44
150	12	2	67.45	-2.80	21.98	3.1	28916 ± 11438	9.2 ± 3.7	-0.54 ± 0.25	0.58 ± 0.17	155 ± 130
619	12	2	67.45	-2.80	21.98	1.4	75090 ± 37898	9.7 ± 3.4	-0.54 ± 0.79	0.31 ± 0.29	49 ± 41
586	15	2	67.31	-2.72	20.55	1.5	122239 ± 67	1.4 ± 1.4	-0.29 ± 0.40	0.39 ± 0.27	36 ± 29
299	15	2	67.31	-2.72	20.55	4.9	122521 ± 28	11.9 ± 1.9	-2.19 ± 0.19	0.37 ± 0.16	81 ± 31
519	16	1	67.55	-2.70	19.80	8.6	17097 ± 47	12.3 ± 2.0	-0.86 ± 0.15	-0.06 ± 0.15	260 ± 34
263	18	1	67.18	-2.96	20.39	19.9	288 ± 4	0.6 ± 0.7	0.37 ± 0.13	-0.19 ± 0.01	75 ± 22
147	19	2	67.45	-2.70	20.28	10.2	131082 ± 36	7.0 ± 0.6	-2.55 ± 0.04	0.77 ± 0.03	239 ± 20
614	19	2	67.45	-2.70	20.28	10.1	131044 ± 6	5.0 ± 0.7	-1.41 ± 0.07	0.30 ± 0.05	59 ± 11
572	20	2	67.40	-2.89	20.30	8.0	122705 ± 32	11.4 ± 2.0	-1.51 ± 0.11	0.15 ± 0.08	205 ± 21

634	20	2	67.40	-2.89	20.30	12.4	122747 ± 19	12.1 ± 1.3	-1.78 ± 0.08	0.61 ± 0.07	181 ± 12
148	22	2	67.46	-2.72	19.90	12.3	117432 ± 21	8.0 ± 0.7	-1.93 ± 0.10	0.44 ± 0.06	109 ± 8
615	22	2	67.46	-2.72	19.90	14.8	117561 ± 13	8.3 ± 0.8	-1.56 ± 0.07	0.62 ± 0.06	141 ± 7
153	23	2	67.44	-2.69	20.80	6.7	51570 ± 45	0.2 ± 0.2	-0.96 ± 0.27	0.63 ± 0.15	51 ± 45
325	23	2	67.44	-2.69	20.80	2.7	130615 ± 20	1.1 ± 0.6	-1.01 ± 0.45	0.65 ± 0.12	23 ± 17
134	24	2	67.37	-2.92	19.59	14.5	107215 ± 12	8.1 ± 1.2	-1.79 ± 0.10	0.43 ± 0.06	116 ± 8
653	24	2	67.37	-2.92	19.59	19.4	107242 ± 9	6.6 ± 0.5	-1.90 ± 0.07	0.56 ± 0.06	47 ± 20
190	25	2	67.47	-2.76	19.61	15.3	56643 ± 71	1.3 ± 0.1	0.43 ± 0.06	-0.19 ± 0.01	428 ± 7
610	25	2	67.47	-2.76	19.61	13.2	121864 ± 17	4.4 ± 0.2	-2.55 ± 0.04	0.69 ± 0.07	130 ± 11
532	30	2	67.43	-2.94	20.76	4.6	46404 ± 8826	2.5 ± 1.4	-1.71 ± 0.78	0.09 ± 0.24	53 ± 53
593	30	2	67.43	-2.94	20.76	7.7	92522 ± 25	4.6 ± 0.6	-2.13 ± 0.24	0.04 ± 0.15	39 ± 31
368	31	1	67.56	-3.08	20.67	5.4	130494 ± 47	11.4 ± 1.7	-2.54 ± 0.05	0.73 ± 0.06	179 ± 25
84	32	2	67.52	-3.00	20.67	5.3	144212 ± 23	13.5 ± 1.0	-2.50 ± 0.08	0.58 ± 0.11	75 ± 23
194	32	2	67.52	-3.00	20.67	3.9	144364 ± 22	8.5 ± 2.4	-2.06 ± 0.28	0.36 ± 0.14	42 ± 24
691	33	1	67.17	-2.65	19.76	7.3	57154 ± 20	9.7 ± 2.6	-0.87 ± 0.16	0.03 ± 0.14	90 ± 27
421	34	3	67.40	-2.96	21.55	3.3	119523 ± 146	2.8 ± 2.2	-0.24 ± 0.55	0.04 ± 0.18	314 ± 92
561	34	3	67.40	-2.96	21.55	2.4	119248 ± 49	3.0 ± 2.5	-0.48 ± 0.68	-0.07 ± 0.11	49 ± 33
630	34	3	67.40	-2.96	21.55	5.3	119376 ± 21	3.5 ± 0.9	-0.83 ± 0.14	0.19 ± 0.09	57 ± 26
102	35	2	67.51	-2.83	21.24	3.0	47656 ± 6817	10.4 ± 3.2	-0.84 ± 0.23	0.66 ± 0.12	36 ± 27
529	35	2	67.51	-2.83	21.24	2.1	133797 ± 9129	11.4 ± 2.7	-1.94 ± 0.56	0.66 ± 0.22	44 ± 41
234	37	1	67.70	-2.90	21.71	3.5	80851 ± 1409	12.2 ± 1.9	-2.25 ± 0.26	-0.02 ± 0.14	40 ± 44
502	38	2	67.45	-2.94	19.78	9.6	124065 ± 15	7.1 ± 0.9	-1.13 ± 0.07	-0.07 ± 0.07	126 ± 7

342	38	2	67.45	-2.94	19.78	15.7	124102 ± 13	10.2 ± 1.2	-1.43 ± 0.06	0.30 ± 0.03	168 ± 8
125	39	2	67.34	-2.70	20.23	4.3	98618 ± 69	11.9 ± 2.1	0.03 ± 0.12	-0.16 ± 0.04	311 ± 40
645	39	2	67.34	-2.70	20.23	8.9	140912 ± 17	14.5 ± 0.4	-1.71 ± 0.04	0.15 ± 0.05	138 ± 10
454	40	2	67.31	-2.94	20.69	3.7	118679 ± 36	13.3 ± 1.3	-1.30 ± 0.11	0.71 ± 0.07	49 ± 28
284	40	2	67.31	-2.94	20.69	10.3	118691 ± 25	12.1 ± 1.6	-1.91 ± 0.12	0.50 ± 0.07	188 ± 17
72	41	2	67.43	-2.90	20.87	-0.6	213400 ± 5417	11.7 ± 3.1	-2.02 ± 0.28	0.11 ± 0.35	47 ± 41
535	41	2	67.43	-2.90	20.87	5.4	117574 ± 28	6.6 ± 1.8	-0.96 ± 0.15	0.09 ± 0.12	121 ± 20
453	43	2	67.30	-2.98	20.00	10.3	104303 ± 27	4.8 ± 0.5	-2.34 ± 0.15	0.71 ± 0.07	130 ± 26
283	43	2	67.30	-2.98	20.00	14.5	104352 ± 19	4.5 ± 0.3	-2.54 ± 0.05	0.70 ± 0.07	147 ± 14
385	44	1	67.58	-2.90	20.14	8.4	130473 ± 14	14.5 ± 0.5	-1.53 ± 0.04	0.05 ± 0.06	114 ± 10
304	45	1	67.26	-2.60	20.26	9.2	124172 ± 19	10.5 ± 1.4	-1.81 ± 0.10	0.35 ± 0.07	134 ± 11
422	46	3	67.40	-2.93	19.07	12.8	119668 ± 21	9.5 ± 1.3	-1.31 ± 0.08	0.34 ± 0.05	218 ± 12
569	46	3	67.40	-2.93	19.07	10.8	119749 ± 28	11.4 ± 1.5	-1.46 ± 0.10	0.29 ± 0.07	239 ± 13
631	46	3	67.40	-2.93	19.07	16.7	119698 ± 14	9.8 ± 1.0	-1.64 ± 0.07	0.39 ± 0.04	189 ± 10
363	47	2	67.54	-2.91	21.73	2.1	123928 ± 65	0.8 ± 0.5	-0.73 ± 0.43	0.25 ± 0.26	40 ± 29
198	47	2	67.54	-2.91	21.73	3.7	138443 ± 81	4.4 ± 1.2	-2.09 ± 0.24	0.23 ± 0.30	81 ± 59
450	48	1	67.30	-3.09	20.80	5.5	54641 ± 24377	3.5 ± 5.1	0.03 ± 0.54	0.10 ± 0.27	296 ± 67
577	49	2	67.33	-2.70	21.54	1.1	129602 ± 255	8.5 ± 3.7	-0.87 ± 0.36	0.58 ± 0.17	98 ± 91
646	49	2	67.33	-2.70	21.54	5.5	131025 ± 32	4.4 ± 1.2	-1.07 ± 0.17	-0.11 ± 0.06	143 ± 20
499	51	1	67.60	-2.76	20.50	3.2	127484 ± 72	13.3 ± 1.5	-1.12 ± 0.14	0.38 ± 0.14	207 ± 48
391	53	3	67.43	-2.95	21.37	1.8	139228 ± 14828	11.2 ± 4.0	-1.42 ± 0.31	0.61 ± 0.19	51 ± 48
530	53	3	67.43	-2.95	21.37	1.3	215273 ± 37	5.2 ± 2.7	-1.90 ± 0.07	0.67 ± 0.10	119 ± 16

591	53	3	67.43	-2.95	21.37	2.6	109748 ± 250	10.0 ± 3.9	-0.44 ± 0.32	-0.11 ± 0.08	312 ± 142
684	54	1	67.26	-3.04	20.37	4.6	152561 ± 36	6.2 ± 1.1	-2.13 ± 0.16	0.58 ± 0.18	69 ± 28
225	55	1	67.66	-2.96	20.34	6.3	139851 ± 41	11.1 ± 1.4	-2.36 ± 0.14	0.28 ± 0.12	103 ± 22
65	56	3	67.44	-2.90	20.87	2.6	116760 ± 32	2.3 ± 1.2	0.18 ± 0.29	0.04 ± 0.12	77 ± 25
540	56	3	67.44	-2.90	20.87	4.8	116818 ± 20	3.0 ± 0.9	-0.87 ± 0.21	0.67 ± 0.09	77 ± 29
600	56	3	67.44	-2.90	20.87	6.0	116939 ± 17	13.4 ± 1.2	-2.14 ± 0.14	0.11 ± 0.12	26 ± 16
63	57	3	67.44	-2.88	19.34	11.0	128065 ± 18	6.5 ± 0.8	-1.38 ± 0.08	0.26 ± 0.05	179 ± 10
544	57	3	67.44	-2.88	19.34	13.8	128237 ± 14	13.2 ± 1.1	-1.33 ± 0.05	0.06 ± 0.04	184 ± 9
346	57	3	67.44	-2.88	19.34	12.7	128209 ± 14	9.1 ± 1.0	-1.38 ± 0.05	0.18 ± 0.04	163 ± 9
432	58	2	67.41	-2.92	21.43	3.7	119400 ± 22	1.8 ± 0.3	0.10 ± 0.27	-0.09 ± 0.08	34 ± 23
173	58	2	67.41	-2.92	21.43	3.1	119507 ± 17	11.8 ± 2.2	-1.72 ± 0.21	0.19 ± 0.20	46 ± 28
22	59	2	67.24	-3.03	19.81	4.9	103613 ± 43	3.7 ± 1.1	-1.16 ± 0.19	0.07 ± 0.15	99 ± 25
685	59	2	67.24	-3.03	19.81	13.8	103657 ± 17	14.6 ± 0.4	-1.79 ± 0.06	0.42 ± 0.05	139 ± 10
692	60	1	67.17	-2.68	20.95	8.4	12934 ± 169	2.8 ± 1.5	-0.55 ± 0.27	0.52 ± 0.20	377 ± 40
9	61	3	67.37	-2.73	19.91	3.4	86317 ± 106	0.5 ± 0.4	-1.13 ± 0.47	0.57 ± 0.19	331 ± 64
119	61	3	67.37	-2.73	19.91	9.7	121335 ± 14	13.9 ± 0.8	-1.72 ± 0.07	0.45 ± 0.07	138 ± 9
640	61	3	67.37	-2.73	19.91	14.2	121305 ± 18	13.9 ± 0.6	-1.66 ± 0.05	0.36 ± 0.04	197 ± 13
113	63	2	67.64	-2.92	21.62	3.9	131310 ± 43	12.9 ± 1.7	-1.78 ± 0.14	0.70 ± 0.08	137 ± 36
486	63	2	67.64	-2.92	21.62	1.0	115632 ± 64	0.7 ± 0.4	-1.73 ± 0.57	0.27 ± 0.28	34 ± 28
232	64	1	67.69	-2.94	20.55	4.6	121124 ± 48	11.9 ± 1.7	-2.45 ± 0.12	-0.08 ± 0.10	112 ± 31
358	66	1	67.54	-3.11	20.54	7.4	131459 ± 18	14.4 ± 0.4	-2.55 ± 0.04	0.75 ± 0.04	90 ± 14
474	67	2	67.19	-2.90	21.29	0.4	191580 ± 13282	3.7 ± 2.9	-1.38 ± 0.34	0.28 ± 0.12	45 ± 27

264	67	2	67.19	-2.90	21.29	8.9	118875 ± 21	4.2 ± 0.6	-1.39 ± 0.11	0.56 ± 0.09	144 ± 11
92	70	2	67.55	-2.85	20.89	4.1	130190 ± 16	2.7 ± 0.8	-1.79 ± 0.27	0.30 ± 0.22	27 ± 19
522	70	2	67.55	-2.85	20.89	3.4	130147 ± 18	2.0 ± 1.0	-0.82 ± 0.36	0.66 ± 0.11	24 ± 19
83	71	2	67.52	-3.00	20.25	22.4	2 ± 2	12.7 ± 0.3	-0.47 ± 0.03	-0.19 ± 0.01	82 ± 8
193	71	2	67.52	-3.00	20.25	9.3	3 ± 2	12.8 ± 0.5	-0.49 ± 0.06	-0.18 ± 0.02	75 ± 13
88	73	2	67.50	-2.92	21.86	2.4	169314 ± 46	1.2 ± 0.2	-1.18 ± 0.23	0.72 ± 0.06	41 ± 31
196	73	2	67.50	-2.92	21.86	2.7	105106 ± 10838	8.2 ± 3.9	-0.76 ± 0.27	-0.08 ± 0.12	312 ± 84
23	74	1	67.24	-3.01	21.72	1.5	157057 ± 39793	5.5 ± 3.7	-1.63 ± 0.84	0.36 ± 0.28	90 ± 93
409	75	3	67.46	-2.75	20.07	4.1	101879 ± 71	9.9 ± 3.2	-1.20 ± 0.18	0.18 ± 0.22	143 ± 42
189	75	3	67.46	-2.75	20.07	11.7	101869 ± 17	12.0 ± 1.7	-1.88 ± 0.13	0.58 ± 0.10	132 ± 10
616	75	3	67.46	-2.75	20.07	9.7	101961 ± 22	9.5 ± 2.0	-1.67 ± 0.13	0.68 ± 0.08	137 ± 16
433	77	3	67.40	-2.85	20.93	3.4	122076 ± 43	11.2 ± 2.5	-0.80 ± 0.15	0.34 ± 0.10	70 ± 44
560	77	3	67.40	-2.85	20.93	5.1	121959 ± 21	7.1 ± 1.8	-1.16 ± 0.15	0.33 ± 0.12	73 ± 18
628	77	3	67.40	-2.85	20.93	8.2	122042 ± 23	12.7 ± 1.5	-1.77 ± 0.10	0.47 ± 0.08	78 ± 24
112	78	2	67.63	-2.96	20.07	8.7	22 ± 18	1.8 ± 0.4	0.39 ± 0.10	-0.17 ± 0.03	94 ± 26
485	78	2	67.63	-2.96	20.07	6.7	44537 ± 73	14.0 ± 1.1	-0.90 ± 0.07	0.76 ± 0.04	311 ± 79
579	79	2	67.32	-2.73	19.95	2.6	122020 ± 48	11.0 ± 3.4	-0.92 ± 0.37	0.05 ± 0.16	101 ± 35
301	79	2	67.32	-2.73	19.95	13.9	121903 ± 14	13.8 ± 0.7	-1.60 ± 0.05	0.33 ± 0.04	144 ± 8
607	80	1	67.48	-2.69	20.52	5.8	130045 ± 19	8.3 ± 2.6	-1.10 ± 0.14	0.23 ± 0.08	111 ± 12
696	81	1	67.16	-2.72	19.56	27.0	130440 ± 8	1.8 ± 0.1	-1.59 ± 0.04	0.78 ± 0.02	110 ± 5
17	83	2	67.20	-2.97	19.07	9.6	95087 ± 60	5.5 ± 0.8	-1.87 ± 0.22	0.21 ± 0.16	357 ± 25
678	83	2	67.20	-2.97	19.07	18.2	95093 ± 23	2.2 ± 0.1	-0.74 ± 0.06	-0.17 ± 0.03	341 ± 10

549	84	2	67.42	-2.70	20.59	3.1	130624 ± 24	3.2 ± 2.0	-0.64 ± 0.33	0.64 ± 0.10	42 ± 30
326	84	2	67.42	-2.70	20.59	7.5	130772 ± 20	13.7 ± 1.1	-1.48 ± 0.06	0.27 ± 0.06	145 ± 12
82	85	1	67.51	-3.09	19.94	8.9	139577 ± 24	3.7 ± 0.3	-2.44 ± 0.11	0.74 ± 0.05	97 ± 13
97	86	2	67.51	-2.74	21.78	1.2	100177 ± 445	12.0 ± 2.6	0.31 ± 0.22	0.03 ± 0.13	29 ± 37
525	86	2	67.51	-2.74	21.78	2.4	127237 ± 70	6.0 ± 4.5	-0.77 ± 0.78	0.18 ± 0.23	124 ± 67
31	88	3	67.41	-2.89	21.95	4.0	118045 ± 42	13.9 ± 0.9	-1.26 ± 0.10	-0.14 ± 0.05	141 ± 25
176	88	3	67.41	-2.89	21.95	4.1	117905 ± 87	12.0 ± 2.1	-1.94 ± 0.25	0.49 ± 0.17	228 ± 70
322	88	3	67.41	-2.89	21.95	4.5	118013 ± 22	9.5 ± 2.2	-1.29 ± 0.16	0.10 ± 0.11	40 ± 22
109	89	1	67.61	-3.06	20.51	8.7	118328 ± 20	14.3 ± 0.6	-1.88 ± 0.10	0.08 ± 0.10	127 ± 13
426	90	1	67.41	-3.00	19.36	13.5	119778 ± 15	12.7 ± 1.2	-1.17 ± 0.06	0.21 ± 0.04	180 ± 13
27	91	3	67.42	-2.78	20.00	8.3	124115 ± 42	13.0 ± 1.6	-0.46 ± 0.08	-0.19 ± 0.01	386 ± 25
552	91	3	67.42	-2.78	20.00	8.5	124085 ± 21	11.7 ± 1.7	-1.08 ± 0.08	-0.09 ± 0.06	180 ± 13
329	91	3	67.42	-2.78	20.00	12.3	124067 ± 19	10.2 ± 1.5	-1.38 ± 0.07	0.20 ± 0.04	202 ± 11
76	92	1	67.49	-3.05	21.00	5.7	129355 ± 21	8.8 ± 2.0	-1.40 ± 0.12	0.22 ± 0.08	72 ± 18
56	93	3	67.39	-2.91	21.76	3.5	119250 ± 41	3.2 ± 1.2	-1.01 ± 0.43	0.22 ± 0.21	75 ± 48
564	93	3	67.39	-2.91	21.76	1.7	119950 ± 58	9.1 ± 4.0	-1.18 ± 0.53	0.05 ± 0.19	39 ± 32
658	93	3	67.39	-2.91	21.76	3.6	119795 ± 33	4.0 ± 3.0	-0.52 ± 0.60	0.19 ± 0.19	35 ± 23
389	94	2	67.42	-2.98	21.36	2.3	138956 ± 39	10.6 ± 2.8	-1.54 ± 0.21	0.70 ± 0.08	36 ± 27
169	94	2	67.42	-2.98	21.36	2.6	139138 ± 70	3.4 ± 2.0	-1.25 ± 0.54	0.67 ± 0.12	29 ± 21
228	95	1	67.67	-2.95	21.92	2.1	163575 ± 1029	0.6 ± 0.4	-2.00 ± 0.36	0.30 ± 0.28	57 ± 39
259	96	1	67.11	-2.90	19.99	12.7	118568 ± 18	10.8 ± 1.3	-2.04 ± 0.13	0.51 ± 0.07	151 ± 11
57	97	3	67.39	-2.91	21.45	4.2	120172 ± 20	9.0 ± 2.6	-1.27 ± 0.18	0.40 ± 0.14	49 ± 25

138	97	3	67.39	-2.91	21.45	4.3	119996 ± 24	6.3 ± 1.8	-1.55 ± 0.20	0.49 ± 0.16	40 ± 21
659	97	3	67.39	-2.91	21.45	4.3	120262 ± 35	9.4 ± 3.1	-1.09 ± 0.23	0.58 ± 0.11	135 ± 24
257	98	1	67.09	-2.93	19.89	11.7	138441 ± 40	1.6 ± 0.2	-2.34 ± 0.30	0.66 ± 0.09	427 ± 7
85	99	2	67.50	-2.99	21.56	0.2	101679 ± 10962	10.3 ± 3.3	0.08 ± 0.39	0.03 ± 0.19	59 ± 60
509	99	2	67.50	-2.99	21.56	1.6	135106 ± 11187	4.1 ± 3.9	-1.96 ± 0.64	0.41 ± 0.30	89 ± 72
44	100	1	67.37	-3.07	21.90	2.0	95694 ± 20482	11.7 ± 2.5	-0.78 ± 0.88	0.30 ± 0.35	134 ± 113
237	101	1	67.70	-2.87	21.39	0.5	128749 ± 28526	8.6 ± 4.2	-0.58 ± 0.74	0.22 ± 0.29	174 ± 132
381	102	2	67.58	-2.84	21.47	2.1	130662 ± 103	7.9 ± 3.5	-0.90 ± 0.28	0.39 ± 0.21	63 ± 40
215	102	2	67.58	-2.84	21.47	3.1	112454 ± 19927	0.6 ± 0.4	-1.29 ± 0.58	0.42 ± 0.27	282 ± 157
377	104	2	67.59	-2.88	20.41	2.5	125414 ± 7960	3.9 ± 4.3	-0.82 ± 0.77	0.46 ± 0.26	31 ± 23
482	104	2	67.59	-2.88	20.41	4.1	121838 ± 56	4.5 ± 0.9	-2.15 ± 0.24	0.65 ± 0.12	101 ± 40
694	105	1	67.18	-2.79	19.33	17.2	119130 ± 12	13.2 ± 0.8	-1.71 ± 0.06	0.40 ± 0.03	130 ± 8
373	106	2	67.59	-2.84	20.03	5.3	129407 ± 33	12.1 ± 2.0	-1.35 ± 0.12	0.43 ± 0.10	166 ± 16
213	106	2	67.59	-2.84	20.03	6.3	129573 ± 53	14.1 ± 0.8	-1.62 ± 0.06	0.10 ± 0.09	314 ± 28
584	107	2	67.30	-2.71	19.44	5.0	122103 ± 28	1.9 ± 1.3	0.15 ± 0.44	-0.10 ± 0.09	98 ± 18
308	107	2	67.30	-2.71	19.44	20.0	121837 ± 14	12.1 ± 0.7	-1.41 ± 0.04	0.10 ± 0.03	226 ± 8
405	109	3	67.50	-2.83	19.45	5.7	121800 ± 9	2.1 ± 0.1	-0.35 ± 0.09	-0.14 ± 0.06	53 ± 21
183	109	3	67.50	-2.83	19.45	13.5	121675 ± 18	14.1 ± 0.8	-1.59 ± 0.05	0.03 ± 0.06	199 ± 10
353	109	3	67.50	-2.83	19.45	10.2	121764 ± 21	12.1 ± 1.5	-1.31 ± 0.08	0.22 ± 0.05	196 ± 13
677	110	1	67.21	-2.99	21.54	6.5	149195 ± 15	2.6 ± 0.4	-1.58 ± 0.09	0.74 ± 0.05	47 ± 20
668	112	1	67.20	-2.81	21.41	7.6	118029 ± 15	13.6 ± 1.1	-1.64 ± 0.10	0.41 ± 0.08	92 ± 22
467	114	3	67.32	-2.84	21.33	1.1	159331 ± 2251	6.2 ± 3.1	-0.74 ± 0.18	0.65 ± 0.15	79 ± 62

583	114	3	67.32	-2.84	21.33	2.0	119674 ± 438	4.3 ± 3.2	-0.79 ± 0.55	0.36 ± 0.28	123 ± 68
288	114	3	67.32	-2.84	21.33	6.7	119810 ± 16	12.4 ± 1.7	-1.85 ± 0.12	0.68 ± 0.08	75 ± 24
62	115	3	67.44	-2.87	20.47	6.8	128273 ± 11	13.5 ± 1.2	-2.03 ± 0.12	0.52 ± 0.11	48 ± 22
507	115	3	67.44	-2.87	20.47	7.1	128322 ± 17	13.6 ± 1.1	-1.68 ± 0.07	-0.13 ± 0.05	103 ± 15
347	115	3	67.44	-2.87	20.47	6.6	128348 ± 19	10.3 ± 1.8	-1.26 ± 0.09	0.29 ± 0.06	116 ± 11
5	116	2	67.37	-2.87	21.85	4.1	120404 ± 1735	11.1 ± 5.2	-1.74 ± 0.91	0.55 ± 0.33	165 ± 121
656	116	2	67.37	-2.87	21.85	3.2	119324 ± 49	5.3 ± 3.3	-1.04 ± 0.42	0.59 ± 0.13	98 ± 50
462	117	3	67.33	-2.76	19.49	4.2	121413 ± 53	4.3 ± 1.1	-1.53 ± 0.27	0.36 ± 0.23	106 ± 48
580	117	3	67.33	-2.76	19.49	9.4	121287 ± 15	7.7 ± 0.9	-1.58 ± 0.10	0.25 ± 0.08	96 ± 13
648	117	3	67.33	-2.76	19.49	22.4	121315 ± 8	8.2 ± 0.2	-1.59 ± 0.03	0.34 ± 0.03	121 ± 5
87	118	2	67.50	-2.97	20.43	9.4	120593 ± 20	9.3 ± 1.6	-1.22 ± 0.10	0.14 ± 0.07	160 ± 14
510	118	2	67.50	-2.97	20.43	6.2	120549 ± 12	6.1 ± 1.2	-1.21 ± 0.11	0.47 ± 0.10	63 ± 18
33	120	3	67.41	-2.90	21.42	2.8	121169 ± 20	0.7 ± 0.4	0.05 ± 0.28	0.11 ± 0.21	39 ± 31
174	120	3	67.41	-2.90	21.42	4.4	121136 ± 38	7.9 ± 2.6	-1.43 ± 0.21	0.62 ± 0.12	124 ± 23
320	120	3	67.41	-2.90	21.42	5.5	121209 ± 43	12.8 ± 1.6	-1.55 ± 0.12	0.27 ± 0.11	198 ± 33
80	121	2	67.48	-2.93	20.12	16.0	117790 ± 17	11.4 ± 1.0	-1.74 ± 0.07	0.49 ± 0.05	82 ± 10
513	121	2	67.48	-2.93	20.12	12.3	117867 ± 11	10.3 ± 1.4	-1.46 ± 0.09	0.26 ± 0.05	93 ± 10
425	122	1	67.42	-3.00	21.78	2.4	138876 ± 38	0.9 ± 0.5	-0.15 ± 0.32	0.35 ± 0.23	21 ± 16
188	123	2	67.49	-2.73	19.36	11.7	124538 ± 19	9.2 ± 1.0	-1.51 ± 0.07	0.05 ± 0.06	189 ± 10
609	123	2	67.49	-2.73	19.36	14.1	124620 ± 15	7.4 ± 0.9	-1.20 ± 0.06	0.15 ± 0.04	198 ± 9
417	124	1	67.41	-3.16	20.09	3.9	92527 ± 34	12.1 ± 2.3	-1.27 ± 0.20	0.51 ± 0.20	49 ± 30
271	125	1	67.23	-2.68	20.98	7.7	141569 ± 23	14.7 ± 0.3	-1.79 ± 0.06	-0.10 ± 0.07	167 ± 13

42	126	1	67.38	-3.12	19.72	9.0	123896 ± 18	13.5 ± 1.1	-1.39 ± 0.06	0.08 ± 0.06	149 ± 10
233	128	1	67.68	-2.91	21.53	2.2	131787 ± 2848	7.1 ± 3.6	-1.20 ± 0.35	0.17 ± 0.22	178 ± 105
428	129	3	67.41	-2.94	20.29	7.5	119864 ± 29	11.6 ± 1.8	-0.99 ± 0.09	0.09 ± 0.07	179 ± 15
171	129	3	67.41	-2.94	20.29	3.9	212287 ± 250	13.6 ± 1.2	-1.83 ± 0.04	-0.19 ± 0.01	427 ± 9
318	129	3	67.41	-2.94	20.29	11.0	119942 ± 23	11.6 ± 1.6	-1.37 ± 0.09	0.29 ± 0.05	224 ± 13
267	130	1	67.26	-2.59	19.78	10.9	124163 ± 18	9.6 ± 1.6	-1.27 ± 0.08	0.25 ± 0.04	182 ± 11
197	131	1	67.54	-2.92	20.95	5.3	138449 ± 23	11.5 ± 1.7	-2.41 ± 0.13	0.68 ± 0.08	63 ± 24
371	132	2	67.57	-2.97	21.53	2.4	167866 ± 1566	2.2 ± 0.5	-1.35 ± 0.15	0.60 ± 0.11	263 ± 54
202	132	2	67.57	-2.97	21.53	2.7	151882 ± 15	7.8 ± 3.2	-1.58 ± 0.19	0.66 ± 0.12	42 ± 27
407	133	2	67.50	-2.86	19.74	0.1	109426 ± 12855	9.4 ± 3.5	-0.35 ± 0.47	0.21 ± 0.28	120 ± 70
515	133	2	67.50	-2.86	19.74	6.8	119944 ± 22	8.4 ± 1.5	-0.98 ± 0.09	-0.10 ± 0.08	116 ± 10
48	134	2	67.37	-2.94	19.98	9.3	138672 ± 15	14.5 ± 0.3	-1.66 ± 0.03	0.24 ± 0.04	127 ± 6
652	134	2	67.37	-2.94	19.98	5.7	138694 ± 28	13.2 ± 1.5	-1.42 ± 0.07	0.54 ± 0.05	157 ± 14
47	135	3	67.36	-2.94	20.21	8.1	118700 ± 25	13.9 ± 0.8	-1.62 ± 0.08	0.53 ± 0.08	147 ± 14
131	135	3	67.36	-2.94	20.21	5.3	118649 ± 41	13.2 ± 1.5	-1.99 ± 0.18	0.64 ± 0.11	153 ± 28
293	135	3	67.36	-2.94	20.21	0.3	139693 ± 55825	9.1 ± 3.9	-1.08 ± 0.74	0.35 ± 0.29	229 ± 125
6	137	3	67.37	-2.88	20.31	10.9	118160 ± 21	11.3 ± 1.5	-1.31 ± 0.09	-0.05 ± 0.07	205 ± 12
136	137	3	67.37	-2.88	20.31	8.3	117841 ± 32	13.2 ± 1.3	-1.86 ± 0.13	0.45 ± 0.11	210 ± 19
655	137	3	67.37	-2.88	20.31	11.8	118268 ± 21	9.5 ± 1.3	-1.14 ± 0.08	0.16 ± 0.05	222 ± 14
524	138	1	67.51	-2.74	19.04	28.4	3 ± 2	12.5 ± 0.1	-0.36 ± 0.02	-0.20 ± 0.00	138 ± 6
459	139	2	67.34	-2.95	20.14	7.9	119264 ± 22	12.0 ± 2.0	-1.49 ± 0.13	0.48 ± 0.09	119 ± 15
291	139	2	67.34	-2.95	20.14	15.4	119228 ± 12	14.2 ± 0.5	-1.63 ± 0.04	0.46 ± 0.04	141 ± 8

54	140	3	67.39	-2.96	19.79	8.2	119101 ± 11	14.4 ± 0.5	-1.63 ± 0.07	0.22 ± 0.07	82 ± 17
562	140	3	67.39	-2.96	19.79	6.1	119094 ± 28	9.9 ± 1.9	-1.35 ± 0.13	0.11 ± 0.10	133 ± 17
622	140	3	67.39	-2.96	19.79	10.2	119195 ± 16	12.9 ± 1.3	-1.53 ± 0.08	0.15 ± 0.06	120 ± 9
236	141	1	67.70	-2.88	21.28	2.2	32487 ± 34158	5.9 ± 4.7	-1.21 ± 0.88	0.37 ± 0.28	91 ± 73
108	143	2	67.59	-2.91	19.29	8.2	140254 ± 24	14.8 ± 0.2	-1.50 ± 0.04	-0.19 ± 0.01	205 ± 16
478	143	2	67.59	-2.91	19.29	7.4	140130 ± 33	14.6 ± 0.2	-1.33 ± 0.04	-0.18 ± 0.02	262 ± 23
440	144	3	67.40	-2.81	21.07	1.7	120084 ± 43	12.1 ± 2.4	-0.49 ± 0.15	-0.11 ± 0.09	32 ± 23
556	144	3	67.40	-2.81	21.07	3.4	119913 ± 29	12.6 ± 1.8	-1.32 ± 0.15	0.24 ± 0.15	28 ± 27
340	144	3	67.40	-2.81	21.07	3.9	119893 ± 40	7.7 ± 2.3	-1.77 ± 0.27	0.58 ± 0.14	78 ± 38
429	145	3	67.41	-2.93	20.61	5.5	120070 ± 18	10.9 ± 2.5	-1.09 ± 0.16	0.01 ± 0.09	78 ± 30
172	145	3	67.41	-2.93	20.61	0.1	133961 ± 13329	9.1 ± 3.6	-0.73 ± 0.46	0.15 ± 0.21	105 ± 120
319	145	3	67.41	-2.93	20.61	9.6	120056 ± 21	12.9 ± 1.3	-1.80 ± 0.08	0.40 ± 0.06	68 ± 16
356	146	1	67.53	-3.13	21.68	1.0	131079 ± 22152	8.4 ± 3.6	-0.66 ± 0.53	0.05 ± 0.17	212 ± 122
30	147	2	67.41	-2.88	21.26	6.1	119212 ± 25	14.2 ± 0.7	-1.19 ± 0.06	-0.05 ± 0.08	154 ± 13
323	147	2	67.41	-2.88	21.26	7.2	119268 ± 17	10.1 ± 1.9	-1.53 ± 0.14	0.45 ± 0.09	73 ± 20
434	148	3	67.40	-2.87	20.00	7.6	119078 ± 22	12.5 ± 1.7	-1.01 ± 0.08	0.05 ± 0.07	156 ± 14
575	148	3	67.40	-2.87	20.00	10.5	119162 ± 20	5.9 ± 0.7	-1.04 ± 0.07	0.09 ± 0.06	189 ± 12
627	148	3	67.40	-2.87	20.00	14.8	119271 ± 10	14.2 ± 0.5	-1.61 ± 0.04	0.37 ± 0.03	119 ± 9
471	150	2	67.21	-2.82	21.69	0.2	106360 ± 1038	11.9 ± 2.4	0.33 ± 0.15	-0.13 ± 0.09	33 ± 29
669	150	2	67.21	-2.82	21.69	3.8	143658 ± 47	4.7 ± 0.9	-2.05 ± 0.25	0.61 ± 0.14	49 ± 30
218	151	1	67.56	-2.75	21.16	4.2	134613 ± 35	12.9 ± 1.5	-1.89 ± 0.13	0.18 ± 0.14	121 ± 37
18	152	2	67.22	-2.94	20.90	1.7	73819 ± 41	11.7 ± 2.5	-0.12 ± 0.23	0.41 ± 0.22	49 ± 41

679	152	2	67.22	-2.94	20.90	5.5	159360 ± 26	3.8 ± 0.5	-2.22 ± 0.15	0.65 ± 0.10	32 ± 20
226	153	1	67.66	-2.95	21.73	3.4	50745 ± 738	0.7 ± 0.4	-2.00 ± 0.57	0.30 ± 0.29	129 ± 101
553	154	1	67.40	-2.60	20.73	1.7	97088 ± 107	11.8 ± 2.3	0.16 ± 0.22	0.07 ± 0.21	120 ± 137
680	155	1	67.21	-2.93	20.72	4.3	147654 ± 28	12.7 ± 1.6	-2.16 ± 0.19	0.42 ± 0.25	50 ± 29
25	156	2	67.26	-2.91	20.99	1.3	161430 ± 232	13.4 ± 0.6	-1.33 ± 0.07	0.12 ± 0.06	385 ± 69
689	156	2	67.26	-2.91	20.99	1.0	157482 ± 171	13.2 ± 1.2	-1.19 ± 0.08	0.28 ± 0.06	283 ± 57
357	157	1	67.55	-3.12	21.20	4.2	131504 ± 13	8.5 ± 2.8	-1.92 ± 0.20	0.67 ± 0.09	46 ± 19
177	158	1	67.51	-2.60	19.84	6.7	101431 ± 27	2.4 ± 0.6	-0.95 ± 0.26	0.12 ± 0.16	94 ± 17
415	159	3	67.46	-2.88	20.42	7.8	151929 ± 11	4.9 ± 0.5	-1.82 ± 0.07	0.73 ± 0.06	45 ± 18
506	159	3	67.46	-2.88	20.42	8.6	151884 ± 25	4.1 ± 0.3	-2.27 ± 0.16	0.19 ± 0.22	79 ± 22
350	159	3	67.46	-2.88	20.42	9.9	151927 ± 15	4.7 ± 0.5	-1.73 ± 0.05	0.57 ± 0.06	114 ± 8
547	160	2	67.41	-2.68	19.59	3.9	130767 ± 27	12.5 ± 1.9	-1.26 ± 0.10	0.11 ± 0.10	80 ± 26
334	160	2	67.41	-2.68	19.59	9.1	130774 ± 16	13.8 ± 0.9	-1.49 ± 0.05	0.33 ± 0.05	142 ± 9
26	161	3	67.41	-2.78	19.94	5.3	124489 ± 32	8.7 ± 1.8	-1.63 ± 0.14	-0.09 ± 0.09	115 ± 16
551	161	3	67.41	-2.78	19.94	9.2	124507 ± 20	5.9 ± 0.6	-1.42 ± 0.07	-0.11 ± 0.06	143 ± 12
338	161	3	67.41	-2.78	19.94	12.1	124564 ± 15	6.6 ± 0.7	-1.49 ± 0.07	0.34 ± 0.05	119 ± 9
261	162	1	67.17	-3.01	20.72	8.9	135195 ± 15	4.8 ± 0.5	-2.56 ± 0.04	0.47 ± 0.13	84 ± 16
383	163	2	67.58	-2.86	21.45	1.2	26070 ± 37252	9.5 ± 4.8	-0.17 ± 0.81	0.10 ± 0.25	93 ± 87
206	163	2	67.58	-2.86	21.45	3.8	137334 ± 60	8.5 ± 2.3	-2.42 ± 0.16	0.46 ± 0.19	140 ± 44
463	164	3	67.30	-2.79	19.48	7.0	118281 ± 28	13.4 ± 1.3	-1.27 ± 0.10	0.16 ± 0.09	154 ± 18
588	164	3	67.30	-2.79	19.48	7.8	118375 ± 28	13.1 ± 1.4	-1.21 ± 0.11	0.19 ± 0.08	186 ± 24
309	164	3	67.30	-2.79	19.48	16.6	118418 ± 12	14.6 ± 0.3	-1.88 ± 0.05	0.51 ± 0.04	151 ± 9

460	165	2	67.35	-2.94	21.99	1.2	192602 ± 76	3.0 ± 0.5	-1.47 ± 0.10	0.41 ± 0.09	333 ± 25
292	165	2	67.35	-2.94	21.99	4.3	117474 ± 38	4.5 ± 1.0	-1.95 ± 0.26	0.62 ± 0.13	67 ± 48
492	166	1	67.68	-2.76	21.39	0.3	144114 ± 23	4.3 ± 1.9	0.07 ± 0.20	-0.17 ± 0.03	20 ± 14
404	167	3	67.48	-2.82	21.52	2.4	179421 ± 73	0.5 ± 0.3	-2.34 ± 0.21	0.37 ± 0.27	75 ± 46
191	167	3	67.48	-2.82	21.52	3.4	48827 ± 160	8.3 ± 4.8	-0.37 ± 0.38	-0.11 ± 0.09	48 ± 54
354	167	3	67.48	-2.82	21.52	0.8	111725 ± 45933	7.2 ± 4.1	-1.27 ± 0.70	0.36 ± 0.28	183 ± 117
78	168	2	67.48	-2.95	21.34	2.9	81623 ± 58	4.7 ± 2.3	0.11 ± 0.29	-0.10 ± 0.13	165 ± 49
511	168	2	67.48	-2.95	21.34	1.1	190086 ± 83	1.9 ± 0.5	-1.51 ± 0.22	0.31 ± 0.20	45 ± 36
468	169	3	67.32	-2.86	20.86	3.3	130572 ± 58	12.2 ± 2.1	-1.97 ± 0.20	0.69 ± 0.08	67 ± 40
137	169	3	67.32	-2.86	20.86	4.4	130367 ± 40	6.2 ± 3.5	-1.77 ± 0.34	0.49 ± 0.17	86 ± 16
286	169	3	67.32	-2.86	20.86	7.9	130393 ± 18	11.3 ± 1.5	-1.25 ± 0.06	-0.17 ± 0.03	129 ± 12
101	171	2	67.52	-2.82	20.41	5.1	37672 ± 260	13.0 ± 1.9	-0.96 ± 0.11	0.74 ± 0.06	353 ± 63
528	171	2	67.52	-2.82	20.41	3.3	152065 ± 19	9.9 ± 2.7	-1.56 ± 0.12	0.71 ± 0.07	61 ± 22
255	173	1	67.09	-2.96	20.20	12.0	109998 ± 23	14.5 ± 0.4	-2.40 ± 0.09	0.76 ± 0.03	162 ± 13
2	174	3	67.38	-2.77	19.93	5.4	119936 ± 33	9.6 ± 2.1	-1.68 ± 0.17	0.53 ± 0.15	125 ± 21
122	174	3	67.38	-2.77	19.93	11.9	119926 ± 15	7.3 ± 0.8	-1.54 ± 0.09	0.42 ± 0.06	116 ± 8
337	174	3	67.38	-2.77	19.93	13.3	120035 ± 14	13.2 ± 0.9	-1.79 ± 0.06	0.63 ± 0.06	106 ± 8
35	175	2	67.40	-2.85	20.87	4.7	120801 ± 54	12.1 ± 2.0	-1.28 ± 0.13	0.22 ± 0.12	205 ± 21
558	175	2	67.40	-2.85	20.87	6.2	120971 ± 26	11.5 ± 2.1	-1.11 ± 0.11	0.12 ± 0.10	135 ± 16
362	176	2	67.55	-2.93	20.21	10.4	80833 ± 28	1.4 ± 0.1	0.05 ± 0.05	0.77 ± 0.03	228 ± 25
204	176	2	67.55	-2.93	20.21	9.2	166458 ± 17	3.0 ± 0.1	-2.57 ± 0.02	0.43 ± 0.09	134 ± 9
111	177	2	67.61	-2.97	20.88	2.3	126088 ± 35238	9.0 ± 3.7	-1.89 ± 0.96	0.37 ± 0.24	64 ± 75

484	177	2	67.61	-2.97	20.88	0.4	210098 ± 18063	0.8 ± 1.3	-1.66 ± 0.51	0.25 ± 0.33	128 ± 90
699	180	1	67.15	-2.82	20.94	7.6	119440 ± 25	11.3 ± 1.9	-1.46 ± 0.11	0.28 ± 0.07	105 ± 16
71	181	3	67.43	-2.89	21.07	6.0	121313 ± 27	12.4 ± 1.7	-1.44 ± 0.11	0.46 ± 0.09	114 ± 22
542	181	3	67.43	-2.89	21.07	3.3	121411 ± 42	9.4 ± 3.3	-0.93 ± 0.21	0.11 ± 0.13	120 ± 26
602	181	3	67.43	-2.89	21.07	6.1	121463 ± 9	13.7 ± 1.1	-1.92 ± 0.10	0.37 ± 0.10	37 ± 22
256	182	1	67.12	-2.95	21.10	5.1	77577 ± 34	7.2 ± 1.7	-2.35 ± 0.19	0.35 ± 0.27	55 ± 32
10	183	3	67.34	-2.73	21.91	0.9	128202 ± 82	13.0 ± 1.3	0.01 ± 0.09	0.52 ± 0.15	238 ± 45
127	183	3	67.34	-2.73	21.91	2.6	51482 ± 9	5.4 ± 2.2	0.12 ± 0.21	0.22 ± 0.19	28 ± 19
647	183	3	67.34	-2.73	21.91	3.1	118167 ± 35	6.0 ± 3.2	-0.89 ± 0.38	0.64 ± 0.14	76 ± 67
16	184	2	67.23	-2.99	20.79	2.5	91901 ± 9195	12.2 ± 2.8	-1.14 ± 0.24	-0.07 ± 0.12	45 ± 70
676	184	2	67.23	-2.99	20.79	7.9	132618 ± 17	2.9 ± 0.5	-1.69 ± 0.10	0.65 ± 0.09	49 ± 29
439	185	3	67.39	-2.81	20.85	4.4	120569 ± 32	11.9 ± 2.1	-1.21 ± 0.12	0.26 ± 0.11	44 ± 25
123	185	3	67.39	-2.81	20.85	8.0	120518 ± 29	12.2 ± 1.7	-2.04 ± 0.16	0.57 ± 0.12	161 ± 23
339	185	3	67.39	-2.81	20.85	7.0	120656 ± 23	12.2 ± 1.7	-1.32 ± 0.09	0.22 ± 0.07	130 ± 15
554	186	1	67.41	-2.60	20.38	2.7	134334 ± 62	1.3 ± 0.6	-1.94 ± 0.42	0.47 ± 0.24	46 ± 30
366	187	1	67.57	-3.12	21.68	1.2	193404 ± 75	3.4 ± 0.3	-1.05 ± 0.02	-0.18 ± 0.02	309 ± 21
667	188	1	67.21	-2.77	21.53	6.5	119321 ± 37	9.1 ± 2.2	-1.16 ± 0.15	0.26 ± 0.07	219 ± 25
475	189	2	67.21	-2.91	20.40	1.9	118485 ± 55	3.5 ± 2.6	-0.67 ± 0.39	0.62 ± 0.16	48 ± 51
682	189	2	67.21	-2.91	20.40	8.7	118626 ± 10	10.9 ± 1.6	-1.84 ± 0.11	0.73 ± 0.06	19 ± 13
445	190	3	67.39	-2.89	21.24	3.5	118053 ± 27	11.6 ± 2.5	-0.77 ± 0.16	-0.12 ± 0.06	85 ± 28
566	190	3	67.39	-2.89	21.24	3.1	118220 ± 13	4.4 ± 2.8	-0.10 ± 0.37	-0.12 ± 0.08	40 ± 23
661	190	3	67.39	-2.89	21.24	3.7	118197 ± 44	2.5 ± 1.4	-0.27 ± 0.29	0.68 ± 0.09	153 ± 28

518	191	1	67.53	-2.67	21.47	1.4	153328 ± 1850	12.5 ± 1.8	-1.23 ± 0.08	0.28 ± 0.07	131 ± 49
105	192	1	67.60	-3.04	21.93	4.1	130623 ± 23	1.3 ± 0.7	-0.00 ± 0.41	0.18 ± 0.25	96 ± 18
441	194	2	67.40	-2.85	21.47	1.3	189585 ± 3433	1.8 ± 1.1	-1.56 ± 0.68	0.64 ± 0.16	47 ± 35
559	194	2	67.40	-2.85	21.47	1.3	8323 ± 4182	0.8 ± 0.5	-1.99 ± 0.45	0.25 ± 0.28	48 ± 39
392	195	3	67.42	-2.94	20.43	6.3	120041 ± 30	7.1 ± 2.0	-1.23 ± 0.16	0.69 ± 0.08	120 ± 14
531	195	3	67.42	-2.94	20.43	6.4	120034 ± 18	13.4 ± 1.2	-1.27 ± 0.07	-0.04 ± 0.09	73 ± 15
592	195	3	67.42	-2.94	20.43	9.0	120153 ± 18	13.5 ± 1.2	-1.74 ± 0.07	0.34 ± 0.06	129 ± 10
41	197	3	67.41	-2.89	21.75	4.7	119841 ± 136	12.7 ± 1.8	-2.04 ± 0.21	0.69 ± 0.09	392 ± 34
162	197	3	67.41	-2.89	21.75	4.3	119754 ± 39	14.1 ± 0.9	-2.25 ± 0.16	0.73 ± 0.06	29 ± 24
312	197	3	67.41	-2.89	21.75	4.5	119871 ± 30	12.7 ± 1.7	-2.16 ± 0.19	0.68 ± 0.09	45 ± 29
77	198	2	67.48	-3.00	20.51	6.5	130692 ± 31	8.2 ± 1.5	-2.43 ± 0.13	0.01 ± 0.13	41 ± 24
508	198	2	67.48	-3.00	20.51	4.0	130445 ± 17	2.4 ± 0.7	-1.78 ± 0.25	0.64 ± 0.13	17 ± 13
13	199	3	67.36	-2.77	19.88	2.9	105599 ± 19262	1.6 ± 2.6	-1.14 ± 0.69	0.54 ± 0.22	282 ± 100
129	199	3	67.36	-2.77	19.88	7.5	74680 ± 50	5.6 ± 0.9	-2.18 ± 0.27	-0.02 ± 0.14	103 ± 47
643	199	3	67.36	-2.77	19.88	7.4	110031 ± 75	2.0 ± 0.4	-1.27 ± 0.24	0.76 ± 0.04	384 ± 31
578	200	2	67.32	-2.72	19.47	3.2	121323 ± 76	7.6 ± 3.4	-0.91 ± 0.24	0.25 ± 0.22	186 ± 40
300	200	2	67.32	-2.72	19.47	15.5	121228 ± 15	14.1 ± 0.6	-1.84 ± 0.05	0.30 ± 0.04	158 ± 10
43	201	1	67.36	-3.10	20.91	8.0	83435 ± 7	2.6 ± 0.5	-1.19 ± 0.14	-0.10 ± 0.08	34 ± 19
100	202	3	67.51	-2.79	20.24	1.2	98266 ± 53978	5.0 ± 4.2	-1.38 ± 0.80	0.28 ± 0.28	181 ± 116
181	202	3	67.51	-2.79	20.24	11.0	124499 ± 8	7.7 ± 0.5	-2.33 ± 0.12	-0.12 ± 0.06	79 ± 11
613	202	3	67.51	-2.79	20.24	8.8	124540 ± 22	6.1 ± 0.6	-2.02 ± 0.14	0.14 ± 0.12	126 ± 16
61	203	3	67.43	-2.86	20.64	6.2	117751 ± 29	10.4 ± 1.9	-1.23 ± 0.14	0.33 ± 0.09	129 ± 14

545	203	3	67.43	-2.86	20.64	6.1	117738 ± 17	8.6 ± 2.1	-1.07 ± 0.13	0.21 ± 0.08	97 ± 14
605	203	3	67.43	-2.86	20.64	6.3	117750 ± 26	11.6 ± 1.9	-1.43 ± 0.12	0.12 ± 0.08	86 ± 17
266	204	1	67.19	-2.83	21.03	7.4	144437 ± 21	14.1 ± 0.8	-1.86 ± 0.05	0.24 ± 0.07	131 ± 11
117	205	2	67.37	-2.63	19.72	7.6	103931 ± 14	14.0 ± 0.9	-1.67 ± 0.10	0.33 ± 0.10	72 ± 19
333	205	2	67.37	-2.63	19.72	16.4	103919 ± 12	14.7 ± 0.3	-1.80 ± 0.05	0.50 ± 0.05	119 ± 8
79	207	2	67.49	-2.93	21.23	4.8	124205 ± 40	5.4 ± 2.6	-0.99 ± 0.50	0.44 ± 0.15	168 ± 20
512	207	2	67.49	-2.93	21.23	2.1	124136 ± 43	9.0 ± 3.6	-0.28 ± 0.25	0.30 ± 0.15	68 ± 35
430	208	3	67.42	-2.93	21.15	5.6	119025 ± 23	12.0 ± 2.1	-1.20 ± 0.14	0.30 ± 0.09	59 ± 28
533	208	3	67.42	-2.93	21.15	4.0	119296 ± 55	12.8 ± 1.7	-1.13 ± 0.14	-0.00 ± 0.11	197 ± 26
594	208	3	67.42	-2.93	21.15	6.8	119028 ± 25	12.8 ± 1.6	-1.74 ± 0.11	0.70 ± 0.07	129 ± 17
64	209	3	67.44	-2.90	21.05	7.4	120596 ± 19	11.3 ± 1.9	-1.59 ± 0.12	0.41 ± 0.09	122 ± 16
541	209	3	67.44	-2.90	21.05	4.3	120750 ± 48	6.9 ± 3.5	-0.43 ± 0.23	0.32 ± 0.09	211 ± 23
601	209	3	67.44	-2.90	21.05	7.2	120675 ± 22	13.4 ± 1.3	-1.52 ± 0.08	0.41 ± 0.08	125 ± 14
229	210	1	67.65	-2.87	20.80	7.0	14 ± 8	13.0 ± 1.1	-0.53 ± 0.10	-0.14 ± 0.07	85 ± 23
4	212	3	67.38	-2.86	21.29	5.6	119012 ± 20	13.3 ± 1.4	-1.33 ± 0.10	0.13 ± 0.11	127 ± 13
143	212	3	67.38	-2.86	21.29	4.2	70198 ± 365	0.6 ± 0.4	-0.71 ± 0.24	0.64 ± 0.12	13 ± 10
665	212	3	67.38	-2.86	21.29	6.7	119104 ± 23	11.6 ± 1.9	-1.38 ± 0.11	0.21 ± 0.08	73 ± 25
629	214	1	67.39	-2.84	19.02	23.5	121868 ± 9	12.6 ± 0.4	-1.40 ± 0.02	0.23 ± 0.02	166 ± 6
265	215	1	67.17	-2.87	20.14	11.7	101655 ± 3	3.9 ± 0.3	-2.28 ± 0.14	0.71 ± 0.07	15 ± 11
268	216	1	67.26	-2.64	21.30	6.6	119451 ± 23	10.7 ± 2.2	-1.56 ± 0.15	0.25 ± 0.09	120 ± 17
412	218	3	67.46	-2.81	20.83	5.7	124028 ± 30	12.3 ± 1.7	-1.14 ± 0.09	-0.13 ± 0.06	167 ± 21
151	218	3	67.46	-2.81	20.83	9.8	124003 ± 16	14.0 ± 0.8	-1.57 ± 0.05	0.06 ± 0.06	152 ± 8

621	218	3	67.46	-2.81	20.83	7.4	124210 ± 24	13.6 ± 1.0	-1.61 ± 0.07	0.46 ± 0.07	142 ± 15
235	219	1	67.69	-2.89	21.68	2.7	139764 ± 5887	9.6 ± 2.5	-2.31 ± 0.18	0.11 ± 0.22	36 ± 32
145	220	1	67.45	-2.62	20.69	5.2	44067 ± 31686	4.8 ± 5.4	-1.14 ± 0.59	0.20 ± 0.27	290 ± 138
695	221	1	67.16	-2.79	20.34	6.7	119646 ± 49	7.7 ± 1.0	-2.43 ± 0.13	0.53 ± 0.14	213 ± 20
11	222	2	67.37	-2.74	20.38	1.9	73415 ± 399	12.2 ± 2.3	-0.41 ± 0.22	0.01 ± 0.17	96 ± 64
120	222	2	67.37	-2.74	20.38	6.2	116700 ± 48	12.5 ± 1.7	-1.90 ± 0.17	0.11 ± 0.14	211 ± 26
124	223	2	67.34	-2.64	19.04	10.3	90137 ± 64	10.2 ± 2.2	-2.16 ± 0.19	0.74 ± 0.05	430 ± 6
644	223	2	67.34	-2.64	19.04	47.2	23 ± 3	12.7 ± 0.1	-0.38 ± 0.01	-0.20 ± 0.00	98 ± 4
58	224	3	67.44	-2.79	19.15	13.1	119500 ± 15	10.1 ± 1.1	-1.73 ± 0.09	0.41 ± 0.06	140 ± 9
155	224	3	67.44	-2.79	19.15	14.4	119439 ± 13	8.7 ± 0.7	-1.44 ± 0.06	0.32 ± 0.04	164 ± 7
330	224	3	67.44	-2.79	19.15	14.8	119482 ± 13	10.4 ± 1.2	-1.89 ± 0.08	0.71 ± 0.05	127 ± 8
260	225	1	67.12	-2.90	21.08	7.6	142310 ± 17	10.1 ± 1.2	-1.95 ± 0.09	0.27 ± 0.08	112 ± 11
548	226	2	67.41	-2.69	20.57	6.4	21 ± 15	12.9 ± 1.0	-0.18 ± 0.10	-0.17 ± 0.03	148 ± 21
335	226	2	67.41	-2.69	20.57	17.0	90 ± 6	12.6 ± 0.2	-0.26 ± 0.03	-0.20 ± 0.00	93 ± 9
449	227	1	67.26	-3.11	21.99	0.2	144391 ± 41	9.3 ± 3.7	0.35 ± 0.10	-0.03 ± 0.04	58 ± 35
408	228	2	67.49	-2.90	20.57	5.7	118078 ± 10	11.8 ± 1.8	-0.96 ± 0.09	-0.17 ± 0.03	39 ± 24
514	228	2	67.49	-2.90	20.57	7.5	118147 ± 27	12.7 ± 0.8	-0.58 ± 0.06	-0.19 ± 0.01	238 ± 16
46	229	2	67.38	-3.00	21.02	6.7	119349 ± 7	1.4 ± 0.1	0.04 ± 0.06	0.68 ± 0.08	52 ± 16
650	229	2	67.38	-3.00	21.02	6.8	119594 ± 25	13.6 ± 1.2	-1.53 ± 0.08	0.27 ± 0.07	80 ± 19
469	232	1	67.28	-2.78	19.54	2.3	118553 ± 70	9.7 ± 2.9	-0.33 ± 0.21	0.53 ± 0.15	149 ± 32
587	233	2	67.31	-2.73	20.43	3.6	101874 ± 65	6.3 ± 2.2	-1.97 ± 0.28	0.58 ± 0.17	46 ± 31
302	233	2	67.31	-2.73	20.43	15.4	101361 ± 24	4.1 ± 0.2	-2.57 ± 0.03	0.69 ± 0.08	254 ± 10

376	234	2	67.61	-2.87	21.32	1.1	168784 ± 4720	11.3 ± 2.9	-1.29 ± 0.24	0.66 ± 0.13	43 ± 40
483	234	2	67.61	-2.87	21.32	1.4	156368 ± 209	9.0 ± 3.6	-1.66 ± 0.37	0.59 ± 0.16	63 ± 57
185	235	2	67.46	-2.66	20.25	7.2	104149 ± 75	5.3 ± 0.8	-2.14 ± 0.22	0.01 ± 0.14	347 ± 55
606	235	2	67.46	-2.66	20.25	8.6	104408 ± 27	6.8 ± 0.6	-2.48 ± 0.10	0.54 ± 0.12	123 ± 18
81	236	1	67.50	-3.17	21.09	1.6	160929 ± 164	10.0 ± 2.9	-1.57 ± 0.17	0.68 ± 0.11	36 ± 28
230	237	1	67.64	-2.85	21.37	2.9	23892 ± 14880	2.0 ± 2.6	0.06 ± 0.40	-0.02 ± 0.15	48 ± 52
494	238	1	67.68	-2.80	20.42	2.2	126875 ± 81	9.9 ± 3.2	-0.90 ± 0.23	0.28 ± 0.16	159 ± 43
60	239	3	67.43	-2.81	19.22	9.8	16 ± 14	13.0 ± 0.8	-0.40 ± 0.07	-0.15 ± 0.06	93 ± 19
159	239	3	67.43	-2.81	19.22	40.5	2 ± 2	12.6 ± 0.2	-0.43 ± 0.02	-0.20 ± 0.00	110 ± 4
332	239	3	67.43	-2.81	19.22	44.0	82 ± 3	12.6 ± 0.1	-0.30 ± 0.01	-0.20 ± 0.00	112 ± 6
231	240	1	67.67	-2.96	20.90	5.4	38553 ± 3285	2.2 ± 1.9	-0.60 ± 0.34	0.66 ± 0.14	179 ± 58
495	241	1	67.65	-2.81	20.22	4.4	92667 ± 136	1.8 ± 0.6	-0.46 ± 0.36	0.58 ± 0.17	388 ± 36
374	242	2	67.59	-2.84	21.11	1.3	70874 ± 2301	11.7 ± 2.5	-0.05 ± 0.19	0.49 ± 0.24	34 ± 24
214	242	2	67.59	-2.84	21.11	3.1	9842 ± 14360	10.6 ± 3.0	-0.30 ± 0.30	0.38 ± 0.35	311 ± 132
435	243	3	67.40	-2.88	21.87	0.2	100859 ± 868	10.7 ± 2.8	0.25 ± 0.19	-0.07 ± 0.10	159 ± 158
574	243	3	67.40	-2.88	21.87	0.1	97743 ± 1871	2.9 ± 2.2	-1.70 ± 0.65	0.47 ± 0.25	109 ± 92
637	243	3	67.40	-2.88	21.87	1.0	118819 ± 4445	10.3 ± 3.1	-0.09 ± 0.30	-0.04 ± 0.18	233 ± 130
361	245	2	67.55	-2.93	20.01	7.1	102402 ± 39	7.0 ± 1.4	-2.03 ± 0.19	0.67 ± 0.10	99 ± 25
203	245	2	67.55	-2.93	20.01	9.6	102247 ± 15	10.9 ± 1.2	-2.60 ± 0.15	0.31 ± 0.09	77 ± 20
364	246	1	67.55	-3.16	21.60	1.0	189235 ± 21	8.7 ± 1.7	-1.98 ± 0.02	0.75 ± 0.09	64 ± 27
388	247	1	67.42	-3.13	19.60	11.0	8473 ± 15	1.2 ± 0.2	-2.47 ± 0.11	0.01 ± 0.18	15 ± 11
51	248	1	67.39	-3.11	20.47	8.8	124155 ± 14	11.2 ± 1.6	-1.72 ± 0.10	0.32 ± 0.07	63 ± 13

91	249	2	67.56	-2.84	19.68	8.5	138692 ± 20	2.9 ± 0.2	-2.53 ± 0.06	0.38 ± 0.14	34 ± 18
222	249	2	67.56	-2.84	19.68	6.8	138640 ± 28	5.1 ± 0.5	-2.53 ± 0.06	0.73 ± 0.06	116 ± 18
115	250	1	67.64	-2.92	20.77	1.1	103048 ± 8929	12.1 ± 2.5	0.11 ± 0.36	0.19 ± 0.26	240 ± 79
217	251	1	67.57	-2.74	20.32	5.7	134631 ± 28	14.0 ± 0.9	-2.41 ± 0.12	0.65 ± 0.10	130 ± 29
673	252	1	67.19	-2.82	21.53	4.3	142046 ± 29	12.0 ± 1.9	-1.73 ± 0.10	0.31 ± 0.16	106 ± 30
455	253	1	67.35	-3.12	19.93	6.7	76830 ± 1068	6.3 ± 2.0	-2.47 ± 0.13	0.04 ± 0.20	28 ± 21
86	254	2	67.51	-2.99	19.77	8.8	143943 ± 23	14.7 ± 0.2	-1.85 ± 0.04	0.32 ± 0.05	170 ± 13
195	254	2	67.51	-2.99	19.77	6.2	143984 ± 30	9.6 ± 1.3	-2.38 ± 0.14	0.69 ± 0.08	114 ± 15
395	255	1	67.44	-3.09	20.64	8.2	119083 ± 19	1.3 ± 0.1	0.30 ± 0.15	-0.08 ± 0.10	129 ± 12
458	256	2	67.35	-2.98	19.94	10.2	120134 ± 19	4.7 ± 0.4	-2.33 ± 0.14	0.56 ± 0.11	80 ± 22
290	256	2	67.35	-2.98	19.94	13.1	120101 ± 16	5.9 ± 0.3	-2.57 ± 0.03	0.44 ± 0.08	125 ± 9
367	257	1	67.55	-3.09	21.78	2.1	170733 ± 43	7.9 ± 3.9	-1.83 ± 0.29	0.19 ± 0.34	34 ± 26
107	258	1	67.61	-3.01	20.98	5.9	147361 ± 18	8.6 ± 1.2	-2.52 ± 0.07	0.53 ± 0.16	62 ± 19
50	259	1	67.39	-3.11	20.83	3.2	124024 ± 33	1.8 ± 0.9	-0.10 ± 0.30	0.52 ± 0.20	97 ± 27
211	260	1	67.58	-2.79	20.73	5.0	42272 ± 9941	11.7 ± 3.0	-1.01 ± 0.33	0.06 ± 0.23	123 ± 83
209	261	1	67.60	-2.71	19.99	4.4	118841 ± 50	12.5 ± 1.6	-2.46 ± 0.12	0.25 ± 0.18	56 ± 55
262	262	1	67.16	-2.97	20.63	9.6	135529 ± 24	14.6 ± 0.3	-1.60 ± 0.07	0.09 ± 0.20	187 ± 14
110	263	1	67.62	-3.05	21.94	2.4	5514 ± 74	8.8 ± 3.4	0.04 ± 0.25	0.25 ± 0.26	138 ± 69
95	265	2	67.53	-2.89	20.47	5.5	130309 ± 40	4.8 ± 1.6	-1.58 ± 0.17	0.42 ± 0.14	148 ± 30
199	265	2	67.53	-2.89	20.47	6.8	130415 ± 18	13.6 ± 1.2	-2.04 ± 0.10	0.66 ± 0.09	91 ± 14
90	266	2	67.56	-2.82	19.98	8.6	41754 ± 109	1.6 ± 0.5	-0.12 ± 0.32	0.06 ± 0.15	402 ± 27
220	266	2	67.56	-2.82	19.98	14.1	19311 ± 116	7.4 ± 2.2	-1.76 ± 0.16	0.63 ± 0.15	405 ± 24

210	268	1	67.58	-2.77	20.27	4.1	56550 ± 160	8.6 ± 3.2	-1.31 ± 0.30	-0.04 ± 0.13	30 ± 24
470	269	2	67.24	-2.81	21.45	0.8	196127 ± 95	12.2 ± 2.0	-1.88 ± 0.10	0.27 ± 0.17	76 ± 40
274	269	2	67.24	-2.81	21.45	3.3	153115 ± 16	3.7 ± 0.8	-2.33 ± 0.17	0.65 ± 0.13	35 ± 25
34	270	3	67.41	-2.83	19.86	9.3	119171 ± 23	14.3 ± 0.6	-1.58 ± 0.06	0.12 ± 0.07	116 ± 13
557	270	3	67.41	-2.83	19.86	11.8	119255 ± 18	7.8 ± 1.0	-1.14 ± 0.08	0.20 ± 0.05	196 ± 13
317	270	3	67.41	-2.83	19.86	14.2	119240 ± 12	12.0 ± 1.1	-1.49 ± 0.06	0.31 ± 0.04	126 ± 9
546	272	1	67.42	-2.60	20.70	2.0	118155 ± 1412	9.3 ± 3.5	-1.29 ± 0.34	0.42 ± 0.23	150 ± 86
38	273	3	67.40	-2.88	19.73	10.7	117887 ± 20	8.5 ± 0.9	-1.08 ± 0.06	0.13 ± 0.05	213 ± 12
165	273	3	67.40	-2.88	19.73	8.0	117964 ± 24	13.9 ± 0.9	-1.58 ± 0.09	0.28 ± 0.07	158 ± 14
636	273	3	67.40	-2.88	19.73	10.8	117863 ± 23	9.7 ± 1.6	-0.96 ± 0.08	0.24 ± 0.04	218 ± 15
418	274	1	67.40	-3.03	20.61	4.4	112573 ± 76	11.8 ± 2.2	-1.73 ± 0.17	0.63 ± 0.14	238 ± 37
3	275	3	67.38	-2.86	20.85	7.7	122191 ± 9	5.6 ± 0.7	-1.48 ± 0.09	-0.10 ± 0.07	67 ± 15
144	275	3	67.38	-2.86	20.85	6.8	122255 ± 9	2.4 ± 0.5	-0.79 ± 0.13	-0.19 ± 0.01	73 ± 12
657	275	3	67.38	-2.86	20.85	5.9	122347 ± 14	10.3 ± 2.1	-1.20 ± 0.12	0.43 ± 0.07	35 ± 19
698	276	1	67.09	-2.79	21.89	2.8	149702 ± 48	0.7 ± 0.4	-1.04 ± 0.29	0.08 ± 0.22	37 ± 26
420	277	2	67.40	-2.98	21.33	5.3	119029 ± 27	3.8 ± 2.3	-0.51 ± 0.44	0.36 ± 0.10	106 ± 27
310	277	2	67.40	-2.98	21.33	5.3	118958 ± 23	5.5 ± 1.8	-1.05 ± 0.35	0.27 ± 0.10	84 ± 20
447	278	1	67.29	-3.14	21.00	0.9	106960 ± 24617	8.5 ± 4.1	-1.20 ± 0.61	0.26 ± 0.28	262 ± 114
555	279	2	67.39	-2.71	20.75	7.2	89 ± 8	13.0 ± 1.2	-0.64 ± 0.09	-0.17 ± 0.03	16 ± 14
336	279	2	67.39	-2.71	20.75	3.7	62 ± 28	10.8 ± 3.2	-0.25 ± 0.19	-0.07 ± 0.13	61 ± 28
394	280	3	67.42	-2.91	21.73	2.9	119156 ± 19	12.4 ± 1.9	-0.90 ± 0.13	0.12 ± 0.15	27 ± 21
534	280	3	67.42	-2.91	21.73	1.4	118806 ± 603	4.8 ± 3.6	-0.60 ± 0.40	-0.00 ± 0.18	97 ± 78

595	280	3	67.42	-2.91	21.73	3.9	119139 ± 19	11.1 ± 2.5	-1.40 ± 0.15	0.22 ± 0.12	59 ± 32
403	282	3	67.50	-2.82	19.74	5.2	121811 ± 25	9.0 ± 2.3	-1.32 ± 0.18	0.20 ± 0.14	80 ± 28
182	282	3	67.50	-2.82	19.74	8.4	121697 ± 33	7.6 ± 1.2	-1.55 ± 0.12	0.27 ± 0.09	212 ± 18
355	282	3	67.50	-2.82	19.74	7.5	121721 ± 21	9.6 ± 1.7	-1.42 ± 0.11	0.16 ± 0.09	121 ± 15
523	284	1	67.53	-2.67	21.13	1.4	144036 ± 18	7.4 ± 2.8	-0.64 ± 0.11	0.24 ± 0.05	61 ± 24
270	285	1	67.26	-2.67	20.30	12.4	119205 ± 16	4.1 ± 0.8	-0.76 ± 0.26	0.12 ± 0.04	171 ± 12
693	286	1	67.17	-2.73	21.52	4.7	122694 ± 21	13.3 ± 1.4	-1.37 ± 0.09	0.16 ± 0.10	54 ± 29
410	287	3	67.45	-2.79	20.89	3.1	119343 ± 68	12.3 ± 2.0	-0.67 ± 0.12	-0.05 ± 0.12	188 ± 31
149	287	3	67.45	-2.79	20.89	8.8	118867 ± 31	10.3 ± 1.5	-1.77 ± 0.14	-0.11 ± 0.07	214 ± 22
617	287	3	67.45	-2.79	20.89	6.8	118962 ± 29	13.5 ± 1.3	-1.55 ± 0.10	0.27 ± 0.07	152 ± 16
393	289	3	67.43	-2.93	21.69	4.2	96638 ± 98	11.1 ± 2.8	-0.78 ± 0.14	-0.06 ± 0.09	389 ± 34
539	289	3	67.43	-2.93	21.69	2.1	139072 ± 533	12.2 ± 2.1	-1.25 ± 0.17	0.57 ± 0.27	51 ± 33
599	289	3	67.43	-2.93	21.69	5.1	139208 ± 40	11.6 ± 2.0	-1.99 ± 0.14	0.53 ± 0.13	163 ± 20
697	291	1	67.09	-2.79	21.21	6.4	144526 ± 15	6.8 ± 0.7	-1.83 ± 0.07	0.22 ± 0.11	37 ± 22
521	292	1	67.55	-2.76	19.81	-0.2	105566 ± 62719	7.6 ± 4.3	-1.76 ± 1.28	0.32 ± 0.29	227 ± 130
416	293	3	67.47	-2.88	19.18	40.1	0 ± 0	14.8 ± 0.2	-1.48 ± 0.02	0.79 ± 0.01	76 ± 7
505	293	3	67.47	-2.88	19.18	43.3	1 ± 1	14.0 ± 0.6	-1.52 ± 0.02	0.79 ± 0.01	110 ± 5
349	293	3	67.47	-2.88	19.18	38.2	36 ± 5	1.8 ± 1.1	0.41 ± 0.12	-0.20 ± 0.00	111 ± 6
423	294	3	67.40	-2.91	21.02	5.8	118289 ± 38	2.8 ± 2.4	-0.14 ± 0.76	0.30 ± 0.23	195 ± 27
570	294	3	67.40	-2.91	21.02	3.7	118301 ± 43	6.1 ± 2.7	-0.85 ± 0.23	0.50 ± 0.14	145 ± 26
632	294	3	67.40	-2.91	21.02	7.8	118303 ± 23	14.0 ± 0.8	-1.83 ± 0.10	0.29 ± 0.07	127 ± 20
45	296	1	67.37	-3.06	20.24	6.4	152260 ± 22	6.3 ± 0.5	-1.43 ± 0.05	-0.17 ± 0.03	139 ± 10

116	298	2	67.63	-2.92	21.98	3.1	83739 ± 809	11.1 ± 2.8	-1.43 ± 0.25	0.18 ± 0.20	47 ± 41
488	298	2	67.63	-2.92	21.98	2.1	113075 ± 26431	10.5 ± 3.0	-0.98 ± 0.26	-0.11 ± 0.08	381 ± 46
186	299	1	67.48	-2.68	20.04	6.8	92588 ± 12	6.7 ± 1.8	-1.54 ± 0.23	0.45 ± 0.16	82 ± 18
517	301	1	67.54	-2.67	21.52	0.5	112372 ± 4461	0.7 ± 0.8	-2.19 ± 0.34	0.18 ± 0.26	53 ± 41
126	302	2	67.35	-2.72	19.77	8.9	108046 ± 33	7.6 ± 1.7	-1.09 ± 0.11	0.26 ± 0.08	228 ± 22
639	302	2	67.35	-2.72	19.77	19.2	108091 ± 13	10.1 ± 1.0	-1.64 ± 0.06	0.65 ± 0.05	151 ± 7
15	303	3	67.36	-2.90	20.85	7.4	121162 ± 29	14.2 ± 0.7	-1.65 ± 0.06	-0.13 ± 0.06	179 ± 16
135	303	3	67.36	-2.90	20.85	5.5	121101 ± 46	5.0 ± 1.0	-1.59 ± 0.20	0.13 ± 0.19	162 ± 21
296	303	3	67.36	-2.90	20.85	11.9	121255 ± 16	10.1 ± 1.5	-1.47 ± 0.08	0.38 ± 0.04	130 ± 9
1	304	3	67.37	-2.76	21.02	2.6	179333 ± 29	7.1 ± 2.3	-1.94 ± 0.12	0.66 ± 0.23	53 ± 21
121	304	3	67.37	-2.76	21.02	7.0	119231 ± 15	14.5 ± 0.4	-2.22 ± 0.12	0.11 ± 0.10	99 ± 17
642	304	3	67.37	-2.76	21.02	0.8	202999 ± 2	8.8 ± 1.8	-1.05 ± 0.05	0.59 ± 0.04	38 ± 6
576	305	2	67.32	-2.63	21.37	0.7	131450 ± 10328	9.2 ± 3.5	-0.30 ± 0.43	0.17 ± 0.21	108 ± 112
297	305	2	67.32	-2.63	21.37	6.0	124375 ± 10	13.1 ± 1.3	-2.47 ± 0.10	0.71 ± 0.07	40 ± 23
369	306	2	67.58	-2.98	19.70	19.1	27416 ± 3784	12.4 ± 2.1	-2.44 ± 0.71	0.04 ± 0.23	163 ± 74
476	306	2	67.58	-2.98	19.70	12.3	45950 ± 28	8.6 ± 1.7	-2.42 ± 0.15	0.54 ± 0.20	112 ± 31
414	307	3	67.47	-2.85	20.77	3.1	128177 ± 47	4.7 ± 1.2	-2.24 ± 0.25	0.68 ± 0.10	31 ± 23
192	307	3	67.47	-2.85	20.77	6.2	128361 ± 37	6.6 ± 0.7	-2.48 ± 0.10	0.69 ± 0.08	76 ± 36
351	307	3	67.47	-2.85	20.77	6.0	128396 ± 27	11.7 ± 1.7	-2.41 ± 0.13	0.56 ± 0.12	104 ± 21
516	308	1	67.53	-2.66	19.89	5.6	104851 ± 425	13.9 ± 1.9	-1.82 ± 0.13	-0.14 ± 0.06	51 ± 50
89	309	2	67.56	-2.80	20.81	3.8	124562 ± 81	11.6 ± 2.2	-1.71 ± 0.18	-0.09 ± 0.09	215 ± 75
219	309	2	67.56	-2.80	20.81	1.0	108426 ± 45593	9.9 ± 3.6	-0.68 ± 0.78	0.26 ± 0.33	118 ± 84

500	311	1	67.64	-2.83	20.86	1.9	134139 ± 262	8.6 ± 3.6	-1.61 ± 0.31	0.57 ± 0.16	42 ± 30
114	312	2	67.63	-2.92	21.20	5.9	122936 ± 9	6.6 ± 1.1	-2.03 ± 0.16	0.70 ± 0.08	17 ± 13
487	312	2	67.63	-2.92	21.20	3.5	122784 ± 51	2.6 ± 3.4	-0.19 ± 0.59	0.78 ± 0.02	132 ± 35
49	313	3	67.36	-2.92	20.62	6.8	119518 ± 35	12.1 ± 1.7	-1.98 ± 0.15	0.31 ± 0.11	152 ± 21
133	313	3	67.36	-2.92	20.62	7.6	119421 ± 56	9.8 ± 1.8	-2.22 ± 0.18	0.68 ± 0.09	299 ± 30
295	313	3	67.36	-2.92	20.62	12.4	119415 ± 15	13.8 ± 0.8	-1.98 ± 0.07	0.67 ± 0.06	129 ± 8
73	314	1	67.48	-3.17	20.80	2.4	146620 ± 70	0.6 ± 0.4	-0.24 ± 0.25	0.56 ± 0.17	92 ± 39
146	315	1	67.46	-2.65	20.67	5.4	120781 ± 98	3.7 ± 0.3	0.02 ± 0.06	0.78 ± 0.02	433 ± 4
387	316	2	67.58	-2.91	21.21	2.9	139415 ± 29	13.1 ± 1.6	-2.03 ± 0.15	0.43 ± 0.22	31 ± 24
479	316	2	67.58	-2.91	21.21	4.3	98487 ± 109	4.0 ± 0.6	0.07 ± 0.04	0.57 ± 0.08	425 ± 8
451	318	1	67.32	-3.07	21.62	1.9	117737 ± 3978	8.5 ± 4.9	-0.64 ± 0.63	0.31 ± 0.22	183 ± 109
497	319	1	67.60	-2.67	21.71	0.9	132086 ± 73	10.0 ± 3.2	-0.06 ± 0.35	0.03 ± 0.07	120 ± 47
666	321	1	67.22	-2.77	20.41	8.1	101356 ± 24	3.9 ± 0.5	-2.10 ± 0.24	0.31 ± 0.16	61 ± 31
386	322	2	67.58	-2.91	20.79	4.1	140187 ± 41	12.9 ± 1.7	-1.65 ± 0.09	-0.10 ± 0.08	24 ± 25
205	322	2	67.58	-2.91	20.79	5.9	140212 ± 25	14.5 ± 0.4	-1.85 ± 0.07	0.07 ± 0.11	133 ± 15
380	324	2	67.57	-2.82	20.92	1.5	138507 ± 104	9.2 ± 3.9	-0.88 ± 0.37	0.74 ± 0.05	107 ± 66
221	324	2	67.57	-2.82	20.92	4.6	138495 ± 41	10.6 ± 1.8	-2.50 ± 0.10	0.45 ± 0.16	99 ± 29
305	325	1	67.27	-2.61	20.13	9.9	124594 ± 14	12.3 ± 1.3	-1.32 ± 0.06	-0.03 ± 0.07	130 ± 9
472	326	2	67.26	-2.86	20.43	2.9	14030 ± 12748	6.7 ± 3.4	-0.50 ± 0.44	0.32 ± 0.26	118 ± 75
690	326	2	67.26	-2.86	20.43	21.6	107 ± 6	12.7 ± 0.2	-0.36 ± 0.03	-0.19 ± 0.01	81 ± 13
671	327	1	67.19	-2.78	21.59	4.7	141909 ± 25	11.3 ± 2.1	-1.93 ± 0.14	0.64 ± 0.09	60 ± 26
461	328	3	67.35	-2.93	19.89	7.7	119496 ± 24	8.5 ± 1.5	-1.85 ± 0.17	0.43 ± 0.11	100 ± 19

132	328	3	67.35	-2.93	19.89	9.0	119373 ± 24	9.4 ± 1.4	-2.09 ± 0.14	0.41 ± 0.09	150 ± 12
294	328	3	67.35	-2.93	19.89	8.6	119417 ± 25	12.6 ± 1.5	-2.09 ± 0.14	0.63 ± 0.09	99 ± 14
94	329	2	67.54	-2.85	19.55	9.8	130663 ± 22	12.2 ± 1.7	-1.59 ± 0.08	0.52 ± 0.06	213 ± 11
208	329	2	67.54	-2.85	19.55	14.4	130739 ± 17	13.9 ± 0.8	-1.61 ± 0.04	0.31 ± 0.03	230 ± 10
66	330	3	67.43	-2.77	19.39	6.6	32486 ± 29419	1.6 ± 1.3	-1.46 ± 0.79	0.28 ± 0.28	241 ± 179
154	330	3	67.43	-2.77	19.39	12.4	61003 ± 15	12.8 ± 1.6	-1.62 ± 0.15	0.62 ± 0.10	132 ± 17
328	330	3	67.43	-2.77	19.39	13.9	61390 ± 44	12.1 ± 1.4	-2.60 ± 0.29	0.28 ± 0.17	158 ± 56
452	331	1	67.27	-3.05	21.72	0.2	135080 ± 293	10.3 ± 3.4	-0.44 ± 0.23	0.15 ± 0.09	312 ± 82
466	333	3	67.31	-2.83	21.20	0.9	162786 ± 6202	1.6 ± 1.1	-0.37 ± 0.37	0.67 ± 0.13	158 ± 90
589	333	3	67.31	-2.83	21.20	2.0	39520 ± 48	11.2 ± 2.8	0.11 ± 0.19	-0.09 ± 0.09	102 ± 52
289	333	3	67.31	-2.83	21.20	3.6	138593 ± 13760	7.5 ± 2.4	-2.20 ± 0.26	0.22 ± 0.24	371 ± 57
651	334	1	67.38	-2.97	20.60	7.1	92832 ± 77	4.1 ± 1.2	-1.59 ± 0.32	0.55 ± 0.16	304 ± 58
306	335	1	67.27	-2.62	21.01	7.8	124476 ± 26	11.0 ± 1.7	-1.55 ± 0.10	0.35 ± 0.07	165 ± 16
96	337	1	67.53	-2.90	21.13	4.6	138928 ± 12	12.8 ± 1.5	-2.26 ± 0.16	-0.09 ± 0.09	21 ± 18
427	338	3	67.41	-2.96	21.61	4.0	119903 ± 33	6.7 ± 2.1	-0.99 ± 0.15	0.03 ± 0.12	30 ± 20
170	338	3	67.41	-2.96	21.61	9.2	119928 ± 18	13.4 ± 1.1	-1.55 ± 0.07	-0.07 ± 0.07	141 ± 12
590	338	3	67.41	-2.96	21.61	4.5	119868 ± 18	2.3 ± 1.9	-0.29 ± 0.56	0.53 ± 0.15	68 ± 26
365	339	1	67.56	-3.13	21.76	4.9	75434 ± 2391	13.3 ± 1.3	-1.57 ± 0.21	-0.11 ± 0.09	386 ± 46
360	340	2	67.54	-2.98	21.04	2.8	6654 ± 34	0.7 ± 0.3	-0.90 ± 0.60	0.16 ± 0.27	41 ± 34
201	340	2	67.54	-2.98	21.04	3.0	6845 ± 770	6.3 ± 4.2	-0.27 ± 0.36	0.06 ± 0.22	28 ± 28
444	341	3	67.39	-2.89	21.44	3.4	120866 ± 141	11.4 ± 2.3	-0.59 ± 0.14	-0.16 ± 0.04	397 ± 28
140	341	3	67.39	-2.89	21.44	5.7	120835 ± 98	13.3 ± 1.4	-1.96 ± 0.16	0.18 ± 0.15	357 ± 38

662	341	3	67.39	-2.89	21.44	3.0	120680 ± 28	12.8 ± 1.8	-0.80 ± 0.11	-0.14 ± 0.05	75 ± 40
370	342	2	67.58	-2.97	20.62	8.2	83375 ± 10	8.3 ± 2.5	-1.11 ± 0.17	-0.04 ± 0.10	76 ± 16
477	342	2	67.58	-2.97	20.62	5.6	18877 ± 72	8.8 ± 3.8	-0.47 ± 0.28	-0.00 ± 0.16	287 ± 48
59	344	3	67.45	-2.81	20.12	7.1	124272 ± 20	10.9 ± 2.0	-1.85 ± 0.15	0.47 ± 0.11	108 ± 20
157	344	3	67.45	-2.81	20.12	9.2	124321 ± 10	14.2 ± 0.7	-1.71 ± 0.05	0.18 ± 0.06	110 ± 9
620	344	3	67.45	-2.81	20.12	11.1	124493 ± 10	11.5 ± 1.4	-1.42 ± 0.07	0.35 ± 0.04	104 ± 9
490	345	1	67.63	-2.87	21.28	1.0	134949 ± 468	9.3 ± 3.5	-0.60 ± 0.28	0.29 ± 0.15	80 ± 48
29	346	3	67.41	-2.87	20.58	7.4	119084 ± 4	13.7 ± 0.8	-1.74 ± 0.07	0.75 ± 0.04	24 ± 14
168	346	3	67.41	-2.87	20.58	8.4	119052 ± 15	14.1 ± 0.8	-1.61 ± 0.07	-0.08 ± 0.07	115 ± 12
324	346	3	67.41	-2.87	20.58	8.1	119114 ± 19	14.3 ± 0.6	-1.56 ± 0.07	0.39 ± 0.06	96 ± 16
431	347	3	67.41	-2.92	20.82	5.3	119822 ± 55	12.9 ± 1.7	-1.14 ± 0.10	0.17 ± 0.09	283 ± 37
161	347	3	67.41	-2.92	20.82	5.2	119602 ± 22	13.9 ± 0.9	-2.30 ± 0.15	-0.09 ± 0.08	68 ± 26
311	347	3	67.41	-2.92	20.82	7.2	119758 ± 20	11.4 ± 1.8	-1.86 ± 0.12	0.71 ± 0.07	82 ± 17
406	348	3	67.50	-2.84	20.85	3.6	121483 ± 17	10.4 ± 2.4	-0.87 ± 0.14	0.29 ± 0.10	30 ± 20
184	348	3	67.50	-2.84	20.85	6.9	121467 ± 23	13.1 ± 1.5	-1.75 ± 0.09	0.71 ± 0.07	102 ± 13
352	348	3	67.50	-2.84	20.85	6.0	121477 ± 9	13.1 ± 1.4	-1.60 ± 0.09	0.15 ± 0.09	34 ± 22
496	349	1	67.68	-2.85	21.38	1.6	115723 ± 2853	0.7 ± 0.5	-2.01 ± 0.41	0.17 ± 0.26	189 ± 102
118	350	2	67.36	-2.70	21.03	4.3	26779 ± 26	8.1 ± 3.6	-0.69 ± 0.28	0.55 ± 0.20	46 ± 43
638	350	2	67.36	-2.70	21.03	3.6	27635 ± 1522	7.7 ± 2.9	-0.03 ± 0.18	0.29 ± 0.15	225 ± 38
103	351	2	67.52	-2.86	20.50	6.7	121095 ± 22	9.3 ± 1.4	-2.26 ± 0.16	0.69 ± 0.08	85 ± 16
200	351	2	67.52	-2.86	20.50	9.6	121165 ± 19	14.6 ± 0.4	-2.42 ± 0.09	0.75 ± 0.04	103 ± 10
55	352	3	67.39	-2.92	21.41	4.1	120140 ± 34	9.6 ± 2.6	-1.15 ± 0.17	0.21 ± 0.13	74 ± 21

563	352	3	67.39	-2.92	21.41	2.3	120207 ± 55	9.3 ± 3.6	-0.80 ± 0.25	-0.09 ± 0.09	57 ± 29
623	352	3	67.39	-2.92	21.41	3.8	120305 ± 23	9.4 ± 2.4	-1.34 ± 0.17	0.24 ± 0.15	49 ± 28
411	354	3	67.45	-2.80	21.24	3.1	124715 ± 16	9.7 ± 2.7	-1.05 ± 0.15	0.06 ± 0.13	24 ± 18
156	354	3	67.45	-2.80	21.24	7.0	124688 ± 16	6.0 ± 1.0	-1.27 ± 0.10	0.32 ± 0.08	77 ± 13
618	354	3	67.45	-2.80	21.24	4.7	124608 ± 42	2.9 ± 2.3	-0.48 ± 0.46	0.71 ± 0.07	201 ± 33
457	355	1	67.34	-2.98	20.00	11.6	120126 ± 14	5.0 ± 0.7	-1.16 ± 0.08	0.07 ± 0.07	119 ± 10
75	356	1	67.48	-3.09	21.25	4.5	140551 ± 41	13.7 ± 1.0	-2.21 ± 0.16	0.67 ± 0.10	70 ± 27
473	357	2	67.27	-2.88	20.71	1.6	108792 ± 12441	3.8 ± 4.5	-0.26 ± 0.41	0.52 ± 0.24	153 ± 96
285	357	2	67.27	-2.88	20.71	6.3	118819 ± 34	5.1 ± 1.0	-1.57 ± 0.16	0.51 ± 0.13	120 ± 22
464	359	3	67.31	-2.80	19.78	1.2	120348 ± 3903	10.7 ± 3.0	-1.17 ± 0.38	-0.00 ± 0.19	95 ± 74
581	359	3	67.31	-2.80	19.78	7.0	117511 ± 23	5.3 ± 1.9	-0.64 ± 0.46	-0.15 ± 0.04	144 ± 15
303	359	3	67.31	-2.80	19.78	0.4	135816 ± 25738	9.0 ± 3.7	-0.18 ± 0.62	0.05 ± 0.22	136 ± 101
424	360	3	67.39	-2.91	20.98	2.9	119737 ± 37	2.2 ± 1.3	-0.02 ± 0.40	-0.04 ± 0.12	81 ± 34
565	360	3	67.39	-2.91	20.98	4.4	119682 ± 21	8.0 ± 2.0	-1.17 ± 0.15	-0.11 ± 0.07	67 ± 33
624	360	3	67.39	-2.91	20.98	4.3	119897 ± 59	6.2 ± 1.7	-1.26 ± 0.18	0.06 ± 0.14	165 ± 28
438	361	3	67.40	-2.90	21.33	4.5	119954 ± 24	11.8 ± 2.0	-1.42 ± 0.14	0.42 ± 0.14	60 ± 30
571	361	3	67.40	-2.90	21.33	4.2	120195 ± 47	11.1 ± 2.4	-1.17 ± 0.14	-0.14 ± 0.06	168 ± 26
633	361	3	67.40	-2.90	21.33	6.6	120122 ± 46	6.1 ± 2.7	-1.17 ± 0.45	0.67 ± 0.08	236 ± 34
375	362	2	67.59	-2.84	20.49	2.0	132032 ± 20	3.1 ± 2.3	-0.39 ± 0.35	0.71 ± 0.07	29 ± 21
216	362	2	67.59	-2.84	20.49	4.9	131827 ± 35	13.4 ± 1.4	-2.16 ± 0.14	0.24 ± 0.14	125 ± 29
396	363	2	67.47	-2.96	21.03	5.1	118925 ± 13	9.8 ± 2.5	-0.88 ± 0.13	0.16 ± 0.08	38 ± 22
501	363	2	67.47	-2.96	21.03	6.0	120876 ± 27	4.8 ± 2.5	-0.72 ± 0.60	0.07 ± 0.12	131 ± 17

69	364	3	67.43	-2.87	21.43	4.0	119956 ± 28	13.4 ± 1.3	-1.90 ± 0.17	0.59 ± 0.13	69 ± 35
536	364	3	67.43	-2.87	21.43	4.0	120076 ± 42	11.9 ± 2.1	-2.14 ± 0.19	0.56 ± 0.16	28 ± 20
604	364	3	67.43	-2.87	21.43	4.2	120041 ± 19	10.6 ± 2.2	-1.19 ± 0.13	0.02 ± 0.12	64 ± 25
254	365	1	67.15	-2.97	21.27	4.5	70884 ± 36	1.5 ± 0.9	-1.03 ± 0.52	0.26 ± 0.30	57 ± 29
70	366	3	67.43	-2.88	20.10	13.9	127784 ± 13	8.3 ± 0.8	-1.30 ± 0.06	0.22 ± 0.03	167 ± 8
543	366	3	67.43	-2.88	20.10	12.9	127877 ± 13	9.0 ± 1.0	-1.35 ± 0.06	0.25 ± 0.03	144 ± 7
603	366	3	67.43	-2.88	20.10	14.8	127934 ± 12	4.4 ± 0.4	-1.03 ± 0.05	0.15 ± 0.03	179 ± 7
32	367	3	67.41	-2.89	21.93	3.1	119520 ± 23	11.9 ± 2.2	-1.84 ± 0.20	0.69 ± 0.09	27 ± 22
175	367	3	67.41	-2.89	21.93	3.5	119474 ± 45	12.5 ± 1.8	-1.89 ± 0.19	-0.00 ± 0.14	81 ± 38
321	367	3	67.41	-2.89	21.93	2.8	119599 ± 47	10.9 ± 2.6	-1.89 ± 0.26	0.63 ± 0.13	44 ± 30
399	368	3	67.45	-2.94	21.25	6.5	118888 ± 16	1.6 ± 0.1	0.07 ± 0.06	0.46 ± 0.08	89 ± 12
503	368	3	67.45	-2.94	21.25	4.5	118833 ± 56	6.6 ± 2.3	-1.45 ± 0.25	0.64 ± 0.11	91 ± 30
343	368	3	67.45	-2.94	21.25	7.7	118972 ± 17	1.2 ± 0.1	0.05 ± 0.05	0.48 ± 0.08	80 ± 10
401	369	3	67.50	-2.78	19.70	5.3	118828 ± 51	1.7 ± 0.1	0.02 ± 0.12	0.47 ± 0.13	274 ± 32
179	369	3	67.50	-2.78	19.70	4.8	118907 ± 21	3.0 ± 1.1	-0.56 ± 0.18	-0.09 ± 0.10	109 ± 17
611	369	3	67.50	-2.78	19.70	14.9	118902 ± 14	6.3 ± 0.6	-1.79 ± 0.08	0.71 ± 0.06	146 ± 9
446	370	1	67.39	-2.90	21.25	5.3	119917 ± 31	7.4 ± 2.1	-1.09 ± 0.15	0.51 ± 0.11	119 ± 16
372	371	2	67.59	-2.81	20.60	2.9	131912 ± 63	12.0 ± 2.2	-1.59 ± 0.17	0.05 ± 0.16	101 ± 34
212	371	2	67.59	-2.81	20.60	4.4	131745 ± 48	12.8 ± 1.9	-1.97 ± 0.14	0.19 ± 0.13	159 ± 25
269	372	1	67.25	-2.67	19.30	21.1	119395 ± 12	13.2 ± 0.8	-1.64 ± 0.05	0.37 ± 0.03	215 ± 8
397	373	1	67.45	-2.96	20.77	8.0	120947 ± 25	11.4 ± 1.8	-1.19 ± 0.09	0.14 ± 0.07	166 ± 14
686	374	1	67.25	-2.98	20.77	6.8	149129 ± 37	5.5 ± 0.7	-1.36 ± 0.06	-0.18 ± 0.02	202 ± 14

400	375	3	67.45	-2.92	20.18	7.2	123890 ± 20	8.4 ± 1.9	-1.16 ± 0.13	0.28 ± 0.07	113 ± 12
504	375	3	67.45	-2.92	20.18	8.8	123822 ± 10	6.6 ± 0.9	-1.49 ± 0.09	0.28 ± 0.07	80 ± 11
345	375	3	67.45	-2.92	20.18	10.5	123956 ± 11	10.0 ± 1.2	-1.75 ± 0.09	0.29 ± 0.06	87 ± 11
456	376	1	67.33	-3.04	20.33	7.3	94933 ± 30	10.7 ± 2.0	-0.96 ± 0.12	-0.03 ± 0.10	177 ± 27
21	377	1	67.26	-3.04	21.41	2.2	101658 ± 4922	2.1 ± 1.2	-1.86 ± 0.49	0.22 ± 0.28	65 ± 50
67	378	3	67.43	-2.81	19.02	15.1	92772 ± 15	2.1 ± 0.2	-0.72 ± 0.09	-0.04 ± 0.08	165 ± 10
158	378	3	67.43	-2.81	19.02	20.5	92665 ± 10	4.7 ± 0.4	-1.31 ± 0.07	0.27 ± 0.05	150 ± 7
331	378	3	67.43	-2.81	19.02	17.3	92699 ± 15	3.1 ± 0.3	-1.04 ± 0.08	0.12 ± 0.08	171 ± 13
520	379	1	67.55	-2.75	20.63	3.9	134648 ± 20	12.8 ± 1.9	-1.16 ± 0.08	0.54 ± 0.06	73 ± 21
12	380	3	67.35	-2.74	20.70	1.5	100198 ± 25846	10.1 ± 3.4	-0.58 ± 0.62	0.46 ± 0.26	136 ± 110
128	380	3	67.35	-2.74	20.70	3.3	95088 ± 2665	8.5 ± 3.4	-1.39 ± 0.32	0.52 ± 0.20	379 ± 60
641	380	3	67.35	-2.74	20.70	5.3	94683 ± 71	5.6 ± 1.7	-1.76 ± 0.28	0.73 ± 0.06	215 ± 42
187	381	2	67.46	-2.72	19.89	13.7	122511 ± 16	4.6 ± 0.2	-2.57 ± 0.02	-0.01 ± 0.09	141 ± 7
608	381	2	67.46	-2.72	19.89	14.9	122620 ± 14	3.9 ± 0.2	-2.58 ± 0.01	0.61 ± 0.08	136 ± 8
24	383	2	67.25	-2.94	21.55	1.6	90857 ± 8777	8.7 ± 4.8	-0.93 ± 0.45	0.05 ± 0.25	46 ± 72
688	383	2	67.25	-2.94	21.55	3.5	174212 ± 35	3.8 ± 0.9	-1.99 ± 0.16	0.60 ± 0.11	45 ± 24
14	384	3	67.34	-2.84	19.55	9.2	118049 ± 23	12.1 ± 1.6	-1.63 ± 0.12	0.35 ± 0.07	157 ± 14
130	384	3	67.34	-2.84	19.55	15.2	118051 ± 16	14.6 ± 0.4	-2.28 ± 0.07	0.76 ± 0.03	186 ± 10
287	384	3	67.34	-2.84	19.55	21.0	118078 ± 10	14.0 ± 0.4	-1.81 ± 0.04	0.47 ± 0.03	153 ± 7
36	386	3	67.40	-2.87	20.85	5.1	118294 ± 33	12.8 ± 1.8	-1.60 ± 0.15	0.35 ± 0.12	120 ± 21
167	386	3	67.40	-2.87	20.85	8.7	118279 ± 20	12.4 ± 1.5	-2.29 ± 0.17	0.21 ± 0.11	107 ± 15
316	386	3	67.40	-2.87	20.85	8.5	118376 ± 22	11.2 ± 1.8	-1.72 ± 0.13	0.54 ± 0.08	131 ± 13

413	387	3	67.46	-2.83	21.39	3.4	152921 ± 128	3.6 ± 1.3	-1.38 ± 0.15	0.63 ± 0.12	218 ± 76
152	387	3	67.46	-2.83	21.39	4.7	152555 ± 44	3.5 ± 0.5	-2.27 ± 0.24	0.23 ± 0.28	86 ± 29
348	387	3	67.46	-2.83	21.39	5.7	152656 ± 43	2.9 ± 0.5	-1.59 ± 0.09	0.58 ± 0.08	186 ± 26
465	388	3	67.33	-2.80	19.39	4.7	118376 ± 50	8.9 ± 3.2	-0.80 ± 0.39	0.20 ± 0.17	207 ± 37
582	388	3	67.33	-2.80	19.39	9.0	118293 ± 31	13.8 ± 1.0	-1.24 ± 0.08	0.07 ± 0.07	233 ± 19
649	388	3	67.33	-2.80	19.39	17.2	118305 ± 14	12.3 ± 1.0	-1.45 ± 0.06	0.33 ± 0.03	201 ± 9
398	389	1	67.45	-2.94	21.21	3.8	120022 ± 21	1.6 ± 0.3	-0.23 ± 0.20	0.55 ± 0.14	23 ± 16
98	390	2	67.51	-2.76	20.55	3.3	75458 ± 6383	2.9 ± 4.4	-1.64 ± 0.46	0.30 ± 0.31	127 ± 101
526	390	2	67.51	-2.76	20.55	6.5	121209 ± 9	3.7 ± 1.3	-0.79 ± 0.29	0.43 ± 0.09	26 ± 16
359	391	1	67.53	-3.04	20.16	9.1	96319 ± 95	14.3 ± 0.6	-1.55 ± 0.07	0.01 ± 0.09	426 ± 7
99	392	2	67.51	-2.77	19.91	5.0	121927 ± 29	9.6 ± 2.1	-1.49 ± 0.16	0.03 ± 0.14	100 ± 32
527	392	2	67.51	-2.77	19.91	9.9	121927 ± 18	13.3 ± 1.2	-1.48 ± 0.06	0.15 ± 0.06	140 ± 10
273	393	1	67.25	-2.72	20.70	10.2	25291 ± 81	2.4 ± 0.7	-0.60 ± 0.15	0.62 ± 0.13	410 ± 23
178	394	1	67.50	-2.68	19.19	28.0	0 ± 0	12.7 ± 0.2	-0.44 ± 0.02	-0.20 ± 0.00	105 ± 4
20	395	1	67.23	-3.05	21.07	1.5	126264 ± 6695	11.2 ± 3.1	-0.26 ± 0.45	0.66 ± 0.14	100 ± 94
489	396	1	67.64	-2.90	20.93	2.2	126264 ± 30245	4.9 ± 4.6	-0.72 ± 0.82	0.56 ± 0.18	162 ± 99
307	397	1	67.29	-2.63	21.28	5.8	124511 ± 29	14.2 ± 0.7	-1.54 ± 0.07	0.27 ± 0.08	131 ± 16
390	398	3	67.44	-2.95	21.23	3.8	128307 ± 46	10.9 ± 2.3	-1.22 ± 0.15	0.23 ± 0.12	164 ± 30
538	398	3	67.44	-2.95	21.23	-0.9	163957 ± 18400	10.8 ± 2.8	-1.96 ± 0.40	0.67 ± 0.12	93 ± 59
598	398	3	67.44	-2.95	21.23	4.4	128285 ± 16	12.0 ± 2.0	-1.58 ± 0.11	0.34 ± 0.11	38 ± 22
382	399	2	67.57	-2.86	20.28	5.2	131070 ± 26	10.8 ± 2.5	-2.09 ± 0.20	0.63 ± 0.11	100 ± 38
207	399	2	67.57	-2.86	20.28	6.7	131203 ± 21	5.3 ± 1.0	-1.60 ± 0.14	0.42 ± 0.11	101 ± 27

550	400	2	67.42	-2.72	20.62	4.9	130556 ± 28	12.4 ± 1.9	-1.33 ± 0.10	0.24 ± 0.08	129 ± 16
327	400	2	67.42	-2.72	20.62	9.1	130498 ± 19	10.7 ± 1.8	-1.34 ± 0.09	0.41 ± 0.05	154 ± 11
379	401	2	67.59	-2.91	21.72	2.2	114999 ± 260	0.9 ± 0.7	-1.57 ± 0.61	0.64 ± 0.14	107 ± 68
480	401	2	67.59	-2.91	21.72	1.7	152129 ± 59	2.4 ± 0.7	-2.30 ± 0.22	0.17 ± 0.26	41 ± 32
378	402	1	67.64	-2.90	21.90	1.5	46027 ± 41126	10.6 ± 3.1	-0.04 ± 0.54	0.25 ± 0.24	73 ± 99
8	403	3	67.38	-2.89	21.84	4.0	119300 ± 69	11.2 ± 2.7	-1.86 ± 0.28	0.71 ± 0.07	172 ± 66
141	403	3	67.38	-2.89	21.84	3.8	119544 ± 20	9.7 ± 2.1	-2.38 ± 0.17	0.56 ± 0.16	37 ± 23
654	403	3	67.38	-2.89	21.84	2.9	119542 ± 41	11.7 ± 2.4	-1.14 ± 0.16	0.12 ± 0.14	76 ± 45
585	404	2	67.31	-2.72	19.35	5.6	121656 ± 28	6.0 ± 1.6	-0.65 ± 0.12	-0.13 ± 0.05	153 ± 18
298	404	2	67.31	-2.72	19.35	4.5	121898 ± 61	1.9 ± 0.6	0.28 ± 0.23	-0.10 ± 0.07	289 ± 29
68	405	3	67.43	-2.85	20.41	6.5	137412 ± 30	6.7 ± 0.9	-2.48 ± 0.10	0.57 ± 0.13	122 ± 16
160	405	3	67.43	-2.85	20.41	9.9	137352 ± 22	7.1 ± 0.6	-2.54 ± 0.05	0.69 ± 0.07	153 ± 13
597	405	3	67.43	-2.85	20.41	8.1	137440 ± 18	8.3 ± 1.1	-2.29 ± 0.14	0.38 ± 0.11	84 ± 14
28	406	3	67.42	-2.87	19.57	13.1	119691 ± 15	9.9 ± 1.0	-1.87 ± 0.09	0.36 ± 0.06	161 ± 11
537	406	3	67.42	-2.87	19.57	9.0	119800 ± 25	11.4 ± 1.6	-1.07 ± 0.08	0.04 ± 0.07	201 ± 14
596	406	3	67.42	-2.87	19.57	16.4	119720 ± 13	12.7 ± 0.9	-1.47 ± 0.05	0.18 ± 0.04	175 ± 9
493	407	1	67.69	-2.79	21.54	-0.2	124293 ± 2495	10.2 ± 3.4	-1.31 ± 0.40	0.60 ± 0.17	171 ± 112
670	409	1	67.18	-2.77	20.84	8.0	119890 ± 21	11.5 ± 1.9	-1.39 ± 0.11	0.39 ± 0.06	129 ± 15
448	410	1	67.31	-3.14	21.61	1.5	193086 ± 144	0.5 ± 0.2	-0.90 ± 0.09	0.48 ± 0.09	29 ± 21
402	411	3	67.51	-2.78	20.05	4.9	117710 ± 132	14.3 ± 1.3	0.17 ± 0.12	-0.14 ± 0.05	424 ± 6
180	411	3	67.51	-2.78	20.05	9.4	121588 ± 14	14.0 ± 0.8	-1.73 ± 0.06	0.02 ± 0.09	121 ± 11
612	411	3	67.51	-2.78	20.05	8.9	121691 ± 20	9.8 ± 1.5	-1.17 ± 0.08	-0.05 ± 0.08	160 ± 12

74	412	1	67.49	-3.15	19.57	10.3	130561 ± 21	12.6 ± 1.7	-2.01 ± 0.12	0.33 ± 0.07	157 ± 15
272	413	1	67.25	-2.69	19.55	16.0	119524 ± 12	14.0 ± 0.7	-2.10 ± 0.08	0.52 ± 0.05	136 ± 7
19	417	2	67.19	-2.93	20.30	1.3	90329 ± 98	4.4 ± 2.6	-0.35 ± 0.27	0.72 ± 0.07	402 ± 27
681	417	2	67.19	-2.93	20.30	24.6	184 ± 5	11.9 ± 2.6	-0.35 ± 0.22	-0.20 ± 0.00	73 ± 10
52	419	1	67.39	-3.03	21.86	4.0	75852 ± 2914	3.4 ± 3.1	-1.29 ± 0.27	-0.12 ± 0.07	244 ± 92
491	420	1	67.63	-2.86	20.66	2.6	131428 ± 17	9.7 ± 3.4	-1.53 ± 0.20	0.65 ± 0.11	35 ± 27
258	421	1	67.12	-2.91	21.61	3.9	145856 ± 17	5.5 ± 0.9	-2.42 ± 0.14	0.38 ± 0.22	33 ± 23
384	422	2	67.58	-2.88	19.61	14.1	103720 ± 18	7.4 ± 0.5	-2.29 ± 0.13	0.14 ± 0.08	147 ± 20
481	422	2	67.58	-2.88	19.61	16.7	103773 ± 16	7.9 ± 0.8	-2.18 ± 0.15	0.36 ± 0.06	139 ± 10
419	423	1	67.41	-3.00	20.25	5.6	119832 ± 25	8.7 ± 1.7	-2.26 ± 0.20	0.50 ± 0.15	45 ± 35
93	425	2	67.56	-2.85	20.25	6.8	130625 ± 24	12.8 ± 1.6	-2.38 ± 0.13	0.36 ± 0.11	92 ± 15
223	425	2	67.56	-2.85	20.25	4.9	130715 ± 30	3.5 ± 1.0	-1.70 ± 0.18	0.69 ± 0.09	108 ± 22
53	431	1	67.38	-3.02	20.68	1.1	107251 ± 62584	7.6 ± 4.3	-1.75 ± 1.29	0.31 ± 0.29	222 ± 129

Bibliography

[1] C. A. Wirtz, "Einiges zur Statistik der Radialbewegungen von Spiralnebeln und Kugelsternhaufen," Astronomische Nachrichten **215**, 349 (1922).

[2] E. Hubble, "Cepheids in Spiral Nebulae," Pop. Astr. **33**, 252 (1925).

[3] E. Hubble, "A Relation between Distance and Radial Velocity among Extra-Galactic Nebulae," Proceedings of the National Academy of Sciences of the United States of America **15**, 3, 168 (1929).

[4] W. Herschel, "On the Construction of the Heavens," Philosophical Transactions of the Royal Society of London **75**, 213 (1785).

[5] H. D. Curits, "Descriptions of 762 Nebulae and Clusters Photographed with the Crossley Reflector," Publications of Lick Observatory **13**, 9 (1918).

[6] E. Hubble and M. L. Humason, "The Velocity-Distance Relation among Extra-Galactic Nebulae," ApJ **74**, 43 (1931).

[7] F. Zwicky, "Die Rotverschiebung von extragalaktischen Nebeln," Helvetica Physica Acta **6**, 110 (1933).

[8] F. Zwicky, "On the Masses of Nebulae and of Clusters of Nebulae," ApJ **86**, 217 (1937).

[9] H. W. Babcock, "The rotation of the Andromeda Nebula," Lick Observatory bulletin **19**, 41 (1939).

[10] F. D. Kahn and L. Woltjer, "Intergalactic Matter and the Galaxy," ApJ **130**, 705 (1959).

[11] V. C. Rubin and W. K. Ford Jr., "Rotation of the Andromeda Nebula from a Spectroscopic Survey of Emission Regions," ApJ, **159**, 379 (1970).

[12] J. P. Ostriker, P. J. E. Peebles, and A. Yahil, "The size and mass of galaxies, and the mass of the universe," ApJ **193**, L1 (1974).

[13] J. Einasto, E. Saar, A. Kaasik, and A. D. Chernin, "Missing mass around galaxies - Morphological evidence," Nature **252**, 111 (1974).

[14] J. P. Ostriker and P. J. E. Peebles, "A Numerical Study of the Stability of Flattened Galaxies: or, can Cold Galaxies Survive?" ApJ **186**, 467 (1973).

[15] S. F. Shandarin, A. G. Doroshkevich, and Ya B. Zel'dovich, "The large-scale structure of the universe," Soviet Physics Uspekhi **26**, 46 (1983).

[16] F. Halzen and S. R. Klein, "Invited Review Article: IceCube: An instrument for neutrino astronomy," Review of Scientific Instruments **81**, 24 (2010).

[17] M. Shaposhnikov, "Sterile neutrinos in cosmology and how to find them in the lab," Journal of Physics: Conference Series **136**, 2 (2008).

[18] J. Ellis, et al., "Supersymmetric relics from the big bang," Nuclear Physics B **238**, 453 (1984).

[19] J. Preskill, M. B. Wise, and F. Wilczek, "Cosmology of the invisible axion," Physics Letters B **120**, 127 (1983).

[20] G. Steigman and M. S. Turner, "Cosmological constraints on the properties of weakly interacting massive particles," Nuclear Physics B **253**, 375 (1985).

[21] K. Griest, "Galactic microlensing as a method of detecting massive compact halo objects," ApJ **366**, 412 (1991).

[22] B. Paczynski, "Gravitational microlensing by the galactic halo," ApJ **304**, 1 (1986).

[23] M. Davis et al., "A survey of galaxy redshifts. II - The large scale space distribution," ApJ **253**, 423 (1982).

[24] S. D. M. White, C. S. Frenk, and M. Davis, "Clustering in a neutrino-dominated universe," ApJ **274**, L1 (1983).

[25] M. Davis et al., "The evolution of large-scale structure in a universe dominated by cold dark matter," ApJ **292**, 371 (1985).

[26] D. Clowe, A. Gonzalez, M. Markevitch, "Weak-Lensing Mass Reconstruction of the Interacting Cluster 1E 0657-558: Direct Evidence for the Existence of Dark Matter," ApJ **604**, 596 (2004).

[27] M. Markevitch et al., "Direct Constraints on the Dark Matter Self-Interaction Cross Section from the Merging Galaxy Cluster 1E 0657-56," ApJ **606**, 819 (2004).

[28] A. Klypin et al., "Where Are the Missing Galactic Satellites?," ApJ **522**, 82 (1999).

[29] B. Moore et al., "Dark Matter Substructure within Galactic Halos," ApJ **524**, 19 (1999).

[30] A. Drlica-Wagner et al., "Eight Ultra-faint Galaxy Candidates Discovered in Year Two of the Dark Energy Survey," ApJ **813**, 109 (2015).

[31] T. Sawala et al., "The APOSTLE simulations: solutions to the Local Group's cosmic puzzles," MNRAS **457**, 1931 (2016).

[32] J. F. Navarro et al., "The diversity and similarity of simulated cold dark matter haloes," MNRAS **402**, 21 (2010).

[33] M. G. Walker and J. Pearrubia, "A Method for Measuring (Slopes of) the Mass Profiles of Dwarf Spheroidal Galaxies," ApJ **742**, 19 (2011).

[34] F. Governato et al., "Cuspy no more: how outflows affect the central dark matter and baryon distribution in Λ cold dark matter galaxies," MNRAS **422**, 1231 (2012).

[35] A. Di Cintio et al., "The dependence of dark matter profiles on the stellar-to-halo mass ratio: a prediction for cusps versus cores," MNRAS **437**, 415 (2014).

[36] M. Boylan-Kolchin, J. S. Bullock, and M. Kaplinghat, "Too big to fail? The puzzling darkness of massive Milky Way subhaloes," MNRAS **415**, 40 (2011).

[37] M. Boylan-Kolchin, J. S. Bullock, and M. Kaplinghat, "The Milky Way's bright satellites as an apparent failure of ΛCDM ," MNRAS **422**, 1203 (2012).

[38] A. R. Wetzel et al., "Reconciling Dwarf Galaxies with ?CDM Cosmology: Simulating a Realistic Population of Satellites around a Milky Way-mass Galaxy," ApJL **827**, 23 (2016).

[39] J. S. Bullock and M. Boylan-Kolchin, "Small-Scale Challenges to the ?CDM Paradigm," Annual Review of Astronomy and Astrophysics **55**, 343 (2017).

[40] A. G. Riess et al., "Observational Evidence from Supernovae for an Accelerating Universe and a Cosmological Constant," AJ **116**, 1009 (1998).

[41] S. Perlmutter et al., "Measurements of Ω and Λ from 42 High-Redshift Supernovae," ApJ **517**, 565 (1999).

[42] S. J. Maddox et al., "Galaxy correlations on large scales," MNRAS **242**, 43 (1990).

[43] G. Efstathiou, W. J. Sutherland, and S. J. Maddox, "The cosmological constant and cold dark matter," Nature **348**, 705 (1990).

[44] A. H. Guth, "Inflationary universe: A possible solution to the horizon and flatness problems," PhsRevD **23**, 347 (1981).

[45] S. Cole et al., "Large-scale structure in COBE-normalized cold dark matter cosmogonies," MNRAS **289**, 37 (1997).

[46] M. J. Pierce et al., "The Hubble constant and Virgo cluster distance from observations of Cepheid variables," Nature **371**, 385 (1994).

[47] W. L. Freedman et al., "Distance to the Virgo cluster galaxy M100 from Hubble Space Telescope observations of Cepheids," Nature **371**, 757 (1994).

[48] B. Chaboyer et al., "A Lower Limit on the Age of the Universe," Science **271**, 957 (1996).

[49] D. H. Weinberg et al., "Observational probes of cosmic acceleration," Physics Reports **530**, 87 (2013).

[50] D. Huterer and M. S. Turner, "Prospects for probing the dark energy via supernova distance measurements," Physical Review D **60**, 8 (1999).

[51] DES Collaboration, "Dark Energy Survey year 1 results: Cosmological constraints from galaxy clustering and weak lensing," Physical Review D **98**, xx (2018).

[52] E. Rozo et al., "Cosmological Constraints from the Sloan Digital Sky Survey maxBCG Cluster Catalog," ApJ **708**, 645 (2010).

[53] J. Dunkley et al, "Five-Year Wilkinson Microwave Anisotropy Probe Observations: Likelihoods and Parameters from the WMAP Data," ApJ Supplement **180**, 306 (2009).

[54] A. Vikhlinin et al., "Chandra Cluster Cosmology Project III: Cosmological Parameter Constraints," ApJ **692**, 1060 (2009).

[55] A. Mantz, S. W. Allen, D. Rapetti, and H. Ebeling, "The observed growth of massive galaxy clusters - I. Statistical methods and cosmological constraints," MNRAS **406**, 1759 (2010)

[56] A. Einstein, "Die Feldgleichungen der Gravitation," SPAW, 844 (1915).

[57] F. W. Dyson, A. S. Eddington, and C. Davidson, "A Determination of the Deflection of Light by the Sun's Gravitational Field, from Observations Made at the Total Eclipse of May 29, 1919," Phil. Trans. of the Roy. Soc. of London **220**, 291 (1919).

[58] M. Bartelmann, "TOPICAL REVIEW Gravitational lensing," Classical and Quantum Gravity **27**, 23 (2010).

[59] H. Hoekstra et al., "Masses of Galaxy Clusters from Gravitational Lensing," Space Science Reviews **177**, 75 (2013).

[60] G. Soucail et al., "A blue ring-like structure, in the center of the A 370 cluster of galaxies," A&A **172**, L14 (1987).

[61] M. Bradač et al., "Strong and weak lensing united. I. The combined strong and weak lensing cluster mass reconstruction method," A&A **437**, 39 (2005).

[62] M. Meneghetti et al., "Weighing simulated galaxy clusters using lensing and X-ray," A&A **514**, A93 (2010).

[63] M. Bradač et al., "Revealing the Properties of Dark Matter in the Merging Cluster MACS J0025.4-1222," ApJ **687**, 959 (2008).

[64] A. B. Newman et al., "The Dark Matter Distribution in A383: Evidence for a Shallow Density Cusp from Improved Lensing, Stellar Kinematic, and X-ray Data," ApJ Letters **728**, L39 (2011).

[65] J. A. Tyson,F. Valdes, and R. .A Wenk, "Detection of systematic gravitational lens galaxy image alignments - Mapping dark matter in galaxy clusters," ApJ **349**, L1 (1990).

[66] H. Hoekstra, "A comparison of weak-lensing masses and X-ray properties of galaxy clusters," MNRAS **379**, 317 (2007).

[67] V. L. Corless and L. J. King, "A statistical study of weak lensing by triaxial dark matter haloes: consequences for parameter estimation," MNRAS **380**, 149 (2007).

[68] M. R. Becker and A. V. Kravtsov, "On the Accuracy of Weak-lensing Cluster Mass Reconstructions," ApJ **740**, 17 (2011).

[69] T. McClintock et al., "Dark Energy Survey Year 1 results: weak lensing mass calibration of redMaPPer galaxy clusters," MNRAS **482**, 1352 (2019).

[70] K. Miyaoka et al., "Multiwavelength study of X-ray luminous clusters in the Hyper Suprime-Cam Subaru Strategic Program S16A field," Publications of the Astronomical Society of Japan **70**, S22 (2018).

[71] N. Scoville et al., "The Cosmic Evolution Survey (COSMOS): Overview," ApJ Supplement **172**, 1 (2007)

[72] A. Leauthaud et al., "A Weak Lensing Study of X-ray Groups in the Cosmos Survey: Form and Evolution of the Mass-Luminosity Relation," ApJ **709**, 97 (2010).

[73] C. L. Sarazin, "X-ray emission from clusters of galaxies," Cambridge Astrophysics Series (1986).

[74] R. Sadat, "Clusters of Galaxies and Mass Estimates," Astronomical Society of the Pacific Conference Series **126**, 349 (1997).

[75] B. R. McNamara and P. E. J. Nulsen, "Heating Hot Atmospheres with Active Galactic Nuclei," Annual reviews of A&A **45**, 117 (2007).

[76] N. Gupta et al., "SZE observables, pressure profiles and centre offsets in Magneticum simulation galaxy clusters," MNRAS **469**, 3069 (2017).

[77] A. Vikhlinin et al., "Chandra Sample of Nearby Relaxed Galaxy Clusters: Mass, Gas Fraction, and Mass-Temperature Relation," ApJ **640**, 691 (2006).

[78] R. W. Schmidt and S. W. Allen, "The dark matter haloes of massive, relaxed galaxy clusters observed with Chandra," MNRAS **379**, 209 (2007).

[79] A. E. Evrard et al, "Virial Scaling of Massive Dark Matter Halos: Why Clusters Prefer a High Normalization Cosmology," ApJ **672**, 122 (2008).

[80] A. Diaferio and M. J. Geller, "Infall Regions of Galaxy Clusters," ApJ **481**, 633 (1997).

[81] G. A. Mamon, A. Biviano, and G. Bou, "MAMPOSSt: Modelling Anisotropy and Mass Profiles of Observed Spherical Systems - I. Gaussian 3D velocities," MNRAS **429**, 3079 (2013).

[82] S. Bocquet et al., "Mass Calibration and Cosmological Analysis of the SPT-SZ Galaxy Cluster Sample Using Velocity Dispersion σ_v and X-Ray Y_X Measurements," ApJ **799**, 214 (2015).

[83] M. White, J. D. Cohn, and R. Smit, "Cluster galaxy dynamics and the effects of large-scale environment," MNRAS **408**, 1818 (2010).

[84] N. Kaiser, "Clustering in real space and in redshift space," MNRAS **227**, 1 (1987).

[85] E. Regos and M. J. Geller, "Infall patterns around rich clusters of galaxies," AJ **98**, 755 (1989).

[86] A. Diaferio, "Mass estimation in the outer regions of galaxy clusters," MNRAS **309**, 610 (1999).

[87] K. Rines et al., "CAIRNS: The Cluster and Infall Region Nearby Survey. I. Redshifts and Mass Profiles," AJ **126**, 2152 (2003).

[88] K. Rines and A. Diaferio, "CIRS: Cluster Infall Regions in the Sloan Digital Sky Survey. I. Infall Patterns and Mass Profiles," AJ **132**, 1275 (2006).

[89] K. Rines et al., "Measuring the Ultimate Halo Mass of Galaxy Clusters: Redshifts and Mass Profiles from the Hectospec Cluster Survey (HeCS)," ApJ **767**, 15 (2013).

[90] M. J. Geller, A. Diaferio, and M. J. Kurtz, "The Mass Profile of the Coma Galaxy Cluster," ApJ **517**, L23 (1999).

[91] J. Sohn et al., "The Massively Accreting Cluster A2029," ApJ **871**, 129 (2019).

[92] D. Merritt, "The distribution of dark matter in the coma cluster," ApJ **313**, 121 (1987).

[93] E. Rasia, G. Tormen, and L. Moscardini, "A dynamical model for the distribution of dark matter and gas in galaxy clusters," MNRAS **351** 237 (2004).

[94] D. Nagai, A. Vikhlinin, and A. V. Kravtsov, "Testing X-Ray Measurements of Galaxy Clusters with Cosmological Simulations," ApJ **655**, 98 (2007).

[95] A. Simionescu et al., "Baryons at the Edge of the X-ray-Brightest Galaxy Cluster," Science **331**, 1576 (2011).

[96] L. Old et al., "Galaxy Cluster Mass Reconstruction Project - III. The impact of dynamical substructure on cluster mass estimates," MNRAS **475**, 853 (2018).

[97] Z. Lukić et al., "The Structure of Halos: Implications for Group and Cluster Cosmology," ApJ **692**, 217 (2009).

[98] J. Binney and S. Tremaine, "Galactic Dynamics: Second Edition," Princeton University Press (2008).

[99] G. Fasano et al., "Morphological fractions of galaxies in WINGS clusters: revisiting the morphology-density paradigm," MNRAS **449**, 3927 (2015).

[100] D. Richstone, A. Loeb, and E. L. Turner, "A lower limit of the cosmic mean density from the ages of clusters of galaxies," ApJ **393**, 477 (1992).

[101] M. Girardi et al., "Velocity Dispersions and X-Ray Temperatures of Galaxy Clusters," ApJ **457**, 61 (1996).

[102] J. Pinkney et al., "Evaluation of Statistical Tests for Substructure in Clusters of Galaxies," ApJS **104**, 1 (1996).

[103] C. D. Shane and C. A. Wirtanen, "The distribution of extragalactic nebulae," AJ **59**, 285 (1954).

[104] M. J. West and G. .D Bothun, "A reanalysis of substructure in clusters of galaxies and their surroundings," ApJ **350**, 36 (1990).

[105] C. M. Bird and T. C. Beers, "Astronomical applications of distribution shape estimators," AJ **105**, 1596 (1993).

[106] A. Pisani, "A Non-Parametric and Scale-Independent Method for Cluster Analysis - Part One - the Univariate Case," MNRAS **265**, 706 (1993).

[107] K. M. Ashman et al., "Detecting bimodality in astronomical datasets," AJ **108**, 2348 (1994).

[108] M. J. Geller and T. C. Beers, "Substructure within clusters of galaxies," Astronomical Society of the Pacific **94**, 412 (1982).

[109] M. J. West, A. Oemler, and A. Dekel, "Subclustering in rich clusters of galaxies and their environs," ApJ **327**, 1 (1988).

[110] E. Salvador-Solé, G. Gonzalez-Casado, and J. M. Solanes, "Small-scale substructure in relaxed clusters. I - Statistical characterization. II - Clustering model," ApJ **410**, 1 (1993).

[111] E. Slezak, A. Bijaoui, and G. Mars, "Identification of structures from galaxy counts - Use of the wavelet transform," A&A **227**, 301 (1990).

[112] A. Dressler and S. A. Shectman, "Evidence for substructure in rich clusters of galaxies from radial-velocity measurements," AJ **95**, 985 (1988).

[113] A. Pisani, "A non-parametric and scale-independent method for cluster analysis - II. The multivariate case," MNRAS **278**, 697 (1996).

[114] E. Escalera and A. Mazure, "Wavelet analysis of subclustering - an illustration, Abell 754," ApJ **388**, 23 (1992).

[115] A. Biviano et al., "The ESO Nearby Abell Cluster Survey. XI. Segregation of cluster galaxies and subclustering," A&A **387**, 8 (2005).

[116] M. Girardi et al., "CLASH-VLT: Substructure in the galaxy cluster MACS J1206.2-0847 from kinematics of galaxy populations," A&A **579**, A4 (2015).

[117] H. Yu et al., "Identification of Galaxy Cluster Substructures with the Caustic Method," ApJ **810**, 37 (2015).

[118] H. Yu et al., "Blooming Trees: Substructures and Surrounding Groups of Galaxy Clusters," ApJ **860**, 118 (2018).

[119] E. Tucker et al., "Magellan/M2FS Spectroscopy of Galaxy Clusters: Stellar Population Model and Application to Abell 267," AJ **154**, 113 (2017).

[120] E. Tucker et al., "Galaxy Cluster Mass Estimates in the Presence of Substructure," arXiv:1810.10474

[121] J. Fraunhofer, "Bestimmung des Brechungs- und des Farbenzerstreungs-Vermgens verschiedener Glasarten, in Bezug auf die Vervollkommnung achromatischer Fernrhre," Annalen der Physik **56**, 264 (1817).

[122] J. Fraunhofer, "Kurzer Bericht von den Resultaten neuerer Versuche ber die Gesetze des Lichtes, und die Theorie derselben," Annalen det Physik **74**, 337 (1823).

[123] D. G. Fabricant,R. G. Fata, and H. W. Epps, "Binospec: a dual-beam wide-field optical spectrograph for the converted MMT," SPIE **3355**, 232 (1998).

[124] J. M. Hill et al., "Multiple object spectroscopy - The Medusa spectrograph," ApJ **242**, L69 (1980).

[125] M. Mateo et al., "M2FS: the Michigan/Magellan Fiber System," SPIE **8446**, 84464Y (2012).

[126] BOSS Collaboration, "The Ninth Data Release of the Sloan Digital Sky Survey: First Spectroscopic Data from the SDSS-III Baryon Oscillation Spectroscopic Survey," ApJS **203**, 21 (2012).

[127] SDSS Collaboration, "The 13th Data Release of the Sloan Digital Sky Survey: First Spectroscopic Data from the SDSS-IV Survey Mapping Nearby Galaxies at Apache Point Observatory," ApJSS **233**, 25 (2017).

[128] D. Tody, "The IRAF Data Reduction and Analysis System," SPIE **627**, 733 (1986).

[129] A. Einstein, "Über einen die Erzeugung und Verwandlung des Lichtes betreffenden heuristischen Gesichtspunkt," Annalen der Physik **322**, 132 (1905).

[130] W. J. Percival et al., "The 2dF Galaxy Redshift Survey: the power spectrum and the matter content of the Universe," MNRAS **327**, 1297 (2001).

[131] J. A. Peacock et al., "A measurement of the cosmological mass density from clustering in the 2dF Galaxy Redshift Survey," Nature **410**, 169 (2001).

[132] E. Hawkins et al., "The 2dF Galaxy Redshift Survey: correlation functions, peculiar velocities and the matter density of the Universe," MNRAS **346**, 78 (2003).

[133] M. Colless et al., "The 2dF Galaxy Redshift Survey: spectra and redshifts," MNRAS **328**, 1039 (2001).

[134] SDSS Collaboration, "The Seventh Data Release of the Sloan Digital Sky Survey," ApJS **182**, 543 (2009).

[135] BOSS Collaboration, "The Baryon Oscillation Spectroscopic Survey of SDSS-III," AJ **145**, 10 (2013).

[136] eBOSS Collaboration, "The SDSS-IV Extended Baryon Oscillation Spectroscopic Survey: Overview and Early Data," AJ **151**, 44 (2016).

[137] B. Garilli et al., "The Vimos VLT deep survey. Global properties of 20,000 galaxies in the IAB ¡ 22.5 WIDE survey," A&A **486**, 683 (2008).

[138] A. Marchetti et al., "The VIMOS Public Extragalactic Redshift Survey (VIPERS): spectral classification through principal component analysis," MNRAS **428**, 1424 (2013).

[139] P. Rosati et al, "CLASH-VLT: A VIMOS Large Programme to Map the Dark Matter Mass Distribution in Galaxy Clusters and Probe Distant Lensed Galaxies," The Messenger **158**, 48 (2014).

[140] G. A. Oyarzún et al., "A Comprehensive Study of Lyα Emission in the High-redshift Galaxy Population," ApJ **843**, 133 (2017).

[141] L. Jiang et al., "A Magellan M2FS Spectroscopic Survey of Galaxies at 5.5 ¡ z ¡ 6.8: Program Overview and a Sample of the Brightest Lyα Emitters," ApJ **846**, 134 (2017).

[142] A. Dressler et al., "Studying the Star Formation Histories of Galaxies in Clusters from Composite Spectra," ApJ **617**, 867 (2004).

[143] M. G. Voit, "Tracing cosmic evolution with clusters of galaxies," Reviews of Modern Physics **77**, 207 (2005).

[144] C. Jones et al., "Hot Baryons in Deep Potential Wells: IXO Studies of Hot Gas in Galaxies, Groups and Clusters," Bulletin of the American Astronomical Society **41**, 351 (2009).

[145] M. J. Geller et al., "Measuring the Mass Distribution in Galaxy Clusters," ApJ **764**, 58 (2013).

[146] J. P. Kneib, "Gravitational Lensing by Clusters of Galaxies," A Pan-Chromatic View of Clusters of Galaxies and the Large-Scale Structure **740**, 24 (2008).

[147] D. E. Applegate et al., "Weighing the Giants - III. Methods and measurements of accurate galaxy cluster weak-lensing masses," MNRAS **439**, 48 (2014).

[148] E. J. Gonzalez et al., "Low X-ray luminosity galaxy clusters - III. Weak lensing mass determination at $0.18 < z < 0.70$," MNRAS **452**, 2225 (2015).

[149] A. Barreira et al., "Galaxy cluster lensing masses in modified lensing potentials," MNRAS **454**, 4085 (2015).

[150] L. Guennou et al., "Mass profile and dynamical status of the $z \sim 0.8$ galaxy cluster LCDCS 0504," A&A **566**, A149 (2014).

[151] J. W. Moffat and S. Rahvar, "The MOG weak field approximation - II. Observational test of Chandra X-ray clusters," MNRAS **441**, 3724 (2014).

[152] . M. Girardi et al., "A multiwavelength view of the galaxy cluster Abell 523 and its peculiar diffuse radio source," MNRAS **456**, 2829 (2016)

[153] R. A. Sunyaev and Y. B. Zeldovich, "Small-Scale Fluctuations of Relic Radiation," Astrophysics and Space Science **7**, 3 (1970).

[154] M. Birkinshaw, S. F. Gull, and H. Hardebeck, "The Sunyaev-Zeldovich effect towards three clusters of galaxies," Nature **309**, 34 (1984).

[155] M. Birkinshaw, "The Sunyaev-Zel'dovich effect," Physics Reports **310**, 97 (1999).

[156] D. Stock et al., "The projected gravitational potential of the galaxy cluster MACS J1206 derived from galaxy kinematics," A&A **584**, A63 (2015).

[157] A. Biviano et al., "The dynamics of $z \sim 1$ clusters of galaxies from the GCLASS survey," A&A **594**, A51 (2016).

[158] A. Dressler et al., "Demonstrating Diversity in Star-formation Histories with the CSI Survey," ApJ **833**, 251 (2016).

[159] L. A. Tasca et al., "The VIMOS Ultra Deep Survey first data release: Spectra and spectroscopic redshifts of 698 objects up to $z_{\rm spec} \sim 6$ in CANDELS," A&A **600**, A110 (2017).

[160] J. Sohn et al., "The Velocity Dispersion Function of Very Massive Galaxy Clusters: Abell 2029 and Coma," ApJSS **229**, 20 (2017).

[161] M. J. Geller et al., "A Redshift Survey of the Strong-lensing Cluster Abell 383," ApJ **783**, 52 (2014).

[162] A. Biviano et al., "CLASH-VLT: The mass, velocity-anisotropy, and pseudo-phase-space density profiles of the z = 0.44 galaxy cluster MACS J1206.2-0847," A&A **558**, A1 (2013).

[163] A. Dressler et al., "IMACS: The Inamori-Magellan Areal Camera and Spectrograph on Magellan-Baade," Publications of the Astronomical Society of the Pacific **123**, 288 (2011).

[164] A. Oemler et al., "The IMACS Cluster Building Survey. I. Description of the Survey and Analysis Methods," ApJ **770**, 61 (2013).

[165] J. I. Bailey, M. L. Mateo, and J. D. Crane, "Achieving decameter velocity precision with a multi-object spectrograph," SPIE **9147**, 91476P (2014).

[166] J. I. Bailey et al., "Multiplexing Precision RVs: Searching for Close-in Gas Giants in Open Clusters," AJ **152**, 9 (2016).

[167] C. I. Johnson et al., "AGB Sodium Abundances in the Globular Cluster 47 Tucanae (NGC 104)," AJ **149**, 71 (2015).

[168] C. I. Johnson et al., "A Spectroscopic Analysis of the Galactic Globular Cluster NGC 6273 (M19)," AJ **150**, 63 (2015).

[169] I. U. Roederer et al., "Detailed chemical abundances in NGC 5824: another metal-poor globular cluster with internal heavy element abundance variations," MNRAS **455**, 2417 (2016).

[170] C. I. Johnson et al., "A Chemical Composition Survey of the Iron-complex Globular Cluster NGC 6273 (M19)," ApJ **836**, 168 (2017).

[171] I. U. Roederer et al., "Detailed Chemical Abundances in the r-process-rich Ultra-faint Dwarf Galaxy Reticulum 2," AJ **151**, 82 (2016).

[172] M. G. Walker et al., "Magellan/M2FS Spectroscopy of the Reticulum 2 Dwarf Spheroidal Galaxy," ApJ **808**, 108 (2015).

[173] M. G. Walker et al., "Magellan/M2FS Spectroscopy of Tucana 2 and Grus 1," ApJ **819**, 53 (2016).

[174] J. D. Simon et al., "Stellar Kinematics and Metallicities in the Ultra-faint Dwarf Galaxy Reticulum II," ApJ **808**, 95 (2015).

[175] B. M. Tinsley, "Galactic Evolution," A&A **20**, 383 (1972).

[176] L. Searle, W. L. Sargent, and W. G. Bagnuolo, "The History of Star Formation and the Colors of Late-Type Galaxies," ApJ **179**, 427 (1973).

[177] R. B. Larson and B. M. Tinsley, "Star formation rates in normal and peculiar galaxies," ApJ **219**, 46 (1978).

[178] J. Walcher et al., "Fitting the integrated spectral energy distributions of galaxies," Astrophysics and Space Science **331**, 1 (2011).

[179] Y. Han and Z. Han, "BayeSED: A General Approach to Fitting the Spectral Energy Distribution of Galaxies," ApJSS **215**, 2 (2014).

[180] J. Chevallard and S. Charlot, "Modelling and interpreting spectral energy distributions of galaxies with BEAGLE," MNRAS **462**, 1415 (2016).

[181] S. Meneses-Goytia et al., "Single stellar populations in the near-infrared. II. Synthesis models," A&A **582**, A97 (2015).

[182] M. G. Walker, E. W. Olszewski, and M. Mateo, "Bayesian analysis of resolved stellar spectra: application to MMT/Hectochelle observations of the Draco dwarf spheroidal," MNRAS **448**, 2717 (2015).

[183] SDSS Collaboration, "The Eleventh and Twelfth Data Releases of the Sloan Digital Sky Survey: Final Data from SDSS-III," ApJS **219**, 12 (2015).

[184] S. E. Koposov et al., "Accurate Stellar Kinematics at Faint Magnitudes: Application to the Boötes I Dwarf Spheroidal Galaxy," ApJ **736**, 146 (2011).

[185] P. J. Rousseeuw and C. Croux, "Alternatives to the Median Absolute Deviation," Journal of the American Statistical Association **88**, 424 (1993).

[186] T. O. Husser et al., "A new extensive library of PHOENIX stellar atmospheres and synthetic spectra," A&A **553**, A6 (2013).

[187] C. Conroy and J. E. Gunn, "The Propagation of Uncertainties in Stellar Population Synthesis Modeling. III. Model Calibration, Comparison, and Evaluation," ApJ **712**, 833 (2010).

[188] A. Dotter et al., "The Dartmouth Stellar Evolution Database," ApJS **178**, 89 (2008).

[189] G. Chabrier, "Galactic Stellar and Substellar Initial Mass Function," The Publications of the Astronomical Society of the Pacific **115**, 763 (2003).

[190] M. Koleva et al., "ULySS: a full spectrum fitting package," A&A **501**, 1269 (2009).

[191] F. Feroz and M. P. Hobson, "Multimodal nested sampling: an efficient and robust alternative to Markov Chain Monte Carlo methods for astronomical data analyses," MNRAS **384**, 449 (2008).

[192] F. Feroz, M. P. Hobson, and M. Bridgers, "MULTINEST: an efficient and robust Bayesian inference tool for cosmology and particle physics," MNRAS **398**, 1601 (2009).

[193] I. V. Chilingarian et al., "Kinematics and stellar populations of low-luminosity early-type galaxies in the Abell 496 cluster," A&A **486**, 85 (2008).

[194] I. V. Chilingarian et al., "NBursts: Simultaneous Extraction of Internal Kinematics and Parametrized SFH from Integrated Light Spectra," Stellar Populations as Building Blocks of Galaxies, Proceedings of IAU Symposium **241**, 175 (2007).

[195] D. Le Borgne et al., "Evolutionary synthesis of galaxies at high spectral resolution with the code PEGASE-HR. Metallicity and age tracers," A&A **425**, 881 (2004).

[196] M. Postman et al., "The Cluster Lensing and Supernova Survey with Hubble: An Overview," ApJS **199**, 25 (2012).

[197] O. Graur et al., "Type-Ia Supernova Rates to Redshift 2.4 from CLASH: The Cluster Lensing And Supernova Survey with Hubble," ApJ **783**, 28 (2014).

[198] B. Patel et al., "Three Gravitationally Lensed Supernovae behind CLASH Galaxy Clusters," ApJ **786**, 9 (2014).

[199] L. G. Strolger et al., "The Rate of Core Collapse Supernovae to Redshift 2.5 from the CANDELS and CLASH Supernova Surveys," ApJ **813**, 93 (2015).

[200] A. G. Riess et al., "Type Ia Supernova Distances at Redshift ¿1.5 from the Hubble Space Telescope Multi-cycle Treasury Programs: The Early Expansion Rate," ApJ **853**, 126 (2018).

[201] N. Pirzkal et al., "Not In Our Backyard: Spectroscopic Support for the CLASH z=11 Candidate MACS 0647-JD," ApJ **804**, 11 (2015).

[202] K. Umetsu et al., "CLASH: Mass Distribution in and around MACS J1206.2-0847 from a Full Cluster Lensing Analysis," ApJ **755**, 56 (2012).

[203] D. Coe et al., "CLASH: Precise New Constraints on the Mass Profile of the Galaxy Cluster A2261," ApJ **757**, 22 (2012).

[204] D. Gruen et al., "Weak lensing analysis of RXC J2248.7-4431," MNRAS **432**, 1455 (2013).

[205] E. Medezinski et al., "CLASH: Complete Lensing Analysis of the Largest Cosmic Lens MACS J0717.5+3745 and Surrounding Structures," ApJ **777**, 43 (2013).

[206] C. Grillo et al., "CLASH-VLT: Insights on the Mass Substructures in the Frontier Fields Cluster MACS J0416.1-2403 through Accurate Strong Lens Modeling," ApJ **800**, 38 (2015).

[207] G. B. Caminha et al., "CLASH-VLT: A highly precise strong lensing model of the galaxy cluster RXC J2248.7-4431 (Abell S1063) and prospects for cosmography," A&A **587**, A80 (2016).

[208] I. Balestra et al., "CLASH-VLT: Dissecting the Frontier Fields Galaxy Cluster MACS J0416.1-2403 with 800 Spectra of Member Galaxies," ApJSS **224**, 33 (2016).

[209] B. Sartoris et al., "CLASH-VLT: Constraints on the Dark Matter Equation of State from Accurate Measurements of Galaxy Cluster Mass Profiles," ApJL **783**, L11 (2014).

[210] L. Pizzuti et al., "CLASH-VLT: testing the nature of gravity with galaxy cluster mass profiles," Journal of Cosmology and Astroparticle Physics **4**, 23 (2016).

[211] L. Pizzuti et al., "CLASH-VLT: constraints on f(R) gravity models with galaxy clusters using lensing and kinematic analyses," Journal of Cosmology and Astroparticle Physics **7**, 23 (2017).

[212] V. Presotto et al., "Intracluster light properties in the CLASH-VLT cluster MACS J1206.2-0847," A&A **565**, A126 (2014).

[213] M. Annunziatella et al., "CLASH-VLT: The stellar mass function and stellar mass density profile of the z = 0.44 cluster of galaxies MACS J1206.2-0847," A&A **571**, A80 (2014).

[214] M. Annunziatella et al., "CLASH-VLT: Environment-driven evolution of galaxies in the z = 0.209 cluster Abell 209," A&A **585**, A160 (2016).

[215] C. Maier et al., "CLASH-VLT: Strangulation of cluster galaxies in MACS J0416.1-2403 as seen from their chemical enrichment," A&A **590**, A108 (2016).

[216] I. Balestra et al., "CLASH-VLT: spectroscopic confirmation of a z = 6.11 quintuply lensed galaxy in the Frontier Fields cluster RXC J2248.7-4431," A&A **559**, L9 (2013).

[217] A. von der Linden et al., "Weighing the Giants - I. Weak-lensing masses for 51 massive galaxy clusters: project overview, data analysis methods and cluster images," MNRAS **439**, 2 (2014).

[218] K. Umetsu et al., "CLASH: Weak-lensing Shear-and-magnification Analysis of 20 Galaxy Clusters," ApJ **795**, 163 (2014).

[219] A. Rabitz et al., "Probing the dynamical and X-ray mass proxies of the cluster of galaxies Abell S1101," A&A **597**, A24 (2017).

[220] E. Churazov, A. Vikhlinin, and R. Sunyaev, "(No) dimming of X-ray clusters beyond $z \sim 1$ at fixed mass: crude redshifts and masses from raw X-ray and SZ data," MNRAS **450**, 1984 (2015).

[221] K. J. Rines et al., "HeCS-SZ: The Hectospec Survey of Sunyaev-Zeldovich-selected Clusters," ApJ **819**, 63 (2016).

[222] M. P. van Haarlem et al., "The Dynamics of the Outer Regions of the Coma Cluster," MNRAS **264**, 71 (1993).

[223] B. Aryal et al., "Spatial orientation of angular momentum vectors of galaxies in six rotating clusters," MNRAS **434**, 1939 (2013).

[224] H. M. Tovmassian, "The Rotation of Galaxy Clusters," Astrophysics **58**, 328 (2015).

[225] M. Manolopoulou and M. Plionis, "Galaxy cluster's rotation," MNRAS **465**, 2616 (2017).

[226] L. X. Li, "Effect of the Global Rotation of the Universe on the Formation of Galaxies," General Relativity and Gravitation **30**, 497 (1998).

[227] J. Materne and U. Hopp, "The cluster of galaxies SC0316-44 - Does it rotate?" A&A **124**, L13 (1983).

[228] W. R. Oegerle and J. M. Hill, "Structure, rotation, and the peculiar velocity cD galaxy in Abell 2107," AJ **104**, 2078 (1992).

[229] H. S. Hwang and M. H. Lee, "Searching for Rotating Galaxy Clusters in SDSS and 2dFGRS," ApJ **662**, 236 (2007).

[230] M. Kalinkov et al., "Rotation of the cluster of galaxies A2107," MNRAS **359**, 1491 (2005).

[231] M. Bianconi, S. Ettori, and C. Nipoti, "Gas rotation in galaxy clusters: signatures and detectability in X-rays," MNRAS **434**, 1565 (2013).

[232] A. Hou et al., "Statistical Tools for Classifying Galaxy Group Dynamics," ApJ **702**, 1199 (2009).

[233] R. Coziol et al., "The Dynamical State of Brightest Cluster Galaxies and The Formation of Clusters," ApJ **137**, 4795 (2009).

[234] M. Einasto et al., "Multimodality in galaxy clusters from SDSS DR8: substructure and velocity distribution," A&A **540**, A123 (2012).

[235] R. Barrena et al., "The dynamical status of the galaxy cluster Abell 115," A&A **469**, 861 (2007).

[236] G. Chon, H. Bhringer, and G. P. Smith et al, "Statistics and implications of substructure detected in a representative sample of X-ray clusters," A&A **548**, A59 (2012).

[237] J. Dubinski and R. G. Carlberg, "The structure of cold dark matter halos," ApJ **378**, 496 (1991).

[238] J. F. Navarro, C. S. Frenk, and S. D .M. White, "The Structure of Cold Dark Matter Halos," ApJ **462**, 563 (1996).

[239] J. F. Navarro, C. S. Frenk, and S. D .M. White, "A Universal Density Profile from Hierarchical Clustering," ApJ **490**, 493 (1997).

[240] S. Y. Kim, A. H. G. Peter, and D. Wittman, "In the wake of dark giants: new signatures of dark matter self-interactions in equal-mass mergers of galaxy clusters," MNRAS **469**, 1414 (2017).

[241] D. Harvey et al., "A detection of wobbling brightest cluster galaxies within massive galaxy clusters," MNRAS **472**, 1972 (2017).

[242] Y. Y. Zhang et al., "Probing cluster dynamics in RXC J1504.1-0248 via radial and two-dimensional gas and galaxy properties," A&A **542**, A106 (2012).

[243] J. C. Richardson et al., "PAndAS' Progeny: Extending the M31 Dwarf Galaxy Cabal," ApJ **732**, 76 (2011).

[244] M. Bartelmann, "Arcs from a universal dark-matter halo profile," A&A **313**, 697 (1996).

[245] A. Klypin et al., "MultiDark simulations: the story of dark matter halo concentrations and density profiles," MNRAS **457**, 4340 (2016).

[246] V. Springel, "The cosmological simulation code GADGET-2," MNRAS **364**, 1105 (2005).

[247] Planck Collaboration, "Planck 2013 results. XVI. Cosmological parameters," A&A **571**, A16 (2014).

[248] P. S. Behroozi, R. H. Wechsler, and H. Y. Wu, "The ROCKSTAR Phase-space Temporal Halo Finder and the Velocity Offsets of Cluster Cores," ApJ **762**, 109 (2013).

[249] P. Behroozi et al., "UniverseMachine: The Correlation between Galaxy Growth and Dark Matter Halo Assembly from z=0-10," arXiv:1806.07893 (2018).

[250] M. Ho et al., "A Robust and Efficient Deep Learning Method for Dynamical Mass Measurements of Galaxy Clusters," arXiv:1902.05950 (2019).

[251] W. J. Handley, M. P. Hobson, and A. N. Lasenby, "POLYCHORD: next-generation nested sampling," MNRAS **453**, 4384 (2015).

[252] M. Baldi, "The CoDECS project: a publicly available suite of cosmological N-body simulations for interacting dark energy models," MNRAS **422**, 1028 (2012).

[253] M. Ntampaka et al., "Dynamical Mass Measurements of Contaminated Galaxy Clusters Using Machine Learning," ApJ **831**, 135 (2016).

[254] R. E. Kass and A. E. Raftery, "Bayes Factors," Journal of the American Statistical Association **90**, 773 (1995).

[255] T. C. Beers, M. J. Geller, and J. P. Huchra, "Galaxy clusters with multiple components. I - The dynamics of Abell 98," ApJ **257**, 23 (1982).

[256] M. J. Geller, "When clusters are superclusters," Comments on Astrophysics **10**, 47 (1984).

[257] N. Okabe et al., "LoCuSS: Subaru Weak Lensing Study of 30 Galaxy Clusters," Publications of the Astronomical Society of Japan **62**, 811 (2010).

[258] R. Wojtak, S. Gottlöber and A. Klypin, "Orbital anisotropy in cosmological haloes revisited," MNRAS **434**, 1576 (2013).

[259] G. A. Mamon and E. L. Lokas, "Dark matter in elliptical galaxies - II. Estimating the mass within the virial radius," MNRAS **363**, 705 (2005).

[260] A. A. Dutton and A. V. Macci, "Cold dark matter haloes in the Planck era: evolution of structural parameters for Einasto and NFW profiles," MNRAS **441**, 3359 (2014).

[261] B. Diemer, Benedikt and A. V. Kravtsov, "A Universal Model for Halo Concentrations," ApJ **799**, 108 (2015).

[262] H. Yu et al., "The Unrelaxed Dynamical Structure of the Galaxy Cluster Abell 85," ApJ **831**, 156 (2016).

[263] A. Liu et al., "Inside a Beehive: The Multiple Merging Processes in the Galaxy Cluster Abell 2142," ApJ **863**, 102 (2018).

[264] N. Okabe and G. P. Smith, "LoCuSS: weak-lensing mass calibration of galaxy clusters," MNRAS **461**, 3794 (2016).

[265] E. Jiménez-Bailón, M. Lozada-Muñoz, and J. A. L. Aguerri, "X-ray emission from RX J1720.1+2638 and Abell 267: A comparison between a fossil and a non-fossil system," Astronomische Nachrichten **334**, 377 (2013).

[266] B. J. Brewer and D. Foreman-Mackey, "DNest4: Diffusive Nested Sampling in C++ and Python," arXiv:1606.03757 (2016).

[267] J. A. Newman et al., "The DEEP2 Galaxy Redshift Survey: Design, Observations, Data Reduction, and Redshifts," ApJS **208**, 5 (2013).

[268] S. Fabbro et al., "An application of deep learning in the analysis of stellar spectra," MNRAS **475**, 2978 (2017).

[269] T. Yang and X. Li, "An autoencoder of stellar spectra and its application in automatically estimating atmospheric parameters," MNRAS **452**, 158 (2015).

[270] X. R. Li, R. Y. Pan, and F. Q. Duan, "Parameterizing Stellar Spectra Using Deep Neural Networks," Research in Astronomy and Astrophysics **17**, 36 (2017).